SAND2010-8202P

Generic Disposal System Environment Modeling – Fiscal Year 2010 Progress Report

Fuel Cycle Research & Development

Prepared for
U.S. Department of Energy
Used Fuel Disposition

Yifeng Wang and Joon H. Lee (editors)
Sandia National Laboratories

September 17, 1020

Sandia National Laboratories is a multi-program laboratory managed and operated by Sandia Corporation, a wholly owned subsidiary of Lockheed Martin Corporation, for the U.S. Department of Energy's National Nuclear Security Administration under contract DE-AC04-94AL85000

Reviewed by:

Acting Director, Fuel Cycle Research and Development

Robert Price Date

Concurred by:

Director, AFCI Technical Integration Office

Phillip Finck Date

Approved by:

Deputy Assistant Secretary, Fuel Cycle Management

(AFCI Program Manager) Paul Lisowski Date

SUMMARY

The Generic Disposal System Environment (GDSE) model development is focused on the comparative study of different disposal environments to support the development of long-term Used Fuel Disposition (UFD) strategy:

1. Develop a fundamental understanding of disposal system performance in a range of environments for potential wastes that could arise from future nuclear fuel cycle alternatives through theory, simulation, testing, and experimentation.
2. Develop a computational modeling capability for the performance of storage and disposal options for a range of fuel cycle alternatives, evolving from generic models to more robust models of performance assessment.

The GDSE work develops necessary modeling tools that can be used to support management decision and task prioritization related to the development of alternative nuclear waste disposal strategies.

The GDSE modeling activities summarized in this report follow the two main themes: (1) development of simplified performance assessment (PA) models for different disposal environments, and (2) detailed process-level studies to support PA model development. For FY10, the former is focused on four generic disposal environments (salt, granite, clay, and deep borehole) and the latter on the thermal-hydrologic-mechanical-chemical couplings in the near-field of a clay repository. Parallel to the main themes, the GDSE modeling work in FY 10 also intends (1) to impose a uniform set of assumptions on different GDSE models to facilitate inter-model comparisons and (2) at the same time to develop the GDSE models that will be flexible enough to deal with future repository configurations and engineering designs.

This report, consisting of six self-contained chapters, summarizes the work accomplished for the GDSE model development in FY10:

- Chapter 1 intends to provide a unified source-term model and dose calculation module for different GDSE models. The description of inventory data synthesis, thermal output calculations for various waste forms, and our initial attempt to capture the thermal effect on radionuclide solubilities are provided.
- Chapters 2, 3, and 5 describe the initial version of GDSE models for salt, granite, and deep borehole disposal environments and discuss the preliminary results of model analyses. The model simulations show that soluble, non-sorbing fission products, particularly ^{129}I and ^{79}Se, are major contributors to the total radionuclide dose release. The sensitivity analyses indicate that groundwater flow rate, waste form degradation rate, and radionuclide sorption are among the main factors that control total dose release.
- The work described in Chapter 4 is focused on the enhancement of structural flexibility for the clay GDSE model. The general model framework has been established and preliminary demonstration testing has been performed. Preliminary results indicate that a wide range of output can be generated for different fuel cycle scenarios. The modeling approach presented in this chapter may be applicable to other disposal environments as well.

- Chapter 6 is focused on the development of process-level models for capturing complex thermal-hydrologic-mechanical-chemical couplings in the near-field of a clay repository. The purpose of this study is to demonstrate the current modeling capabilities in dealing with coupled processes in a potential clay repository. The process-level understanding is the key to the confidence building of a PA-level model.

GDSE model development is a continuing process, and the models described in this chapter are all preliminary. Nevertheless, the work presented in this report constitutes the first necessary step toward the ultimate goal for fully comparable and highly flexible GDSE models. The future work may include:

- Refining repository performance scenarios for each disposal environment based on more systematic Feature, Event, and Process (FEP) analysis. This work will be closely coordinated with other FEP analysis and screening activities.
- Continuing develop a unified source term model and impose a consistent set of assumptions on all GDSE models. This may require development of a centralized GDSE PA database.
- Enhancing GDSE model capabilities by integrating more physical/chemical process components into the models. For example, it is desirable to explicitly incorporate near-field thermal evolution and its impacts on water flow and radionuclide mobility. To do so requires the thermal models with various levels of complexity.
- Closely working the engineered barrier system (EBS) evaluation and tool development team to incorporate EBS components into the GDSE models as they become available.
- Continuing key physical/chemical process studies related to nuclear waste disposal. The work documented in Chapter 6 provides a good example for future studies in this area. The similar approach can be extended to other systems.

CONTENTS

SUMMARY 3

Chapter 1 Toward Comparative Generic Disposal System Environment (GDSE) modeling: Development of Unified Reference Source-Term Model 8
1. Introduction 8
2. General Model Development Approach 9
3. Reference Repository Layout 9
4. Waste Package Configurations 10
5. Waste Inventory 10
6. Waste Package Thermal Heat Output 17
7. Waste Package Temperature 21
8. Waste Form Degradation 21
9. Near-Field Volume 22
10. Radionuclide Solubility 23
11. Repository Waste Inventory Scenarios 29
12. Radionuclide Release Scenarios 29
13. Generic Reference Biosphere Model 30
14. Concluding remarks 30
15. References 31

Chapter 2 Salt Generic Disposal System Environment Model 32
1. Introduction 32
2. Conceptual Model 32
3. Model Implementation and Structure 34
4. Model results 38
5. Summary and Discussion 43
6. References 44

Chapter 3 Granite Generic Disposal System Environment Model 46
1. Introduction 46
2. Model Description 46
2.1. Granite GDSE Model Structure 46
2.2. Near Field of Granite GDSE 48
2.3. Far Field of Granite GDSE 50
2.4. Implementation of Uncertain Parameters in Granite GDSE 52
3. Model Results 52
4. Concluding Remark 68
5. References 68

Chapter 4 Clay Generic Disposal System Environment Model 70
1. Introduction 70

2. Model Description 70
2.1. Clay Thermal Model 73
2.2. Clay Long Term Repository Performance GDSE Model 74
3. Demonstration 90
3.1. Thermal Model 91
3.2. Long Term Repository Performance Model 94
4. Conclusions 99
5. References 100
Appendix A: Comparison of Numerical Approach for Two-Dimensional Modeling of the Far Field with Analytic Solutions 102

Chapter 5 Deep Borehole Generic Disposal System Environment Model 109
1. Introduction 109
2. Conceptual Model 109
3. Model Implementation and Structure 112
4. Model results 116
5. Summary and Discussion 120
6. References 122

Chapter 6 Clay Generic Disposal System Environment Model: Process-Level Models 123
1. Introduction 123
2. Constitutive Relationships for Elastic Deformation of Indurated Clay Rock 124
2.1. Stress-strain relationship 124
2.2. Stress-dependent hydraulic properties 127
2.3. Effective stress for fractures involving rock swelling 130
2.4. Data Analyses 132
2.5. Summary and Directions of Future Research 140
3. THM Modeling in Clay/Shale Environments 140
3.1. Modeling Tools for Coupled THM processes 141
3.2. Comparison of ROCMAS and TOUGH-FLAC to Other THM codes 145
3.3. Simulation of a Generic Repository in Clay Host Rock 146
4. THC Modeling in clay/shale Environments 151
4.1. TOUGHREACT Code 151
4.2. Application of TOUGHREACT to Bentonite-Filled EBS and Clay Formation 153
5. Knowledge Gaps and R&D Plan 162
6. Summary and FEPs Crosswalk 171
7. References 174

Chapter 1 Toward Comparative Generic Disposal System Environment (GDSE) modeling: Development of Unified Reference Source-Term Model

Joon H Lee, Carlos Jove-Colon and Yifeng Wang

Sandia National Laboratories

1. Introduction

In order to make meaningful comparisons of waste isolation performance for different geological disposal system environment (GDSE) options, it is necessary to employ, to the extent applicable, uniform modeling assumptions and approaches in the analysis. For this effort, a reference source-term model was developed for use across GDSE options. The reference source-term model has incorporated the following model components and/or analyses:

- Reference repository layout
- Waste package configurations
- Inventory for different waste types [the commercial used nuclear fuels (UNF), the existing DOE high-level waste (HLW), and the hypothetical reprocessing high-level waste of commercial UNF]
- Waste package thermal heat output
- Waste package temperature
- Solubility of key radionuclides
- Waste form degradation
- Near-field volume
- Repository waste inventory scenarios
- Repository radionuclide release and transport scenarios
- Reference biosphere model

The reference source-term model was implemented in Goldsim and provided as a model template to GDSE option analysis. Although it is not part of the reference source-term model, the biosphere model is included in the Goldsim model template to allow application of uniform dose conversion calculations for the GDSE analysis. This chapter discusses the implementation of the reference source-term model.

The GDSE model development is a continuing process. Development of the reference source model described in this chapter is the first necessary step toward the ultimate goal for fully comparable GDSE models. Given the fact that each GDSE model described in this report is still at its preliminary stage, and because of the tight time constraints, not all components proposed in the reference source model have been implemented in fiscal year 2010. Specifically, because the thermal history calculation has not been fully implemented in the Goldsim source-term model by the time of the report preparation, the source-term model in the version described here uses a constant ambient temperature of 25 °C for the waste package and near-field

environment. This limits the application of the temperature-dependent radionuclide solubility model for the near-field water to 25°C. Also, because of time constraint, the GDSE analysis for this fiscal year did not consider performance of the waste package. However, certain aspects of waste package configurations are included for use in other sub-model components, including repository footprint, waste package radionuclide inventory, waste package heat output, etc.

It should be also noted that, because time constraint, the proposed reference source model has not been uniformly implemented across all GDSE models presented in this report. Up to date, this model has been implemented only for the salt, granite, and deep borehole disposal options to the extent applicable.

2. General Model Development Approach

Figure 1 shows the general conceptual approach for modeling each GDSE. The GDSE models are developed using the GoldSim software (GoldSim 2009), with additional codes linked to GoldSim as necessary. For simplicity, a disposal system is divided into two regions, termed the "near field" and "far field" regions. Key processes such as radionuclide dissolution/precipitation (solubility), dispersion, matrix diffusion, and reversible sorption are included in each GDSE model. The "near field" region represents the region surrounding the Engineered barrier system (EBS) (e.g., the first several meters of a GDSE). A one-dimensional network of "batch reactor" mixing cells is used to model contaminant transport through this region. Hydrologic and geochemical properties of the mixing cells are determined from literature. Except the deep borehole GDSE analysis as described in Chapter 5, ambient geochemical conditions are applied in the near field to determine dissolved concentration limits. Details regarding the reference source-term model are described in this chapter. Details of the far-field model for individual GDSEs are described in their respective chapters.

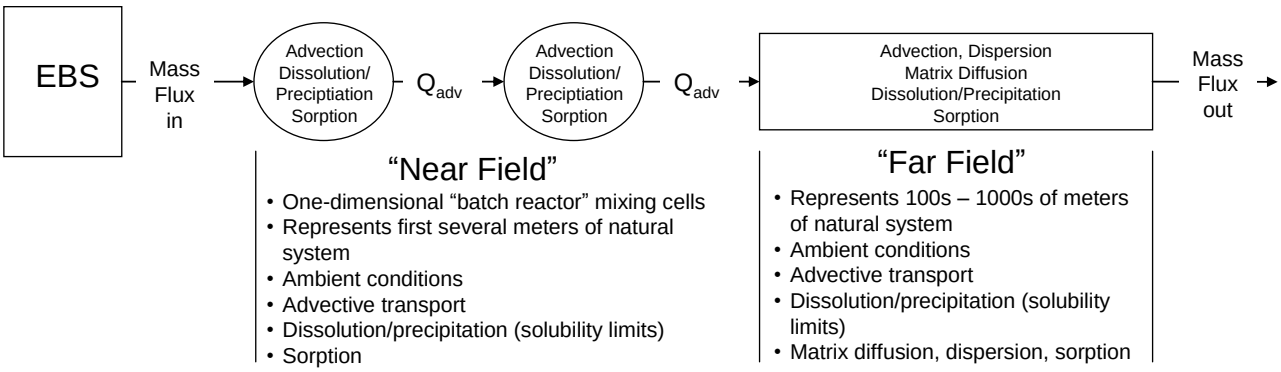

Note: Figure is schematic only and shows the general conceptualization of the GDSE models. The specific representation of the reference source-term model is discussed in this section, and that of the far-field model of each GDSE is discussed in its respective section.

Figure 1: Overall conceptual approach for modeling "generic" disposal system environments (GDSEs)

3. Reference Repository Layout

For simplification, it is assumed that repository has a square footprint. Knowing the total number of waste packages (N_{WP}) to be disposed of in the repository, the side length (L_{Rep}) of a square repository footprint can be calculated as follows:

$$\frac{L_{Rep}}{L_{WP} + S_{WP}} \times \frac{L_{Rep}}{S_{drift}} = N_{WP} \quad , \tag{1}$$

where L_{WP} is the length of waste package (5.5 m), S_{WP} is the spacing between waste packages (6 m), and S_{drift} is the spacing between emplacement tunnels (25 m). The waste package length is from the package design for the German salt repository program (Janberg and Spilker 1998). The values for the waste package spacing and emplacement tunnel spacing were taken from the SKB repository design (Claesson and Probert 1996; SKB 2006).

4. Waste Package Configurations

The waste cask design for spent nuclear fuels of the German salt disposal program (Janberg and Spilker 1998) was used for the waste package configurations for the source-term model. The outer diameter of waste package is 1.56 m, and the outer length 5.5 m. Each waste package is assumed to hold 10 PWR commercial used fuel assemblies, 5 DOE HLW canisters, or 5 reprocessing HLW canisters. As mentioned above, this year's GDSE analysis did not consider performance of waste package. The assumed waste package configurations are used in sub-model components such as repository footprint, waste package radionuclide inventory, waste package heat output, etc.

5. Waste Inventory

Three different types of high-level radioactive waste (HLW) were considered in the source-term model: commercial used nuclear fuel (UNF), existing DOE HLW, and reprocessing HLW of the commercial used nuclear fuel. The source-term model radionuclide inventory analysis was based on the detailed fuel cycle waste inventory analysis provided by Carter and Luptak (2010).

Commercial Used Nuclear Fuel Inventory: The once-through fuel cycle waste inventory analysis considers four scenarios to evaluate the projected increases in the commercial light water reactor (LWR) UNF inventory. The scenarios are considered to provide a wide range of LWR fuel inventory for use in future analysis (Carter and Luptak 2010, section 3.2). The source-term model inventory analysis uses Scenario 1, which assumes no replacement of existing nuclear generation reactors. Selection of this scenario for the source-term analysis is arbitrary, and it can be revised as needed in future analyses. For this scenario, a total of 140,000 metric tons uranium (MTU) used fuel is estimated to be discharged from reactors (Carter and Luptak 2010, Table 3-5). Out of the total inventory, 91,000 MTU is for the pressurized water reactors (PWR) used fuels with an estimated total of 209,000 assemblies. This is equivalent to 0.435 MTU per PWR assembly.

For simplification, the total inventory is converted to the equivalent PWR inventory, resulting in a total of 321,540 PWR assemblies. The source-term model assumes that a waste package contains 10 PWR assemblies, and a total of 32,154 waste packages are needed for disposal of the commercial UNF.

The isotopic inventory of the UNF is assumed to be represented by the PWR fuel with a burn-up of 60 GWd/MTIHM and 4.73% enrichment and aged 30 years after discharge from reactor (Carter and Luptak 2010, table C-1). The isotopic inventory for the radionuclides of the commercial UNF included in the source-term model is shown in Table 1.

Table 1: Isotopic inventory for commercial UNF used for the GDSE source-term models

Isotope	Half Life (years)	Fractional Mass Inventory	Isotope mass per WP (g)
Ac-227	2.18E+01	2.7469E-13	1.1960E-06
Am-241	4.32E+02	8.7003E-04	3.7882E+03
Am-243	7.37E+03	1.8796E-04	8.1841E+02
C-14	5.71E+03	3.1524E-07	1.3726E+00
Cl-36	3.01E+05	3.4808E-07	1.5156E+00
Cm-245	8.50E+03	6.6221E-06	2.8833E+01
Cs-135	2.30E+06	5.3570E-04	2.3325E+03
Cs-137	3.01E+01	7.2561E-04	3.1593E+03
I-129	1.70E+07	2.1754E-04	9.4720E+02
Nb-93	1.36E+01	4.9591E-04	2.1592E+03
Np-237	2.14E+06	8.5892E-04	3.7398E+03
Pa-231	3.25E+04	7.1103E-10	3.0959E-03
Pb-210	2.26E+01	7.8324E-15	3.4103E-08
Pd-107	6.50E+06	2.8663E-04	1.2480E+03
Pu-238	8.77E+01	3.4170E-04	1.4878E+03
Pu-239	2.41E+04	5.1487E-03	2.2418E+04
Pu-240	6.54E+03	2.8427E-03	1.2377E+04
Pu-241	1.44E+01	2.6198E-04	1.1407E+03
Pu-242	3.76E+05	5.6750E-04	2.4709E+03
Ra-226	1.60E+03	2.2081E-12	9.6141E-06
Ra-228	6.70E+00	1.4339E-18	6.2431E-12
Sb-126	3.61E-05	1.6470E-12	7.1713E-06
Se-79	6.50E+04	7.2769E-06	3.1684E+01
Sn-126	1.00E+05	3.4663E-05	1.5092E+02
Sr-90	2.91E+01	3.0809E-04	1.3414E+03
Tc-99	2.13E+05	8.8739E-04	3.8638E+03
Th-229	7.90E+03	4.4252E-12	1.9267E-05
Th-230	7.54E+03	1.5838E-08	6.8961E-02
Th-232	1.41E+10	4.2412E-09	1.8466E-02
U-232	6.89E+01	3.1642E-09	1.3777E-02

Isotope	Half Life (years)	Fractional Mass Inventory	Isotope mass per WP (g)
U-233	1.59E+05	9.7002E-09	4.2235E-02
U-234	2.45E+05	2.1220E-04	9.2392E+02
U-235	7.04E+08	3.7329E-03	1.6253E+04
U-236	2.34E+07	4.3349E-03	1.8874E+04
U-238	4.46E+09	6.3215E-01	2.7524E+06
Zr-93	1.53E+06	1.0193E-03	4.4382E+03

DOE High-Level Radioactive Waste: All existing DOE high-level radioactive waste (HLW) is assumed to be immobilized in borosilicate glass logs. The source-term analysis uses the best-estimate projected total number of DOE HLW canisters documented in the fuel cycle inventory analysis report (Carter and Luptak 2010, table 2-2); the best estimate projection is 25,016 canisters. The source-term model assumes that each waste package contains 5 HLW canisters, and a total of 5,003 waste packages are needed for disposal of the DOE HLW.

The isotope inventory of the DOE HLW is given for each radionuclide in terms of the total radioactivity (*Ci*) in the fuel cycle inventory analysis report (Carter and Luptak 2010, table F-1). The radioactivity was converted to the equivalent mass (m_i) for each radionuclide as follows:

$$m_i\,(g) = \frac{A_i \cdot t_{\frac{1}{2},i} \cdot MW_i}{0.693 \cdot N_A} \qquad (2)$$

where A_i is the radioactivity of radionuclide i, $t_{1/2,i}$ is the half-life of radionuclide i, MW_i is the molecular weight of radionuclide i, and N_A is the Avogadro constant (6.023×10^{23}). The total mass of radionuclides of the existing DOE HLW is estimated 1,759 MT. This gives 0.07 MT of radionuclides per HLW canister, and 0.35 MT of radionuclides per waste package. The isotopic inventory per HLW canister and per waste package is given in Table 2.

Table 2: Isotopic Inventory for DOE HLW used for the source-term model analysis

Isotope	Half Life (years)	Fractional Mass Inventory	Isotope mass per canister (g)	Isotope mass per WP (g)
Ac-227	2.18E+01	1.139E-09	8.010E-05	4.005E-04
Am-241	4.32E+02	4.022E-04	2.829E+01	1.414E+02
Am-243	7.37E+03	2.732E-05	1.922E+00	9.608E+00
C-14	5.71E+03	1.747E-08	1.228E-03	6.142E-03
Cl-36	3.01E+05	0.000E+00	0.000E+00	0.000E+00
Cm-245	8.50E+03	5.428E-07	3.817E-02	1.909E-01
Cs-135	2.30E+06	1.759E-03	1.237E+02	6.184E+02
Cs-137	3.01E+01	2.219E-03	1.561E+02	7.804E+02
I-129	1.70E+07	1.802E-04	1.268E+01	6.338E+01
Nb-93	1.36E+01	0.000E+00	0.000E+00	0.000E+00
Np-237	2.14E+06	3.004E-04	2.113E+01	1.056E+02
Pa-231	3.25E+04	3.452E-06	2.427E-01	1.214E+00
Pb-210	2.26E+01	1.317E-13	9.264E-09	4.632E-08
Pd-107	6.50E+06	2.188E-05	1.539E+00	7.696E+00
Pu-238	8.77E+01	2.070E-04	1.456E+01	7.279E+01
Pu-239	2.41E+04	1.749E-03	1.230E+02	6.151E+02
Pu-240	6.54E+03	1.865E-04	1.312E+01	6.559E+01
Pu-241	1.44E+01	2.468E-06	1.736E-01	8.678E-01
Pu-242	3.76E+05	2.154E-05	1.515E+00	7.573E+00
Ra-226	1.60E+03	5.747E-11	4.042E-06	2.021E-05
Ra-228	6.70E+00	4.563E-11	3.209E-06	1.604E-05
Sb-126	3.61E-05	5.728E-12	4.029E-07	2.014E-06
Se-79	6.50E+04	3.085E-04	2.169E+01	1.085E+02
Sn-126	1.00E+05	1.215E-04	8.548E+00	4.274E+01
Sr-90	2.91E+01	9.262E-04	6.514E+01	3.257E+02
Tc-99	2.13E+05	3.212E-03	2.259E+02	1.129E+03
Th-229	7.90E+03	9.980E-09	7.019E-04	3.509E-03
Th-230	7.54E+03	4.546E-09	3.197E-04	1.599E-03
Th-232	1.41E+10	9.894E-02	6.958E+03	3.479E+04
U-232	6.89E+01	1.141E-09	8.022E-05	4.011E-04

Isotope	Half Life (years)	Fractional Mass Inventory	Isotope mass per canister (g)	Isotope mass per WP (g)
U-233	1.59E+05	5.300E-05	3.727E+00	1.864E+01
U-234	2.45E+05	7.431E-05	5.226E+00	2.613E+01
U-235	7.04E+08	3.732E-03	2.625E+02	1.312E+03
U-236	2.34E+07	2.863E-04	2.014E+01	1.007E+02
U-238	4.46E+09	8.821E-01	6.204E+04	3.102E+05
Zr-93	1.53E+06	1.739E-03	1.223E+02	6.115E+02

Reprocessing High-Level Radioactive Waste: The fuel cycle inventory analysis report discusses several candidate reprocessing methods for commercial UNF and their potential waste streams (Carter and Luptak 2010, Section 4). For simplification, the following assumptions are made for "hypothetical" reprocessing of commercial UNF:

- Ninety nine percent (99%) of uranium and plutonium are recovered. All others including minor transuranic elements and fission products of the commercial UNF inventory (140,000 MTU) remain in the waste streams.
- Reprocessing HLW is immobilized in borosilicate glass as for the DOE HLW.
- Reprocessing HLW is encapsulated at the same radionuclide mass loading as for the DOE HLW (i.e., 0.07 MT radionuclide mass per canister).

Note that the above assumptions result in higher concentrations of fission products in the hypothetical reprocessing waste streams and glass waste form than the DOE HLW. The total radionuclide mass of the hypothetical reprocessing HLW is estimated 1,426 MT (after removing 99% of uranium and plutonium). With a radionuclide mass loading of 0.07 MT per canister, this is equivalent to a total of 20,276 canisters. The source-term model assumes that each waste package contains five reprocessing HLW canisters, and a total of 4,055 waste packages are needed for disposal. The isotopic inventory for reprocessing waste is given in Table 3.

Table 3: Isotope Inventory for Reprocessing HLW Used for Source-term Model Analysis

Isotope	Half Life (years)	Fractional Mass Inventory	Isotope mass per canister (g)	Isotope mass per WP (g)
Ac-227	2.18E+01	2.6969E-11	1.8967E-06	9.4833E-06
Am-241	4.32E+02	8.5419E-02	6.0073E+03	3.0037E+04
Am-243	7.37E+03	1.8454E-02	1.2978E+03	6.4892E+03
C-14	5.71E+03	3.0950E-05	2.1766E+00	1.0883E+01
Cl-36	3.01E+05	0.0000E+00	0.0000E+00	0.0000E+00
Cm-245	8.50E+03	6.5015E-04	4.5724E+01	2.2862E+02
Cs-135	2.30E+06	5.2594E-02	3.6989E+03	1.8494E+04
Cs-137	3.01E+01	7.1239E-02	5.0101E+03	2.5051E+04
I-129	1.70E+07	2.1358E-02	1.5021E+03	7.5104E+03
Nb-93	1.36E+01	6.8717E-07	4.8327E-02	2.4164E-01
Np-237	2.14E+06	8.4328E-02	5.9306E+03	2.9653E+04
Pa-231	3.25E+04	6.9808E-08	4.9094E-03	2.4547E-02
Pb-210	2.26E+01	7.6897E-13	5.4080E-08	2.7040E-07
Pd-107	6.50E+06	2.8141E-02	1.9791E+03	9.8956E+03
Pu-238	8.77E+01	3.3547E-05	2.3593E+00	1.1797E+01
Pu-239	2.41E+04	5.0549E-04	3.5550E+01	1.7775E+02
Pu-240	6.54E+03	2.7909E-04	1.9628E+01	9.8141E+01
Pu-241	1.44E+01	2.5721E-05	1.8089E+00	9.0446E+00
Pu-242	3.76E+05	5.5717E-05	3.9184E+00	1.9592E+01
Ra-226	1.60E+03	2.1679E-10	1.5246E-05	7.6230E-05
Ra-228	6.70E+00	1.4077E-16	9.9004E-12	4.9502E-11
Sb-126	3.61E-05	1.6170E-10	1.1372E-05	5.6861E-05
Se-79	6.50E+04	7.1444E-04	5.0245E+01	2.5122E+02
Sn-126	1.00E+05	3.4031E-03	2.3933E+02	1.1967E+03
Sr-90	2.91E+01	3.0248E-02	2.1273E+03	1.0636E+04
Tc-99	2.13E+05	8.7123E-02	6.1272E+03	3.0636E+04
Th-229	7.90E+03	4.3446E-10	3.0554E-05	1.5277E-04
Th-230	7.54E+03	1.5550E-06	1.0936E-01	5.4680E-01
Th-232	1.41E+10	4.1639E-07	2.9284E-02	1.4642E-01
U-232	6.89E+01	3.1066E-10	2.1848E-05	1.0924E-04

Isotope	Half Life (years)	Fractional Mass Inventory	Isotope mass per canister (g)	Isotope mass per WP (g)
U-233	1.59E+05	9.5236E-10	6.6977E-05	3.3489E-04
U-234	2.45E+05	2.0833E-05	1.4652E+00	7.3258E+00
U-235	7.04E+08	3.6649E-04	2.5775E+01	1.2887E+02
U-236	2.34E+07	4.2559E-04	2.9931E+01	1.4966E+02
U-238	4.46E+09	6.2063E-02	4.3648E+03	2.1824E+04
Zr-93	1.53E+06	1.0008E-01	7.0381E+03	3.5191E+04

6. Waste Package Thermal Heat Output

Waste package thermal heat output is one of the most important parameters for repository design and thermal load management. Using the isotopic inventory per waste package discussed above, ORIGEN simulations were conducted to calculate the waste package heat outputs as function of time for the three different waste types. The ORIGEN simulation results were then fit to the functional form of

$$\ln Q = -m \cdot t + b \quad , \tag{3}$$

where Q is the waste package heat output in watts (W), t is the time in years, m is the slope, and b is the intercept. The curve-fitting was done for a sequence of time intervals where within each interval the simulation results show a linear relationship between the $\ln Q$ and t. Within each interval, the curve-fit equations are expressed as the following form:

$$Q = C_0 \exp\left(\frac{-t}{C_1}\right) \tag{4}$$

C_0 and C_1 are fitted constants. This particular functional form for the waste package heat output is used to conform to the input required for the analytical solution to calculate the waste package temperature as a function of time as discussed in Section 7 of this chapter.

Commercial UNF Waste Package: The resulting curve fits for the heat output of the commercial UNF waste package for various time periods are given in Equations (5) to (9). A plot of the heat output equations and ORIGEN simulation results are shown in Figure 2. Equation (10) ($Q_{UNF\ WP,total}$), which combines Equations (5) to (9), is used in an analytical heat-conduction solution to calculate the commercial UNF waste package temperature as a function of time. As shown in Figure 2, because of the way that the equations are added, the total heat output ($Q_{UNF\ WP,total}$) slightly over-estimates the ORIGEN results.

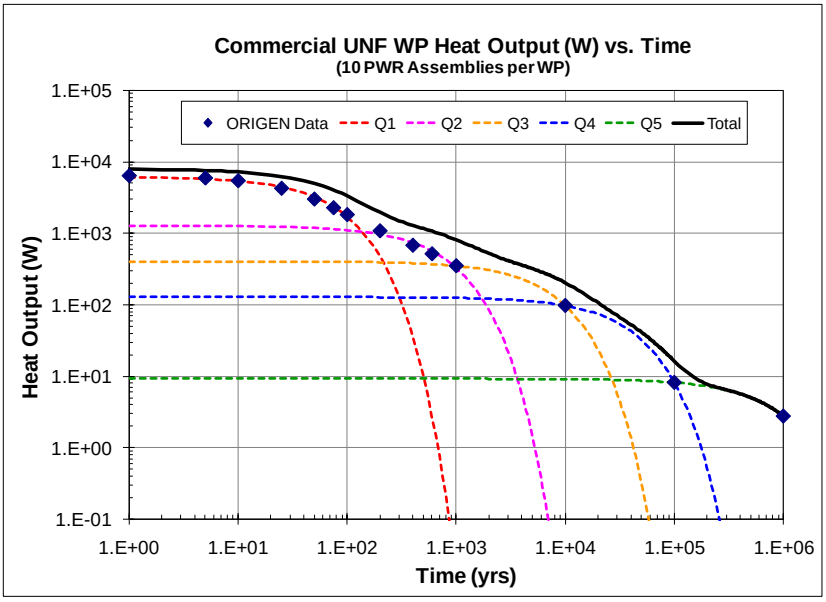

Figure 2: Curve-fit to the ORIGEN calculation data for thermal heat output of commercial UNF waste package as a function of time.

$$Q_{UNF\ WP,1} = 6134\ \exp\left(\frac{-t}{78}\right)\ \ for\ 1\ to\ 10^2\ years \tag{5}$$

$$Q_{UNF\ WP,2} = 1266\ \exp\left(\frac{-t}{739}\right)\ \ for\ 10^2\ to\ 10^3\ years \tag{6}$$

$$Q_{UNF\ WP,3} = 403\ \exp\left(\frac{-t}{7035}\right)\ \ for\ 10^3\ to\ 10^4\ years \tag{7}$$

$$Q_{UNF\ WP,4} = 128\ \exp\left(\frac{-t}{36308}\right)\ \ for\ 10^4\ to\ 10^5\ years \tag{8}$$

$$Q_{UNF\ WP,5} = 9.2\ \exp\left(\frac{-t}{829680}\right)\ \ for\ 10^5\ to\ 10^6\ years \tag{9}$$

$$Q_{UNF\ WP,total} = Q_{UNF\ WP,1} + Q_{UNF\ WP,2} + Q_{UNF\ WP,3} + Q_{UNF\ WP,4} + Q_{UNF\ WP,5} \tag{10}$$

DOE HLW Waste Package: The equations to calculate the heat output of the DOE HLW waste package for various time periods are given in Equations (11) to (16). Figure 3 shows a plot of the heat output equations and ORIGEN simulation results. Equation (16) for $Q_{HLW\ WP,total}$, which adds the equations for each time period, is used in the analytical solution to calculate the DOE HLW waste package temperature as a function of time. Like the commercial UNF waste package, the total heat output equation ($Q_{HLW\ WP,total}$) slightly over-estimates the ORIGEN results. Compared to the commercial UNF waste package, the DOE HLW waste package releases less heat and is expected to have a lower temperature history in the repository.

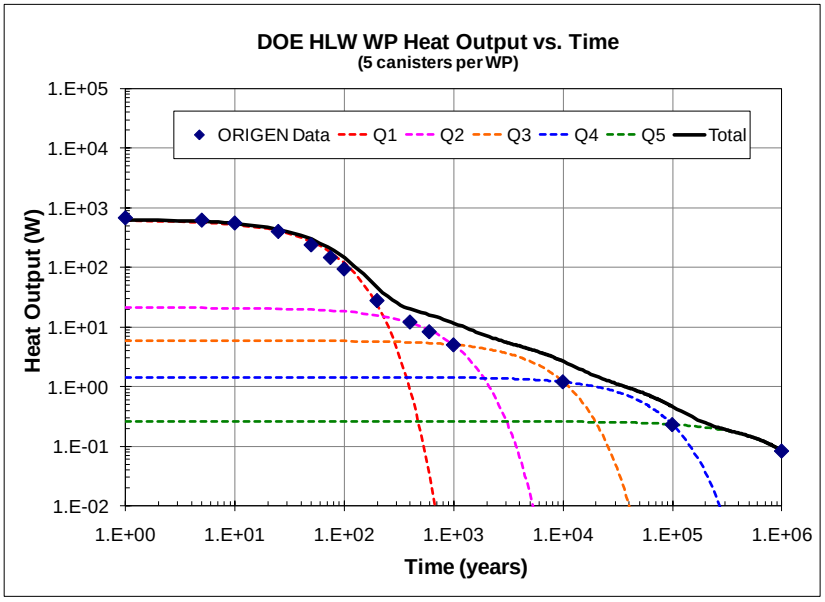

Figure 3: Curve-fit to the ORIGEN calculation data for thermal heat output of DOE HLW waste package as a function of time.

$$Q_{\mathbf{HLW\ WP,1}} = \mathbf{612}\ \exp\left(\frac{-t}{\mathbf{61}}\right) \quad for\ \mathbf{1}\ to\ \mathbf{2\times10^{2}}\ years \tag{11}$$

$$Q_{HLW\ WP,\mathbf{2}} = 21\ \exp\left(\frac{-t}{\mathbf{693}}\right) \quad for\ 4\times\mathbf{10^{2}}\ to\ \mathbf{10^{3}}\ years \tag{12}$$

$$Q_{HLW\ WP,\mathbf{3}} = 5.89\ \exp\left(\frac{-t}{\mathbf{6291}}\right) \quad for\ \mathbf{10^{3}}\ to\ \mathbf{10^{4}}\ years \tag{13}$$

$$Q_{HLW\ WP,\mathbf{4}} = 1.44\ \exp\left(\frac{-t}{\mathbf{54330}}\right) \quad for\ \mathbf{10^{4}}\ to\ \mathbf{10^{5}}\ years \tag{14}$$

$$Q_{HLW\ WP,5} = 0.26\ \exp\left(\frac{-t}{880816}\right)\ \ for\ 10^5\ to\ 10^6\ years \tag{15}$$

$$Q_{HLW\ WP,total} = Q_{HLW\ WP,1} + Q_{HLW\ WP,2} + Q_{HLW\ WP,3} + Q_{HLW\ WP,4} + Q_{HLW\ WP,5} \tag{16}$$

Reprocessing HLW Waste Package: The equations to calculate the heat output of the waste package of the "hypothetical" reprocessing HLW are given in Equations (17) to (21). Figure 4 shows a plot of the heat output equations and ORIGEN simulation results. Equation (21) for $Q_{RW\ WP,total}$ is used in the analytical solution to calculate the reprocessing HLW waste package temperature as a function of time. Like two other waste-type waste packages, the total heat output equation ($Q_{RW\ WP,total}$) slightly over-estimates the ORIGEN results. The reprocessing HLW waste package has the highest heat output among the three waste types, because of the concentration of fission products in the waste stream as a result of recovery of 99% uranium and plutonium from the 140,000 MTU commercial UNF with all other components remaining in the waste stream.

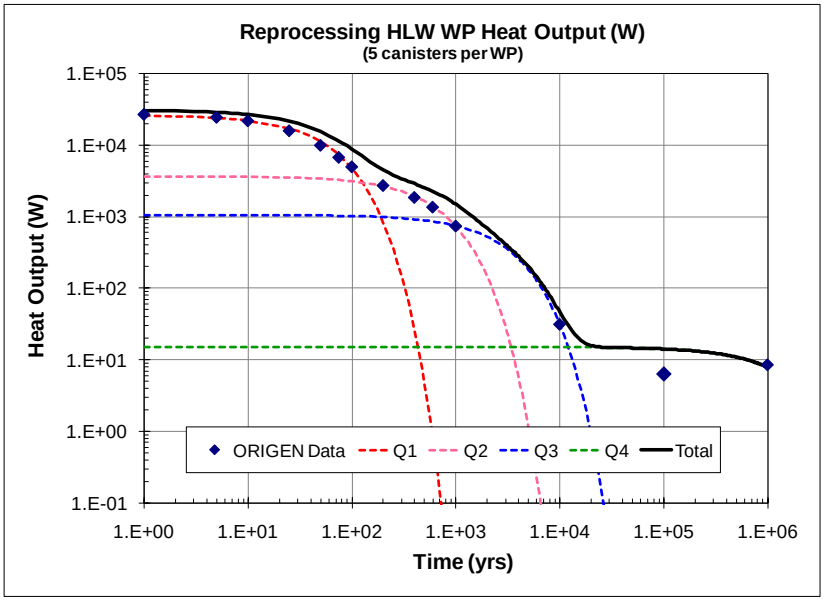

Figure 4: Curve-fit to the ORIGEN calculation data for thermal heat output of reprocessing HLW waste package as a function of time.

$$Q_{RW\,WP,1} = 26163\ \exp\left(\frac{-t}{58}\right)\ for\ 1\ to\ 10^2\ years \quad (17)$$

$$Q_{RW\,WP,2} = 3679\ \exp\left(\frac{-t}{620}\right)\ for\ 10^2\ to\ 10^3\ years \quad (18)$$

$$Q_{RW\,WP,3} = 1060\ \exp\left(\frac{-t}{2840}\right)\ for\ 10^3\ to\ 10^4\ years \quad (19)$$

$$Q_{RW\,WP,4} = 15.14\ \exp\left(\frac{-t}{1537910}\right)\ for\ 10^4\ to\ 10^6\ years \quad (20)$$

$$Q_{RW\,WP,total} = Q_{RW\,WP,1} + Q_{RW\,WP,2} + Q_{RW\,WP,3} + Q_{RW\,WP,4} \quad (21)$$

7. Waste Package Temperature

Decay heat from high-level radioactive waste and resulting thermal perturbations potentially have potential to significantly affect many associated processes (thermal, hydrological, mechanical and chemical processes) in the near-field. As an initial effort to address this issue, the waste package heat output as a function of time has been analyzed for the three waste-type waste packages and implemented in the source-term model (see Section 6 of this chapter). The heat output model is used as the time-varying heat source input to an analytical solution developed to calculate the waste package temperature evolution with time in a geologic repository. This analytical solution was developed by Claesson and Probert (1996, section 7), which allows explicit calculation of near-field temperature evolution inside a GDSE model.

Because of time constraints, the analytical solution was not fully implemented in the source-term model in time for this report preparation. Instead, for the deep borehole GDSE analysis (Chapter 5 of the report), a constant temperature of 100°C, which is the calculated ambient temperature at the waste disposal zone (Brady et al., 2009), is assumed for the waste package for the entire analysis time period. For other GDSE options, a constant temperature of 25°C is assumed for the waste package and near-field for the entire analysis time period. The calculation of near-field temperature evaluation and its impact on near-field chemistry are planned to be implemented in next fiscal year.

8. Waste Form Degradation

As discussed above, the current source-term model includes two types of waste form: commercial UNF matrix and borosilicate glass. The waste form degradation in the source-term analysis is modeled with the yearly fractional degradation rates (i.e., fraction of remaining waste mass degraded per year), with a distribution that captures potential range of degradation rates in the GDSE conditions. All GDSE options considered are expected to be in chemically reducing

conditions with varying degrees of redox conditions of water in contact with the waste form. In the current GDSE model a constant rate is applied to all waste; no temperature dependence is modeled at this time.

For the commercial UNF waste form, which is predominantly UO_2, uncertainty in the degradation rate is modeled with a log-triangular distribution with mode of $10^{-7}\ yr^{-1}$ and lower and upper bounds of $10^{-8}\ yr^{-1}$ and $10^{-6}\ yr^{-1}$ respectively. The rate range is from the SKB spent nuclear fuel degradation model for its repository situated in a chemically reducing environment (SKB 2006, sections 10.5.3 and 10.6.4).

The borosilicate glass waste form degradation is much less sensitive to the redox condition of water contacting the waste form. A fractional degradation rate model was developed using the literature data for degradation of similar glasses exposed in geologic environments (Ojovan et al. 2005; BSC 2004, table 6-14). The rate model is expressed as log-uniform distribution with the minimum and maximum values of $3.4 \times 10^{-6}\ yr^{-1}$ and $3.4 \times 10^{-3}\ yr^{-1}$ respectively.

9. Near-Field Volume

To estimate the dissolved concentrations of radionuclides released from the waste form in the source-term, the amount of water that is in contact with the waste form and available to dissolve released radionuclides needs to be calculated. As noted above, all GDSE options considered are assumed to be located in a saturated environment. For this report, the source-term model conceptualizes the near-field of a GDSE as a large set of uniformly mixed compartments. This is a reasonable assumption for the scoping analysis, considering that waste package performance is not taken into account for the analysis and that the entire waste inventory becomes available for reactions in the near-field from time zero.

In the source-term model, the near-field *bulk* volume is defined as the square repository footprint area times the height. The emplacement tunnels of a granite or clay GDSE are likely to maintain the structural shape for an extended period of time after repository closure, and after collapse of the tunnels are likely to remain more porous than the host rock. In this respect, the source-term model defines the near-field height of a granite and clay GDSE as twice the waste package outer diameter. For a salt GDSE, in which the remaining space of the emplacement tunnels is likely closed by the salt creep closure, the near-field height is defined as the waste package outer diameter. The near-field heights in the source-term model are arbitrary and will be updated as needed in future analyses.

The so-defined near-field has two major constituents: 1) degraded engineered materials (e.g., waste form, waste package, backfill, etc.), and 2) host rock. The source-term model calculates the water volume available in each of the two constituents by multiplying the bulk volume of each constituent with its respective porosity. The total water volume available in the near-field is the sum of the water volume in each constituent.

10. Radionuclide Solubility

Radionuclide solubility is an important parameter that controls dissolved concentrations of mobilized radionuclides in groundwater. Radionuclide solubility is affected at varying degrees by various geochemical condition parameters, including redox condition of contacting water, temperature, pH, and presence and concentrations of other dissolved species. As an initial effort to address the effect of geochemical conditions on radionuclide solubility, the GDSE analysis considers two redox conditions for groundwater: 1) reducing condition water in the near field, and 2) less reducing or slightly oxidizing water in the far field.

- The reducing condition water represents the groundwater in the near-field that may experience elevated temperature conditions from the thermal perturbations caused by the decay heat of emplaced waste.
- The less reducing or slightly oxidizing water represents the groundwater away from the near-field that is not subject to thermal perturbation and remains at the site ambient temperature.

For the solubility of key radionuclides in the near-field water, the thermodynamic data of relevant species at elevated temperatures were collected, and calculations were performed to develop the temperature dependence of the solubility. These calculations were performed with computer code EQ3/6 and an enhanced thermodynamic database for dilute solutions (Wolery and Jarek, 2003). The results are shown in Figures (5) through (9). The calculation results show that the temperature dependence of radionuclide solubility is rather complex. For example, uranium exhibits a retrograded behavior while neptunium displays a monotonic increase in solubility with temperature. It should be pointed out that these calculations are rather preliminary because of the limited thermodynamic data available for elevated temperatures.

As discussed above, because of time constraints, the near-field temperature evolution is not fully implemented in the current set of GDSE models. Consequently, only the radionuclide solubilities at ambient temperature are used. These solubilities were calculated from two well-studied brines from the WIPP site: 1) ERDA-6 represents concentrated brines derived from the brine pocket beneath the repository; and 2) DOE-2_UNC represents a dilute brine at the interface between the near field and the far field. The former brine (ERDA-6) is representative of chemically reducing condition, and the latter brine (DOE-2_UNC) represents a much less reducing condition. The chemical compositions of the two brines are given in Table 4. The solubilities of radionuclides were calculated with EQ3/6 and an enhanced Pitzer thermodynamic database (Wolery and Jarek, 2003). The results are shown in Tables 5 and 6. In principle, the calculated solubilities are only applicable to a salt repository. However, just for model demonstration, because of time constraints, these solubilities are also applied to other disposal environments such as granite and deep borehole environments. For future work, the solubility calculations will be performed for each individual disposal environment.

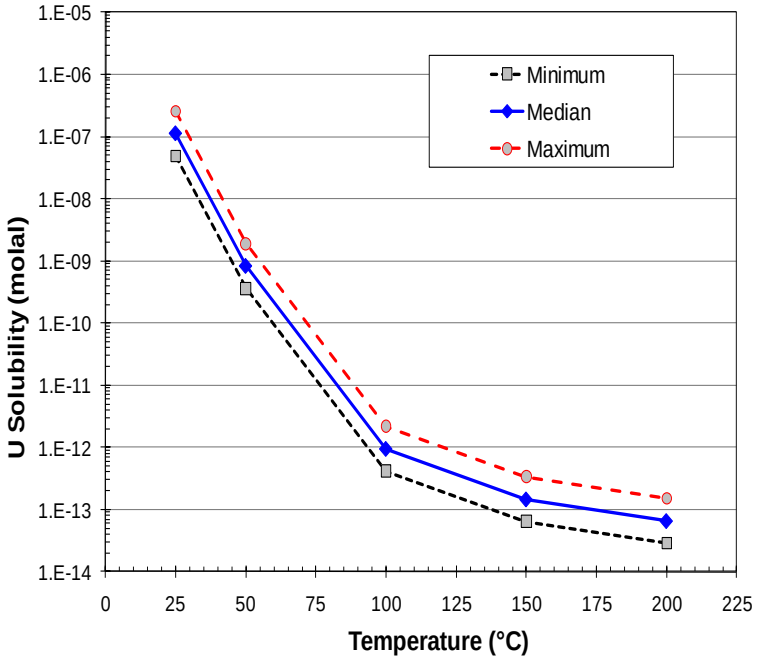

Figure 5: Uranium solubility as a function of temperature in the near-field water.

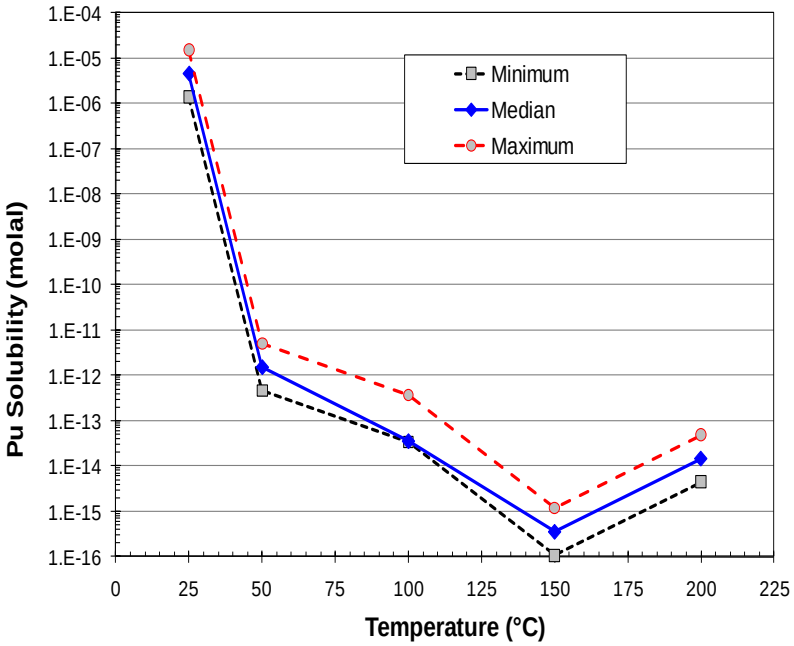

Figure 6: Plutonium solubility as a function of temperature in the near-field water

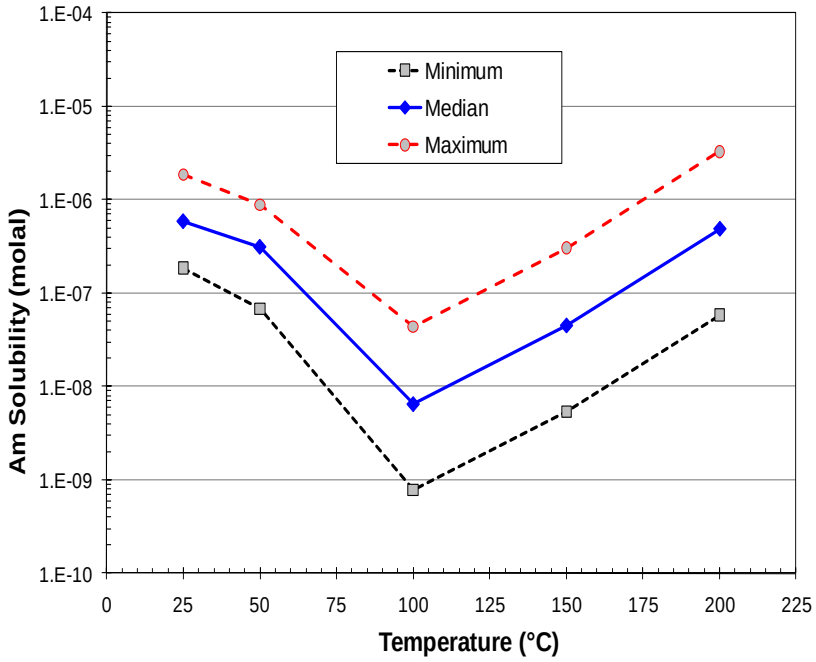

Figure 7: Americium solubility as a function of temperature in the near-field water.

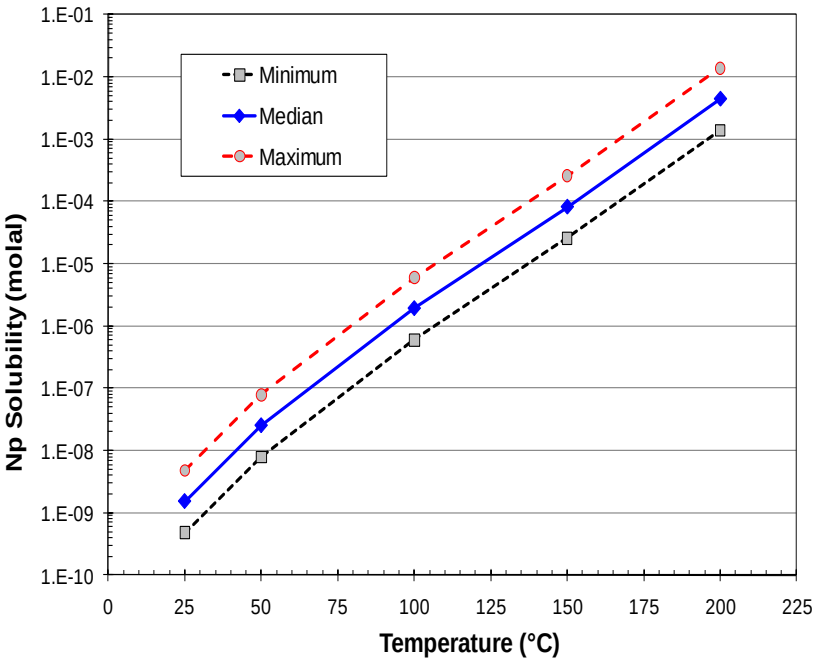

Figure 8: Neptunium solubility as a function of temperature in the near-field water.

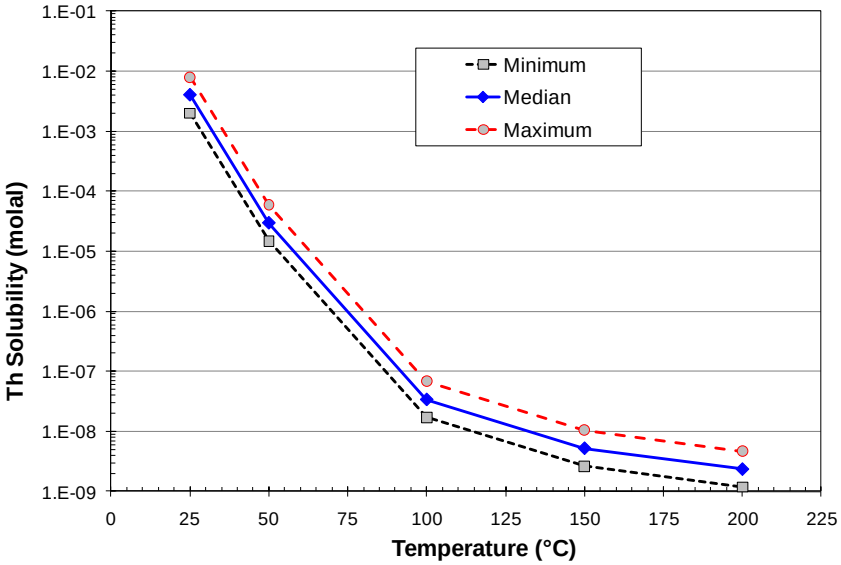

Figure 9: Thorium solubility as a function of temperature in the near-field water.

Table 4: Chemical Composition of ERDA-6 and DOE-2_UNC Culebra Groundwaters.

Parameter	ERDA-6 [1]	Units	Culebra [2]	Units
Eh	-152	Millivolts	-	-
pH	6.42	pH unit	7	pH unit
Ba^{2+}	0.76	mg/L	-	mg/L
Ca^{2+}	490	mg/L	1960	mg/L
Cs^{+}	2.5	mg/L	-	mg/L
Li^{+}	240	mg/L	-	mg/L
Mg^{2+}	450	mg/L	1060	mg/L
K^{+}	3800	mg/L	410	mg/L
Na^{+}	112000	mg/L	18400	mg/L
Sr^{2+}	18	mg/L	-	mg/L
Br-	880	mg/L	-	mg/L
Cl^{-}	170000	mg/L	34600	mg/L
F^{-}	1.7	mg/L	-	mg/L
I^{-}	28	mg/L	-	mg/L
SO_4^{2-}	16000	mg/L	3950	mg/L
HPO_4^{2-} [3]	0.37	mg/L	-	mg/L
Al^{3+}	2.4	mg/L	-	mg/L
$B(OH)_3(aq)$ [4]	680	mg/L	-	mg/L
Cu^{2+}	0.49	mg/L	-	mg/L
Fe^{2+}	3.6	mg/L	-	mg/L
Mn^{2+}	6.9	mg/L	-	mg/L
HCO_3^{-}	0.016	Molarity	67 [5]	mg/L
$SiO_2(aq)$	45	mg/L	-	mg/L
Zn^{2+}	0.55	mg/L	-	mg/L

Notes:
(1) Source: D'Appolonia Consulting Engineers, Inc., 1983, Report TME-3153, Table C.2. All concentrations of chemical components are average from multiple analyses.
(2) Source: Siegel et al. (1991), table 2-2, DOE-2_UNC groundwater composition.
(3) Given as "Phosphate" in the source but entered as HPO_4^{2-} in the EQ3/6 input file.
(4) Given as "Boron" in the source but entered as $B(OH)_3(aq)$ in the EQ3/6 input file.
(5) Given as alkalinity in the source.

Table 5: Elemental Solubility of Select Radionuclides in Near-Field Water

Element	Temperature (°C)	Distribution Type	Description (solubility in molal)
U	25	Triangular	4.89E-08 (min); 1.12E-07 (mode); 2.57E-07 (max)
	50	Triangular	3.63E-10 (min); 8.27E-10 (mode); 1.91E-09 (max)
	100	Triangular	4.17E-13 (min); 9.46E-13 (mode); 2.19E-12 (max)
	150	Triangular	6.40E-14 (min); 1.46E-13 (mode); 3.36E-13 (max)
	200	Triangular	2.88E-14 (min); 6.54E-14 (mode); 1.51E-13 (max)
Pu	25	Triangular	1.40E-06 (min); 4.62E-06 (mode); 1.53E-05 (max)
	50	Triangular	4.62E-13 (min); 1.53E-12 (mode); 5.07E-12 (max)
	100	Triangular	3.40E-14 (min); 3.56E-14 (mode); 3.73E-13 (max)
	150	Triangular	1.08E-16 (min); 3.56E-16 (mode); 1.18E-15 (max)
	200	Triangular	4.44E-15 (min); 1.47E-14 (mode); 4.87E-14 (max)
Am	25	Triangular	1.85E-07 (min); 5.85E-07 (mode); 1.85E-06 (max)
	50	Triangular	6.80E-08 (min); 3.12E-07 (mode); 8.81E-07 (max)
	100	Triangular	7.80E-10 (min); 6.50E-09 (mode); 4.37E-08 (max)
	150	Triangular	5.39E-09 (min); 4.50E-08 (mode); 3.05E-07 (max)
	200	Triangular	5.82E-08 (min); 4.86E-07 (mode); 3.29E-06 (max)
Np	25	Triangular	4.79E-10 (min); 1.51E-09 (mode); 4.79E-09 (max)
	50	Triangular	7.91E-09 (min); 2.50E-08 (mode); 7.91E-08 (max)
	100	Triangular	6.00E-07 (min); 1.90E-06 (mode); 6.00E-06 (max)
	150	Triangular	2.55E-05 (min); 8.08E-05 (mode); 2.55E-04 (max)
	200	Triangular	1.38E-03 (min); 4.37E-03 (mode); 1.38E-02 (max)
Th	25	Triangular	2.00E-03 (min); 4.00E-03 (mode); 7.97E-03 (max)
	50	Triangular	1.48E-05 (min); 2.95E-05 (mode); 5.92E-05 (max)
	100	Triangular	1.71E-08 (min); 3.37E-08 (mode); 6.79E-08 (max)
	150	Triangular	2.62E-09 (min); 5.20E-09 (mode); 1.04E-08 (max)
	200	Triangular	1.18E-09 (min); 2.33E-09 (mode); 4.68E-09 (max)
Tc	All temperature	Log-Triangular	4.56E-10 (min); 1.33E-08 (mode); 3.91E-07 (max)
Sn	All temperature	Triangular	9.87E-09 (min); 2.66E-08 (mode); 7.15E-08 (max)
C, Cl, Cs, I, Se, Sr	All temperature	n/a	No solubility limit

Note: Elements Ac, Cm, Nb, Pa, Pd, Ra, Sb, Zr are known to be solubility-limited, but are implemented as no solubility-limited in the source-term model because their solubility calculations have not been completed.

Table 6: Elemental Solubility of Select Radionuclides in Ambient-Temperature Far-Field

Element	Distribution Type	Description (solubility in molal)
U	Triangular	9.16E-05 (min); 2.64E-04 (mode); 7.62E-04 (max)
Pu	Triangular	7.80E-07 (min); 2.58E-06 (mode); 8.55E-06 (max)
Am	Triangular	3.34E-07 (min); 1.06E-06 (mode); 3.34E-06 (max0
Np	Log-triangular	1.11E-06 (min); 1.11E-05 (mode); 1.11E-04 (max)
Th	Triangular	8.84E-06 (min); 1.76E-05 (mode); 3.52E-05 (max)
Sn	Triangular	1.78E-08 (min); 4.80E-08 (mode); 1.29E-07 (max)
C, Cl, Cs, I, Se, Sr, Tc	n/a	No solubility limit

Note: Elements Ac, Cm, Nb, Pa, Pd, Ra, Sb, Zr are known to be solubility-limited, but are implemented as no solubility-limited in the source-term model because their solubility calculations have not been completed.

11. Repository Waste Inventory Scenarios

Two waste inventory scenarios were considered in the GDSE analysis:

- Scenario 1: commercial UNF and DOE HLW
- Scenario 2: DOE HLW and reprocessing HLW

The source-term model has incorporated the two waste inventory scenarios with a simple module to switch from one scenario to another. Scenario 1 considers a total of 37,157 waste packages (32,154 commercial UNF waste packages plus 5,003 DOE HLW waste packages), and a square repository footprint with a side of 3,270 m based on the reference waste package spacing. Scenario 2 considers a total of 9,058 waste packages (5,003 DOE HLW waste packages plus 4,055 reprocessing HLW waste packages) and a smaller square repository footprint (a side of 1,615 m).

12. Radionuclide Release Scenarios

Two scenarios are considered for radionuclide release from a GDSE: the reference (or undisturbed) case and the disturbed case. The reference case releases radionuclides by a sequence of typical processes that are expected to occur in a generic repository. The disturbed case represents a non-typical process that provides a fast pathway for radionuclide release to the far-field from a GDSE due to human intrusions. The human intrusion scenario assumes a single borehole penetration through a waste package at 1,000 years after repository closure. In a tight repository environment, such as in a salt repository, waste packages are expected to be encapsulated by salt due to salt creeping, thus limiting the inventory available for release during a human intrusion. To capture this effect, the number of waste packages affected (one penetrated plus, if any, neighboring packages affected) is randomly sampled between one and five (uniform distribution). This represents the total amount of waste inventory that becomes available for the

fast pathway release by human intrusions. The associated processes for the fast pathway release are specific to the geologic settings and features of each GDSE. Separate source-term models were developed and implemented for each of the two release scenarios. For both scenarios, the source-term model does not consider potential performance benefits of waste packages; that is, waste form starts to degrade at time zero and the waste package presents no barrier to the movement of radionuclides.

13. Generic Reference Biosphere Model

Radiation exposure, or dose, is used as a performance metric in the GDSE analysis. Dose is used so that effects of various radionuclides can be combined in a simple manner. Dose is used rather than radiotoxicity because dose reflects the attenuation of radionuclides by the geologic environment. Biosphere dose conversion factors developed in the International Atomic Energy Agency's (IAEA) BIOMASS project for a simple drinking water well pathway (Example Reference Biosphere 1B (ERB 1B)) were adopted for the GDSE analysis (IAEA 2003). The ERB 1B is deliberately designed to be very simple, being focused on a simple biosphere system and single exposure pathway. It is characterized by a drinking water well bored through the overburden into an aquifer that has been contaminated by radionuclides released from the repository. Previous experience from more comprehensive biosphere modeling studies has shown that a drinking water well may sometimes represent a significant or even, depending on other aspects of the assessment context, a dominant pathway for release and exposure (IAEA 2003).

The generic reference biosphere is assumed to be located at 5 km down-gradient from the GDSE boundary. The ERB 1B dose conversion factors were equally used at the outer boundary across different GDSE options. Note that applying the biosphere conversion factor at the boundary location is an arbitrary modeling choice to produce the uniform performance measure for comparative studies of the considered GDSE options and does not indicate any realistic dose implications. In addition, the determination of biosphere dose conversion factors does not depend on the GDSE, but rather on the biosphere beyond the GDSE, the habits of the population in that biosphere, and potentially the regulatory framework. A variety of biospheres and local populations could be present over a given GDSE and the resulting dose conversion factors may vary significantly. Therefore, the results presented in this report *should not* be construed as being indicative of the true performance of the GDSE options or compared to any regulatory performance objectives regarding repository performance.

14. Concluding remarks

As one of the overall goals of the GDSE modeling, we have been in the process to develop a consistent set of assumptions across different disposal environments such that the results obtained for individual disposal environments can be meaningfully compared. A significant effort has been made along this direction in fiscal year 2010, but much more still remains to be done, especially in the area of directly incorporating near-field thermal evolution and its impact on repository performance in each GDSE model.

15. References

Brady, Patrick V., Arnold, Bill W., Freeze, Geoff A., Swift, Peter N., Bauer, Stephen J., Kanney, Joseph L., Rechard, Robert P., and Stein, Joshua S., 2009. "Deep Borehole Disposal of High-Level Radioactive Waste", Sandia Report SAND2009-4401, Sandia National Laboratories, Albuquerque, NM.

BSC (Bechtel SAIC Company), 2004. Defense HLW Glass Degradation Model, ANL-EBS-MD-000016 REV 02, Las Vegas, Nevada, Bechtel SAIC Company.

Carter, J. T., and Luptak, A. J., 2010. Fuel Cycle Potential Waste Inventory for Disposition, Fuel Cycle Research & Development, U.S. DOE, Report FCRR&D-USED-2010-000031, January 2010.

Claesson, J., and Probert, T., 1996. "Temperature Field Due to Time-Dependent Heat Sources in a Large Rectangular Grid – Derivation of Analytical Solution", Technical Report 96-12, Swedish Nuclear Fuel and Waste Management (SKB).

Curti, E. and Hummel, W., 1999. "Modeling the solubility of zirconia in a repository for high-level radioactive waste", Journal of Nuclear Materials, Vol.274, iss.1, p.189-196.

D'Appolonia Consulting Engineers, Inc., 1983. "Brine reservoirs in the Castile Formation Waste Isolation Pilot Plant (WIPP) project, Southeastern New Mexico", Westinghouse Electric Corporation – Waste Isolation Division Carlsbad, NM., report TME 3153.

Goldsim Technology Group, 2009. "Users Guide, GoldSim Probabilistic Simulation Environment," Version 10.0.

IAEA (International Atomic Energy Agency), 2003, "Reference Biospheres for Solid Radioactive Waste Disposal", IAEA-BIOMASS-6, July 2003.

Janberg, K., and Spilker, H., 1998. Status of the Development of Final Disposal Casks and Prospects in Germany, Nuclear Technology, Vol. 121, pp. 136-147.

Ojovan, M.I., Hand, R.J., Ojovan, N.V., and Lee, W.E., 2005. "Corrosion of Alkali-Borosilicate Waste Glass K-26 in Non-Saturated Conditions," J. Nuclear Materials, Vol. 340, pp. 12-24.

Siegel, M. D., Lambert, S. J., and Robinson, K. L., 1991. "Hydrogeochemical Studies of the Rustler Formation and Related Rocks in the Waste Isolation Pilot Plant Area, Southeastern New Mexico", SNL Report SAND88-0196, 694 p.

SKB (Swedish Nuclear Fuel and Waste Management Co.), 2006. Long-term Safety for KBS-3 Repositories at Forsmark and Laxemar — A First Evaluation, Technical Report TR-06-09.

Wolery, T.W. and Jarek, R.L., 2003. "EQ3/6, Version 8.0, Software User's Manual", U.S. Department of Energy, Office of Civilian Radioactive Waste Management, Office of Repository Development, Las Vegas, Nevada.

Chapter 2 Salt Generic Disposal System Environment Model

Joon H Lee, Yifeng Wang and Malcolm Siegel

Sandia National Laboratories

1. Introduction

This chapter summarizes the development of the salt Generic Disposal System Environment (GDSE) model and the preliminary model results. For a better comparison among the different disposal environments, a uniform set of modeling assumptions and approaches are applied, to the extent applicable, to all GDSE analyses. For this effort, as discussed in Chapter 1, the reference source-term model was developed and provided as the Goldsim template for use by all GDSE analysis. A representative far-field model for a salt GDSE was developed. This chapter describes the conceptual model for a salt GDSE, the model implementation and structure, the preliminary model analysis results, and future work.

2. Conceptual Model

The conceptual model for radionuclide release and transport from a salt GDSE was developed using the literature data of existing salt repository sites including the WIPP site. Figure 1 shows a schematic for the conceptual model for radionuclide release and transport in a salt GDSE. Two scenarios are considered for repository radionuclide release and transport: the reference case, and the disturbed case. The reference case releases radionuclides by a sequence of typical processes that are expected to occur in a salt GDSE, and the disturbed case represents a non-typical process that provides a fast pathway for radionuclide to the far-field due to human intrusion.

The reference case assumes that a marker bed below the repository provides the major pathway for radionuclide release and transport from the repository. The marker bed is assumed to be composed of a mixture of evaporite minerals (such as anhydrite) and clay. As discussed in the source-term model discussion (Chapter 1), no waste package performance is considered, and the waste form degradation starts at time zero, releasing radionuclides into the near-field. Dissolved radionuclide concentration in the near-field is determined by the amount of radionuclides released from the waste form (constrained by the waste form degradation rate), the amount of water available in the near-field, and the solubility if it is subject to its solubility limit. The solubility for the near-field water is applied (See Chapter 1).

Dissolved radionuclides in the near-field are released to a marker bed below the repository, which is assumed to run horizontally in parallel with the repository (Figure 1). The model does not consider the distance between the bottom (or floor) of repository and the marker bed and assumes no resistance to the flow and radionuclide transport over this distance. The marker bed is assumed to be one-meter thick, with its width to be the same as that of repository; the marker-bed cross sectional area to water flow is the bed thickness times the width. As shown

in the figure, dissolved radionuclides are transported into the marker bed over its length below the repository.

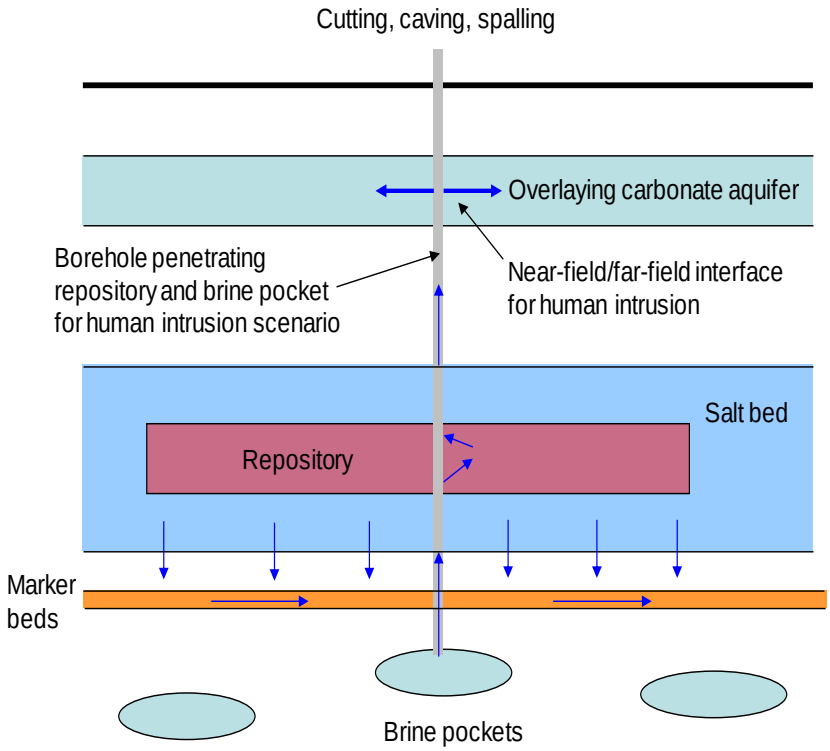

Figure 1: A schematic showing the conceptual model for radionuclide release and transport from a salt generic repository.

Radionuclides are transported advectively in the marker bed to a drinking well location 5 km down-gradient from the edge of the repository, where a hypothetical biosphere exists. The brine flow rates in the marker bed away from the repository are estimated from the WIPP site data (Helton et al. 1998, figures 7.6.2 and 7.6.5). Radiation exposure, or dose, is used as a performance metric for the salt GDSE analysis. As discussed in the source-term model, the IAEA Example Reference Biosphere 1B (ERB 1B) dose model (IAEA 2003) was used to calculate the dose from the dissolved radionuclide concentration at the hypothetical drinking well location, although it is extremely unlikely that groundwater drawn from a bedded salt formation would be potable with significant treatment, and that recharge in the marker beds would sustain well withdrawal over a long period of time.

The disturbed scenario is represented by a "stylized" human intrusion scenario. In this scenario it is assumed that a single borehole penetrates a waste package and a brine pocket below the repository at 1,000 years after repository closure. The number of waste packages affected (one penetrated plus, if any, neighboring packages affected) is randomly sampled between one and five (uniform distribution), and this represents the total amount of waste inventory that becomes available for the fast pathway release by the human intrusion. Dissolved radionuclides from the affected waste packages are carried upward through the borehole by pressurized brines

from the brine pocket, and released to an overlying carbonate aquifer. The brine flow rate through the borehole is sampled between 0.1 and 5.0 m^3/yr (uniform distribution) (Helton et al. 1998). The overlying aquifer is assumed to comprise primarily dolomite matrix with clays dispersed in the matrix.

The dissolved radionuclide concentrations in the aquifer are checked against the solubility for the far-field water before they are transported in the aquifer to a drinking well location 5 km down-gradient from the repository boundary. As for the reference case, the same hypothetical biosphere is assumed to exist at that location, and the reference biosphere model (IAEA ERB 1B model) is applied to calculate the dose.

As discussed in the source-term model section (Chapter 1), two repository waste inventory scenarios are considered for each of the cases. For the reference case, the waste inventory for Scenario 1 comprises the commercial UNF and DOE HLW. The waste inventory for Scenario 2 comprises the DOE HLW and reprocessing HLW. Scenario 1 takes a square repository footprint with a side of 3,270 m for disposal of a total of 37,157 waste packages (32,154 commercial UNF waste packages plus 5,003 DOE HLW waste packages). Scenario 2 needs a smaller square repository footprint with a side of 1,615 m for a total of 9,058 waste packages (5,003 DOE HLW waste packages plus 4,055 reprocessing HLW waste packages).

For simplification, for the disturbed case, scenario 1 considers only the commercial UNF waste packages are affected, and scenario 2 only the DOE HLW waste packages are affected. Note that applying the biosphere model at the hypothetical drinking well location is an arbitrary modeling choice to produce the uniform performance measure for comparative studies of a salt GDSE and does not indicate any realistic dose implications. Therefore, the results presented in this report *should not* be construed as being indicative of the true performance of a GDSE or compared to any regulatory performance objectives regarding repository performance.

3. Model Implementation and Structure

This section discusses the implementation and structure of the salt GDSE model. Goldsim was used as the framework for model implementation and simulations. Figures 2 and 3 show the Goldsim model structure for the salt GDSE model for the reference case and the disturbed case respectively. The figures also show the near-field and far-field model components for each case. The model components are given specific names to indicate their corresponding functionalities. The reference source-term model discussed in Chapter 1 is implemented in the following model components: *Materials*, *RN_Inventory*, *Near_field*, and *Uncertain_Parameters*. The reference biosphere model is implemented in the *Results* model component for dose calculations. The *NF_Interface* model component interfaces between the near-field and the far-field models. The *Uncertain_Parameters* model component contains all uncertain model parameters.

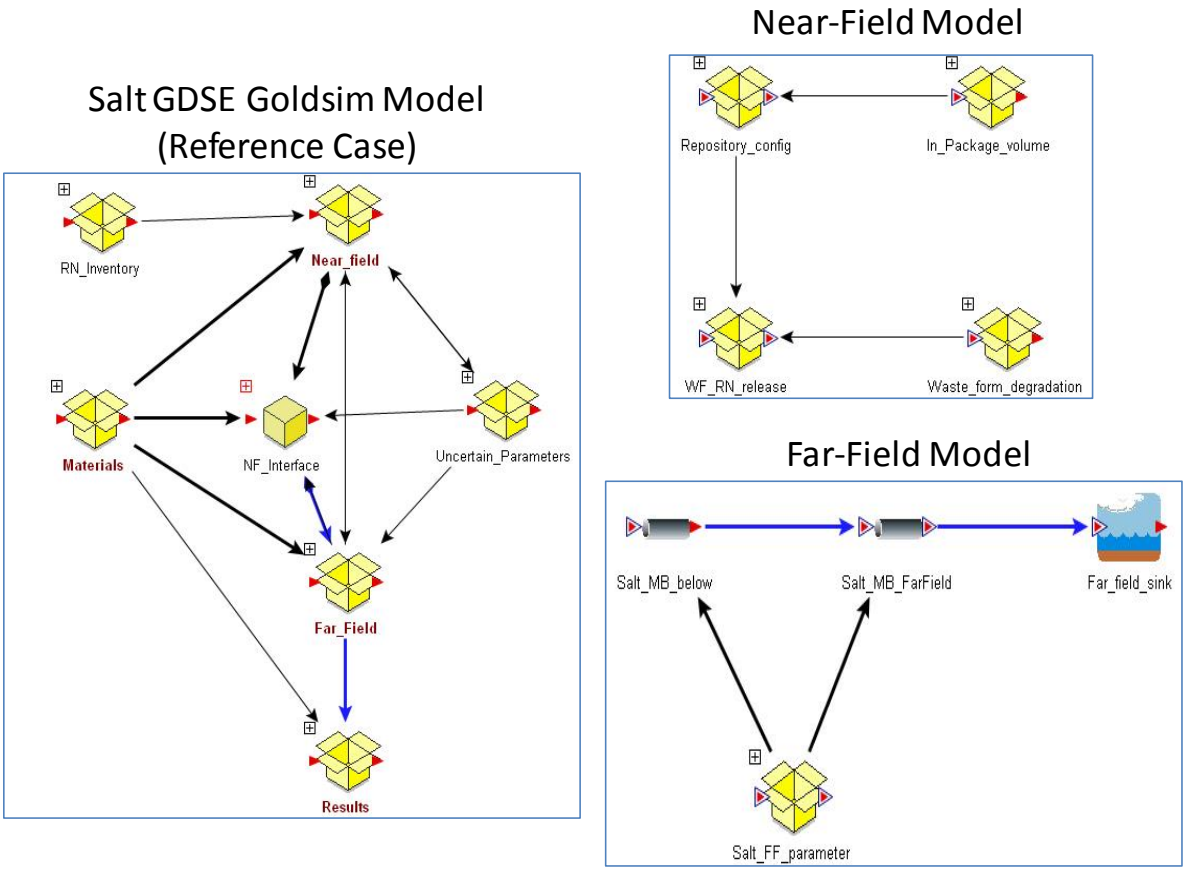

Figure 2: Goldsim model structure for the salt GDSE model and near-field and far-field model components for the reference case

Goldsim model structure for the salt GDSE model and near-field and far-field model components for the reference case

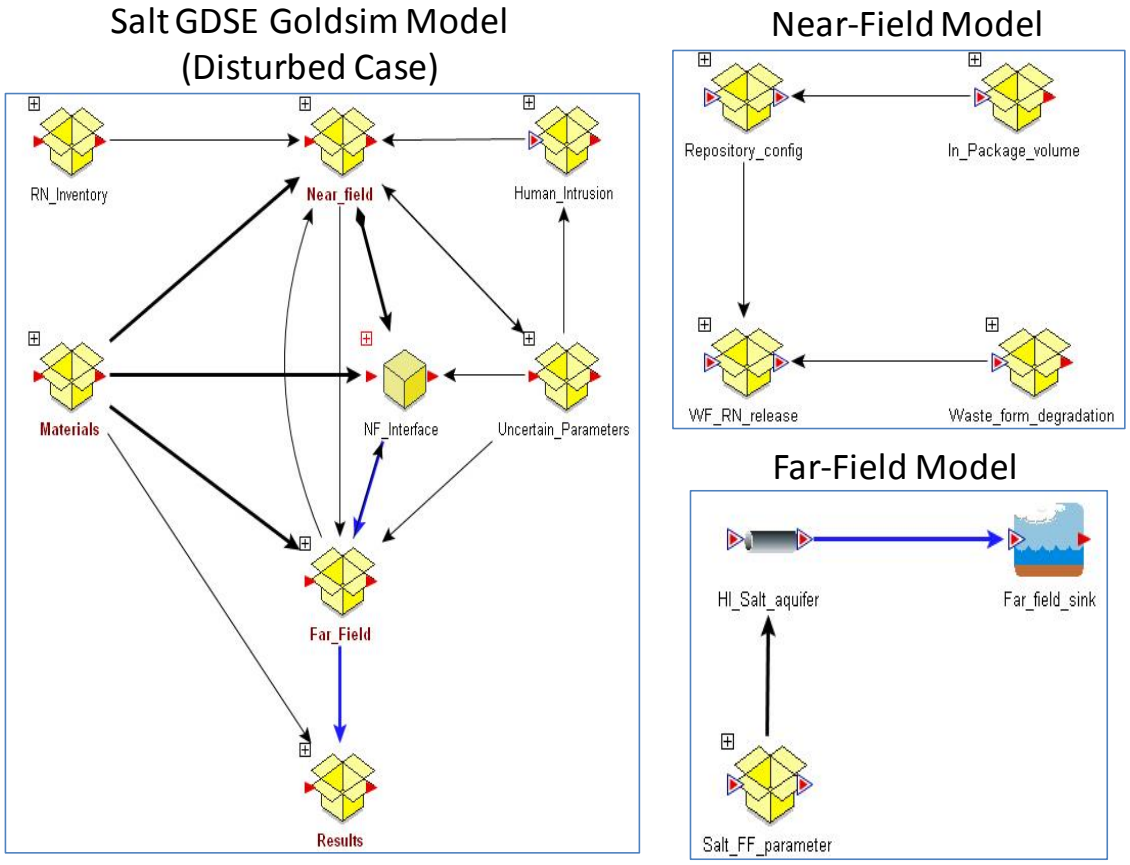

Figure 3: The Goldsim model structure for the salt GDSE model and near-field and far-field model components for the disturbed case

The reference case and disturbed case models have similar structures, except the latter has an additional model component, *Human_Intrusion*, which executes a borehole penetration through the repository at 1,000 years and fast pathway transport of dissolved radionuclides from the near field to the overlying aquifer. Other major differences between the reference case and the disturbed case models are the implementation of the far-field model (see the far-field model structure inserts in the figures). The far-field radionuclide transport is modeled with a Goldsim pipe model. In the reference case model (Figure 2), the *Salt_MB_below* pipe model simulates radionuclide transport in the marker bed below the repository, and, as discussed in the conceptual model, radionuclides enter the pipe component over its length (i.e., over the length of the marker bed below the repository). The *Salt_MB_FarField* pipe model simulates radionuclide transport in a 5-km long marker bed from the edge of the repository to the location of a hypothetical drinking water well. The pipe model parameters for the marker bed are listed in Table 1. The rate of brine flow in the marker bed away from the repository is estimated based on the Waste Isolation Pilot plant (WIPP) results. A more realistic rate can be estimated by accounting for

various gas generation processes in the repository, which definitely needs to be included as future work. For the disturbed case, the *HI_Salt_aquifer* pipe model simulates radionuclide transport in the overlying aquifer to the location of a hypothetical drinking water well 5 km downstream from the location of borehole penetration. Table 2 lists the pipe model parameters for the overlying carbonate aquifer.

Table 1: Far-field model parameters for the marker beds for the reference case of salt GDSE

Parameter	Distribution Type	Parameter Value and Description	Source
Thickness	Constant	1 m	Vaughn et al. (2000)
Porosity	Constant	0.01	
Density	Constant	2500 kg/m^3	
Brine flow rate below repository (m/yr)	Log-uniform	1.0E-08 (min); 3.0E-02 (max)	Helton et al. (1998), Fig 7.6.2
Brine flow rate away from repository (m/yr)	Log-uniform	1.0E-08 (min); 2.0E-02 (max)	Helton et al. (1998), Fig 7.6.5
Longitudinal Dispersivity	Constant	10% of flow conduit length	
Kd for U (ml/g)	Uniform	0.2 (min); 1 (max)	Lappin et al. (1989); McKinley and Scholtis (1992); Muller et al. (1981); Tien et al. (1983)
Kd for Pu (ml/g)	Uniform	70 (min); 100 (max)	
Kd for Np (ml/g)	Uniform	1 (min); 10 (max)	
Kd for Am (ml/g)	Uniform	25 (min); 100 (max)	
Kd for Th (ml/g)	Uniform	100 (min); 1000 (max)	
Kd for Tc (ml/g)	Uniform	0 (min); 2 (max)	
Kd for Cs (ml/g)	Uniform	1 (min); 20 (max)	
Kd for Sr (ml/g)	Uniform	1 (min); 80 (max)	
Kd for C, Cl, I, Se & Sn	Constant	0 (no sorption)	

Note: Kds for all other radionuclides not listed in the table were assumed zero (no sorption on the marker bed filling medium) because data was not available for the marker bed filling medium.

Table 2: Far-field model parameters for overlying carbonate aquifer for the disturbed case of salt GDSE

Parameter	Distribution Type	Parameter Value and Description	Source
Aquifer thickness	Constant	4 m	Lappin et al. (1989), Table E-6; Brush and Storz (1996)
Matrix porosity	Uniform	0.07 (min); 0.3 (max)	
Bulk density	Constant	2800 kg/m^3	
Matrix Tortuosity	Uniform	0.03 (min); 0.5 (max)	
Brine flow rate upward through borehole (m^3/yr)	Uniform	0.1 (min); 5.0 (max)	Helton et al., 1998
Aquifer water flow rate (m/yr)	Log-uniform	3.15E-03 (min); 3.15E+01 (max)	Helton et al. (1998), Fig. 12.1.1
Longitudinal Dispersivity	Constant	10% of flow conduit length	
Kd for U (ml/g)	Uniform	0.03 (min); 20 (max)	Brush and Storz (1996); Muller et al. (1981); Pepping et al. (1983); Tien et al. (1983)
Kd for Pu (ml/g)	Log-uniform	20 (min); 1.0E+04 (max)	
Kd for Np (ml/g)	Log-uniform	1 (min); 200 (max)	
Kd for Am (ml/g)	Uniform	20 (min); 400 (max)	
Kd for Th (ml/g)	Log-uniform	7.0E+02 (min); 1.0E+04 (max)	
Kd for Tc (ml/g)	Triangular	0 (min); 50 (mode); 100 (max)	
Kd for Cs (ml/g)	Triangular	40 (min); 500 (mode); 3000 (max)	
Kd for Sr (ml/g)	Triangular	5 (min); 13 (mode); 4.0E+04 (max)	
Kd for I (ml/g)	Uniform	0.01 (min); 100 (max)	
Kd for C, Cl, Se & Sn	Constant	0 (no sorption)	

Note: Kds for all other radionuclides not listed in the table were assumed zero (no sorption on the marker bed filling medium) because data was not available for the aquifer medium.

4. Model results

The Goldsim analysis was performed probabilistically, with 100 realizations for each case and a time period of one million years. The model results are presented in terms of the mean dose (mrem/yr) by individual radionuclides. It is noted that this model is the initial effort of the salt GDSE analysis tool development and needs further improvement and refinements as the study progresses. Also note that using the mean dose is an arbitrary choice to present and discuss the analysis results in order to facilitate comparative studies among the GDSE options and does not indicate any realistic dose implications. Therefore, the results presented in this

section *should not* be construed as being indicative of the true performance of a salt GDSE or compared to any regulatory performance objectives regarding repository performance.

Figure 4 shows the mean doses by major dose-contributing radionuclides for the waste inventory scenario 1 (commercial UNF plus DOE HLW) for the reference case. The dominant long-term dose contributor is ^{129}I, and this is expected based on the following characteristics of the radionuclide: 1) no solubility limit, 2) weak sorption on marker bed filling materials, 3) extremely long half-life (17 million years), and 4) a significant inventory in the waste (about 950 g per commercial UNF waste package and about 65 g per DOE HLW waste package). The mean dose for ^{79}Se is comparable to that of ^{129}I for up to about 200,000 years, and this is consistent for the radionuclide's properties that are similar to those of ^{129}I listed above, except a shorter half-life (65,000 years). There are conflicting data on the ^{79}Se half-life in the literature, which has been variously reported as 6.5×10^{4} years (used in the model), 2.95×10^{5} years, 4.8×10^{5} years, 6.5×10^{5} years, and 1.13×10^{6} years (Jiang et al. 2001). Also the selenium solubility in water is highly uncertain. The metal selenium is insoluble in water, but it can also be released as soluble selenate ion (SeO_4^{2-}), which is not readily sorbed to geologic materials. More work is needed to better characterize and quantify dissolution and sorption behavior of selenium in a geologic repository environment.

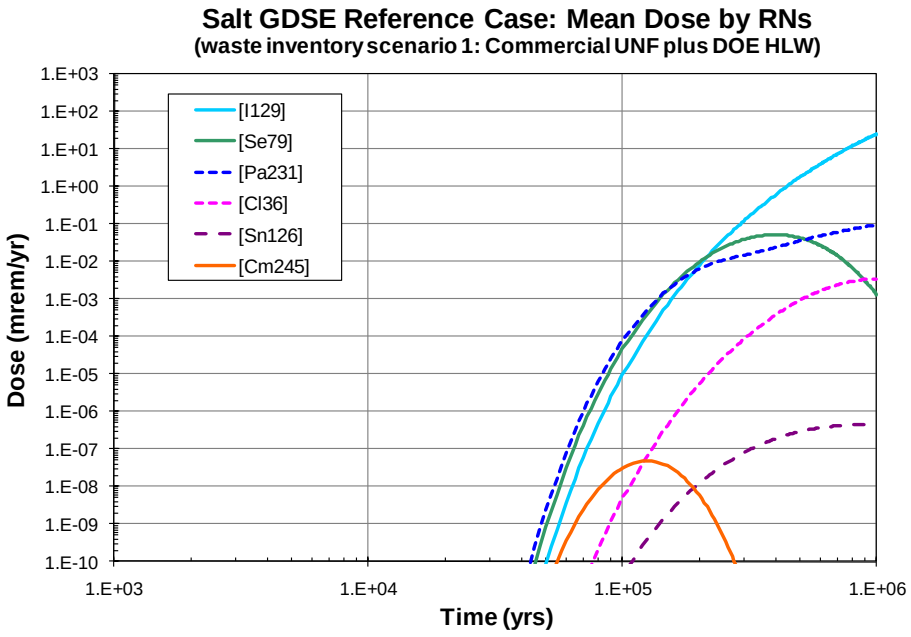

Figure 4: Mean dose by radionuclides for the waste inventory scenario 1 (commercial UNF plus DOE HLW) of the reference case for salt GDSE.

The doses for ^{231}Pa (decay daughter of ^{235}U) and ^{245}Cm are the weakest estimates as the radionuclides are described in the model as non-solubility-limited and non-sorbing because of a lack of sorption data and incomplete solubility analysis for the radionuclides. In reality the metal protactinium and curium are likely insoluble in water, and their oxides are expected to be

sparsely soluble in water. Their sorption on geologic materials is likely to be comparable to that of other actinide elements. If data allowed for the suspected dissolution and sorption behaviors of the radionuclides to be included in the model, doses for the radionuclides would not show up in the figure. If the doses for ^{231}Pa and ^{245}Cm are excluded, the major long-term dose contributors are ^{129}I, ^{79}Se, and ^{36}Cl, all of which are fission products with high solubilities in water and no or very weak sorption on geologic materials.

The results for the waste inventory scenario 2 (DOE HLW plus reprocessing HLW) are shown in Figure 5. Compared to the inventory scenario 1, this scenario requires a smaller number of waste packages (9,058 waste packages vs. 37,157 waste packages) and a one-fourth of the repository footprint area. This in turn takes a smaller volume of near-field, therefore a smaller amount of near-field water, resulting in higher concentrations of soluble radionuclides (such as ^{129}I and ^{79}Se) in the near-field water. In addition, because of the assumptions made for the reprocessing HLW (see Chapter 1), the fission products inventory on a per-waste package basis is higher than that for scenario 1. For example, each reprocessing HLW waste package contains about 7,500 g of ^{129}I and about 250 g of ^{79}Se, which is about eight times greater than the per-waste package inventory mass of the radionuclides of commercial UNF. Their impacts are shown in Figure 5 as having about two orders of magnitude higher mean dose for ^{129}I than the inventory scenario 1. The dose for ^{79}Se is about 10 times higher than that for inventory scenario 1.

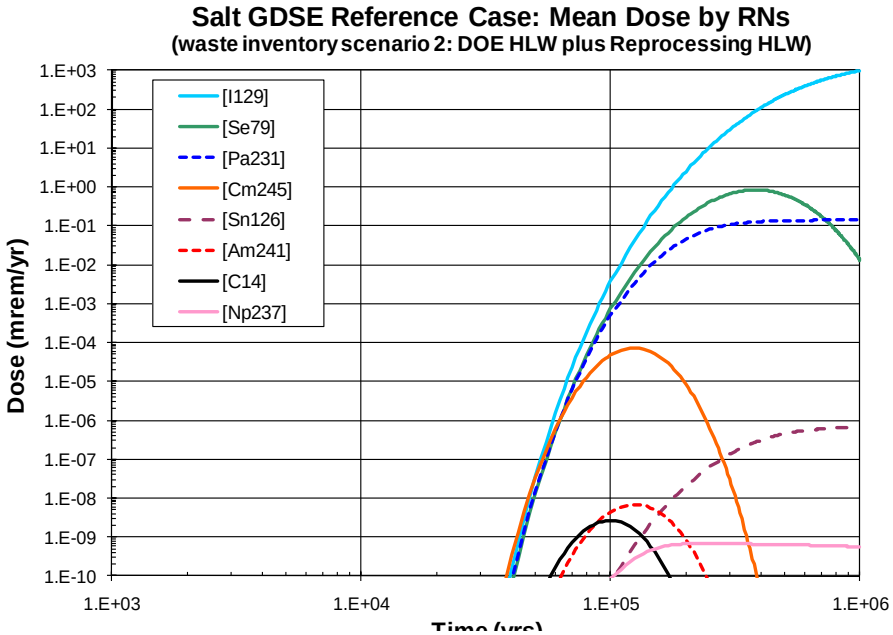

Figure 5: Mean dose by radionuclides for the waste inventory scenario 2 (DOE HLW plus reprocessing HLW) of the reference case for salt GDSE.

The same explanations offered for the inventory scenario 1 are applicable to the doses for ^{231}Pa and ^{245}Cm in Figure 5, and the doses can be ignored. It is interesting to note that, although minor, the doses for three additional radionuclides ^{241}Am, ^{14}C, and ^{237}Np are relevant on the

scale of the figure. Also note that the ^{36}Cl dose is absent in the figure because both the DOE HLW and reprocessing HLW do not have ^{36}Cl inventory.

Figure 6 shows the model results for inventory scenario 1 of the disturbed case; the dose histories are very different from those for the reference case. In this case, for demonstration, only commercial UNF waste packages are assumed to be affected by a single borehole penetration at 1,000 years, and the number of waste packages affected (i.e., the amount of waste inventory affected) are sampled between one and five. The dissolved radionuclides in the near-field water are transported upward by pressurized brine flow through the borehole and released directly to the overlying aquifer. The aquifer water flow rate is several orders of magnitude greater than the flow rate in the marker bed, and the radionuclides are transported at much greater rates (Tables 1 and 2).

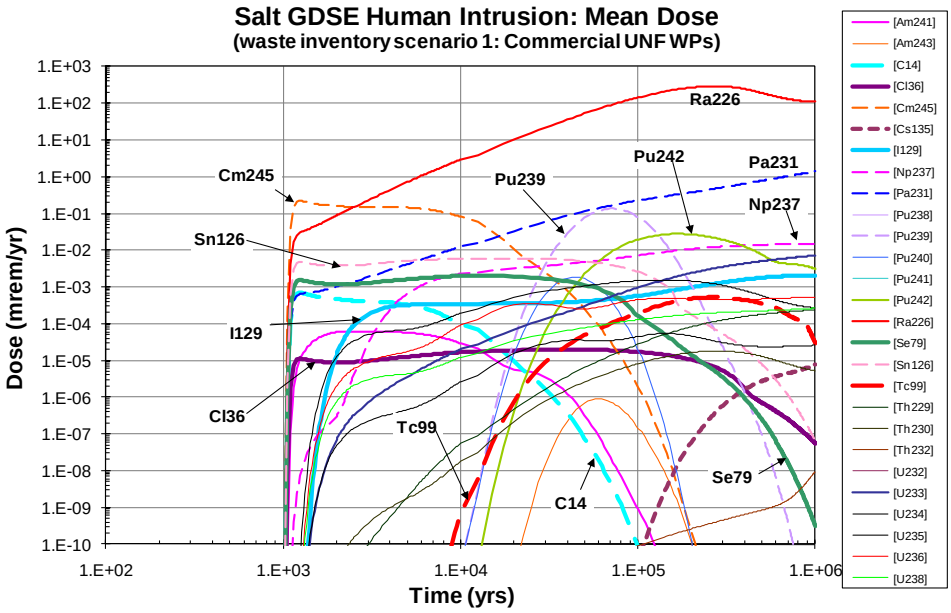

Figure 6: Mean dose by radionuclides for the waste inventory scenario 1 (commercial UNF) of the disturbed case for salt GDSE.

As shown in Figure 6, ^{226}Ra is the dominant dose contributor, which is a daughter of the decay chain:

$$^{242}\text{Pu}\ (3.76\times10^{5}\ \text{yrs}) \rightarrow {}^{238}\text{U}\ (4.46\times10^{9}\ \text{yrs}) \rightarrow {}^{234}\text{U}\ (2.45\times10^{5}\ \text{yrs}) \rightarrow {}^{230}\text{Th}\ (7.54\times10^{4}\ \text{yrs}) \rightarrow {}^{226}\text{Ra}\ (1.6\times10^{3}\ \text{yrs})$$

The initial inventory of ^{226}Ra is very small (9.6×10^{-6} g per commercial UNF waste package), so most of the dose for ^{226}Ra is likely to originate from the daughter of the above decay chain. In addition, due to a lack of data, radium is modeled as having no solubility-limit and as non-sorbing. However, radium is known to readily sorb on soil, clays and other geologic materials (Ames et al. 1983; Langmuir et al. 1985; Bassot et al. 2001). The radium solubility in water is dependent on the type of radium-containing minerals; for example, the solubilities of radium sulfate and carbonate are low, but solubilities of radium nitrate, chloride and iodate are high (Sebesta et al. 1981; Lind et al. 1918; Kaufmann et al. 1976). In general radium is not mobile in groundwater. If more representative values for the radium solubility and sorption were implemented, the dose for ^{226}Ra would have been much lower. Additional studies are needed to better characterize and quantify the dissolution and sorption behavior of radium in geologic environments.

As discussed in the reference case results, the doses for ^{231}Pa and ^{245}Cm can be ignored. Compared to the reference case results, the doses for the soluble, non-sorbing fission products, particularly ^{129}I and ^{79}Se are much lower, while the doses for actinides including ^{239}Pu, ^{242}Pu and ^{237}Np are much higher. The lower doses for the fission products are due to their lower total inventory available for release (i.e., up to five affected waste packages), and the higher doses for the actinides are due to the direct release of the radionuclides in the aquifer with higher water flow rates, resulting in an early arrival of higher concentrations of the radionuclides at the biosphere drinking water well prior to their significant decay.

The disturbed case results for the waste inventory scenario 2 are shown in Figure 7. In this case, only DOE HLW waste packages (between one and five waste packages) are assumed to be affected by a single borehole penetration. In general, the results are similar to those for inventory scenario 1 and the same analysis and explanations are applicable to the current results. One additional note to make is that the dose for ^{79}Se is much higher than that for ^{129}I for the inventory scenario 2 compared to inventory scenario 1; this can be explained with the following two aspects: 1) a greater ^{79}Se inventory in a DOE HLW waste package (about 110 g per package) than in a commercial UNF waste package (about 32 g per package), and 2) sorption of ^{129}I in the aquifer while no sorption of ^{79}Se.

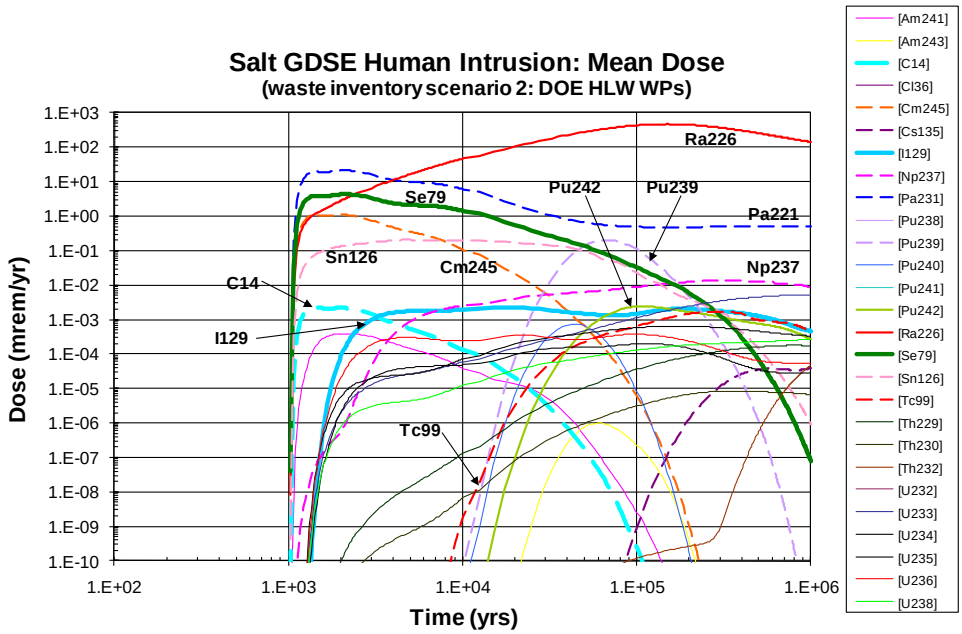

Figure 7: Mean dose by radionuclides for the waste inventory scenario 2 (DOE HLW) of the disturbed case for salt GDSE

5. Summary and Discussion

This chapter presents an initial version of the salt GDSE model and discusses the preliminary model results. The current model is an initial outcome of the long term effort to develop a salt GDSE analysis tool and it will be further improved and refined as the study progresses. The current model analysis helps to draw the following important considerations and thoughts for the near-term improvement of the on-going efforts on the salt GDSE model development and analysis.

- Soluble, non-sorbing fission products, particularly ^{129}I and ^{79}Se, are the major dose contributors. In the current model, ^{79}Se is modeled as soluble and non-sorbing in generic salt repository environments. However, the solubility and sorption behavior of selenium in reducing geologic environments are uncertain, and improvement is needed to better characterize and quantify the chemical properties. In addition, the half-life of ^{79}Se has been reported variously ranging from 6.5×10^{4} to 1.13×10^{6} years. A more accurate half-life estimate of this radionuclide is needed.

- The solubility and sorption data for some actinides (e.g., protactinium and curium) and decay daughters (e.g., radium) are not available. Because of the lack of data, these elements are modeled as being soluble and non-sorbing in the current model, and as a

result some of them (i.e., ^{131}Pa, ^{245}Cm, and ^{226}Ra) show up un-expectedly as significant dose contributors in the model results. Improvement is needed to better characterize and quantify the chemical properties of these radionuclides.

- Radionuclide release pathways and scenarios are important to the analysis of a generic salt repository, and this could be true to any generic repositories. Additional studies are needed to revise and improve the conceptual models for the release pathways and scenarios that are representative of a salt GDSE.

The salt GDSE model analysis has also identified the following important knowledge gaps to improve and enhance the confidence of the future model analysis.

- Repository thermal loading by high-level radioactive waste, and the effect on the engineered barrier and near-field performance.
- Creep closure of salt bedrock under the influence of thermal perturbation, and the effect on the engineered barrier and near-field performance.
- Water flow and radionuclide transport under the influence of thermal perturbation in generic salt repository environment, and the effect on the engineered barrier and near-field performance and far-field performance.
- Near-field chemistry and radionuclide mobility in generic salt repository environment (high ionic strength brines, elevated temperatures and reducing condition).
- Waste package and waste canister degradation in a generic salt repository environment
- Degradation for candidate waste form types in a generic salt repository environment
- Waste stream types and inventory estimates, particularly for reprocessing high-level waste.

6. References

Ames, L.L., McGarrah, J.E., and Walker, B.A., 1983. "Sorption of Uranium and Radium by Biotite, Muscovite, and Phlogopite," Clays and Clay Minerals, Vol. 31, pp. 343-351.

Bassot, S., Mallet, C., and Stammose, D. 2001. "Experimental Study and Modeling of the Radium Sorption onto Goethite," Materials Research Society Symposium Proceedings, Vol. 663.

Brush, L. H. and Storz, L. J., 1996. "Revised Ranges and Probability Distributions of Kds for Dissolved Pu, Am, U, Th, and Np in the Culebra for the PA Calculations to Support the WIPP CCA, in US DOE. 1996. Title 40 CFR Part 191 Compliance Certification Application, Appendix MASS, Attachment 15-1". DOE/CAO-1996-2184. Carlsbad, NM: US DOE Carlsbad Area Office, 1996.

Helton, J.C., Bean, J.E., Berglund, J.W., Davis, F.J., Economy, K., Garner, J.W., Johnson, J.D., MacKinnon, R.J., Miller, J., O'Brien, D.G., Ramsey, J.L., Schreiber, J.D., Shinta, A.,

Smith, L.N., Stoelzel, D.M., Stockman, C., and Vaughn, P., 1998. "Uncertainty and Sensitivity Analysis Results Obtained in the 1996 Performance Assessment for the Waste Isolation Pilot Plant", SAND98-0365, Albuquerque, NM, Sandia National Laboratories.

Jiang, S.S., He, M., Diao, L.J., Guo, J.R., and Wu, S.Y., 2001. "Remeasurement of the Half-Life of ^{79}Se with the Projectile X-Ray Detection Method," Chinese Physics Letter, Vol. 18, pp. 746-749.

Kaufmann, R.F., Eadie, G.G., and Russell, C.R., 1976. "Effects of Uranium Mining and Milling on Ground Water in the Grants Mineral Belts, New Mexico," Ground Water, Vol. 14, pp. 296-308.

Langmuir, D., and Riese, A.C., 1985. "The Thermodynamic Properties of Radium," Geochimica et Cosmochimica Acta, Vol. 49, pp. 1593-1601.

Lappin, A.R., R.L. Hunter, D.P. Garber and P.B. Davies, ed. 1989. "Systems Analysis, Long-Term Radionuclide Transport, and Dose Assessments, Waste Isolation Pilot Plant (WIPP), Southeastern New Mexico; March 1989", SAND89-0462. Albuquerque, NM: Sandia National Laboratories.

Lind, S.C., Underwood, J.E., and Whittemore, C.F., 1918. "The Solubility of Pure Radium Sulfate, "J. of the American Chemical Society, Vol. 40, pp. 465-472.

McKinley, I.G. and A. Scholtis, 1992. Compilation and comparison of radionuclide sorption databases used in recent performance assessments. *Radionuclide Sorption Safety Evaluation Perspectives, Proceedings of an NEA Workshop,* OECD, Paris, France, pp 21-55.

Muller, A.B., Finley, N. C. and Pearson, J. Jr. 1981. *Geochemical Parameters used in the Bedded Salt Reference Repository Risk Assessment Methodology. NUREG/CR-1996; SAND0557,* Sandia National Laboratories, Albuquerque, NM.

Pepping, R. E., Chu, M. S., and Siegel, M. D., 1983. Technical Assistance for Regulatory 26 Development: Review and Evaluation of the Draft EPA Standard 40CFR191 for Disposal of High-Level Waste, Volume 4: A Simplified Analysis of a Hypothetical Repository in a Bedded Salt Formation, NUREG/CR-3235, Sandia National Laboratories, Albuquerque, NM.

Sebesta, F., Benes, P., Sedlacek, J., John, J., and Sandrik, R., 1981. "Behavior of Radium and Barium in a System Including Uranium Mine Waste Waters and Adjacent Surface Waters," Environmental Science and Technology, Vol. 15, pp. 71-75.

Tien, P.L., Nimick, F., Muller, A., Davis, P., Guzowski, R., Duda, L. and Hunter, R., 1983. *Repository Site Data and Information in Bedded Salt: Palo Duro Basin, Texas. NUREG/CR-3129, SAND82-2223.* Sandia National Laboratories, Albuquerque, NM.

Vaughn, P., Bean, J.E., Helton, J.C., Lord, M.E., MacKinnon, R.J., and Schreiber, J.D., 2000. "Representation of Two-Phase Flow in the Vicinity of the Repository in the 1996 Performance Assessment for the Waste Isolation Pilot Plant," *Reliability Engineering and System Safety,* Volume 69, pp 205-226.

Chapter 3 Granite Generic Disposal System Environment Model

Shaoping Chu

Los Alamos National Laboratory

1. Introduction

This chapter discusses the development of the granite Generic Disposal System Environment (GDSE) model and presents preliminary model results. For a better comparison among the different disposal environments, a uniform set of assumptions about model configurations is developed and applied to both salt and granite model cases (See Chapter 2). The reference source-term model implemented as a Goldsim template is developed by Sandia National Laboratories and is described in Chapter 1. The granite GDSE model adopts this template and incorporates an additional module on radionuclide diffusion through the bentonite backfill buffer around waste packages in the near field. The far-field component of the granite GDSE is developed by incorporating the Finite Element Heat and Mass Transfer (FEHM) code (Zyvoloski et al., 1997, 2007) into the GoldSim model (GoldSim, 2007). The system level generic granite GDSE model couples the near field and the far field components for performance assessment simulations.

2. Model Description

The granite GDSE model is comprised of two major components, the near field and the far field. This section summarizes the modeling approaches used for both. The versions of codes used for this study are: GoldSim (version 10.11) and FEHM (version 3.0).

2.1. Granite GDSE Model Structure

The structure of the overall granite GDSE model is shown in Figure 1. The near-field and far-field models are coupled through the near-far interface (*NF_interface*) component. The model assumes that the repository is located in a saturated, chemically-reducing environment below the water table. For simplification, the repository is assumed to have a square footprint with 25 m spacing between emplacement tunnels and 6 m between waste packages. Three waste types are considered: commercial used nuclear fuel (UNF), existing DOE high level waste (HLW) and reprocessing waste (RW). The model includes 36 radionuclides, accounting for both in-growth of daughters and isotopic mixing among radionuclides. A hypothetical biosphere (the performance measure boundary) is assumed to be located 5 km from the repository edge. The model analysis runs 100 Monte-Carlo realizations for a time period of 1 million years. The *Uncertain_Parameters* component performs sampling for uncertain parameters for 100-realization simulations. IAEA BIOMASS Example Reference Biosphere 1B (ERB1B) dose model is used to convert the output radionuclide concentrations in the ground water at the hypothetical drinking well location to an estimate of annual dose based on drinking well water

consumption (IAEA, 2003). The *NF_interface* component shown in Figure 1 calculates the total radionuclide flux from the near field to the far field.

The near-field model shown in Figure 2A includes the following major components:

- *Waste_form_degradation*: Calculate radionuclide release rates from waste degradation based on the assigned value of annual fraction waste form degradation rate.
- *WF_RN_release*: Calculate the radionuclide to the near-field as a function of waste form degradation, radionuclide solubility, and available water volume in the near-field.
- *Repository_config & In_Package_volume*: Calculates the near-field void volume (i.e., the near-field water volume) of the granite GDSE.

The far-field model shown in Figure 2B includes the far-field reactive transport model FEHM, and is discussed in Section 2.3.

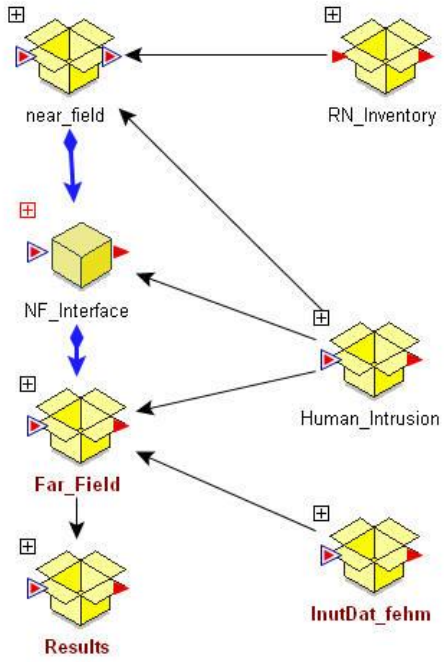

Figure 1: Overview of structure of granite GDSE model

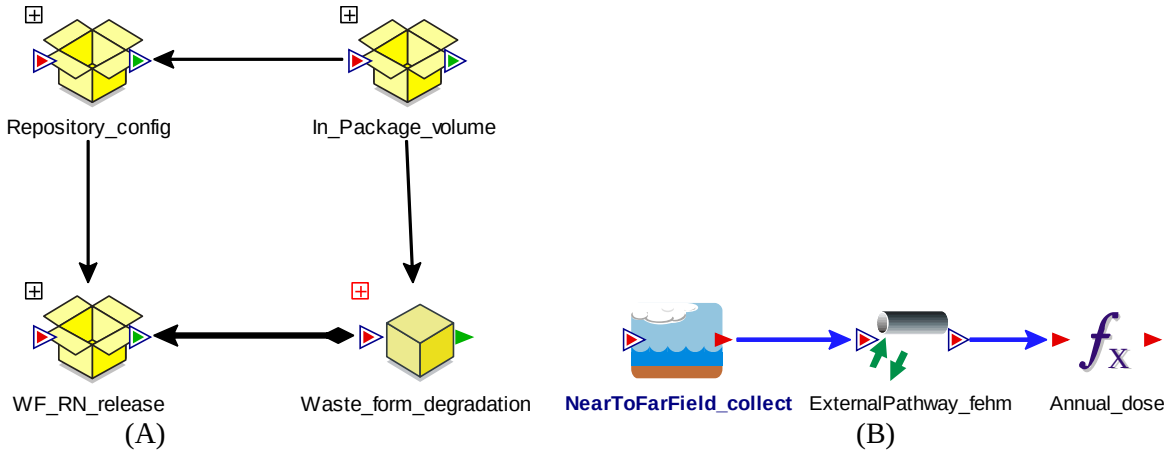

Figure 2: Granite GDSE (A) Near-Field and (B) Far-Field model component structure

2.2.Near Field of Granite GDSE

The near-field represents physical domains and flow paths that control waste form dissolution and radionuclide transport before radionuclides enter the nearby aquifer. The relevant physical and chemical characteristics and processes in the near field include: repository layout, radionuclide inventory and waste form degradation, near-field solubility control, radionuclide release from near-field, solubility control at the near-field and far-field interface, human intrusion, and diffusion through bentonite buffer material. Detailed discussion for the inventory and source term model can be found in Chapter 1. Two potential radionuclides release scenarios are considered in the model analysis.

Human intrusion: Assume that a single borehole penetrates through the repository at 1,000 years, creating a fast pathway for radionuclide release to the overlying aquifer.

Diffusion through bentonite buffer: Bentonites have been proposed as a buffer material for geological disposal of radioactive waste. In a water-saturated environment, the fluid in the bentonite backfill is almost static because of the very low permeability in the medium, and the advective transport is negligible. The only significant transport in the near field is the diffusion of radionuclides through the bentonite buffer coupled with radionuclide sorption to bentonite material. Some waste packages may directly intersect with fractures in the surrounding granite rock. Radionuclides released from these waste packages are transported to the nearby aquifer through fast fracture flows. The bentonite buffer properties, diffusivities and sorption coefficients that affect the transport of key radionuclides are listed in Table 1.

Table 1: Bentonite buffer parameters used in granite GDSE model

Parameter[1]	Stochastic Parameter type	Base Case Value	Distribution Parameters
Density (kg/m^3)	Constant	1700	N/A
Porosity	Constant	0.3	N/A
Tortuosity	Constant	0.13	N/A
Thickness (m)	Constant	0.36	N/A
Effective diffusivity D_e (m^2/s), Ac	Uniform	2.52×10^{-8}	Range: 5.1×10^{-10}-5.0×10^{-8}
D_e (m^2/s), Am	Uniform	2.52×10^{-8}	Range: 5.1×10^{-10}-5.0×10^{-8}
D_e (m^2/s), C	Constant	8.8×10^{-10}	N/A
D_e (m^2/s), Cl	Uniform	8.55×10^{-12}	Range: 4.1×10^{-12}-1.3×10^{-11}
D_e (m^2/s), Cm	Uniform	2.52×10^{-8}	Range: 5.1×10^{-10}-5.0×10^{-8}
D_e (m^2/s), Cs	Uniform	9.52×10^{-9}	Range: 2.04×10^{-9}-1.7×10^{-8}
D_e (m^2/s), I	Uniform	1.14×10^{-9}	Range: 3.0×10^{-11}-2.24×10^{-9}
D_e (m^2/s), Np	Uniform	8.76×10^{-9}	Range: 5.13×10^{-10}-1.7×10^{-8}
D_e (m^2/s), Pa	Uniform	8.76×10^{-9}	Range: 5.13×10^{-10}-1.7×10^{-8}
D_e (m^2/s), Pu	Uniform	1.44×10^{-8}	Range: 2.55×10^{-10}-2.86×10^{-8}
D_e (m^2/s), Ra	Uniform	2.59×10^{-9}	Range: 8.53×10^{-11}-5.1×10^{-9}
D_e (m^2/s), Se	Uniform	2.92×10^{-11}	Range: 7.1×10^{-12}-5.13×10^{-11}
D_e (m^2/s), Sn	Uniform	7.81×10^{-10}	Range: 1.8×10^{-10}-1.38×10^{-9}
D_e (m^2/s), Sr	Uniform	2.59×10^{-9}	Range: 8.53×10^{-11}-5.1×10^{-9}
D_e (m^2/s), Tc	Uniform	9.35×10^{-8}	Range: 8.5×10^{-8}-1.02×10^{-7}
D_e (m^2/s), Th	Uniform	2.0×10^{-8}	Range: 1.07×10^{-10}-4.0×10^{-8}
D_e (m^2/s), U	Uniform	9.27×10^{-9}	Range: 1.53×10^{-9}-1.7×10^{-8}
D_e (m^2/s), Nb	Constant	8.97×10^{-11}	N/A
D_e (m^2/s), Pb	Constant	8.97×10^{-11}	N/A
D_e (m^2/s), Pd	Constant	8.97×10^{-11}	N/A
D_e (m^2/s), Sb	Constant	8.97×10^{-11}	N/A
D_e (m^2/s), Zr	Constant	8.97×10^{-11}	N/A
Sorption coefficient K_d (cc/g), Ac	Uniform	14850	Range: 300-29400
K_d (cc/g), Am	Uniform	14850	Range: 300-29400
K_d (cc/g), C	Constant	5	N/A

K_d (cc/g), Cm	Uniform	14850	Range: 300-29400
K_d (cc/g), Cs	Uniform	560	Range: 120-1000
K_d (cc/g), I	Uniform	6.5	Range: 0-13
K_d (cc/g), Np	Uniform	515	Range: 30-1000
K_d (cc/g), Pa	Uniform	515	Range: 30-1000
K_d (cc/g), Pu	Uniform	8475	Range: 150-16800
K_d (cc/g), Ra	Uniform	1525	Range: 50-3000
K_d (cc/g), Se	Uniform	17	Range: 4-30
K_d (cc/g), Sn	Uniform	485.5	Range: 112-859
K_d (cc/g), Sr	Uniform	1525	Range: 50-3000
K_d (cc/g), Tc	Uniform	55000	Range: 50000-60000
K_d (cc/g), Th	Uniform	11782	Range: 63-23500
K_d (cc/g), U	Uniform	545	Range: 90-1000
K_d (cc/g), Cl	Constant	0	N/A
K_d (cc/g), Nb	Constant	0	N/A
K_d (cc/g), Pb	Constant	0	N/A
K_d (cc/g), Pd	Constant	0	N/A
K_d (cc/g), Sb	Constant	0	N/A
K_d (cc/g), Zr	Constant	0	N/A

[1] Parameters source: (Hansen et al., 2010; Itälä, 2009; Montes-H et al., 2005; Pusch & Svemar, 1993; Tanhua-Tyrkkö, 2009). Note : For the species Nb, Pb, Pd, Sb, Zr and Cl, diffusion and/or sorption parameters were not readily available, and because this run was performed as a generic version to investigate the feasibility of the modeling system, placeholder values for diffusion and a sorption coefficient of 0 were used for computational expediency.

2.3.Far Field of Granite GDSE

The Finite Element Heat and Mass Transfer (FEHM) code (Zyvoloski et al., 1997, 2007) is coupled to the GoldSim model to represent the far-field component of the granite GDSE model. This approach enables the full capabilities of FEHM to be employed in the calculation. In many instances, a process model of a component of the natural system is developed with a full three-dimensional representation using a code like FEHM (e.g. the unsaturated and saturated zone components of the Yucca Mountain repository system). This capability development, described below, is therefore a significant improvement in our ability to integrate process level models in disposal system analyses.

In this generic, non-site-specific study, no process model is available to integrate into the granite GDSE model. Therefore, a more generic approach to representing the far field is required to capture the key hydrologic, and physical and chemical transport processes. A simple yet flexible far-field pathway model using FEHM has been developed for this purpose. The model consists of radionuclide decay and in-growth, advection, matrix diffusion, and sorption, all

features that are implemented using FEHM's reactive transport modeling capability. The advection term is parameterized using a feature that enables the user to prescribe a distribution of advective travel times through a hydrologic pathway. This flexibility enables study of potentially very heterogeneous domains that may give rise to a broad distribution of advective transport times. The user inputs the statistical parameters of the residence time distribution (RTD), or an arbitrary distribution is read from a file, and the model automatically constructs a simplified pathway model that reproduces that distribution. We call this approach an RTD-based transport model. The groundwater speed for generic granite GDSE simulations is sampled through stochastic distribution with a mean value of 10 m/yr. On top of the advective component, the model uses FEHM's Generalized Dual Porosity Model (GDPM) feature to include diffusive exchange between the flowing porosity and the surrounding rock matrix. Because the model is established using a numerical modeling approach in FEHM, any other relevant transport process that is included in FEHM is made available as well. In this study, diffusion, radioactive decay and tracking of decay chains, and sorption (with an equilibrium "Kd approach") are used in the results that follow. An extensive theory was developed to implement this RTD-based model, the details of which are provided in FY08 GNEP report Appendix B.1 (Chu et. al., 2008).

The FEHM code was modified to couple with GoldSim for probabilistic simulations for granite generic repository studies. In the coupled model, GoldSim performs the overall time steps of the model run and radionuclide mass is transferred to and from FEHM at each time step. This capability was implemented by using GoldSim Contaminant Transport Module External pathway, which calls FEHM as a dynamic link library (dll). GoldSim passes a string of variables into each FEHM simulation to initialize the coupled simulation as well as at each GoldSim time step during the system level simulation. These variables include: time, the number of species that FEHM will be simulating, and the amount of mass entering the groundwater pathway.

GoldSim initializes the simulation by passing the first time increment to FEHM. In the FEHM simulation, GoldSim passes the mass associated with each radionuclide arriving into the groundwater pathway during that time step. FEHM accepts the incoming mass and adds it to the ongoing calculation of transport through the RTD-based model for the far field pathway to the far-field boundary using the model described above. The cumulative transport of each species, including radioactive decay, is calculated. FEHM can be invoked in a way that enables multiple, smaller time steps to be taken within each GoldSim time step to ensure that the tracer transport solution converges to an accurate solution. At the end of each GoldSim time step, FEHM passes back into GoldSim any mass reaching the far-field boundary. Mass reaching the far-field boundary is either from the initial input of the primary species from the source region or in-growth of daughter products formed during transport along the groundwater pathway.

The FEHM input data files contain inputs such as diffusion and sorption parameters that are to be generated from a stochastic distribution. To accomplish this in a flexible way, a DLL was developed to alter the data in the FEHM input files at the beginning of each realization. The DLL INPUTDAT is invoked by GoldSim initially, before GoldSim executes FEHM, to generate an input data file for each FEHM realization run. For each realization, the INPUTDAT program samples the input parameters from a stochastic distribution generated by GoldSim, and places them in the correct places in the input data template to create a new input data file for that FEHM realization. This development was done in a general way, such that any parameter in the FEHM input file can be generated stochastically and placed into the file at runtime.

2.4. Implementation of Uncertain Parameters in Granite GDSE

Uncertainty in the expected behavior of a generic granite repository requires that the granite GDSE model analyses be probabilistic in order to capture the likely range of potential outcomes. The granite GDSE model evaluates likely future outcomes by conducting multiple realizations using value distributions of uncertain parameters that may be important to a generic granite repository performance. The model realizations are performed using various combinations of parameter values sampled from the parameter-value distributions. Each of the combinations of parameter values is representative of a subset of the likely range of potential outcomes. Table 2A lists the uncertain model parameters implemented in the granite GDSE near-field model. Table 2B lists the uncertain model parameters implemented in the granite GDSE far-field model. Fractional release rates of different waste types were sampled stochastically.

3. Model Results

This section discusses the preliminary results of the granite GDSE model analysis. Two independent radionuclide release scenarios are simulated:

1) Disturbed Scenario (human intrusion): Assume a single borehole penetrates through the repository at 1,000 years, thus creating a fast pathway for radionuclide transport to the overlying aquifer. The flow rate up the borehole is sampled through a distribution with a mean value 2.55 m^3/yr. The number of waste packages affected (i.e., waste inventory affected) by a single borehole penetration is sampled between 1 and 5. Two cases are considered for this scenario:
   - Case I: Assume only commercial UNF WPs are affected by human intrusion (HI). No DOE HLW inventory is affected.
   - Case II: Assume only DOE HLW WPs are affected by HI. No reprocessing HLW inventory is affected.

2) Undisturbed Scenario (diffusion through bentonite buffer): In this scenario radionuclides released from degrading waste form are transported out of the waste package by diffusion through the bentonite buffer. Some waste packages directly intersect with fractures in the surrounding granite rock, and radionuclides released from these waste packages directly enter into fractures for fast pathway transport. The flow rate upward in the intersected fractures is sampled with a mean value of 0.45×10^{-3} m^3/yr per waste package for commercial UNF and 0.14×10^{-3} m^3/yr per waste package for DOE HLW and reprocessing HLW. For those waste packages releasing radionuclides to the fractures, the model assumes a fraction (between 0.1 and 1 percent) of the affected inventory is available for the advective transport in the fractures, and the fraction is sampled between the bounds. Two cases are considered for this scenario:
   - Case I: The inventory considered includes commercial UNF plus DOE HLW
   - Case II: The inventory considered includes reprocessing HLW plus DOE HLW

Table 2A. Near Field parameters for 36 radionuclides

Parameter[1]	Stochastic Parameter type	Base Case Value	Distribution Parameters
UNF matrix degradation rate (1/yr)	Log-triangular	1.528×10^{-7}	1×10^{-8}, 1×10^{-7}, 1×10^{-6}
HLW and RW degradation rate (borosilicate glass) (1/yr)	Log-uniform	4.917×10^{-4}	3.4×10^{-6}, 3.4×10^{-3}
Porosity, inside waste package	Uniform	0.4	Range: 0.3-0.5
Porosity, bed rock	Uniform	0.00525	Range: 0.0005-0.01
Porosity, overlaying aquifer	Uniform	0.1	Range: 0.05-0.15
Waste package temperature (C)	Constant	25	N/A
Waste package size, outer diameter (m)	Constant	1.56	N/A
Waste package size, outer length (m)	Constant	5.517	N/A
Number of waste packages -UNF	Constant	32154	N/A
Number of waste packages -HLW	Constant	5003	N/A
Number of waste packages -RW	Constant	4055	N/A
Number of waste packages (WP) affected by a single drilling through repository	Uniform	3	Range: 1-5
Percent of WPs affected by canister failure and diffuse through bentonite buffer (%)	Uniform	0.55	Range: 0.1-1
Portion of HLW WPs affected by canister failure and diffuse through bentonite buffer	Uniform	0.5	Range: 0-1
Water flow rate up a single borehole through granite GDSE, -human intrusion scenario (m^3/yr)	Uniform	2.55	Range: 0.1-5
Water flow rate up fracture intersecting UNF waste package, -undisturbed scenario (m^3/yr/per canister)	Constant	0.45×10^{-3}	N/A
Water flow rate up fracture intersecting HLW/RW waste package, -undisturbed scenario (m^3/yr/per canister)	Constant	0.14×10^{-3}	N/A
Solubility-near field, Ac (mg/L)	Constant	unlimited	N/A

Solubility-near field, Am (mg/L)	Triangular	0.21237	0.045, 0.1423, 0.45
Solubility-near field, C (mg/L)	Constant	unlimited	N/A
Solubility-near field, Cl (mg/L)	Constant	unlimited	N/A
Solubility-near field, Cm (mg/L)	Constant	unlimited	N/A
Solubility-near field, Cs (mg/L)	Constant	unlimited	N/A
Solubility-near field, I (mg/L)	Constant	unlimited	N/A
Solubility-near field, Nb (mg/L)	Constant	unlimited	N/A
Solubility-near field, Np (mg/L)	Triangular	0.0005359	0.000113, 0.000359, 0.00113
Solubility-near field, Pa (mg/L)	Constant	unlimited	N/A
Solubility-near field, Pb (mg/L)	Constant	unlimited	N/A
Solubility-near field, Pd (mg/L)	Constant	unlimited	N/A
Solubility-near field, Pu (mg/L)	Triangular	1.7206	0.338, 1.119, 3.705
Solubility-near field, Ra (mg/L)	Constant	unlimited	N/A
Solubility-near field, Sb (mg/L)	Constant	unlimited	N/A
Solubility-near field, Se (mg/L)	Constant	unlimited	N/A
Solubility-near field, Sn (mg/L)	Triangular	0.00453	0.00124, 0.00335, 0.00901
Solubility-near field, Sr (mg/L)	Constant	unlimited	N/A
Solubility-near field, Tc (mg/L)	Log-triangular	3.165×10^{-3}	4.512×10^{-5}, 1.321×10^{-3}, 3.87×10^{-2}
Solubility-near field, Th (mg/L)	Triangular	1080.7	464.7, 927.3, 1850.1
Solubility-near field, U (mg/L)	Triangular	0.0331	0.0116, 0.0267, 0.0611
Solubility-near field, Zr (mg/L)	Constant	unlimited	N/A
Solubility-NF interface, Ac (mg/L)	Constant	unlimited	N/A
Solubility-NF interface, Am (mg/L)	Triangular	0.3827	0.0811, 0.256, 0.811
Solubility-NF interface, C (mg/L)	Constant	unlimited	N/A
Solubility-NF interface, Cl (mg/L)	Constant	unlimited	N/A
Solubility-NF interface, Cm (mg/L)	Constant	unlimited	N/A
Solubility-NF interface, Cs (mg/L)	Constant	unlimited	N/A
Solubility-NF interface, I (mg/L)	Constant	unlimited	N/A
Solubility-NF interface, Nb (mg/L)	Constant	unlimited	N/A
Solubility-NF interface, Np (mg/L)	Log-triangular	4.0027	0.262, 2.62, 26.3
Solubility-NF interface, Pa (mg/L)	Constant	unlimited	N/A
Solubility-NF interface, Pb (mg/L)	Constant	unlimited	N/A
Solubility-NF interface, Pd (mg/L)	Constant	unlimited	N/A
Solubility-NF interface, Pu (mg/L)	Triangular	0.9613	0.189, 0.625, 2.07
Solubility-NF interface, Ra (mg/L)	Constant	unlimited	N/A

Solubility-NF interface, Sb (mg/L)	Constant	unlimited	N/A
Solubility-NF interface, Se (mg/L)	Constant	unlimited	N/A
Solubility-NF interface, Sn (mg/L)	Triangular	0.0082	0.00225, 0.00605, 0.0163
Solubility-NF interface, Sr (mg/L)	Constant	unlimited	N/A
Solubility-NF interface, Tc (mg/L)	Constant	unlimited	N/A
Solubility-NF interface, Th (mg/L)	Triangular	4.7667	2.05, 4.09, 8.16
Solubility-NF interface, U (mg/L)	Triangular	88.567	21.8, 62.9, 181
Solubility-NF interface, Zr (mg/L)	Constant	unlimited	N/A

[1] Parameters source: (Neretnieks, 1982; see source term model session for inventory and solubility references)

Table 2B. Far Field hydrologic parameters for 36 radionuclide species

Parameter[1]	**Stochastic Parameter type**	**Base Case Value**	**Distribution Parameters**
Flow Parameters			
Mean of Ln travel time distribution, μ_{ln}	Normal distribution for μ_{ln}	23.482 (ln(s))	23.482, 0.8
Std. Dev. of Ln travel time distribution, σ_{ln}	Normal distribution for $\overline{\sigma}_{ln} = \sigma_{ln} / \mu_{ln}$	0.026487	0.026487, 7.946×10^{-3}
Geometric Parameters			
Aperture (m)	Constant	1×10^{-4}	N/A
Fracture spacing (m)	Constant	25	N/A
Transport Parameters			
Diffusive Tortuosity τ_D, all species	Normal distribution for $\tau_D = D / D_{free}$	0.0144	0.0144, 4.176×10^{-3}
Free-Water diffusion coefficient D_{free} (m^2/s), Am	Constant	9.49×10^{-10}	N/A
D_{free} (m^2/s), C	Constant	1.18×10^{-9}	N/A
D_{free} (m^2/s), Pa	Constant	6.04×10^{-10}	N/A
D_{free} (m^2/s), Ra	Constant	8.89×10^{-10}	N/A
D_{free} (m^2/s), Th	Constant	5.97×10^{-10}	N/A
D_{free} (m^2/s), Sn	Constant	1.55×10^{-9}	N/A
Matrix diffusion	Truncated normal	1.37×10^{-10}	Range:3.75×10^{-11}-3.21×10^{-10},

coefficient (pore diffusivity) D (m^2/s), Cl	distribution		$1.37x10^{-10}$, $1.08x10^{-10}$
D (m^2/s), Cs	Truncated normal distribution	$2.11x10^{-10}$	Range:$1.03x10^{-10}$-$3.75x10^{-10}$, $2.11x10^{-10}$, $1.05x10^{-10}$
D (m^2/s), I	Truncated normal distribution	$1.57x10^{-10}$	Range:$7.96x10^{-11}$-$3.38x10^{-10}$, $1.57x10^{-10}$, $6.02x10^{-10}$
D (m^2/s), Np	Truncated normal distribution	$6.99x10^{-11}$	Range:$2.8x10^{-11}$-$1.1x10^{-10}$, $6.99x10^{-11}$, $2.75x10^{-11}$
D (m^2/s), Pu	Truncated normal distribution	$4.1x10^{-11}$	Range:$2.61x10^{-11}$-$5.63x10^{-11}$, $4.1x10^{-11}$, $1.07x10^{-11}$
D (m^2/s), Se	Truncated normal distribution	$8.93x10^{-11}$	Range:$8.26x10^{-11}$-$9.46x10^{-11}$, $8.93x10^{-11}$, $5.0x10^{-12}$
D (m^2/s), Sr	Truncated normal distribution	$6.65x10^{-11}$	Range:$2.86x10^{-11}$-$4.0x10^{-10}$, $6.65x10^{-11}$, $9.66x10^{-11}$
D (m^2/s), Tc	constant	$4.2x10^{-12}$	N/A
D (m^2/s), U	Truncated normal distribution	$5.14x10^{-12}$	Range:$3.14x10^{-12}$-$6.29x10^{-12}$, $5.14x10^{-12}$, $1.42x10^{-12}$
D (m^2/s), Ac	Constant	$5.0x10^{-11}$	N/A
D (m^2/s), Pb	Constant	$5.0x10^{-11}$	N/A
D (m^2/s), Sb	Constant	$5.0x10^{-11}$	N/A
D (m^2/s), Zr	Constant	$5.0x10^{-11}$	N/A
D (m^2/s), Nb	Constant	$5.0x10^{-11}$	N/A
D (m^2/s), Pd	Constant	$5.0x10^{-11}$	N/A
D (m^2/s), Cm	Constant	$5.0x10^{-11}$	N/A
Matrix sorption coefficient K_d (cc/g), Ac	CDF	3000	(1000,0) (3000,0.5) (5000,1)
K_d (cc/g), Am	CDF	3000	(1000,0) (3000,0.5) (5000,1)
K_d (cc/g), C	CDF	1	(0.5,0) (1,0.5) (2,1)
K_d (cc/g), Cl	Non-sorbing	0	0
K_d (cc/g), Cm	CDF	3000	(1000,0) (3000,0.5) (5000,1)
K_d (cc/g), Cs	CDF	500	(100,0) (500,0.5) (1000,1)
K_d (cc/g), I	Non-sorbing	0	N/A
K_d (cc/g), Nb	CDF	1000	(500,0) (1000,0.5) (3000,1)
K_d (cc/g), Np	CDF	5000	(1000,0) (5000,0.5)(10000,1)
K_d (cc/g), Pa	CDF	1000	(500,0) (1000,0.5) (5000,1)

K_d (cc/g), Pd	CDF	100	(10,0) (100,0.5) (500,1)
K_d (cc/g), Pu	CDF	5000	(1000,0) (5000,0.5)(10000,1)
K_d (cc/g), Ra	CDF	100	(50,0) (100,0.5) (500,1)
K_d (cc/g), Se	CDF	1	(0.5,0) (1,0.5) (5,1)
K_d (cc/g), Sn	CDF	1	(0,0) (1,0.5) (10,1)
K_d (cc/g), Sr	CDF	10	(5,0) (10,0.5) (50,1)
K_d (cc/g), Tc	CDF	1000	(300,0) (1000, 0.5) (3000,1)
K_d (cc/g), Th	CDF	5000	(1000,0) (5000,0.5)(10000,1)
K_d (cc/g), U	CDF	5000	(1000,0) (5000,0.5)(10000,1)
K_d (cc/g), Zr	CDF	1000	(500,0) (1000,0.5) (3000,1)
K_d (cc/g), Pb	Constant	0	N/A
K_d (cc/g), Sb	Constant	0	N/A

[1] Parameters source: (Carbol & Engkvist, 1997; Liu et al., 2006; JAEA database; Chu et. al., 2008). For Ac, Pb, Sb, Zr, Nb, Pd and Cm, diffusion parameters were not readily available (sorption parameters are not readily available for Pb, Sb), and because the model analysis was performed for a generic repository to investigate the feasibility of the modeling system, placeholder values for diffusion and a sorption coefficient of 0 were used for expediency.

-

The descriptions of near-field parameters are provided in Table 2A and far-field parameters in Table 2B. Parameters for representative radionculides are summarized in Table 3. Note that parameter ranges and distributions are selected just for a demonstration purpose of the granite GDSE model analysis, and many of these parameters are site-specific. For elements Ac, Pb, Sb, Zr, Nb, Pd and Cm, the far field diffusion and sorption parameters are not readily available and thus assigned to values of zero. The radionuclide concentrations in the aquifer groundwater at the location of the hypothetical biosphere (5 km downstream from the repository boundary) were analyzed. The analyses were run for 1 million years with 100 Monte Carlo realizations for each case listed above.

Table 3. Parameters for representative radionuclides

Species ID	Atomic Weight (g/mol)	Half-life (year)	Solubility – Near field (mg/L)	Solubility – Near-Far field interface (mg/L)	Far field sorption coefficient Kd (cc/g)	Specific activity (Ci/g)	Dose conversion factor (Sv y^{-1} / Bq y^{-1})
Actinide Parent Species							
Np	237	2.14×10^{6}	5.36×10^{-4}	4.003	5000	0.00070487	1.33×10^{-11}
Pu	238	87.7	1.721	0.961	5000	17.127	2.76×10^{-11}
	239	2.41×10^{4}				0.062066	3.00×10^{-11}
	240	6.54×10^{3}				0.22776	3.00×10^{-11}
	242	3.76×10^{5}				0.0039289	2.88×10^{-11}
Am	241	432	2.12×10^{-1}	3.83×10^{-1}	3000	3.4338	2.40×10^{-11}
	243	7.37×10^{3}				0.19962	2.41×10^{-11}
U	232	68.9	3.315×10^{-2}	8.857×10^{1}	5000	22.365	6.7×10^{-11}
	233	1.59×10^{5}				0.0096498	6.12×10^{-12}
	234	2.45×10^{5}				0.0062357	5.88×10^{-12}
	235	7.04×10^{8}				2.1609×10^{-6}	5.68×10^{-12}
	236	2.34×10^{7}				6.4736×10^{-5}	5.64×10^{-12}
	238	4.46×10^{9}				3.3679×10^{-7}	5.81×10^{-12}
Fission Products and Others							
Tc	99	2.13×10^{5}	3.165×10^{-3}	unlimited	1000	0.016953	7.68×10^{-14}
I	129	1.7×10^{7}	unlimited	unlimited	0	0.00016302	1.32×10^{-11}
Cs	135	2.3×10^{6}	unlimited	unlimited	500	0.0011514	2.40×10^{-13}
Se	79	6.5×10^{4}	unlimited	unlimited	1	0.069662	3.48×10^{-13}
Cl	36	3.01×10^{5}	unlimited	unlimited	0	0.032991	1.116×10^{-13}

Figure 3 shows the mean annual doses by radionuclides at the hypothetical biosphere location (5 km downstream from the repository boundary) for Human Intrusion case, calculated from 100 realizations simulations. The ^{129}I mean annual dose surpasses ^{241}Am, ^{243}Am, ^{239}Pu and ^{240}Pu after a few thousands years, and eventually becomes the dominant contributor toward the end of the 1 million year simulation. The long half-life, high solubility, and weak sorption in the far field of the radionuclide contribute to the high mean dose.

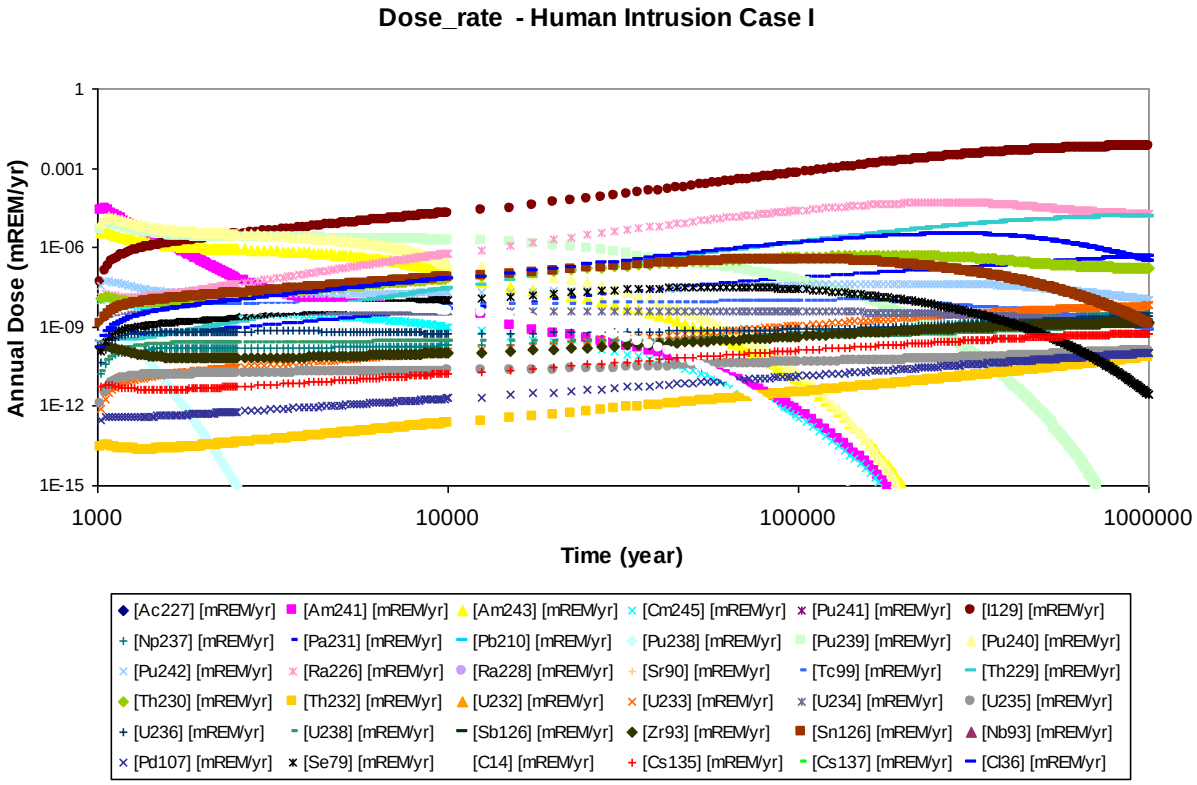

Figure 3: Mean annual dose (mrem/yr) associated with 100 realizations for 36 individual radionuclide species.

Figure 4 shows the ^{135}Cs and ^{129}I annual mean dose for the cases with one waste package release: human intrusion case I (commercial UNF only), human intrusion case II (DOE HLW only), undisturbed case I (commercial UNF only) and undisturbed case II (DOE HLW only). Again ^{129}I shows much higher doses for all 4 cases than ^{135}Cs. Since the DOE HLW glass waste form has a higher degradation rate as compared to the commercial UNF, the human intrusion case II shows the highest mean dose among the four cases. The undisturbed case I and II both show lower mean doses as compared to the human intrusion cases. The ^{129}I mean doses for the undisturbed scenarios are closer to the doses for the human intrusion scenarios in comparison with ^{135}Cs. This is due to ^{135}Cs being retarded more via sorption onto the bentonite buffer.

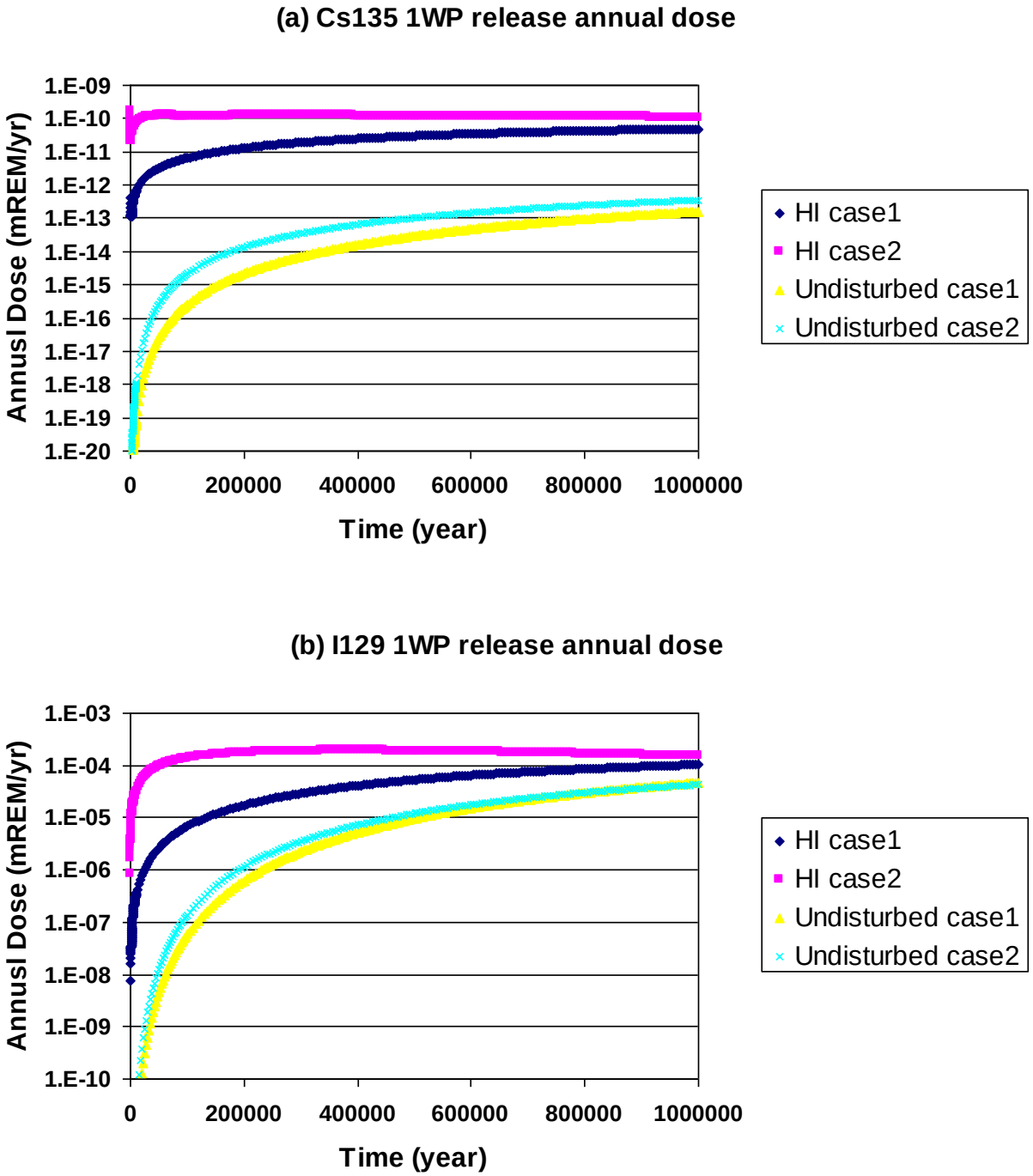

Figure 4: One waste package release annual dose (mrem/yr) for four simulation cases: human intrusion case I (UNF), human intrusion case II (DOE HLW), undisturbed case I (UNF), and undisturbed case II (DOE HLW).

Figure 5 shows the 100 realizations ^{129}I annual dose time histories for the human intrusion case I. The plot displays the Monte Carlo multi-realization stochastic variations of the breakthrough curves. Similarly, Figure 6 shows the probability history of 100 realizations for ^{239}Pu and ^{237}Np dose rate for the human intrusion case to illustrate the spread around the mean annual dose curve. The ^{239}Pu dose plot shows a much narrower uncertainty range band as compared to the ^{237}Np dose plot, and the results imply that for strongly sorbing radionuclides, the associated uncertainties in the dose rate are smaller.

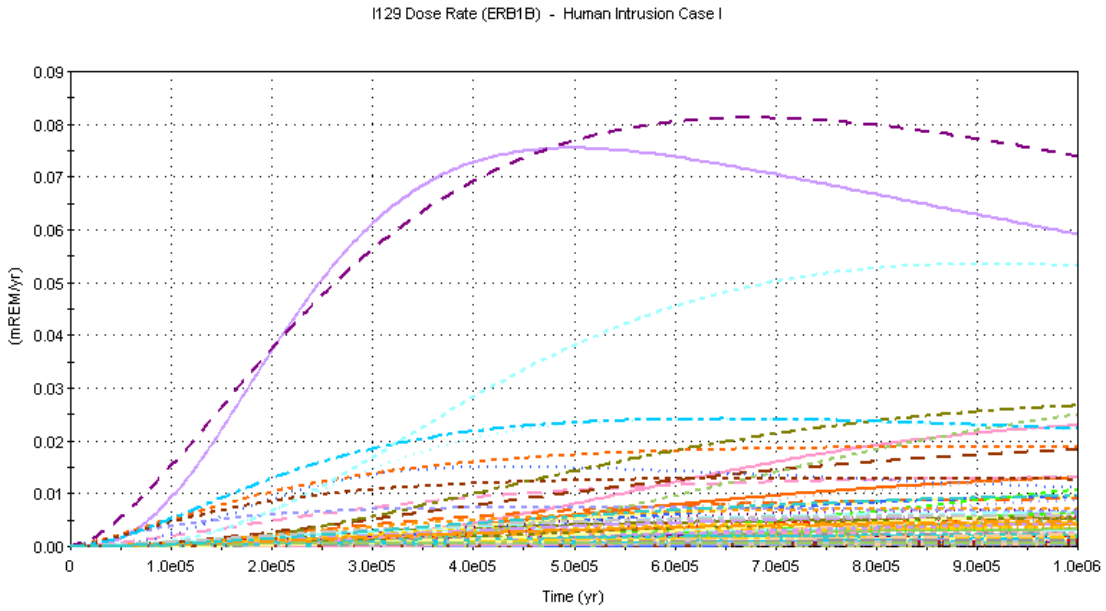

Figure 5: Annual dose (mrem/yr) curves of 100 realizations simulations for ^{129}I.

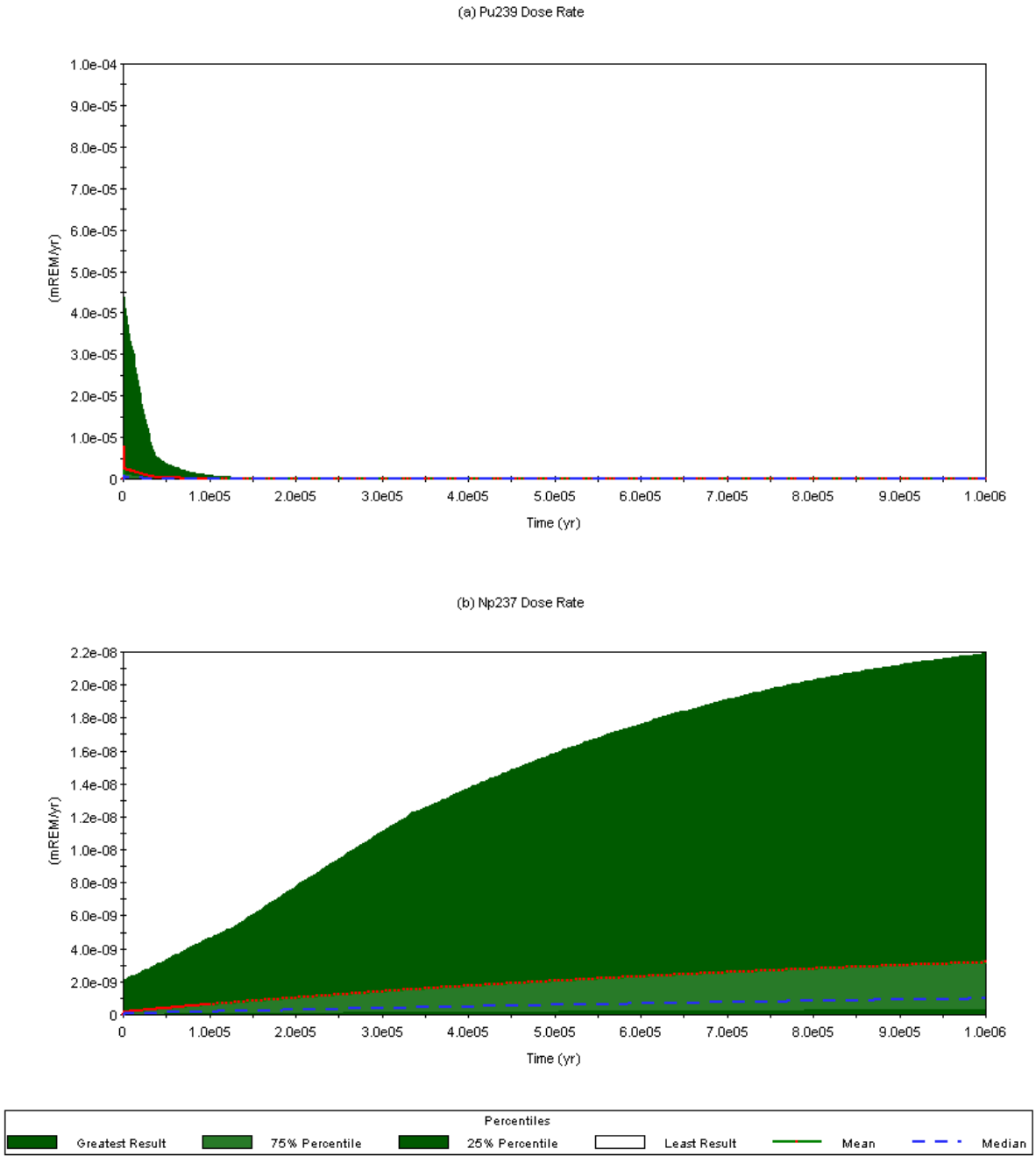

Figure 6: Probabilistic uncertainty ranges in the annual dose (mrem/yr) for (a) ^{239}Pu and (b) ^{237}Np.

A benefit of probabilistic analysis of GDSEs is that the relative importance of various uncertain processes can be examined through a statistical analysis of the Monte Carlo results.

This analysis can guide future work planning to reduce uncertainties in the model analysis or in other ways to improve the model. Figures 7 and 8 illustrate this process.

The annual doses were analyzed using a sensitivity analysis tool (Saltelli and Tarantola, 2002) provided as part of the GoldSim software. The importance analysis of the input variables to the results are statistical measures computed by analyzing multiple realizations of the model in which all of the stochastic variables are simultaneously sampled for each realization of the Monte Carlo simulation. The importance measure is a metric that varies between 0 and 1 representing the fraction of the result's variance that is explained by the variable. This measure is useful in identifying nonlinear, non-monotonic relationships between an input variable and the result (which conventional correlation coefficients may not reveal).

Important parameter uncertainties influencing the overall model uncertainty (as measured by the annual dose in this study) depend on the time frame of interest. Each relevant parameter was ranked in order of importance to the overall uncertainty with respect to the annual dose at 10^4, 10^5, and 10^6 years. The importance measures shown in the following figures are normalized at each time stage so that they can be compared among different time frame of interest.

Figure 7A shows that uncertainty in the mean travel time of water in the far field (LnorMean, LnorSD_norm) has dominant influence on the uncertainty in the ^{129}I annual dose for most of the 1 million year time frame, with decreasing influence toward the end of simulation. The second most important uncertain parameter is the number of affected waste packages (WP_HI_affected) sampled in the near field model, and its influence increases near the end of simulation duration. The third most important uncertain parameter is the commercial UNF waste form degradation rate (UNF_WF_rate), and its influence increases as the simulations proceed towards the end. This implies that at lower UNF fractional degradation rate, for nonsorbing radionuclides such as ^{129}I, the annual dose is controlled more by the uncertainties in the near field model than by the uncertainty in the far-field transport.

Figure 7B shows the similar situation for the ^{129}I annual dose with mean travel time in the far field as the top uncertainty parameter. In this case, DOE HLW glass degradation rate (Glass_WF_rate) shows strong influence at the earlier stage of simulation while the commercial UNF degradation rate (UNF_WF_rate) shows strong influence toward the end of simulation. Also the ^{129}I sorption coefficient for the bentonite buffer (Kd_I_bentonite) shows a comparable effect as the number of waste packages affected and the waste form degradation rates with respect to uncertainty in the annual dose, and with relative a strong influence for the entire simulation duration.

Figures 8 shows a detailed examination of the sensitivity analyses for the ^{239}Pu annual dose for four simulation cases: (a) human Intrusion case I (commercial UNF only), (b) human Intrusion case II (DOE HLW only), (c) undisturbed case I (commercial UNF plus DOE HLW), and (d) undisturbed case II (reprocessing HLW plus DOE HLW). For all four cases, the uncertainty in the mean travel time of water in the far field (LnorMean) has dominant influence on the uncertainty in ^{239}Pu annual dose throughout 1 million year simulation, and this is due to the large ^{239}Pu sorption coefficient in the far field. The DOE HLW degradation rate (Glass_WF_rate) in the human intrusion case II (Figure 8-(b)) shows stronger influence as the second most important uncertain parameter, compared to the slower UNF degradation rate (UNF_WF_rate) in the human intrusion case I (Figure 8-(a)). The undisturbed case I (Figure 8-

(c)) and case II (Figure 8-(d)) both show that the ^{239}Pu sorption on the bentonite buffer (Kd_Pu_bentonite) has almost the same level of influence as the mean travel time of water in the far field, implying that the migration of Pu is retarded considerably via sorption to the bentonite surfaces, and this retardation process in the near field has comparable influence as the retardation in the far field. In the undisturbed case II (Figure 8-(d)), the DOE HLW and reprocessing HLW glass degradation rates (Glass_WF_rate) display a strong influence on the dose at the earlier stage of simulation, and this is due to the higher degradation rate of glass waste form than the commercial UNF degradation rate.

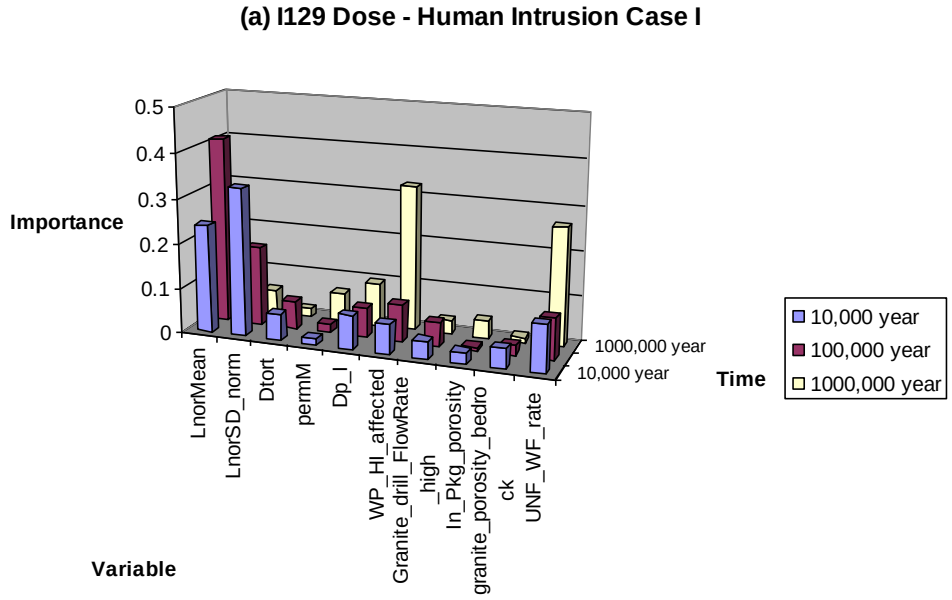

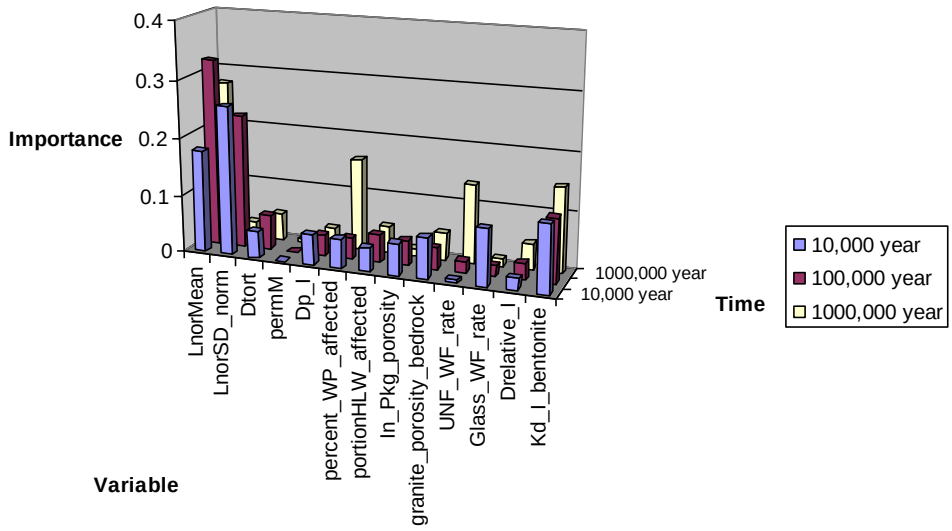

Figure 7: Importance analysis of input parameters with respect to uncertainties in the ^{129}I annual dose at the 5km compliance boundary for (a) human intrusion case I (commercial UNF only) and (b) undisturbed case I (commercial UNF plus DOE HLW). Larger values for a parameter denote that the uncertainties in the parameter have a larger influence on the overall uncertainty in the ^{129}I annual dose.

(a) Pu239 Dose - Human Intrusion Case I

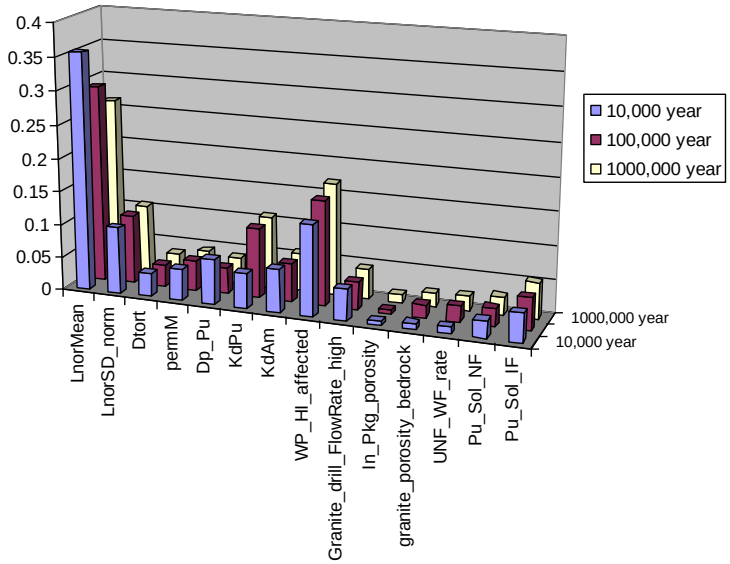

(b) Pu239 Dose - Human Intrusion Case II

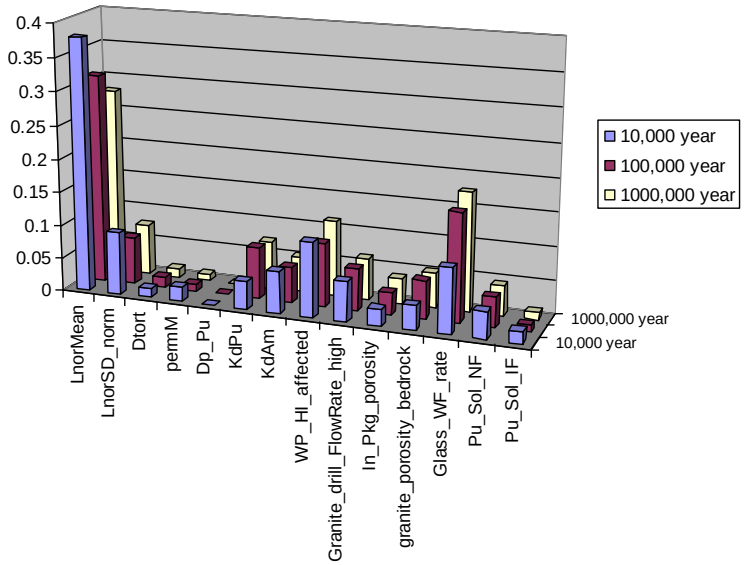

Figure 8: Importance analysis of input parameters with respect to uncertainties in the ^{129}I annual dose at the 5km compliance boundary for (a) human intrusion case I (commercial UNF only) and (b) undisturbed case I (commercial UNF plus DOE HLW). Larger values for a parameter denote that the uncertainties in that parameter have a larger influence on the overall uncertainty in the ^{239}Pu annual dose.

(c) Pu239 Dose - Undisturbed Case I

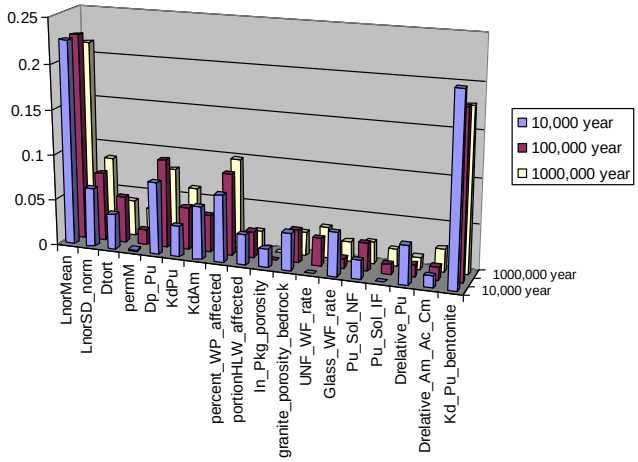

(d) Pu239 Dose - Undisturbed Case II

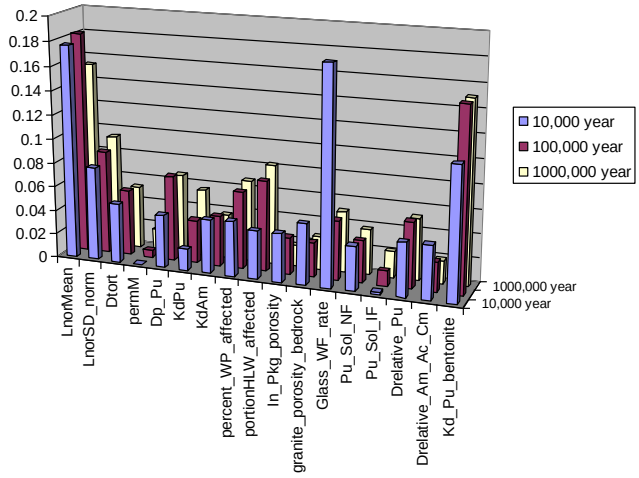

Figure 8: (continued). Importance analysis of input parameters with respect to uncertainties in the ^{239}Pu annual dose at 5km compliance boundary for: (c) undisturbed case I (commercial UNF plus DOE HLW), (d) undisturbed case II (reprocessing HLW plus DOE HLW). Larger values for a parameter denote that the uncertainties in that parameter have a larger influence on the overall uncertainty in the ^{239} Pu annual dose.

4. Concluding Remark

The GDSE model and the results presented in this chapter are preliminary and therefore not indicative of the performance of an actual geologic disposal environment or the potential radiation exposures that could occur in that environment. Rather, they can be used to identify the important processes that may affect repository performance. The intermediate applications of this model may include:

- Identifying which radionuclides are important to the disposal system performance;
- Determining which processes (i.e., solubility, linear sorption) significantly affect the disposal system performance;
- Determining how a waste form with a specific radionuclide inventory affects the disposal system performance;
- Determining how the waste form durability affects the disposal system performance.

Future work includes continual improvement of the existing model by incorporating more detailed processes and performing comparative studies among the different disposal environments.

5. References

Carbol, P., Engkvist, I., 1997, Compilation of radionuclide sorption coefficients for performance assessment, *SKB rapport R-97-13*, September 1997.

Chu, S., Morris, E., Nutt, W., Robinson, B. and Wang, Y., 2008, Generic Repository Concept Analyses to Support the Establishment of Waste Form Performance Requirements – Fiscal Year 2008 Status, *GNEP-WAST-PMO-MI-DV-2008-000146*, September 30, 2008.

GoldSim Technology Group, 2007, "Users Guide, GoldSim Contaminant Transport Module", Version 4.20.

Hansen, F. D., et al., 2010, Shale Disposal of U.S. High-Level Radioactive Waste, Sandia Report, *SAND2010-2843*, Sandia National Laboratories.

IAEA (International Atomic Energy Agency), 2003, "Reference Biospheres" for Solid Radioactive Waste Disposal, *IAEA-BIOMASS-6*, July 2003.

Itälä, A., 2009, Chemical evolution of bentonite buffer in a final repository of spent nuclear fuel during the thermal phase, Report no. *VTT-PUB--721*, 2009-12-15, VTT Technical Research Centre of Finland, Espoo.

Japan Atomic Energy Agency (JAEA) diffusion and sorption coefficient database: *http://migrationdb.jaea.go.jp/english.html*

Liu , J., Lofgren , M. and Neretnieks, I., 2006, SR-Can data and uncertainty assessment: Matrix diffusion and porosity in situ, *SKB report R-06-111*, Swedish Nuclear Fuel and Waste Management Company, 2006.

Montes-H, G., Marty, N., Fritz, B., Clement, A. and Michau, N., 2005, Modelling of long-term diffusion-reaction in a bentonite barrier for radioactive waste confinement, *Applied Clay Science* (2005) Vol.30, iss.3-4, p.181-198

Neretnieks, I., 1982, Leach rates of high level waste and spent fuel: limiting rates as determined by backfill and bedrock conditions, Scientific Basis for Nuclear Waste Management V. *Proceedings of the Materials Research Society Fifth International Symposium on the Scientific Basis for Nuclear Waste* (1982) p.559-568.

Pusch, R. and Svemar, C., 1993, Influence of rock properties on selection of design for a spent nuclear-fuel repository, *Tunnelling and Underground Space Technology* (Jul 1993) Vol.8, iss.3, p.345-356.

Saltelli, A. and Tarantola, S., 2002, On the relative importance of input factors in mathematical models: safety assessment for nuclear waste disposal, *J. Am. Sata. Ass.*, Vol. 97, No. 459.

Tanhua-Tyrkkö, M., 2009, Modelling hydrological and chemical phenomena during interaction of bentonite and high pH plume, June 2009, VTT Technical Research Centre of Finland, Espoo.

Zyvoloski, G. A., Robinson, B. A., Dash, Z. V. and Trease, L. L., 1997, Summary of the models and methods for the FEHM application -A Finite-Element Heat- and Mass-Transfer Code, *LA-13307-MS*, Los Alamos National Laboratory, Los Alamos, New Mexico.

Zyvoloski, G. A., 2007, FEHM: A control volume finite element code for simulating subsurface multi-phase multi-fluid heat and mass transfer. Los Alamos Unclassified Report *LA-UR-07-3359*.

Chapter 4 Clay Generic Disposal System Environment Model

W. Mark Nutt, Ted Bauer, Ed Morris, Nikolai Dosev

Argonne National Laboratory

1. Introduction

The Used Fuel Disposition Campaign (UFD), as part of the DOE Office of Nuclear Energy's (DOE-NE) Fuel Cycle Technology program (FCT) is investigating the disposal of high level radioactive waste (HLW) and used nuclear fuel (UNF) in a variety of geologic media. The feasibility of disposing UNF and HLW in clay media has been investigated and has been shown to be promising (Frank et al., 2010). In addition the disposal of these wastes in clay media is being investigated in Belgium, France, and Switzerland. Thus, argillaceous media is one of the environments being considered by UFD. As identified by researchers at Sandia National Laboratory, potentially suitable formations that may exist in the U.S. include mudstone, clay, shale, and argillite formations (Frank et al., 2010). These formations encompass a broad range of material properties. In this report, reference to clay media is intended to cover the full range of material properties.

This chapter presents the status of the development of simulation models for evaluating the performance of generic clay media. Two simplified coupled models are described: a thermal modeling tool and a long-term repository performance modeling tool. There are multiple uses for these tools within the UFD campaign and the broader FCT program:

- Inform the prioritization of research and development (R&D) activities within the UFD campaign
- Provide metric information regarding waste management that could be used by the FCT systems engineering effort in evaluating various advanced fuel cycle alternatives
- Provide metric information to the FCT System Analysis campaign in the development of fuel cycle system analysis tools.

To support these uses, the generic thermal and repository performance simulation tools have been developed with the flexibility to evaluate not only different properties, but different waste streams/forms and different repository designs and engineered barrier configurations/materials that could be used to dispose of these wastes.

2. Model Description

The development of the clay GDSE models is centered on a requirement of being flexibile to accommodate a variety of different scenarios. These scenarios range from different material properties, different waste forms with varying radionuclide inventories, and different repository and engineered barrier system designs. As such, tool development did not begin with defining a specific scenario around which models would be developed, but rather focused on

developing modeling tools that could then be used to evaluate a wide range of alternative scenarios.

The underlying basis behind the clay GDSE models is termed in this report as a "waste unit cell." Except near the edges, repository designs in general are repeatable configurations of emplaced waste separated by constant distances on the horizontal plane. This symmetry allows for the development of simplified two-dimensional representations of an emplacement location and the surrounding natural media. A wide range of configurations can be modeled using the same overall modeling framework by changing input parameters. This is shown schematically in Figure 1 for different conceptualizations of waste emplacement.

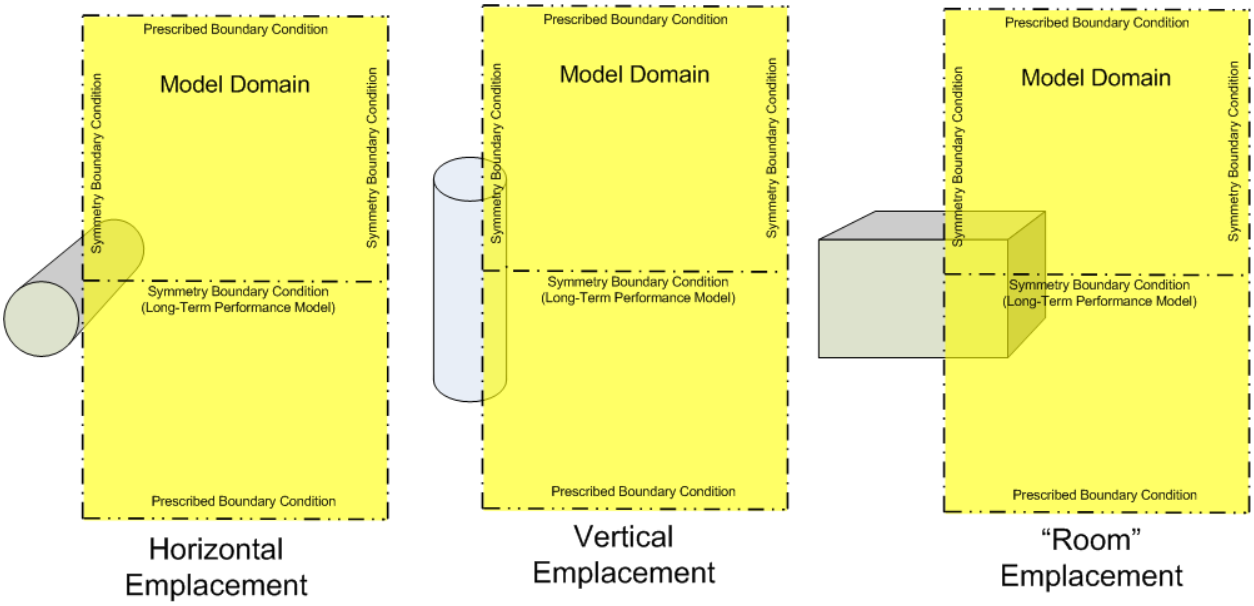

Figure 1. Conceptual Framework for Clay GDSE Models

In evaluating a specific site and design, more elaborate models would likely be used to evaluate three-dimensional and non-symmetric effects. However, the use of symmetrical and prescribed boundary conditions is appropriate when using simplified modeling tools to evaluate generic sites. The specific boundary conditions are discussed in more detail for the thermal and repository performance modeling tools.

The clay GDSE model includes two component models: a model to evaluate the thermal behavior within the GDSE, and a model to evaluate long-term performance. The coupling of these models and their linkage to input data and the results of ancillary calculations and model output is shown in Figure 2.

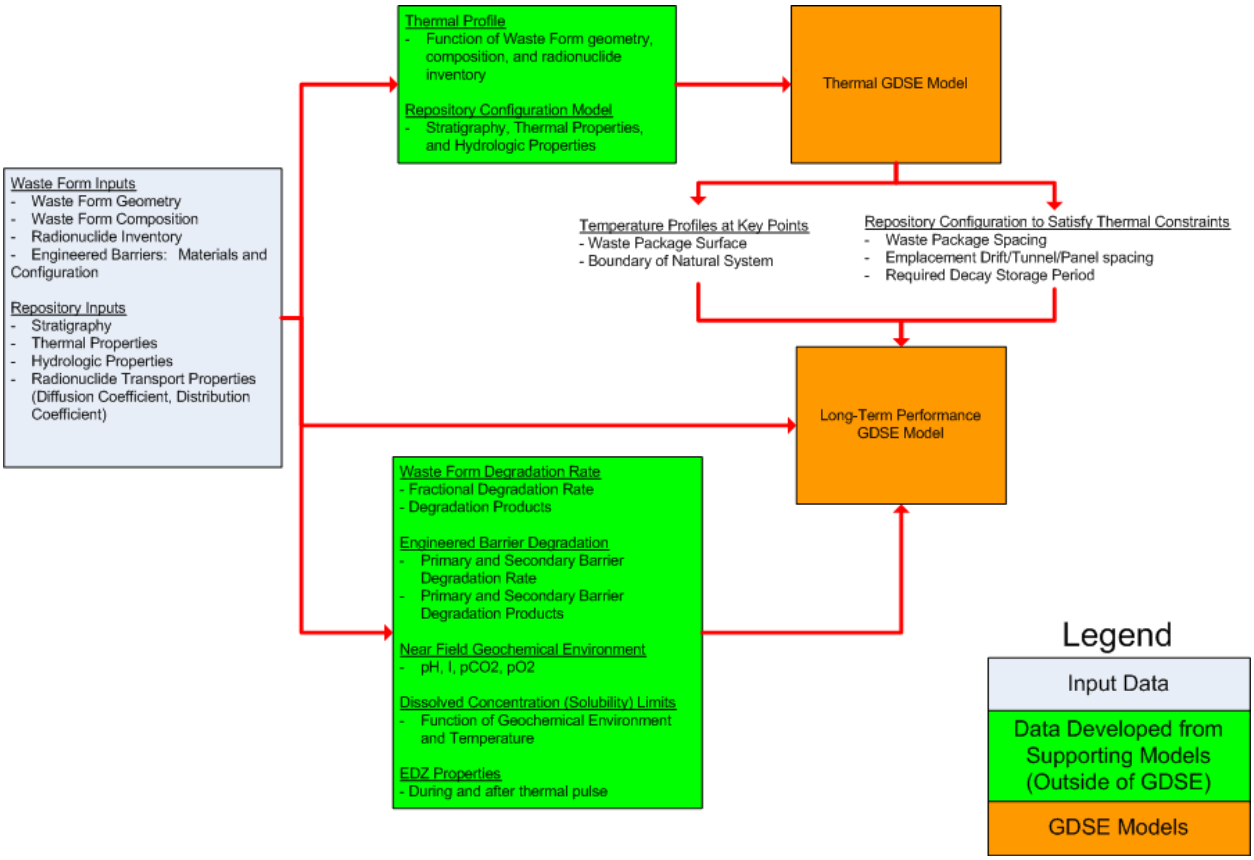

Figure 2. Clay GDSE Model Structure

The Clay Thermal GDSE Model and Long Term Performance GDSE models are supported by information that is generated throughout the FCT program. Waste form properties such as degradation rates and degradation products are developed by the Separations/Waste Form Campaign based on the fuel cycle scenario under consideration. Spent nuclear fuel degradation rates and products are developed within the UFD campaign. Representative properties of generic clay media are developed within the UFD campaign.

The Thermal GDSE model is used to calculate the thermal response for a given waste stream (waste form and inventory), conceptual repository design, and representative clay media properties. The model links with the Long Term Performance GDSE model by determining emplacement spacing and decay storage time required to remain under defined thermal limits (e.g., temperature limit at the wall of a borehole). This information also provides valuable feedback to the FCT program in the form of needed repository footprint and surface storage requirements for a given fuel cycle scenario. With the configuration defined, the Thermal GDSE model also provides temperature profiles at key locations for subsequent use within the Long Term Performance GDSE model (i.e., input for temperature dependent dissolved concentration limits, corrosion rates, etc.).

The Thermal and Long Term Performance GDSE models, their coupling, and their linkages with other data and ancillary model results are discussed in this section.

2.1.Clay Thermal Model

Several computer codes are available to model both thermal and hydrological behavior within a continuous porous and fractured rock medium. These codes use different approaches (e.g., finite difference, finite element), and consider the three major heat transfer processes (conduction, convection, and radiation). A simplified, flexible repository thermal model has been developed for performing integrated near-field and extended far-field heat transfer calculations within a clay generic disposal environment using the commercial SINDA/G thermal network analysis code system (MSC-SINDA, 2010).

Within SINDA/G, explicit configurations of heat-generating waste packages, storage units, and rock layers in a geologic repository environment is envisioned and modeled as a network of modular components, with boundaries, and connections rather than as a single large continuum. Node structure in the model reflects the variety of relevant length scales present within models of components as well as in the integrated model. Smaller nodes in the neighborhood of heat generating components reflect both spatial detail and capture transient behavior of relatively short duration. Larger nodes are adequate for describing the much more slowly varying temperature fields in regions far away from emplaced heat sources. To this end, multinode models that span a wide range of length scales have been developed for the generic clay environment using SINDA/G.

While the primary heat transfer mode in the present model is conduction, other heat transfer modes such as forced ventilation, free convection, and thermal radiation effects can be included as necessary to model a particular conceptual repository configuration.

Robust sparse-matrix implicit solvers are able to efficiently accommodate modeled components having very different length scales and time constants in the same model. These solvers allow time steps in the calculation to reflect the time constants of the actual problem rather than that of the smallest node in the model.

This “network” approach allows the same GDSE model to be used while including a wide variety of material components and configurations. This model flexibility enables change of input not only to thermo-physical properties, but also to the components within a disposal system, the geometric size, and the shape of the modeled repository itself. The SINDA/G thermal model of a generic disposal environment can determine the time-evolution of temperature fields and heat flows associated with emplacement of heat-generating waste forms. Components included in the model framework are heat-generating waste forms or packages, geometrically explicit storage units, such as tunnels or galleries, and the host rock in which these components are embedded.

The component models for the repository concept under consideration include:

- overall geometry of the geologic host;
- the basic storage and emplacement concept, e.g. ventilated tunnels, boreholes (horizontal or vertical), large galleries, etc.;

- availability of ventilation;
- fixed dimensions (e.g. waste package diameters, etc.); and
- location(s) where thermal limits are to be applied.

The representation of the present "generic" disposal system is established from "User Input" that includes:

- the time-dependent waste stream heat source with an identifiable starting point (e.g. discharge from a reactor) as a function of an identifiable "loading metric" (e.g. W/MT or W/ GWd-generated);
- important dimensions, such as: depth below the surface and separation between tunnels/boreholes etc.,;
- key thermal properties of the host rock such as: density, heat capacity, and thermal conductivity (can be anisotropic if needed);
- temperature limits at key locations.

Output from the SINDA/G thermal model of the clay GDSE include:

- Time-dependent temperatures defined at locations within both storage units and the host rock as consistent with user input temperature limits;
- peak values of a loading metric or a minimum "age" of a decaying waste stream (consistent with input temperature limits); and
- summary tables and "CSV" files for subsequent use and plotting of results.

2.2.Clay Long Term Repository Performance GDSE Model

The development of a clay GDSE model was initiated in FY09 under the FCT Separations/Waste Form campaign (Nutt et al., 2009). That model, which focused on diffusive radionuclide transport through the far-field, served as the starting point for the development of the clay media Long Term Repository Performance GDSE model presented herein.

The objective of the clay Long-Repository Term Performance GDSE Model is to integrate all of the key features, events, and processes (FEPs) for a clay generic disposal system into an integrated framework. It is developed using the GoldSim dynamic simulation software (GoldSim Technology Group, 2010), but is intended to be universally used by non-GoldSim practitioners through the use of the free GoldSim Player. All inputs are contained in a Microsoft Excel format that is linked to the GoldSim model. Output of the clay Thermal GDSE will be included as part of the spreadsheet, resulting in a "soft linkage" between the two clay GDSE models. This allows the user the flexibility to evaluate multiple scenarios and conduct sensitivity analyses without having to make changes to the GoldSim model itself, rather only the input needs to be changed.

The overall linkage between the clay GDSE models, the linkage between the input spreadsheet and the clay Long Term Repository Performance GDSE model, and the linkage between the Long Term Repository Performance GDSE model and the broad FEPs categories being used by the UFD campaign is shown in Figure 3.

The general components of the clay Long Term Repository Performance GDSE model are:

- Source Term – waste form and radionuclide inventory
- Primary Engineered Barrier – waste package
- Secondary Engineered Barrier – buffer or other material surrounding a waste package
- Near Field / Excavation Damage Zone (EDZ) – host rock affected by the emplacement of waste
- Far Field – host rock not affected by the emplacement of waste
- Fast Pathways – generic capability to simulate the presence of fast pathways either intersecting the emplaced waste or occurring at some location within the far field (not directly intersecting the waste, but affecting far-field transport behavior).

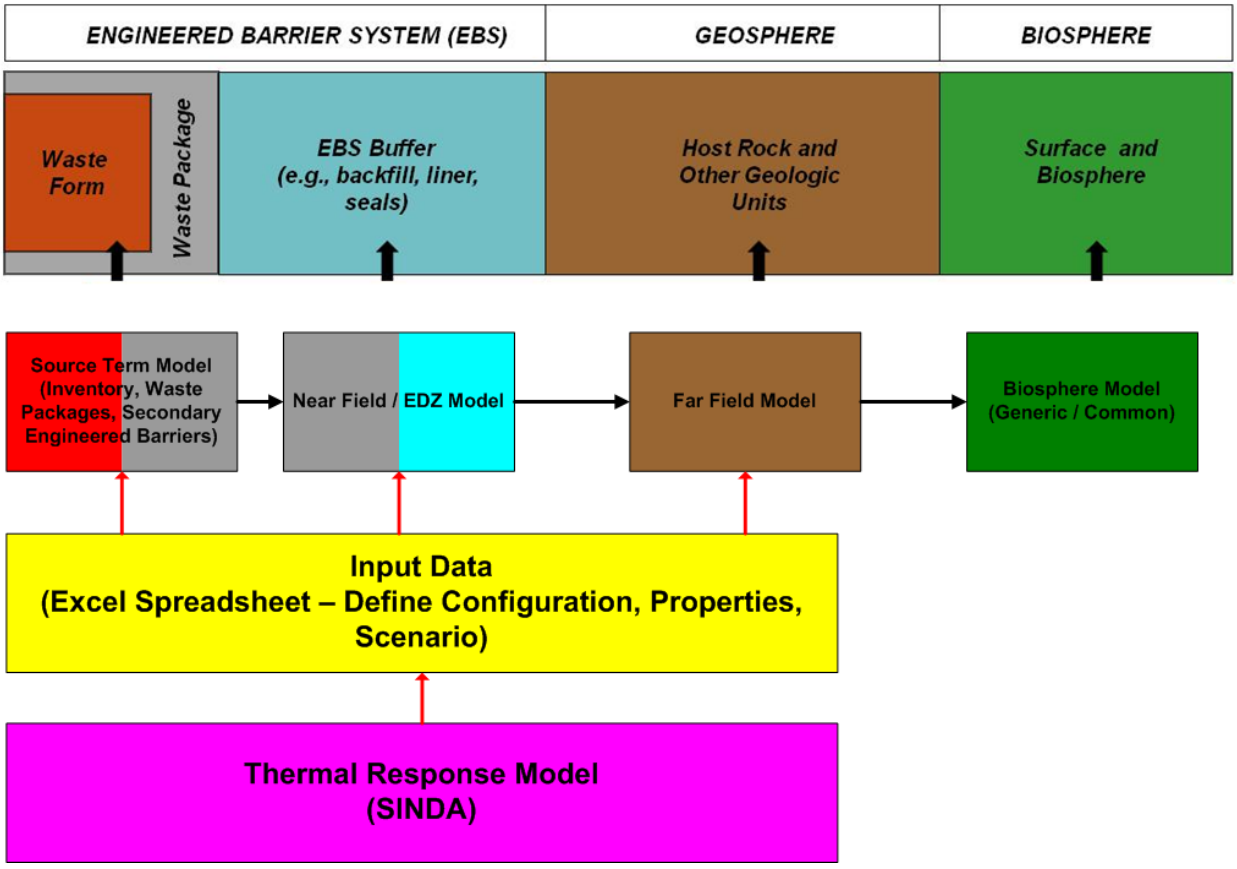

Figure 3. Clay Long-Term Repository Performance GDSE Model Linkages

Source Term, degraded waste form, primary and secondary engineered barriers: The source term, degraded waste form, primary engineered barrier, and secondary engineered barrier components of the clay Long Term Repository Performance GDSE model are shown

schematically in Figure 4. Also shown, is the data and ancillary calculation/modeling results that serve as input to the model. As discussed previously, the user has the capability to change the input parameters through the GDSE input spreadsheet and thus is able to model a wide variety of alternatives within the engineered system of a generic clay conceptual repository design.

The source term for the clay Long Term Repository Performance GDSE model begins with the inventory. The model includes 36 radionuclides important to repository performance. These are input as constants into the model from a spreadsheet as shown in Table 1. A multiplier that can be used to conduct inventory-related sensitivity studies is also included on the input spreadsheet.

The configuration of the engineered barriers is controlled from the input spreadsheet as shown in Table 2. A parameter is included to change the number of discrete units that are represented by the single "unit cell" within the clay Long Term Repository Performance GDSE model. This allows the user to simulate the disposal of waste at multiple identical locations within the model.

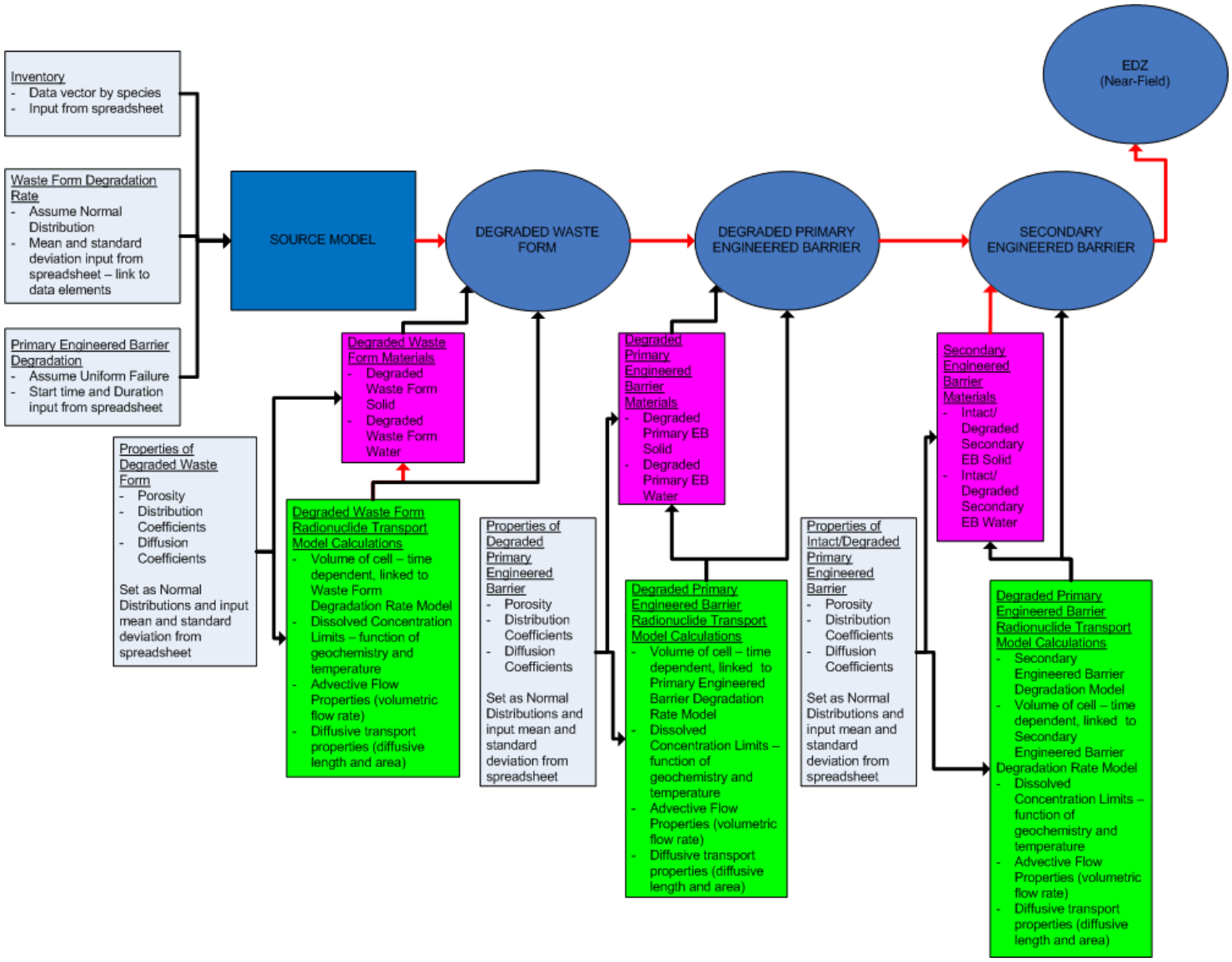
Inventory
- Data vector by species
- Input from spreadsheet
Waste Form Degradation Rate
- Assume Normal Distribution
- Mean and standard deviation input from spreadsheet – link to data elements
Primary Engineered Barrier Degradation
- Assume Uniform Failure
- Start time and Duration input from spreadsheet
SOURCE MODEL
DEGRADED WASTE FORM
DEGRADED PRIMARY ENGINEERED BARRIER
SECONDARY ENGINEERED BARRIER
EDZ (Near-Field)
Degraded Waste Form Materials
- Degraded Waste Form Solid
- Degraded Waste Form Water
Degraded Primary Engineered Barrier Materials
- Degraded Primary EB Solid
- Degraded Primary EB Water
Secondary Engineered Barrier Materials
- Intact/ Degraded Secondary EB Solid
- Intact/ Degraded Secondary EB Water
Properties of Degraded Waste Form
- Porosity
- Distribution Coefficients
- Diffusion Coefficients
Set as Normal Distributions and input mean and standard deviation from spreadsheet
Degraded Waste Form Radionuclide Transport Model Calculations
- Volume of cell – time dependent, linked to Waste Form Degradation Rate Model
- Dissolved Concentration Limits – function of geochemistry and temperature
- Advective Flow Properties (volumetric flow rate)
- Diffusive transport properties (diffusive length and area)
Properties of Degraded Primary Engineered Barrier
- Porosity
- Distribution Coefficients
- Diffusion Coefficients
Set as Normal Distributions and input mean and standard deviation from spreadsheet
Degraded Primary Engineered Barrier Radionuclide Transport Model Calculations
- Volume of cell – time dependent, linked to Primary Engineered Barrier Degradation Rate Model
- Dissolved Concentration Limits – function of geochemistry and temperature
- Advective Flow Properties (volumetric flow rate)
- Diffusive transport properties (diffusive length and area)
Properties of Intact/Degraded Primary Engineered Barrier
- Porosity
- Distribution Coefficients
- Diffusion Coefficients
Set as Normal Distributions and input mean and standard deviation from spreadsheet
Degraded Primary Engineered Barrier Radionuclide Transport Model Calculations
- Secondary Engineered Barrier Degradation Model
- Volume of cell – time dependent, linked to Secondary Engineered Barrier Degradation Rate Model
- Dissolved Concentration Limits – function of geochemistry and temperature
- Advective Flow Properties (volumetric flow rate)
- Diffusive transport properties (diffusive length and area)

Figure 4. Schematic of Source Term, Degraded Waste Form, Primary and Secondary Engineered Barriers Representation

Table 1. Radionuclide inventory. Note that the inventory values shown are example only.

Inventory Multiplier	1.00E+00
Isotope	**Mass (g)**
Ac227	0.00E+00
Am241	1.81E+03
Am243	1.19E+03
C14	1.00E+00
Cl36	0.00E+00
Cm245	4.21E+01
Cs135	3.39E+03
Cs137	8.19E+03
I129	0.00E+00
Nb93	3.15E+03
Np237	5.28E+03
Pa231	0.00E+00
Pb210	0.00E+00
Pd107	0.00E+00
Pu238	1.58E+00
Pu239	2.46E+01
Pu240	6.04E+02
Pu241	3.32E+00
Pu242	1.03E+01
Ra226	0.00E+00
Ra228	0.00E+00
Sb126	0.00E+00
Se79	0.00E+00
Sn126	2.20E+02
Sr90	3.54E+03
Tc99	5.63E+03
Th229	2.38E-05
Th230	2.24E-02
Th232	6.91E-03
U232	7.06E-06
U233	3.78E-06
U234	1.76E-01
U235	4.73E+00
U236	5.49E+00
U238	8.02E-01

Zr93	0.00E+00

Waste Form degradation is currently represented as a single fractional degradation rate that does not vary with time. As information regarding waste form degradation becomes available from the Separations/Waste Form campaign this approach can be changed to better reflect any temporal variation in the fractional degradation rate and any other couplings between the degrading waste form and the rest of the engineered barriers.

Flags in the input spreadsheet are used to control the presence of either a primary or secondary engineered barrier. Thus, for example, different waste package and buffer/backfill configurations can be considered. The time that the primary and secondary engineered barriers fail is input as a discrete time. As with the waste form fractional degradation rate, a more explicit model of the degradation of the primary and secondary barriers could be developed in a future version of the model if warranted.

Table 2. Engineered Barrier System Configuration Parameters

General	
Number of Discrete Units (i.e., waste packages) Represented	1
Waste Form	
Waste Form Fractional Degradation Rate (yr^{-1})	1.00E-09
Primary Engineered Barrier (i.e., Waste Package)	
Primary Engineered Barrier Present (set equal to 1 if present, 0 if not)	1
Waste Package Failure Time (years)	0
Secondary Engineered Barrier (i.e., Buffer)	
Secondary Engineered Barrier Present (set equal to 1 if present, 0 if not)	1
Secondary Engineered Barrier Failure Time (years)	0

Note that the values shown are example only

The degraded waste form, degraded primary engineered barrier, and intact/degraded engineered barrier are modeled each as single batch-reactor mixing cells. The properties are input through the linked spreadsheet as shown in Table 3. It is assumed that diffusion is the primary radionuclide transport mechanism so the batch-reactor mixing cells are diffusively coupled. However, to investigate the effects of advective transport through the engineered barriers, the mixing cells are also advectively linked with the model user able to change the advective flow rate through the input spreadsheet.

The current version of the clay Long Term Repository Performance GDSE model treats these parameters as scalars with no uncertainty. The model can be modified in the future should future investigations indicate that the uncertainty in these parameters should be explicitly represented.

Table 3. Engineered Barrier System Material Properties

Property	Degraded Waste Form	Degraded Primary Engineered Barrier	Intact Secondary Engineered Barrier	Degraded Secondary Engineered Barrier	Distribution Type	Discussion
Material Density (kg/m3)	2000	2000	2000	2000	Scalar	Assumption
Porosity	0.3	0.3	0.3	0.3	Scalar	Assumption
Volume (m3)	1	1	1	1	Scalar	Assumption
Thickness (m)	0.5	0.5	0.5	0.5	Scalar	Assumption
Diffusion Area (m2)	0	0	0	0	Scalar	Assumption
Advective Flow Rate (m3/yr)	1.00E+10	1.00E+10	0	1.00E+10	Scalar	Assumption

Note that the values shown are example only

The ability to simulate dissolution/precipitation and reversible sorption is included in each batch reactor mixing cell. It is assumed that the dissolved concentration limits and distribution coefficients are represented in this initial model as log-triangular and triangular distributions, respectively, with the user having the ability to define the minimum, best estimate, and maximum values of the distribution from the input spreadsheet. The model can be modified in the future should future investigations indicate that different probability distributions should

be used. Future modification may also involve explicit coupling to geochemical conditions and temperature within the batch reactor mixing cells (i.e., explicit coupling with the temperatures

Table 4. Dissolved Concentration Limit Input

Element	Min	Most Likely	Max	Distribution Type	Discussion
Actinium	1.00E+10	1.00E+10	1.00E+10	Log-Triangular Distribution	Assumed infinite solubility
Americium	1.00E+10	1.00E+10	1.00E+10	Log-Triangular Distribution	Assumed infinite solubility
Antimony	1.00E+10	1.00E+10	1.00E+10	Log-Triangular Distribution	Assumed infinite solubility
Carbon	1.00E+10	1.00E+10	1.00E+10	Log-Triangular Distribution	Assumed infinite solubility
Cesium	1.00E+10	1.00E+10	1.00E+10	Log-Triangular Distribution	Assumed infinite solubility
Chlorine	1.00E+10	1.00E+10	1.00E+10	Log-Triangular Distribution	Assumed infinite solubility
Curium	1.00E+10	1.00E+10	1.00E+10	Log-Triangular Distribution	Assumed infinite solubility
Iodine	1.00E+10	1.00E+10	1.00E+10	Log-Triangular Distribution	Assumed infinite solubility
Lead	1.00E+10	1.00E+10	1.00E+10	Log-Triangular Distribution	Assumed infinite solubility
Neptunium	1.00E+10	1.00E+10	1.00E+10	Log-Triangular Distribution	Assumed infinite solubility
Niobium	1.00E+10	1.00E+10	1.00E+10	Log-Triangular Distribution	Assumed infinite solubility
Paladium	1.00E+10	1.00E+10	1.00E+10	Log-Triangular Distribution	Assumed infinite solubility
Protactinium	1.00E+10	1.00E+10	1.00E+10	Log-Triangular Distribution	Assumed infinite solubility
Plutonium	1.00E+10	1.00E+10	1.00E+10	Log-Triangular Distribution	Assumed infinite solubility
Radium	1.00E+10	1.00E+10	1.00E+10	Log-Triangular Distribution	Assumed infinite solubility
Selenium	1.00E+10	1.00E+10	1.00E+10	Log-Triangular Distribution	Assumed infinite solubility
Strontium	1.00E+10	1.00E+10	1.00E+10	Log-Triangular Distribution	Assumed infinite solubility
Technitium	1.00E+10	1.00E+10	1.00E+10	Log-Triangular Distribution	Assumed infinite solubility
Thorium	1.00E+10	1.00E+10	1.00E+10	Log-Triangular Distribution	Assumed infinite solubility
Tin	1.00E+10	1.00E+10	1.00E+10	Log-Triangular Distribution	Assumed infinite solubility
Uranium	1.00E+10	1.00E+10	1.00E+10	Log-Triangular Distribution	Assumed infinite solubility
Zirconium	1.00E+10	1.00E+10	1.00E+10	Log-Triangular Distribution	Assumed infinite solubility

Note that the values shown are example only

Table 5. Distribution Coefficient Input

Element	Min	Most Likely	Max	Distribution Type	Discussion
Actinium	1.00E+00	1.00E+00	1.00E+00	Triangular Distribution	Assumed no sorption
Americium	1.00E+00	1.00E+00	1.00E+00	Triangular Distribution	Assumed no sorption
Antimony	1.00E+00	1.00E+00	1.00E+00	Triangular Distribution	Assumed no sorption
Carbon	1.00E+00	1.00E+00	1.00E+00	Triangular Distribution	Assumed no sorption
Cesium	1.00E+00	1.00E+00	1.00E+00	Triangular Distribution	Assumed no sorption
Chlorine	1.00E+00	1.00E+00	1.00E+00	Triangular Distribution	Assumed no sorption
Curium	1.00E+00	1.00E+00	1.00E+00	Triangular Distribution	Assumed no sorption
Iodine	1.00E+00	1.00E+00	1.00E+00	Triangular Distribution	Assumed no sorption
Lead	1.00E+00	1.00E+00	1.00E+00	Triangular Distribution	Assumed no sorption
Neptunium	1.00E+00	1.00E+00	1.00E+00	Triangular Distribution	Assumed no sorption
Niobium	1.00E+00	1.00E+00	1.00E+00	Triangular Distribution	Assumed no sorption
Paladium	1.00E+00	1.00E+00	1.00E+00	Triangular Distribution	Assumed no sorption
Protactinium	1.00E+00	1.00E+00	1.00E+00	Triangular Distribution	Assumed no sorption
Plutonium	1.00E+00	1.00E+00	1.00E+00	Triangular Distribution	Assumed no sorption
Radium	1.00E+00	1.00E+00	1.00E+00	Triangular Distribution	Assumed no sorption
Selenium	1.00E+00	1.00E+00	1.00E+00	Triangular Distribution	Assumed no sorption
Strontium	1.00E+00	1.00E+00	1.00E+00	Triangular Distribution	Assumed no sorption

Technitium	1.00E+00	1.00E+00	1.00E+00	Triangular Distribution	Assumed no sorption
Thorium	1.00E+00	1.00E+00	1.00E+00	Triangular Distribution	Assumed no sorption
Tin	1.00E+00	1.00E+00	1.00E+00	Triangular Distribution	Assumed no sorption
Uranium	1.00E+00	1.00E+00	1.00E+00	Triangular Distribution	Assumed no sorption
Zirconium	1.00E+00	1.00E+00	1.00E+00	Triangular Distribution	Assumed no sorption

Note that the values shown are example only

produced by the SINDA/G Thermal GDSE model). Tables 4 and 5 show the structure of the input spreadsheet used in this initial model.

Near Field/Excavation Damage Zone: The near field/EDZ component of the clay Long Term Repository Performance GDSE model is shown schematically in Figure 5. Also shown on Figure 5 are the data and ancillary calculation/modeling results that serve as input to the model. As discussed previously, the user has the capability to change the input parameters through the GDSE input spreadsheet and thus is able to model a wide variety of near field/EDZ conditions within generic clay media.

The near field/EDZ is modeled as three linked batch-reactor mixing cells. For simplicity, a one-dimensional slab geometry is assumed. A more detailed representation, such as a cylindrical representation, could be employed in the future if needed. The properties are input through the linked spreadsheet as shown in Table 6. As with the engineered barriers, it is assumed that diffusion is the primary radionuclide transport mechanism so the batch-reactor mixing cells are diffusively coupled. However, to investigate the effects of advective transport through the near field/EDZ, the mixing cells are also advectively linked with the user able to change the advective flow rate through the input spreadsheet.

The current version of the clay Long Term Repository Performance GDSE model treats the parameters shown in Table 6 as scalars with no uncertainty. The model can be modified in the future should future investigations indicate that the uncertainty in these parameters should be explicitly represented. In addition, the current model does not allow for time-dependent evolution of the near field/EDZ properties. This could also be included in a future revision to the model if necessary.

The ability to simulate dissolution/precipitation and reversible sorption is also included in each near field/EDZ batch reactor mixing cell in the same manner as for the engineered barrier system cells. Again, the model can be modified in the future should future investigations indicate that different probability distributions should be used or to involve explicit coupling to geochemical conditions and temperature within the batch reactor mixing cells.

Table 6. Near Field/Excavation Damage Zone Material Properties

Property	Value	Units	Distribution Type	Discussion
Near Field / EDZ Density	2000	kg/m3	Scalar	Assumption
Near Field/EDZ Porosity	0.3	-	Scalar	Assumption
Near Field / EDZ Volume of Single Cell (3-Cell Slab Model)	1	m3	Scalar	Assumption
Near Field / EDZ Thickness of Single Cell (3-Cell Slab Model)	0.5	m3	Scalar	Assumption
Near Field / EDZ Diffusion Area of Single Cell (3-Cell Slab Model)	0	m2	Scalar	Assumption
Near Field / EDZ Diffusion Advective Transport Rate	0.00E+00	m3/yr	Scalar	Assumption

Note that the values shown are example only

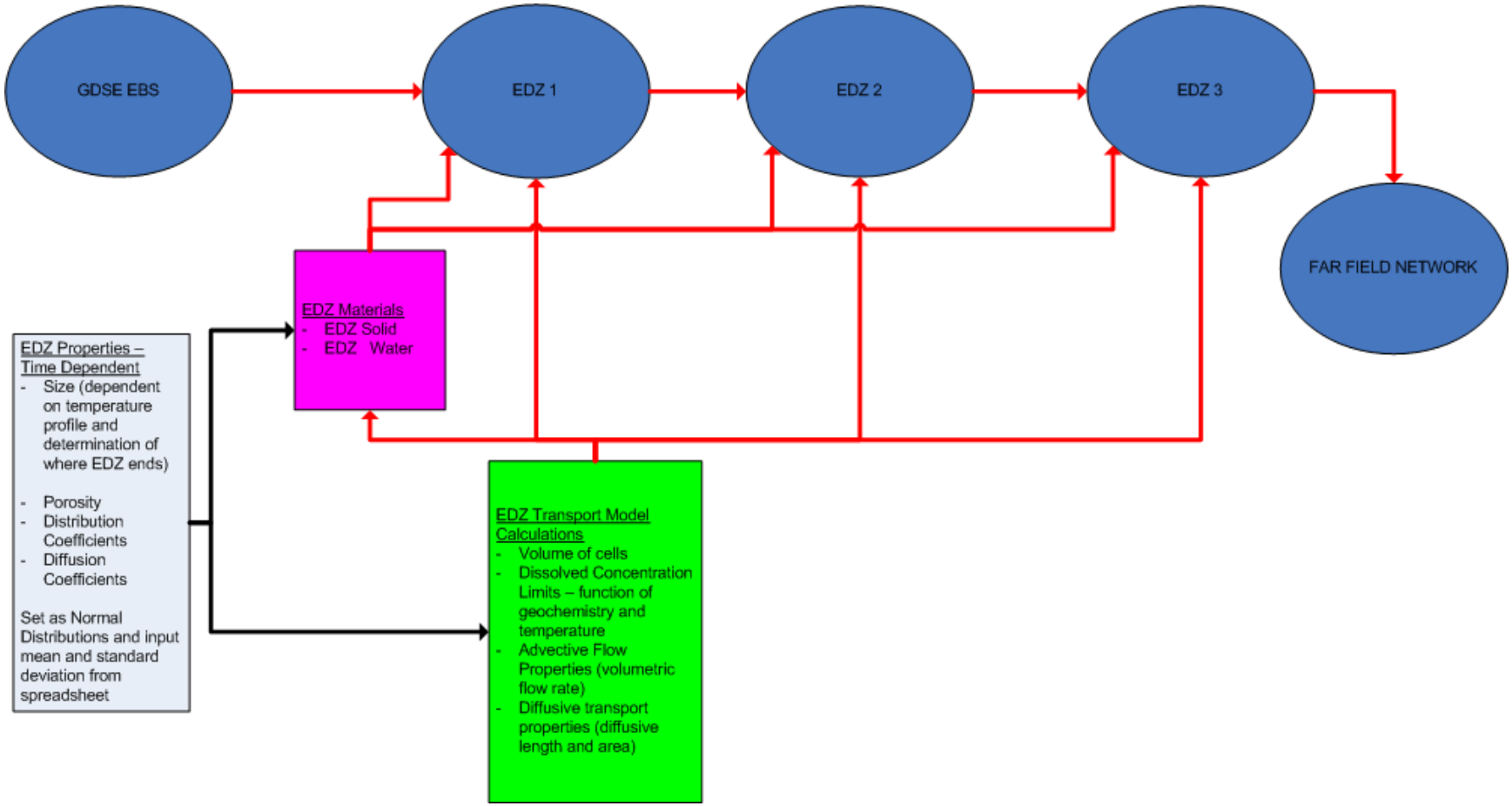

Figure 5. Schematic of Near Field/Excavation Damage Zone Representation

Far Field: The far field component of the clay Long Term Repository Performance GDSE model is shown schematically in Figure 6. This formulation consists of 20x20 node network of batch reactor mixing cells used to represent two-dimensional radionuclide transport. Radionuclide transport is assumed to occur primarily via diffusive mechanisms. The model is configured to include advective coupling between the mixing cells to evaluate sensitivity. Releases from the near field enter the far field at the corner of the far field cell network.

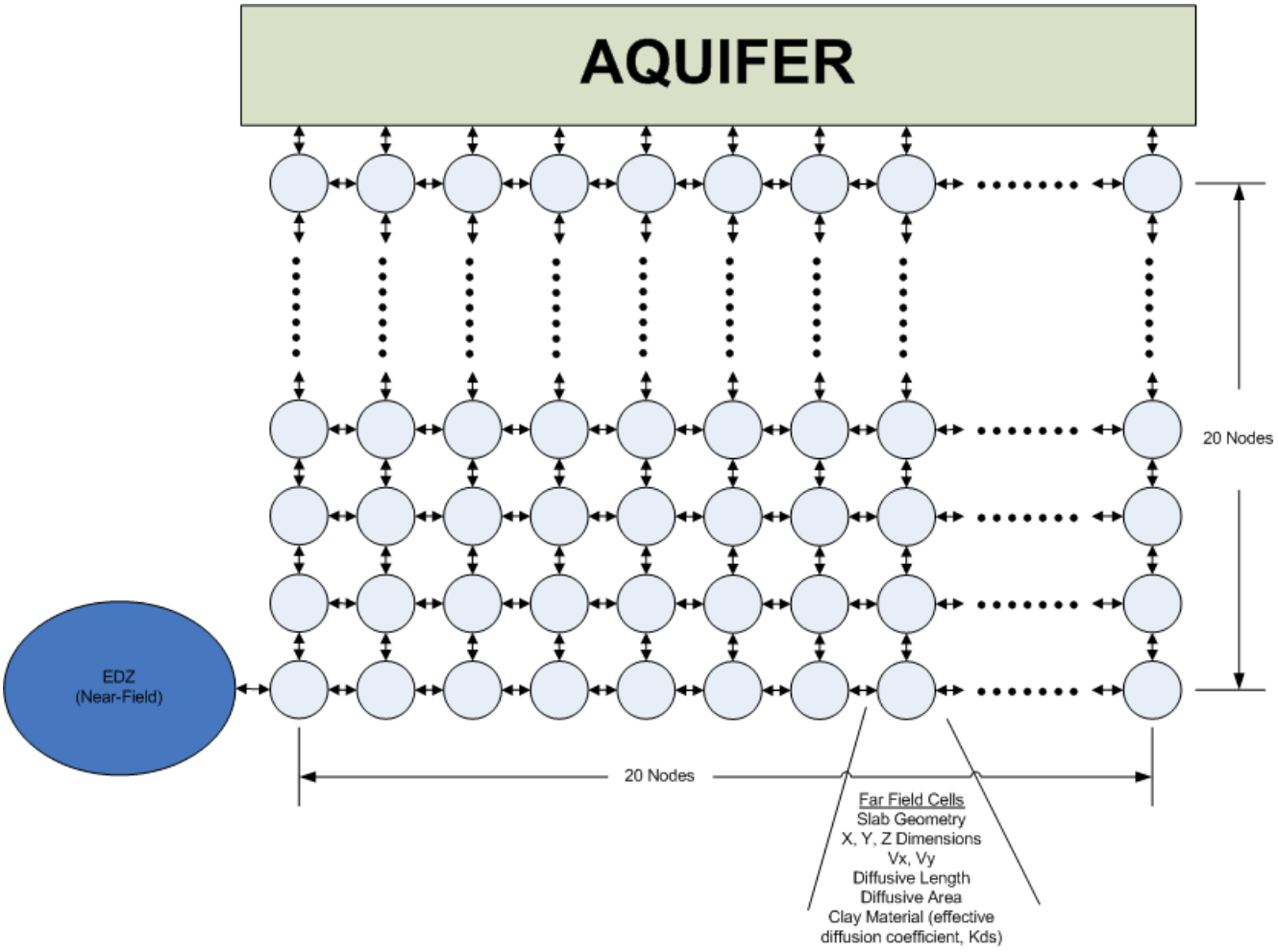

Figure 6. Schematic of Far Field Representation

The following assumptions are inherent in this model.

- The "depth" of each mixing cell equals the "depth" of the unit cell within the model (i.e., distance between the centers of single waste packages in a horizontal emplacement conceptual design)

- Reflective boundary conditions at 1) the center of each emplacement drift/tunnel, 2) at the centerline between emplacement drifts/tunnels, and 3) at the plane of the emplacement drifts.
- Dissolved concentration limits are applied in each mixing cell.
- Reversible sorption in each mixing cell.
- The radionuclide mass flux reaching the aquifer is used to determine the annual dose to the receptor.

The far field domain height, width, and depth are represented parametrically within the model and are defined in the input spreadsheet. Thus, the model is extremely flexible and can accommodate different repository configurations (e.g., spacing of emplaced waste). It is intended that the clay Thermal GDSE model will determine allowable configurations for a prescribed waste form and conceptual repository design that would then be input into the clay Long Term Repository Performance GDSE model.

The ability of the numerical model to represent a wide range of dimensions was examined by comparing numerical and analytic solutions of the same diffusive transport problem. These comparisons are presented in the Appendix. The comparisons indicate that as the aspect ratio becomes larger, agreement between the numerical solution produced by GoldSim and the exact analytic solution deteriorates. However, even with the rather extreme ratio of 15/2, disagreement seems at worst to be only about 10 % at only a few limited locations, primarily in the corners closest to and farthest away from the interface with the near field/EDZ.

The key parameters included in the far field component of the clay Long Term Repository Performance GDSE model are the clay porosity, clay density, effective diffusion coefficient, dissolved concentration limits (solubility limits), and reversible sorption coefficients. The clay porosity and density are entered through the input spreadsheet as shown in Table 7. These properties were assumed to be represented by triangular probability distributions with the user able to enter the parameters that define the distributions. The type of probability distribution can be changed in future revisions to this model should available information indicate.

The ability to simulate dissolution/precipitation and reversible sorption is also included in each far field batch reactor mixing cell in the same manner as was discussed above for the engineered barrier system cells. Again, the model can be modified in the future should future investigations indicate that different probability distributions should be used or to involve explicit coupling to geochemical conditions and temperature within the batch reactor mixing cells.

The current model assumes a constant diffusion coefficient for all elements of 2E-10 m^2/s, based on information obtained from the Belgian repository program. Future work will involve implementing the ability to input element-specific diffusion coefficients into the model through the input spreadsheet.

In order to simulate the effects of advective transport conditions in a clay environment, each of the cells in the 20x20 node network are coupled by advective connections. The user is able to define whether advective transport mechanisms are active for a simulation and define the vertical and horizontal groundwater velocities. It is recognized that applying horizontal advective transport within a cell network that assumes symmetry boundary conditions at its edges does not appropriately represent large-scale horizontal advection. However, this approach does allow the user to establish advective flow away from the emplaced waste in the direction of a hypothetical overlying aquifer. This approach allows for the assessment of the advective transport within a predominately diffusive transport medium.

Table 7. Far Field Material Properties

Property	Min	Most Likely	Max	Units	Distribution Type	Discussion
Clay Porosity	0.325	0.4226	0.481		Triangular	SAFIR 2, Safety Assessment and Feasibility Interim Report 2, ONDRAF/NIRAS, NIROND 2001-06E, December 2001. Available at www.nirond.be/engels/Safir2_eng.php. Parameters from Table 3-33
Clay Density	1888	1980	2135	kg/m3	Triangular	SAFIR 2, Safety Assessment and Feasibility Interim Report 2, ONDRAF/NIRAS, NIROND 2001-06E, December 2001. Available at www.nirond.be/engels/Safir2_eng.php. Parameters from Table 3-33

Note that the values shown are example only

Biosphere: Radiation exposure, or dose, is used as a metric of GDSE performance. Biosphere dose conversion factors developed in the International Atomic Energy Agency's (IAEA) BIOMASS project for a simple drinking water well pathway (ERB 1) were used (IAEA 2003). This biosphere is described as (Chapter 1):

> Example Reference Biosphere 1 (ERB 1) is deliberately designed to be very simple, being focused on a simple biosphere system and single exposure pathway. It is characterized by a drinking water well bored through the overburden into an aquifer that has been contaminated by radionuclide releases from the repository. Previous experience from more comprehensive biosphere modeling studies has shown that a drinking water well may sometimes represent a significant or even, depending on other aspects of the assessment context, a dominant pathway for release and exposure.

The results presented in this report should not be construed as being indicative of the true performance of a disposal system or compared to any regulatory performance objectives regarding repository performance for the following reasons:

- The GDSE models are very simplistic and do not include many of the features, events, and processes that need to be considered in an assessment of disposal system performance.
- The determination of biosphere dose conversion factors does not depend on the GDSE, but rather on the biosphere beyond the GDSE, the habits of the population in that biosphere, and potentially the regulatory framework. A variety of biospheres and local populations could be present over a given GDSE and the resulting dose conversion factors may vary significantly.

Nevertheless, in lieu of a specific site, the reference biosphere allows for the assessment of generic disposal systems environments using a common, representative biosphere for each of the different GDSEs.

Fast Paths: This version of the clay Long Term Repository Performance GDSE model includes fast paths that can be parameterized by the user to evaluate various scenarios. A single one-dimensional advective pathway is included that directly links the degraded waste form mixing cell with the aquifer. The user can input the groundwater velocity through this fast path "pipe" to conduct parametric sensitivity evaluations. This pathway could be used to represent such scenarios as a human intrusion borehole intersecting the waste or transport through a significantly degraded near field/EDZ and seal system to an overlying aquifer.

The model also includes the ability to introduce vertical advective transport within the far field at columns 5, 10, 15, and 20 within the 20x20 node network. This allows for the simulation of fast paths that do not directly intersect the emplaced waste but could degrade the isolation capability of the far field.

3. Demonstration

Activities in Fiscal Year 2010 focused on developing the clay Thermal and Long Term Repository Performance GDSE models. The initial structure of these models has been developed and efforts will continue to refine the models and establish the coupling between them. Ultimately it is intended to couple the models such that the results of the Thermal GDSE model for a given waste form and conceptual repository design are used to establish the repository configuration, the time that the waste would need to be allowed to decay before emplacement, and the temperature histories to use in the Long Term Repository Performance GDSE model.

While the modeling coupling has yet to be completed, this section presents a demonstration of the types of results that are generated with each model and how the coupling would work in the evaluation of a fuel cycle scenario. Estimates of potential waste inventory and waste form characteristics for HLW that could potentially be generated under a variety of commercial fuel cycle alternatives have been developed in order to support subsequent system-level evaluations of disposal system performance (Carter and Luptak, 2010). To date, inventory estimates have been developed for four alternative light water reactor (LWR) recycling processes that differ in the reprocessing method (aqueous vs. electro-chemical), complexity (Pu only or full transuranic (TRU) recovery) and waste forms generated. Potential waste quantities and inventories have been developed on unit base of each MT reprocessed.

The inventory estimate considered different LWR fuel types (boiling and pressurized water reactors), burn-up of the fuel that is reprocessed, and the duration between when the fuel is discharged from the reactor and when it is reprocessed. HLW was assumed to be isolated in borosilicate glass, although alternative waste forms were investigated. Waste loadings in borosilicate glass were constrained by limits to avoid the formation of multi phase glasses. These limits include: 1) a maximum decay heat of 14,000 watts per 2 ft diameter canister to prevent the canister centerline temperature from reaching the transition temperature 2) the molybdenum trioxide solubility is limited to 2.5% by weight, and 3) the noble (Ag, Pd, Rh, Ru) metals are limited to 3% by weight. The limit selected for any representative fuel allows the maximum waste loading and minimum projected waste volume, and mass. The glass is cast into a 2 ft diameter by 15 ft tall canister containing 2900kg of glass.

For this demonstration, two end-member borosilicate glass waste forms from the COEX reprocessing were assumed: HLW generated from reprocessing used PWR fuel with 1) a burn-up of 20 GWd/MT and 100 years between discharge and reprocessing (PWR 20&100), and 2) a burn-up of 60 GWd/MT and 5 years between discharge and reprocessing (PWR 60&5). These two waste forms thus represent the HLW that would be generated from reprocessing younger, high burn-up fuel and older, low burn-up fuel. The waste loading was also limited due to different constraints. The PWR 60&5 HLW loading was limited by the 14,000 watt per canister limit and the PWR 20&100 was limited by the molybdenum trioxide solubility.

3.1.Thermal Model

While the SINDA/G framework can accommodate a wide range of conceptual repository designs, resource limitations necessitated choosing a single conceptual design for demonstrating the applicability of the tool. The initial two-dimensional thermal model of a conceptual repository described for a generic clay environment assumes waste storage in horizontal cylindrical boreholes of infinite length and a fixed depth below a horizontal surface at a fixed temperature of 20 °C. The waste package surface was assumed to make efficient thermal contact with the surrounding clay media. No ventilation or cooling air was assumed to be present.

In this demonstration, the boreholes were assumed to be spaced 30 meters apart and the waste packages emplaced end-to-end. Future analyses could investigate the effects of different spacing. The present evaluation focused on the amount of surface-based decay storage that would be required such that the wastes could be emplaced and meet a 100 °C limit at the borehole wall.

The radionuclide inventory for the borosilicate glass HLW for the COEX PWR 20&100 and COEX PWR 60&30 was obtained from the mass balance calculations used to develop the inventory estimate (Carter and Luptak, 2010). The inventories are determined at the time the HLW form is created. The radionuclide inventories were entered into the Isotope Parameter and Decay Tool, developed by Idaho National Laboratory, to compute the thermal output of the HLW over time. These are shown in Figure 7.

The results show that the HLW thermal output for the COEX PWR 60&5 case is initially dominated by short lived fission products that decay in the first 100-200 years, such as Cs-137 and Sr-90. At this point, the thermal output becomes dominated by Am-241 through approximately 2,000 years. The COEX PWR 20&100 case is also dominated by Cs-137 and Sr-90, however Am-241 is also a significant contributor to the total thermal output from the time the HLW form is created through approximately 2,000 years. This is due to the fact that a significant amount of Pu-241 has decayed to Am-241 during the 100 year period between when the fuel is discharged and when it is reprocessed. The COEX PWR 60&5 case in effect removes the Am-241 inventory from the waste stream by recycling the Pu-241 before it decays. This has a significant effect on the thermal performance within the generic clay environment.

The results from the clay Thermal GDSE model are shown in Figure 8. While the HLW from the COEX PWR 60&5 case initially has a higher thermal output, it is the HLW from the COEX PWR 20&100 case that would require a much longer period of decay storage before it could be emplaced in a borehole within a generic clay media and remain within a 100 °C limit at the borehole wall. The demonstration results indicate that decay storage would be needed for approximately 60-70 years for the COEX PWR 60&5 case and for over 600 years for the COEX PWR 20&100 case. This is entirely due to the decay heat from Am-241.

A follow on evaluation was conducted to determine the amount of de-rating that would be necessary in order for the decay storage duration for the HLW from the PWR 20&100 case to be the same as the PWR 60&5 case. It was found that a 64% reduction in the waste loading would be required. This would correspond to a 64% increase in the number of canisters that would be required if a disposal system thermal requirement would limit waste loading as opposed to the molybdenum trioxide solubility limit. Canister requirements would increase from 0.05 canisters/MT (Carter and Luptak, 2010) to 0.08 canisters/MT for the PWR 20&100 case, still significantly less than 0.23 canisters/MT (Carter and Luptak, 2010) for the PWR 60&5 case. Similar de-rating for both the PWR 60&5 and PWR 20&100 HLW forms would allow for shorter periods of surface decay storage.

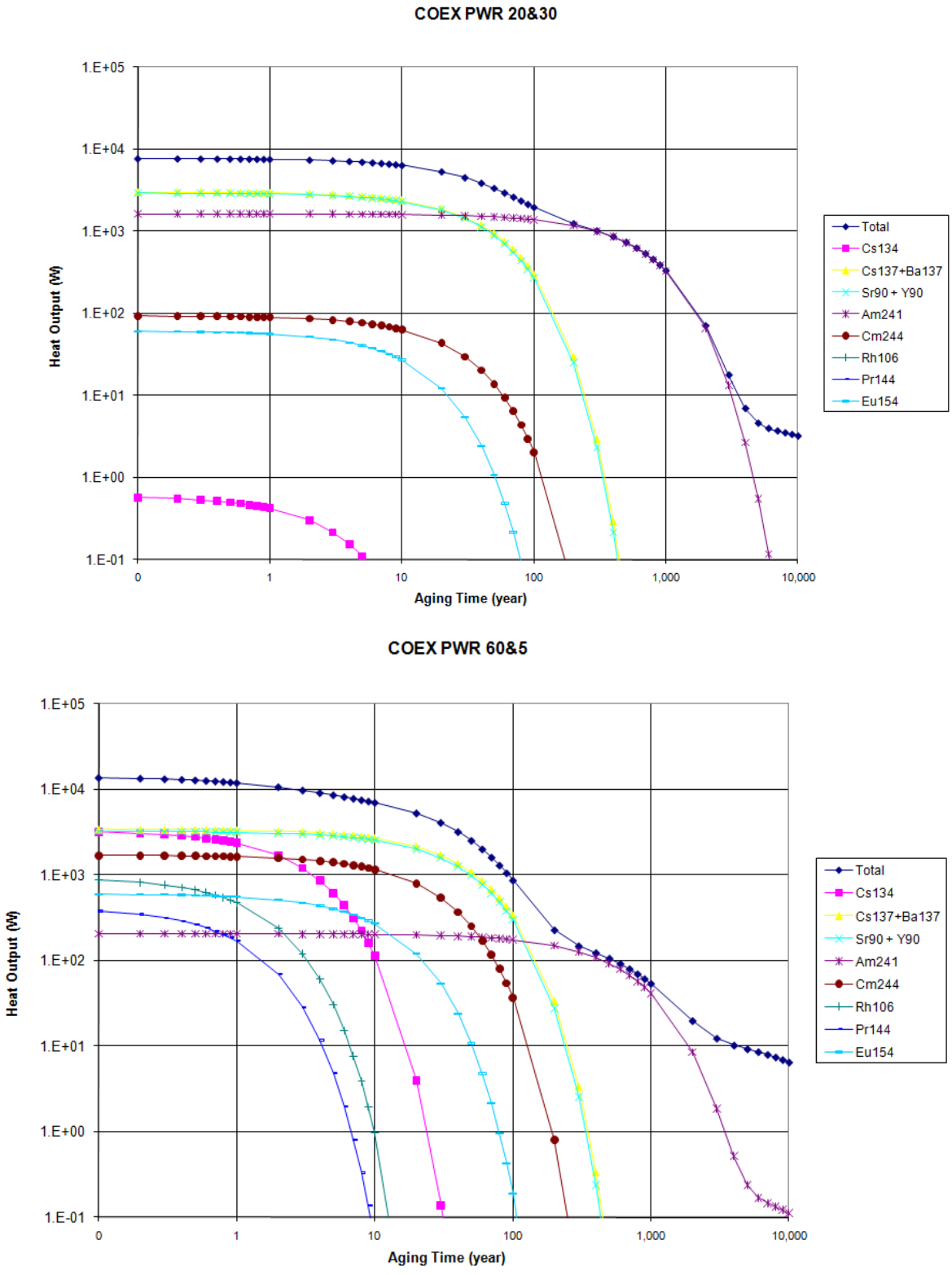

Figure 7. Decay Heat History for Demonstration Waste Forms

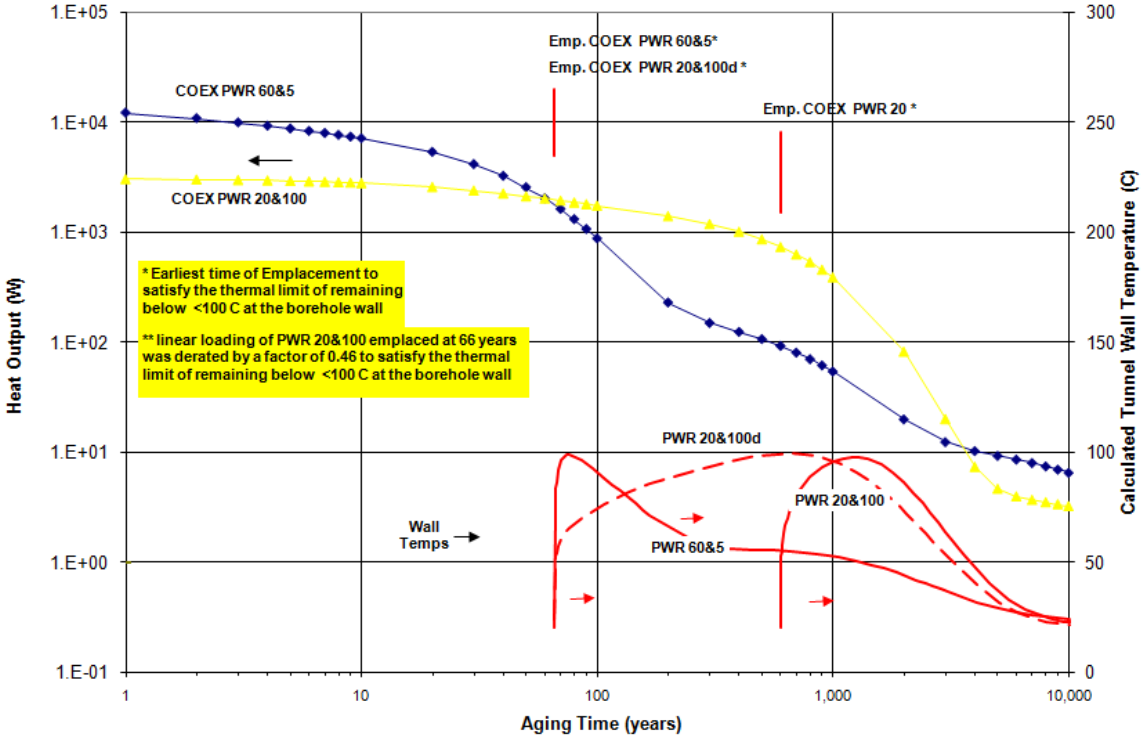

Figure 8. Demonstration Results from the Clay Thermal GDSE Model

These results demonstrate how the clay Thermal GDSE model can be used to inform fuel cycle system-level evaluations. Information regarding waste form loading limitations, surface decay storage requirements, and repository loading requirements can be provided by the model. In addition, the temperature histories produced by the model, such as those shown in Figure 8, can be linked into the clay Long Term Repository Performance GDSE model. Additional work is needed to further develop this tool such that it is flexible to evaluate multiple scenarios and conditions and is linked to the clay Long Term Repository Performance GDSE model. This work is discussed later in this report.

3.2.Long Term Repository Performance Model

Calculations have been carried out using the clay Long Term Repository Performance GDSE model for a hypothetical repository in a clay environment assuming processed waste for PWR spent fuel having a burnup of 60 GWd/MT and a 5-year cooling period and for PWR fuel having a burnup of 20 GWd/MT and a 100-year cooling period (COEX PWR 60&5 and COEX PWR 20&100).

For these calculations, horizontal boreholes are assumed to be spaced 20 m apart and to be infinitely long. A single waste package is assumed to be 5 m in length and waste packages are separated from each other by a space of 3 m. The calculations assume a slice of the repository environment that is 8 m thick in the direction of the boreholes. As discussed above, while the model includes transport cells for modeling transport of material through degraded waste form material, degraded waste package material, and buffering material between the waste package and the wall of the borehole, in the present calculations, once the waste form begins to degrade the released radionuclides pass very rapidly through material in the borehole and into the near field.

The near field/EDZ is assumed to have a thickness of only 0.02 m and a diffusive area of 8 m^2. From the near field/EDZ, radionuclides pass into the far field. Material properties are assumed to be the same in the near field/EDZ and far field and transport through these regions is by diffusion only. Radionuclides enter the far field in the corner of the far-field adjacent to the borehole and pass through the field to the top of the clay layer where a dose rate is calculated as discussed above. As currently modeled, radionuclides can leave the far-field only through the top of the clay layer. Zero mass flux boundary conditions are assumed on the horizontal and vertical boundaries intersecting at the borehole and at the vertical boundary half-way between boreholes. Figure 9 compares the total mean annual dose for the two HLW packages referenced in the foregoing paragraph. The dose rate is normalized to a single waste package. As an approximation, for a repository with a specified number of boreholes and number of waste packages in each borehole, the dose rate would be the product of the number of boreholes, the number of waste packages, and the dose rate shown in the figure. The result shows a rather large peak between 600,000 and 700,000 years followed by a gradually rising dose rate as time approaches 100 million years.

The total mean annual dose for the waste processed from PWR fuel with 60 GWd/MT burnup and 5-year cooling (COEX PWR 60&5) is shown in Figure 10 along with the contributions from ^{99}Tc and ^{231}Pa. The figure shows that the peak in the dose rate between 600,000 and 700,000 years is due entirely to the contribution of ^{99}Tc and that the gradual rise in the dose rate as time approaches 100 million years is due mostly to ^{231}Pa. ^{231}Pa has a half life of 32,800 years and it is concluded that this isotope is the result of the decay of carry-over ^{235}U in the HLW and not due to the initial content of ^{231}Pa in the HLW.

In spite of the lower burnup of the 20 GWd/MT fuel, the amount of ^{99}Tc in the package for waste processed from this fuel contains nearly twice as much ^{99}Tc as the waste package containing process PWR fuel with 60 GWd/MT. For a given mass of fuel, it would be expected that the amount of ^{99}Tc for fuel with a burnup of 20 GWd/MT would be about 1/3 as much as would be found in the 60 GWd/MT fuel. However the packaging for the lower burnup fuel is taking advantage of the lower heat load and including processed waste from a larger mass of spent fuel.

The dissolved concentration limits and retardation factors for the present calculations were taken from the Belgian repository program (SAFIR, 2001). The Belgian documentation includes solubilities for ^{99}Tc but lists the retardation factor as unity. The recent feasibility evalution of shale environments completed by Sandia National Laboratory (Frank et al., 2010)

indicates that the distribution coefficient for ^{99}Tc is in the range of 0 to 250 ml/g. To illustrate the impact of this distribution coefficient, a retardation factor with a triangular distribution ranging from 1 to 1220 with a most likely value of 1000 was arbitrarily assigned to ^{99}Tc. Then the COEX PWR 20&100 case shown in Figure 9 was re-executed. The resulting peak dose rate along with some the dose rates from some of the larger contributors to the dose is shown in Figure 11. The contribution from ^{99}Tc is now orders of several orders of magnitude smaller than the contribution for the case shown in Figure 9 and no longer appears on the graph. For the waste forms considered in this report, knowledge of the transport properties for ^{99}Tc would appear to be very important.

The waste form fractional degradation rate considered in the calculations described in the foregoing paragraphs was assumed to be 10^{-9} per year. A parametric calculation was carried out for the COEX PWR 20&100 case with the degradation rate increased by a factor of one thousand to 10^{-6} per year. The results from this calculation, with no sorption of ^{99}Tc are shown in Figure 12. In Figure 12, the peak annual dose, contributed almost entirely by ^{99}Tc is increased by more than a factor of two. The peak is initially reached at about the same time as in Figure 10, but with the higher degradation rate, the peak is much broader. With the higher degradation rate, ^{99}Tc apparently reaches its solubility limit in the near field with the result that for a considerable period of time the release to the far field is controlled by the diffusion rate in the near field rather than the degradation rate of the waste form. The largest dose rate contributed by actinides, primarily ^{231}Pa is increased by about a factor of ten with the larger degradation rate.

These demonstration results show the types of outputs and analyses that can be conducted with the clay Long Term Repository Performance GDSE model. Additional work is needed to continue testing and improving the model, testing the fast pathway framework, testing and improvement of the spreadsheet interface, and the establishment of linkage with the clay Thermal GDSE model. These activities are discussed later in this report.

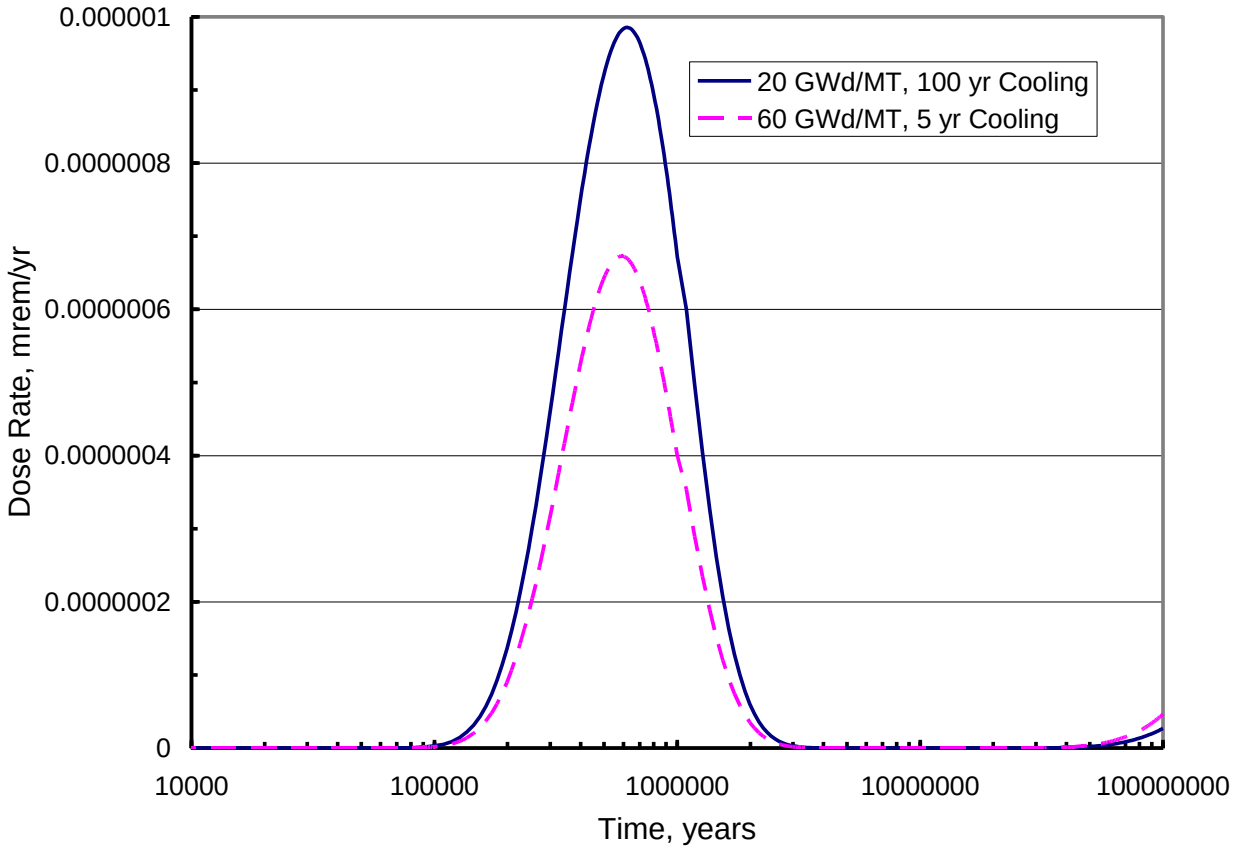

Figure 9. Comparison of Total Annual Dose from Two Demonstration Cases of HLW Processed from Used Nuclear Fuel.

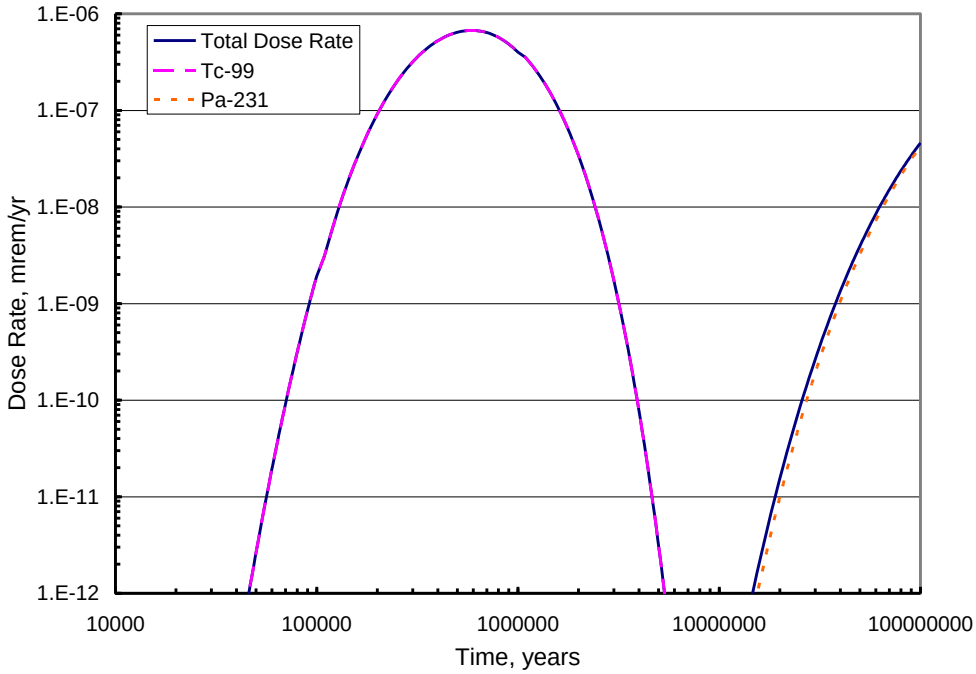

Figure 10. Radionuclide Contribution to the Total Annual Dose for the COEX PWR 60&5 Demonstration Case.

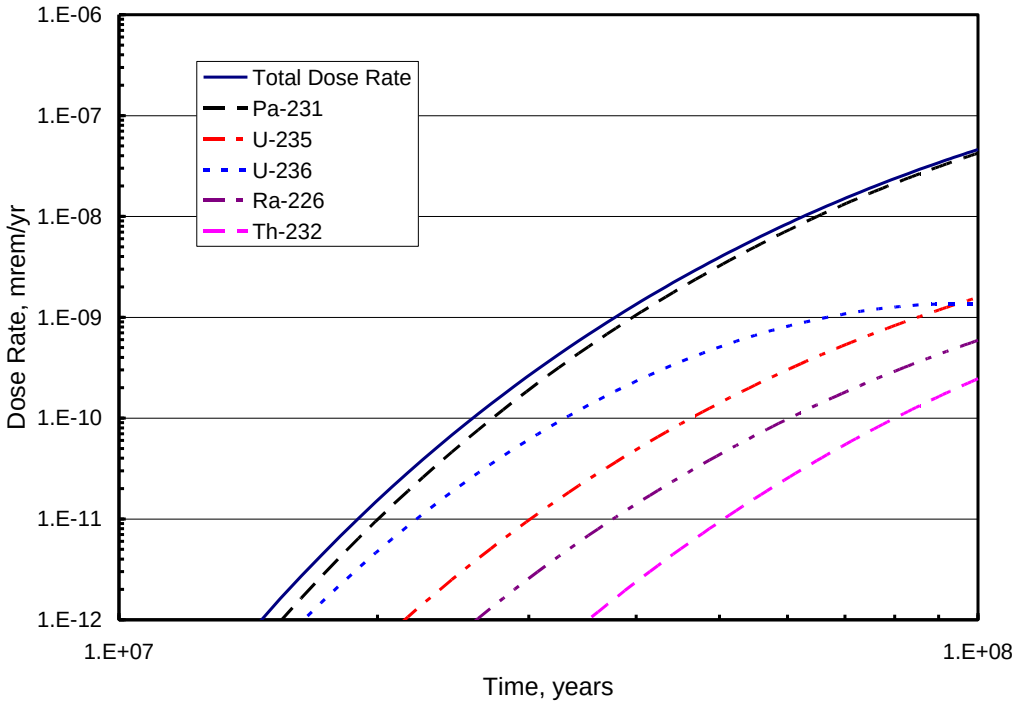

Figure 11. Demonstration Results for COEX PWR 20&100 Case Considering Retardation of 99Tc.

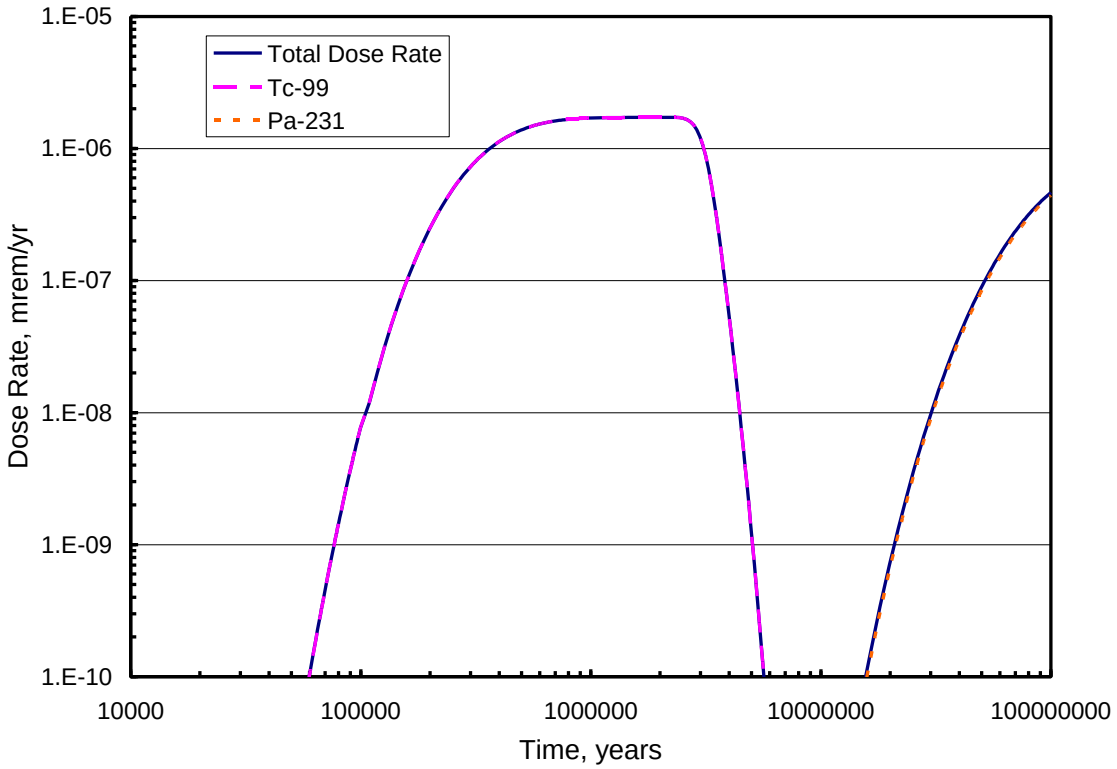

Figure 12. Demonstration Results for the COEX 60&5 Case Considering a 1000x Increase in the Waste Form Fractional Degradation Rate.

4. Conclusions

Fiscal Year 2010 saw the initiation of the development of flexible clay Thermal and Long Term Repository Performance GDSE models. The general model framework was established and limited demonstration testing has been completed. Preliminary results indicate that a wide range of output can be generated for different fuel cycle scenarios to inform not only the UFD campaign, but the entire FCT program as well. Specific output that can be generated for a given fuel cycle scenario include additional limitations on waste loading, requirements for surface-based decay storage, and potential repository footprint. The importance of key features, events, and processes can also be examined, providing feedback to the UFD campaign and helping to establish research and development priorities.

While much work has been completed in establishing the overall structure of the clay GDSE models, additional work is needed to fully develop the tool capability. This includes:

Thermal GDSE Model

- Further testing and model refinement by testing different UNF and HLW inventories (this may provide near-term input to FCT System Engineering efforts).
- Investigation into establishing a user-friendly interface to the SINDA/G platform.
- Investigation into manners to "host" the thermal GDSE model for use by others in the UFD campaign and on the FCT program.
- Establishment of linkage between the Thermal and Long Term Repository Performance GDSE models.
- Development of models that represent conceptual repository designs in more detail (coupling with conceptual design catalog to be developed in Fiscal Year 2011).
- Investigation into the development of automated search capability within SINDA/G for determining spacing of conceptual repository designs, decay storage requirements, and de-rating.

Long-Term Repository Performance GDSE Model

- Testing and refinement of the engineered barrier system and near field/EDZ model components.
- Testing and refinement of the fast pathways features.
- Verification that all features, events, and processes important in a clay environment are structurally captured.
- Improvement in the spreadsheet user interface.
- Development of key result displays and establishment of a user interface with GoldSim.
- Establish coupling with clay Thermal GDSE model.

Development of engineered barrier system models that represent conceptual repository designs in more detail, primarily by implementation and testing within the current framework (coupling with conceptual design catalog to be developed in Fiscal Year 2011).

5. References

Carter, J. and Luptak, A. "Fuel Cycle Potential Waste Inventory for Disposition," FCR&D-USED-2010-000031 Rev 1, March 2010.

GoldSim Technology Group, "GoldSim version 10.11", 2010,.

Hansen, F.D. , Hardin, E.L., Rechard, R.P., Freeze, G.A., Sassani, D.C., Brady, P.V., Stone, C.M., Martinez, M.J., Holland, J.F., Dewers, T., Gaither, K.N., Sobolik, S.R., and Cygan, R.T. "Shale Disposal of U.S. High-Level Radioactive Waste, " SAND2010-2843, May 2010.

MSC-SINDA, "MSC Software Corporation", Santa Ana, CA, 2010.

Nutt, W.M., Wang, Y., and Lee, J. "Generic Repository Concept Analyses to Support the Establishment of Waste Form Performance Requirements – Fiscal Year 2009 Year-End Status", ANL-AFCI-295, September, 2009.

SAFIR 2, "Safety Assessment and Feasibility Interim Report 2", ONDRAF/NIRAS, NIROND 2001-06E, December 2001. (Available at www.nirond.be/engels/Safir2_eng.php).

Appendix A: Comparison of Numerical Approach for Two-Dimensional Modeling of the Far Field with Analytic Solutions

In the absence of advective flow the 20 × 20 matrix of cells used to represent the far-field solves a time dependent diffusion equation in two spatial dimensions. For species that are not limited by solubility and not undergoing radioactive decay, in an isotropic medium this equation is

$$\frac{\partial c}{\partial t} = D\left[\frac{\partial^2 c}{\partial x^2} + \frac{\partial^2 c}{\partial y^2}\right], \tag{1}$$

where t is the time, $0 \le x \le a$ and $0 \le y \le b$ with a the width of the far-field and b the depth, D is the diffusion coefficient, and c is the concentration. Using the technique of separation of variables and applying the initial and boundary conditions

$$c(0,x,y) = \frac{M}{\delta\varepsilon} \text{ when } (0 \le x \le \delta), (0 \le y \le \varepsilon) \text{ and } = 0, \text{ otherwise}, \tag{2}$$

$$D\left.\frac{\partial c}{\partial x}\right|_{x=0} = D\left.\frac{\partial c}{\partial x}\right|_{x=a} = 0 \tag{3}$$

at all times t and positions y, and

$$c(t,x,b) = D\left.\frac{\partial c}{\partial y}\right|_{y=0} = 0 \tag{4}$$

for all values of t and x, the solution for this equation is found to be

$$c(t,x,y) = \sum_{n=0}^{\infty}\sum_{m=0}^{\infty} A_{nm} e^{-k_{nm}t} \cos(\alpha_n x)\cos(\beta_m y). \tag{5}$$

In the foregoing equations, M is the mass (per unit length in a direction perpendicular to the x,y plane) initially confined to the area $(0 \le x \le \delta), (0 \le y \le \varepsilon)$,

$$\alpha_n = \frac{n\pi}{a}, \tag{6}$$

$$\beta_m = \frac{(2m+1)\pi}{2b}, \tag{7}$$

and

$$k_{nm} = D\left(\alpha_n^2 + \beta_m^2\right). \quad (8)$$

When $n = 0$,

$$A_{0m} = \frac{2M}{ab\varepsilon\beta_m}\sin(\beta_m \varepsilon), \quad (9)$$

and when $n > 0$,

$$A_{nm} = \frac{4M}{ab\delta\varepsilon\alpha_n\beta_m}\sin(\alpha_n \delta)\sin(\beta_m \varepsilon). \quad (10)$$

Except when t is near zero, a relatively small number of terms provides adequate convergence for the series in (5).

To provide an indication of the robustness of the GoldSim solution when the 20 × 20 matrix cells represent a variety of sizes and aspect ratios for the rectangular far-field region, the numerical GoldSim solution was compared with the exact solution as given by (5). For this purpose, 10 grams of a test species was inserted at time zero into the GoldSim cell representing the part of the region defined by $(0 \le x \le \delta), (0 \le y \le \varepsilon)$ where $\delta = a/20$ and $\varepsilon = b/20$. This region has a thickness perpendicular to the x, y plane of 1.6 m. In the graphs that follow, the cell where the mass is inserted has the label X1Y1, a cell approximately in the middle of the rectangular region has the label X10Y10, and the cell at the opposite corner of the region from the cell X1Y1 has the label X20Y20. A point at the center of the cell X1Y1 has the coordinates $x = \delta/2$ and $y = \varepsilon/2$, a point at the center of the cell X10Y10 has the coordinates $x = 9.5\delta$ and $y = 9.5\varepsilon$, and a point at the center of the cell X20Y20 has coordinates $x = 19.5\delta$ and $y = 19.5\varepsilon$. The diffusion coefficient has the value 2×10^{-10} m^2/s.

For the first set of comparisons, a square far-field with a width $a = 20$ m and a depth $b = 20$ m is considered. The time dependent concentration in the three cells referred to in the foregoing paragraph is shown in Fig. A-1. Comparisons between the two solutions were also made at several other locations within the matrix with agreement as good as shown for X10Y10 and X20Y20. Agreement is not as good for X1Y1 because the spatial mesh is not sufficient for tracking the step-function behavior of the concentration at early times. Calculations were also completed for square far-fields with dimensions as large as $a = b = 80$ m with the same quality of agreement as shown in Fig. A-1. The only effect of changing the size of the square far-field is to change the time constants k_{nm} in (5).

Results for a second set of calculations for a rectangular far-field with $a = 20$ m and $b = 80$ m. Comparisons between the GoldSim numerical solution and the exact solution from (5) are shown in Fig. A-2. While agreement is not quite as good as is shown in Fig. A-1, the GoldSim numerical result is, nevertheless, within a few percent of the exact solution except in

the cell X1Y1. As in the previous case, results were compared at several additional locations within the far-field and in all cases agreement was as good as or better than shown in Fig. A-2.

A third set of calculations were carried out for a rectangular far-field with $a = 80$ m and $b = 20$ m. Comparisons for this case are shown in Fig. A-3. This case differs from that shown in Fig. A-2 in that leakage occurs along the long side of the rectangle rather than the short side. Agreement between the numerical and exact solutions is slightly worse in this case than in the case shown in Fig. A-2, but even so, the most serious disagreement is only about 4% except in the case of the cell X1Y1.

The fourth set of calculations involved the more extreme aspect ratio in which the rectangular far-field has $a = 20$ m and $b = 150$ m. Results for this case are shown in Fig. A-4. Agreement is very good in the cell near the center of the far-field but GoldSim over-predicts the concentration by slightly more than 10 % at the corner of the rectangle opposite where the mass in inserted. There are other locations in the far-field where the disagreement between GoldSim's numerical solution and the exact solution is similar that shown in Fig. A-4 for the cell X20Y20. It is worth noting that even though the magnitude of the concentration is off, GoldSim seems to make an accurate prediction of the time when the peak concentration occurs.

Comparisons shown in Figs. A-1 through A-4 indicate that as the aspect ratio becomes larger, agreement between the numerical solution produced by GoldSim and the exact solution given by (5) deteriorates. However, even with the rather extreme ratio of 15/2, disagreement seems at worst to be only about 10 %. at only a few limited locations, primarily in the corners closest to and farthest away from where the source was injected. Inserting mass into a single cell at time zero probably offers a more serious challenge to the numerical solution algorithm than the gradual release of mass into this cell over a longer period of time such as occurs in the repository analysis considered in this report. The difficulty could be avoided if it were possible to easily change the number of cells in the x and y directions and thus keep the ratio of the length to width of individual cells close to unity. However, this is not easily accommodated within the GoldSim software.

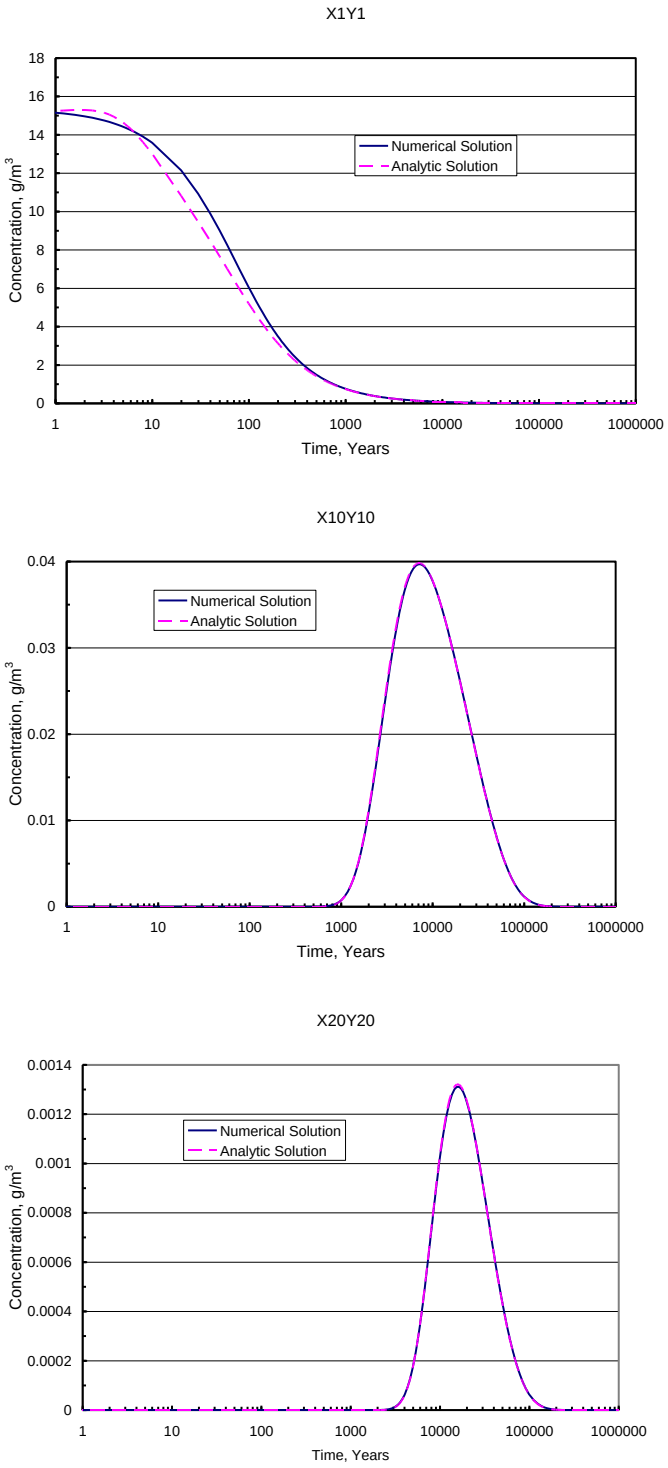

Figure. A-1. Time dependent solutions for $a = 20\ \text{m}\ \ b = 20\ \text{m}$**.**

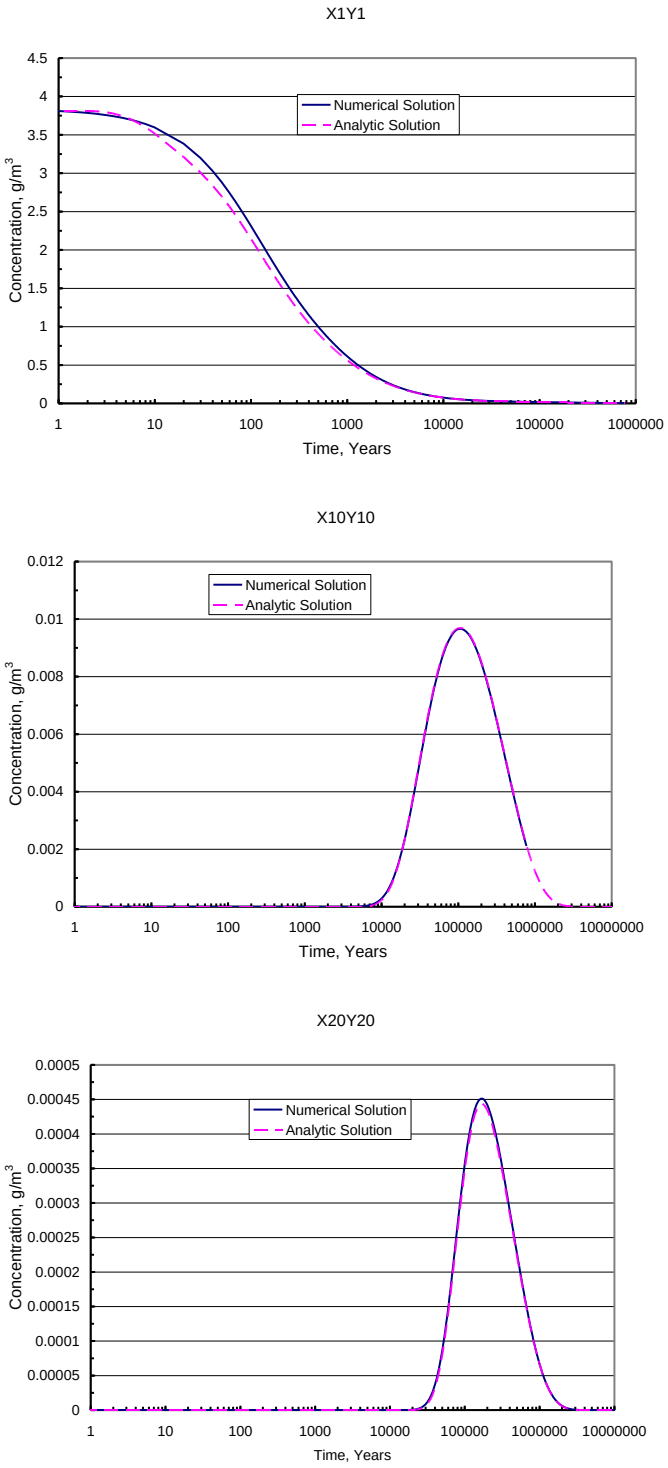

Figure A-2. Time dependent solutions for $a = 20\ \text{m}\ \ b = 80\ \text{m}$.

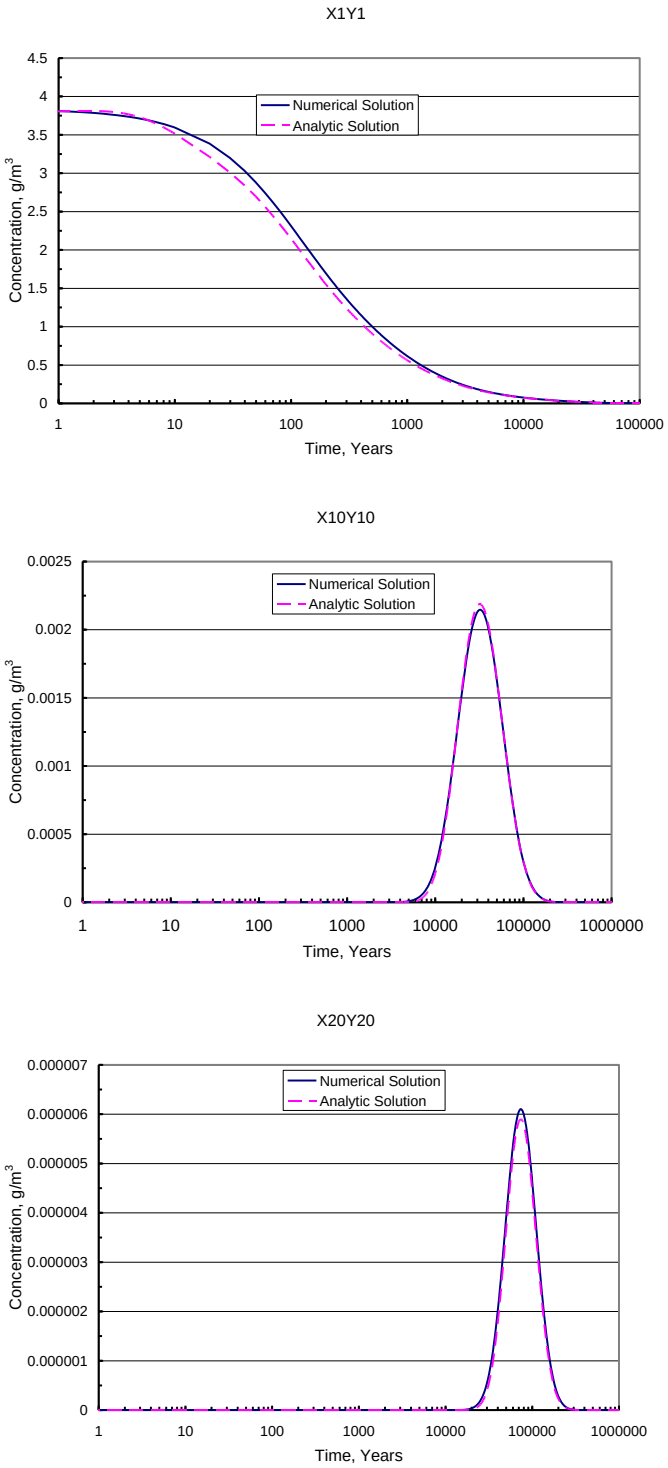

Figure A-3. Time dependent solutions for $a = 80$ m $b = 20$ m.

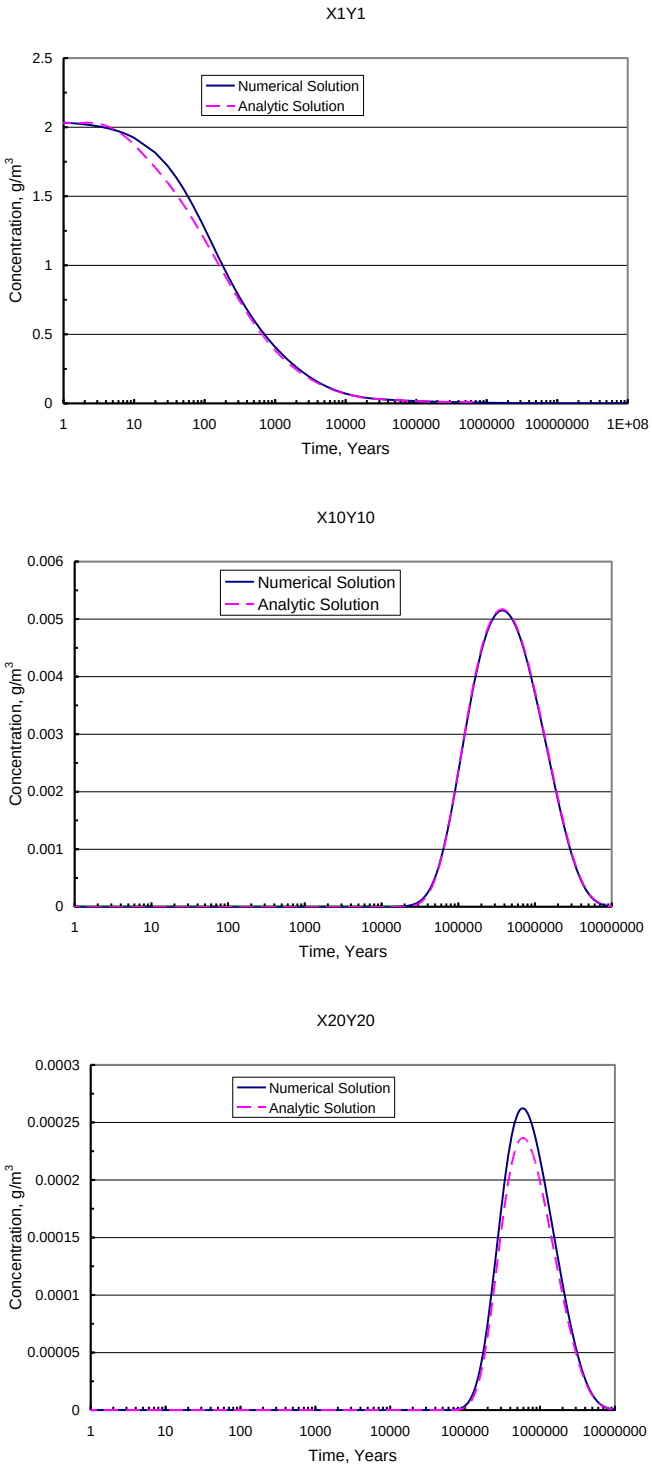

Figure A-4. Time dependent solutions for $a = 20$ m $b = 150$ m.

Chapter 5 Deep Borehole Generic Disposal System Environment Model

Joon H Lee and Yifeng Wang

Sandia National Laboratories

1. Introduction

Deep boreholes at extreme depths have been proposed as an option for permanent disposal of high-level radioactive waste (HLW) and used nuclear fuel (UNF) (Åhäll 2006, Brady et al. 2009; Gibb 1999, Gibb et al. 2008, Harrison 2000). Disposal concepts call for drilling boreholes to a depth of 3 to 5 km into crystalline bedrocks, typically granites. Waste is placed in the lower portion of the hole, and the upper several kilometers of the hole are sealed to provide effective isolation from the biosphere. The potential for excellent long-term performance has been recognized in many previous studies.

Very deep borehole disposal can offer important advantages over the conventional mined geologic disposal in that (1) the repository can be located in stable bedrock at a depth where the groundwater is isolated from the biosphere, and (2) the waste can be deposited and the boreholes permanently sealed without causing long-term disturbances in the density-stratification of the groundwater that surrounds the repository (Åhäll 2006). Another advantage is that it is less vulnerable to impacts from expected events (e.g., changes in groundwater conditions during future glacial periods) as well as undesired events (e.g. such as major earthquakes).

This chapter discusses the deep borehole Geologic Disposal System Environment (GDSE) model and preliminary model results. Three types of high-level radioactive waste (commercial UNF, DOE HLW and reprocessing HLW) are considered for the model analysis, and the radionuclide inventory of the wastes developed for the reference source-term model (Chapter 1) is used in the analysis. The models for water flow and radionuclide transport in a deep borehole were developed using the data and analysis presented in a recent study by Brady et al. (2009), and the details of the model development and implementation are also described in this chapter. The chapter discusses the conceptual model for a deep borehole GDSE, the model implementation and structure, the preliminary model analysis results, and future work.

2. Conceptual Model

The conceptual model for radionuclide release and transport from a deep borehole GDSE was developed using the data and analysis in a recent study by Brady et al. (2009). Figure 1 shows a schematic for the conceptual model for radionuclide release and transport in a deep borehole GDSE. The deep borehole at a total depth of 5,000 m is divided into three zones: the bottom 2,000 m for waste disposal (referred to as the “disposal zone”), the next 1,000 m sealed with bentonite clay (referred to as the “seal zone”), and the top 2,000 m plugged and backfilled with sedimentary rock materials (referred to as the “upper zone”).

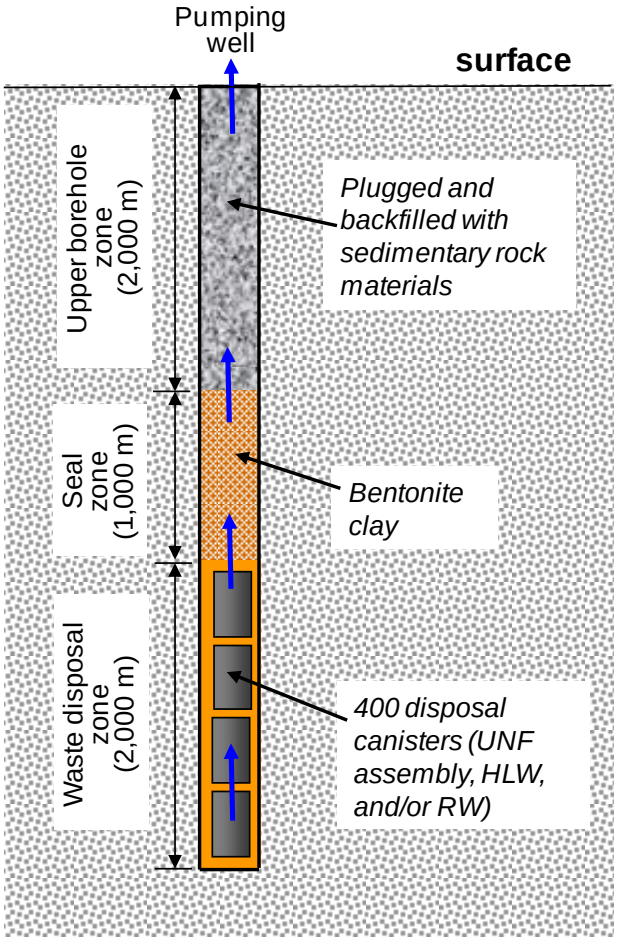

Figure 1. A schematic showing the conceptual model for radionuclide release and transport for a generic deep borehole disposal.

It is assumed that a disposal canister with a length of about 5 m is used to lower the waste to the disposal zone, and that each canister contains one commercial UNF PWR assembly, DOW HLW canister, or reprocessing HLW canister. Each deep borehole can hold a total of 400 disposal canisters. The radionuclide inventory per disposal canister for each waste type is provided in Chapter 1.

As discussed in the reference source-term model section (Chapter 1), two repository waste inventory scenarios are considered: 1) the waste inventory scenario 1 comprises the commercial UNF and DOE HLW, and 2) the waste inventory scenario 2 the DOE HLW and reprocessing HLW. The waste inventory to be disposed of in each borehole is assumed to be proportional to the repository waste inventory. For the waste inventory scenario 1, each borehole has 371 UNF canisters and 29 DOE HLW canisters, and a total of 866 deep boreholes are needed for disposal of the total inventory. For the inventory scenario 2, each borehole holds 221 DOE HLW canisters and 179 reprocessing HLW canisters, and disposal of the total inventory needs a total of 113 deep boreholes.

For simplification, a uniform cross sectional area of 1 m^2 is assumed for the entire length of borehole. The disposal zone is assumed at a constant ambient temperature of 100°C; higher temperatures in the borehole caused by the transient thermal perturbations during relatively short periods following waste disposal are ignored (Brady et al. 2009, figures 5 and 6). No disposal canister performance is considered in the model. The fractional waste form degradation rate models described in the reference source-term model (Chapter 1) are used to model radionuclide release from the respective waste form.

Water movements in and around a deep borehole could be affected by many factors; some of the potential factors that are associated with the deep borehole disposal of HLW may include: 1) elevated pressure driven by thermal expansion of pore water from decay heat; 2) thermally driven convective water flow; 3) presence of fracture flow; 4) groundwater pumping; 5) thermal-hydrological effects of neighboring boreholes; and 6) climate change such as glaciations. The study by Brady et al. (2009) concluded that the water flow driven by the pore water thermal expansion is the only credible water movement that could transport radionuclide advectively upward in the borehole, and that this upward water flows last only for about 200 years after borehole closure following the waste emplacement. Other studies reported the abundance of deep-seated brines in a very deep borehole of 4 km depth, and concluded that the crystalline basement fracture pores are water-saturated and highly connected, which are basic conditions for possible advective water flow (Stober and Bucher 2005a and 2005b).

The deep borehole GDSE model considers two alternative conceptual models for the upward water flows and radionuclide transport in the disposal and seal zones: 1) upward water flow and advective radionuclide transport for the first 200 years, then upward water flows stop and upward radionuclide transport is by diffusion only for the remainder of the simulation (referred to as "transient water flow"); and 2) continuous upward water flow and advective radionuclide transport for the entire analysis time period (referred to as "continuous water flow"). The latter conceptual model is much more conservative than the former for the radionuclide transport.

The model assumes hypothetical continuous groundwater pumping at the surface and continuous upward water flows and advective radionuclide transport in the upper zone. A "hypothetical" biosphere is assumed at the groundwater pumping location, and the reference biosphere model described in the reference source-term model (Chapter 1) is applied to calculate the dose.

The radionuclide solubility for the near-field water at 100°C is applied for the disposal zone. In addition, the model assumes that the iodine solubility in the disposal zone is constrained by adding excess Cu_2O powder in the disposal zone and having copper iodide (CuI) as the controlling solid phase. The iodine solubility in the disposal zone is modeled with a log-triangular distribution with the mode at 1×10^{-4} molal and the lower and upper bounds at 1×10^{-5} and 1×10^{-3} molal respectively. Dissolved radionuclides enter the disposal zone over its length (2,000 m), before they are transported upward to the seal zone and upper zone. Radionuclide sorption is modeled in all three zones using the reversible equilibrium distribution coefficient (Kd) approach.

Note that applying the biosphere model at the hypothetical groundwater pumping location is an arbitrary modeling choice to produce the uniform performance measure for comparative studies of a deep borehole GDSE and does not indicate any realistic dose implications. Therefore, the results presented in this section *should not* be construed as being indicative of the true performance of a deep borehole GDSE or compared to any regulatory performance objectives regarding repository performance.

3. Model Implementation and Structure

This section discusses the implementation and structure of the deep borehole GDSE model. Goldsim (Goldsim 2009) was used as the framework for model implementation and simulations. Figure 2 shows the Goldsim model structure of the deep borehole GDSE model; Figure 3 the model components for radionuclide transport in the borehole.

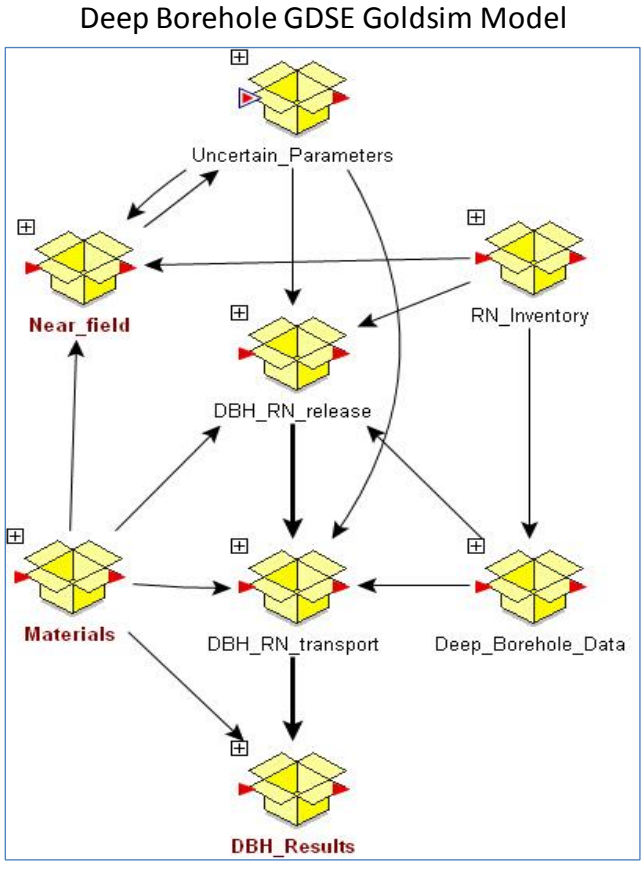

Figure 2. The Goldsim model structure for the deep borehole GDSE model

The model components are given specific names indicative of their function in the overall model. The reference source-term model discussed in Chapter 1 is implemented in the following model components: *Materials*, *RN_Inventory*, *Near_field*, and *Uncertain_Parameters*. The *Deep_Borehole_Data* model component contains deep borehole-specific data and associated calculations. The *DBH_RN_transport* model component calculates radionuclide transport in the three zones of the deep borehole, and the *DBH_RN_release* model component interfaces between the source-term and borehole transport models. The *Uncertain_Parameters* model component contains all uncertain model parameters. The reference biosphere model is implemented in the *DBH_Results* model component and performs the dose calculations.

As shown in Figure 3, radionuclide transport in the three zones of deep borehole is modeled with a Goldsim pipe model (Goldsim 2009). Table 1 lists the transport property parameters for the three zones, including the upward groundwater pore velocity and radionuclide sorption distribution coefficients (Kds). The upward water pore velocity in the disposal seal zone was estimated based on the peak volumetric flow rate of vertical water flows at the top of the disposal zone during the early thermal periods, which was obtained from detailed thermo-hydrologic simulations for a generic deep borehole for HLW disposal (Brady et al. 2009, figure 8). The upward water pore velocity in the seal zone was estimated based on the peak volumetric water flow rate at the top of the seal zone from the same analysis (Brady et al. 2009, figure 8). For the upper zone, the upward water pore velocity was estimated by matching the breakthrough curve of a Goldsim pipe model with the simulated breakthrough curve for the conservative groundwater pumping case (Brady et al. 2009, figure 11).

Table 1. Model Parameters Used for the Deep Borehole GDSE Model

Parameter	Distribution Type	Parameter Value and Description
Waste Disposal Zone		
Length (m)	Constant	2,000.
Cross sectional area (m^2)	Constant	1
Bulk density (kg/m^3)	Constant	2,450
Porosity	Constant	0.034
Tortuosity	Constant	0.324
Upward groundwater pore velocity (m/yr)	Constant	- 0.5 for the first 200 yrs, then zero for the transient flow case; - 0.5 for the entire analysis period for the continuous flow case
Kd for Am, Ac, Cm (ml/g)	Uniform	50 (min); 5.0E+03 (max)
Kd for C (ml/g)	Uniform	0 (min); 6 (max)
Kd for Cs (ml/g)	Uniform	50 (min); 400 (max)
Kd for Np, Pa (ml/g)	Uniform	10 (min); 5.0E+03 (max)
Kd for Pu (ml/g)	Uniform	10 (min); 5.0E+03 (max)
Kd for Ra (ml/g)	Uniform	4 (min); 30 (max)

Kd for Sr (ml/g)	Uniform	4 (min); 30 (max)
Kd for Tc (ml/g)	Uniform	0 (min); 250 (max)
Kd for Th (ml/g)	Uniform	30 (min); 5.0E+03 (max)
Kd for U (ml/g)	Uniform	4 (min); 5.0E+03 (max)
Kd for I (ml/g)	Uniform	0 (min); 1 (max)
Bentonite Seal Zone		
Length (m)	Constant	1,000.
Cross sectional area (m^2)	Constant	1
Bulk density (kg/m^3)	Constant	2,450
Porosity	Constant	0.034
Tortuosity	Constant	0.324
Upward groundwater pore velocity (m/yr)	Constant	- 0.1 for the first 200 yrs, then zero for the transient flow case; - 0.1 for the entire analysis period for the continuous flow case
Kd for Am, Ac, Cm (ml/g)	Uniform	300 (min); 2.94E+04 (max)
Kd for C (ml/g)	Constant	5
Kd for Cs (ml/g)	Uniform	120 (min); 1.0E+03 (max)
Kd for Np, Pa (ml/g)	Uniform	30 (min); 1.0E+03 (max)
Kd for Pu (ml/g)	Uniform	150 (min); 1.68E+04 (max)
Kd for Ra (ml/g)	Uniform	50 (min); 3.0E+03 (max)
Kd for Sr (ml/g)	Uniform	50 (min); 3.0E+03 (max)
Kd for Tc (ml/g)	Uniform	0 (min); 250 (max)
Kd for Th (ml/g)	Uniform	63 (min); 2.35E+04 (max)
Kd for U (ml/g)	Uniform	90 (min); 1.0E+03 (max)
Kd for I (ml/g)	Uniform	0 (min); 13 (max)
Sedimentary-filled Rock Upper Zone		
Length (m)	Constant	2,000.
Cross sectional area (m^2)	Constant	1
Bulk density (kg/m^3)	Constant	2,450
Porosity	Constant	0.01
Tortuosity	Constant	0.215
Groundwater upward pore velocity (m/yr)	Constant	0.24 for the entire analysis period for both the transient and continuous flow cases
Kd for Am, Ac, Cm (ml/g)	Uniform	100 (min); 1.0E+05 (max)
Kd for C (ml/g)	Uniform	0 (min); 2.0E+03 (max)
Kd for Cs (ml/g)	Uniform	10 (min); 1.0E+04 (max)
Kd for Np, Pa (ml/g)	Uniform	10 (min); 1.0E+03 (max)

Kd for Pu (ml/g)	Uniform	300 (min); 1.0E+05 (max)
Kd for Ra (ml/g)	Uniform	5 (min); 3.0E+03 (max)
Kd for Sr (ml/g)	Uniform	5 (min); 3.0E+03 (max)
Kd for Tc (ml/g)	Uniform	0 (min); 1.0E+03 (max)
Kd for Th (ml/g)	Uniform	800 (min); 6.0E+04 (max)
Kd for U (ml/g)	Uniform	20 (min); 1.7E+03 (max)
Kd for I (ml/g)	Uniform	0 (min); 100 (max)
Note: all data in this table are from Brady et al. (2009) and associated supporting materials.		

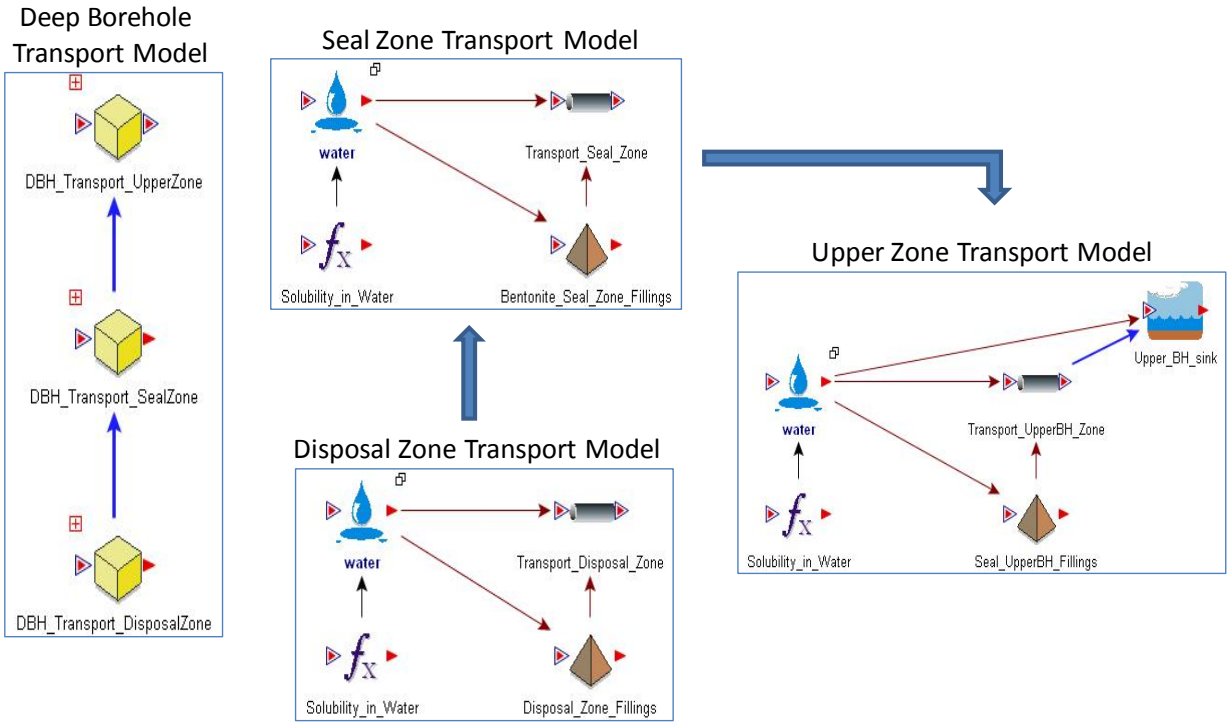

Figure 3. The Goldsim model components for radionuclide transport in the deep borehole of the deep borehole GDSE model

As discussed above, two alternative conceptual models are considered for the upward water flows in the disposal and seal zones: transient flow case, and continuous flow case. For the transient flow case, thermally-driven upward groundwater flows in the disposal and seal zones lasts for only the first 200 years and then stops; this is captured in the model as the upward

advective transport of dissolved radionuclides in the disposal and seal zones for the first 200 years, followed by upward diffusive transport mainly driven by the concentration gradients. The upward groundwater flows in the upper zone operate all the time, driven by a hypothetical continuous groundwater pumping at the surface, which would cause a greater concentration gradient at the seal zone and upper zone interface and a higher upward diffusive flux of radionuclides from the seal zone to the upper zone.

For the continuous water flow case, upward groundwater flows operate all the time in all three zones, and dissolved radionuclides are transported advectively upward in all three zones for the entire analysis period.

The Goldsim analysis is performed probabilistically, with 100 realizations for each case for a time period of one million years.

4. Model results

This section discusses the preliminary results of the deep borehole GDSE model. The model results are presented in terms of the mean dose (mrem/yr) by individual radionuclides for a single deep borehole. It is noted that this model is the initial effort of the deep borehole GDSE analysis tool development and needs further improvement and refinements as the study progresses. Also note that using the mean dose is an arbitrary choice to present and discuss the analysis results in order to facilitate comparative studies among the GDSE options and does not indicate any realistic dose implications. Therefore, the results presented in this section *should not* be construed as being indicative of the true performance of a deep borehole GDSE or compared to any regulatory performance objectives regarding repository performance.

Figure 4 shows the mean doses by major dose-contributing radionuclides for the waste inventory scenario 1 (commercial UNF plus DOE HLW) for the transient water flow case. As discussed above, for the transient flow case, radionuclides are transported by advection only for the first 200 years and by diffusion afterward. All dose-contributing radionuclides with the mean dose greater than 10^{-10} mrem/yr are the fission product radionuclides with a high solubility in water and a high mobility (non sorbing or weakly sorbing). The dominant long-term dose contributor is ^{79}Se, and this is expected based on the following modeling aspects of the radionuclide transport: 1) no solubility limit, 2) non-sorbing to geologic materials, and 3) a significant inventory in the waste (about 3 g per commercial UNF PWR assembly and about 22 g per DOE HLW canister). The mean dose peaks at about 20,000 years and decreases steeply afterward, and this is due mainly to its radioactive decay. There are conflicting data on the ^{79}Se half-life in the literature, which has been variously reported as 6.5×10^4 years (used in the model), 2.95×10^5 years, 4.8×10^5 years, 6.5×10^5 years, and 1.13×10^6 years (Jiang et al. 2001). Also the selenium solubility in groundwater is highly uncertain. The metal selenium is insoluble in water, but it can also be released as soluble selenate ion (SeO_4^{2-}), which is not readily sorbed to geologic materials. More work is needed to better characterize and quantify dissolution and sorption behavior of selenium in a geologic repository environment.

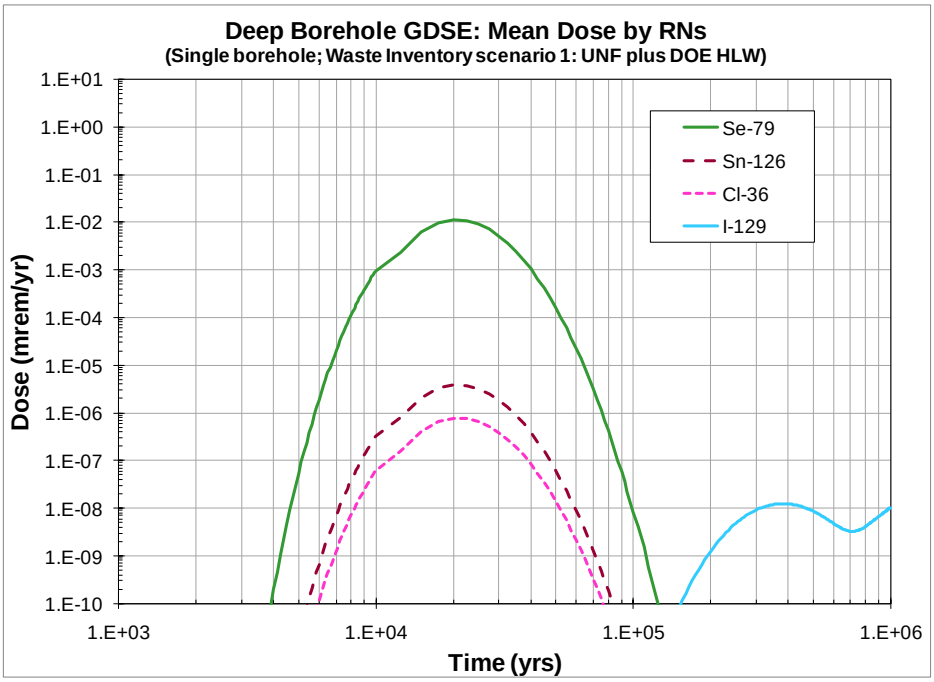

Figure 4. Mean dose by radionuclides for the waste inventory scenario 1 (commercial UNF and DOE HLW) for the transient water flow case of deep borehole GDSE.

The mean doses for other radionuclides (^{126}Sn, ^{36}Cl, and ^{129}I) are insignificant compared to that of ^{79}Se. It is interesting to note that the very long-term mean doses for ^{129}I are greater than those of the other three radionuclides, and this is due mainly to the very long half life of ^{129}I (1.7×10^{7} years).

The single-borehole model results for the waste inventory scenario 2 (DOE HLW plus reprocessing HLW) for the transient water flow case are shown in Figure 5. The mean dose for ^{79}Se is about two orders of magnitude greater than the ^{79}Se mean dose for the inventory scenario 1, and the mean dose for ^{129}I is about one order of magnitude higher than the ^{129}I mean dose for the inventory scenario 1. The ^{126}Sn mean dose is about the same because the dissolved tin concentration is constrained by solubility although the reprocessing HLW has a higher per-canister inventory for ^{126}Sn than the UNF and DOE HLW. Note that the ^{36}Cl dose is absent in the figure because both the DOE HLW and reprocessing HLW do not have ^{36}Cl inventory.

The higher mean doses for ^{79}Se and ^{129}I can be explained by the higher inventory of the radionuclides in the reprocessing HLW. Because of the assumptions made for the reprocessing HLW (see Chapter 1), the fission products inventory on a per-canister basis is higher than that of the inventory scenario 1. For example, each reprocessing HLW canister contains about 50 g of ^{79}Se and about 1,500 g of ^{129}I, which is 15 to 16 times greater than the commercial UNF per-assembly inventory mass of the radionuclides. The effect of the higher inventories is evident in the results.

Figures 6 and 7 show the single borehole model results for the waste inventory scenario 1 and scenario 2 respectively of the continuous waste flow case. For this case, radionuclides are transported by advection for the entire analysis period. While the major dose-contributing radionuclides are the same as the transient flow case, the mean doses for the radionuclides are much higher, and the dose histories are different from the transient flow case. ^{79}Se is still the dominant dose-contributing radionuclide, and the mean dose is about four orders of magnitude higher than the transient flow case. More dramatic changes are seen for the ^{129}I mean doses, which are six to seven orders of magnitude higher than the transient flow case. Four to five orders of magnitude increases in the mean doses are also shown for ^{129}Sn and ^{36}Cl.

The analysis results for the two alternative water flow cases demonstrate the importance of the vertical upward groundwater flows in the borehole and the duration of flows, on the performance of a deep borehole repository for high-level radioactive waste.

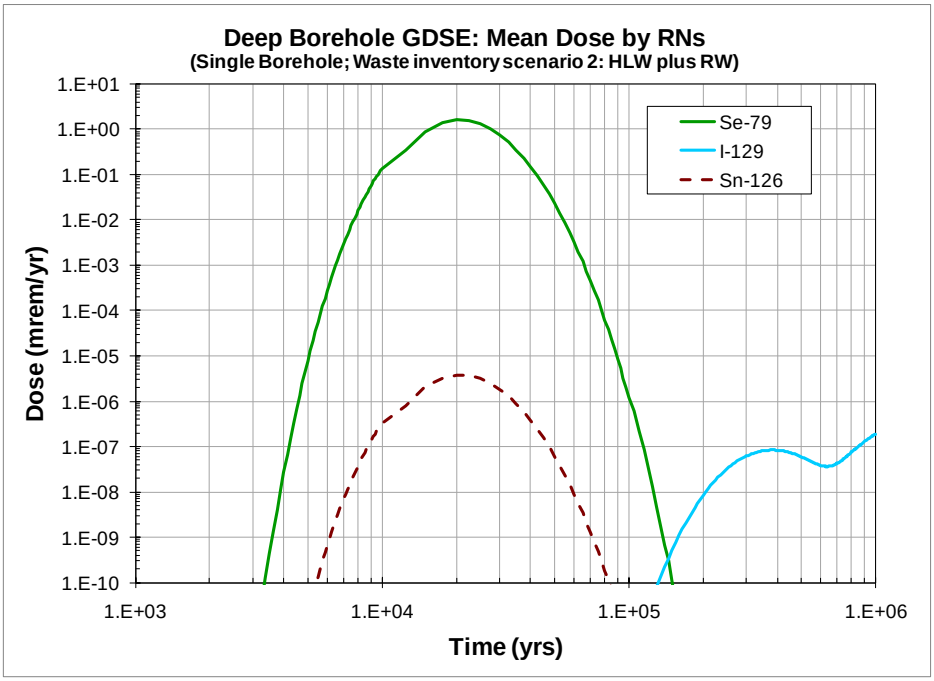

Figure 5. Mean dose by radionuclides for the waste inventory scenario 2 (DOE HLW and reprocessing HLW) for the transient water flow case of deep borehole GDSE.

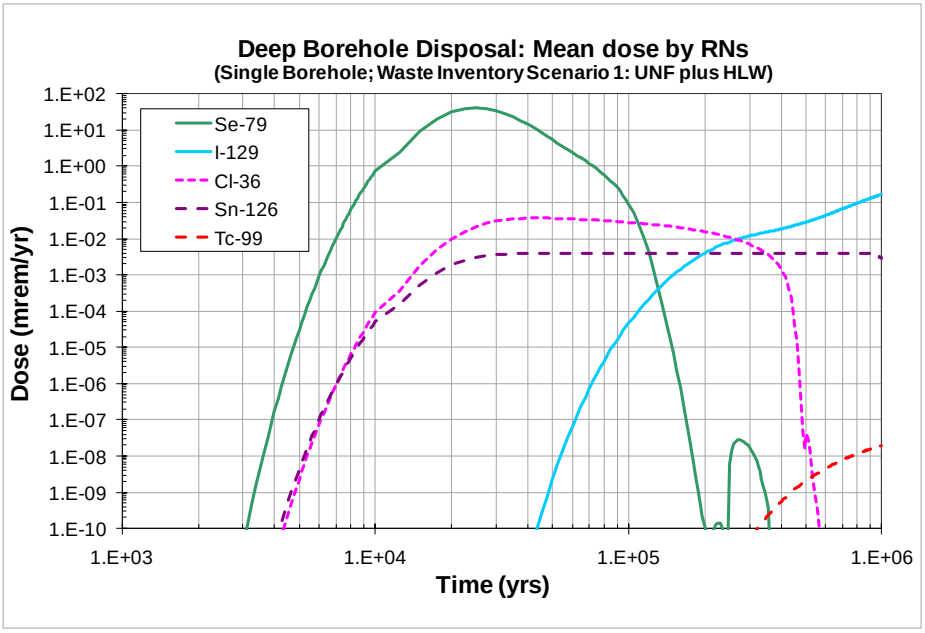

Figure 6. Mean dose by radionuclides for the waste inventory scenario 1 (commercial UNF and DOE HLW) for the continuous water flow case of deep borehole GDSE.

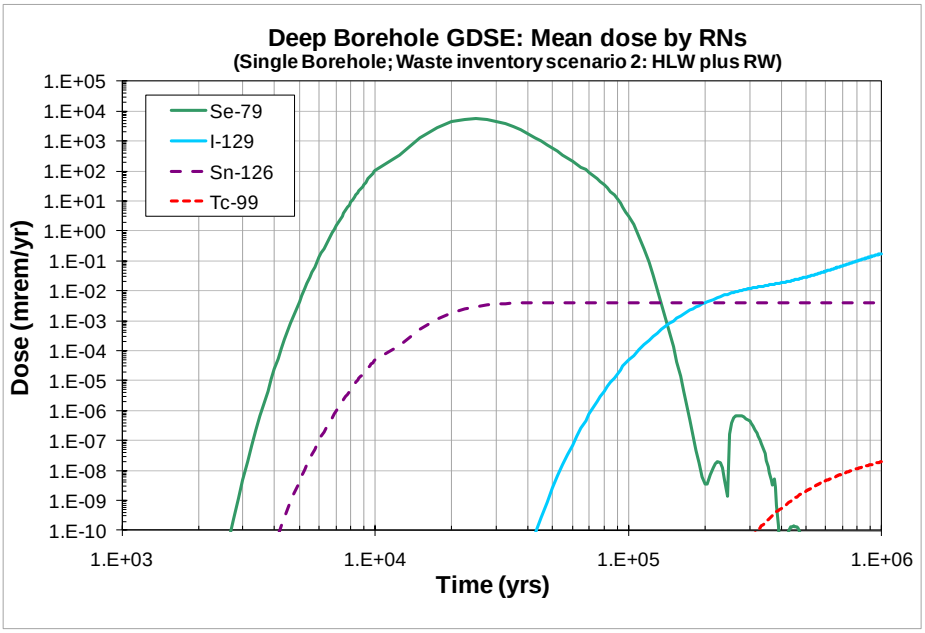

Figure 7. Mean dose by radionuclides for the waste inventory scenario 1 (DOE HLW and reprocessing HLW) for the continuous water flow case of deep borehole GDSE.

5. Summary and Discussion

This section presents an initial version of the deep borehole GDSE model and discusses the preliminary model results. The current model is the initial outcome of longer term efforts to develop a deep borehole GDSE analysis tool and needs further improvement and refinements as the study progresses. The long-term goal of the effort is to develop a highly efficient and flexible analysis tool to evaluate and address, with minimal changes, technical issues associated with different generic repository options. Although it is preliminary, the current model analysis helps to draw some important considerations for the on-going efforts to develop the deep borehole GDSE model and to evaluate the performance.

Movement of deep-seated brines in and around a deep borehole is one of the important parameters to the performance of a deep borehole repository. Brady et al. (2009) concluded no significant water movements in and around a deep borehole, except thermally driven transient water flows during the early thermal perturbation periods. In contrast, field observations and experimental studies of a deep borehole of 4km depth showed the abundance of deep-seated brines and evidence that the water saturated fracture pores in the crystalline basement are highly connected with conditions of possible advective water flow (Stober and Bucher 2005a and 2005b). Additional studies are needed for the thermal-hydrologic processes of deep-seated brines in response to the deep borehole disposal of high-level radioactive waste, including the effect of thermal-hydrologic processes of neighboring multiple boreholes.

Geochemical processes in deep borehole environments are challenging and highly uncertain. Of particular importance to the performance of a deep borehole repository are: stability and dissolution behavior of radionuclide-bearing mineral phases, sorption of radio-elements to geologic materials under conditions found in deep borehole environments including chemically reducing, high ionic strength brines at elevated temperatures. But, little data is available for the above processes and conditions. For example, a majority of the Kd values used to model the radio-element sorption in the deep borehole GDSE model are based on the ambient temperature sorption data. Additional studies and experimental work are needed to better characterize and quantify important geochemical processes in deep borehole environments.

Soluble, non-sorbing (or weakly sorbing) fission product radionuclides, particularly ^{129}I and ^{79}Se (also ^{36}Cl for commercial UNF waste), are the likely major dose contributors for a deep borehole repository. This may be true for other GDSE options as well. In the current deep borehole GDSE model, ^{79}Se is modeled as soluble and non-sorbing. However, the solubility and sorption behaviors of selenium in deep borehole geologic environments are uncertain, and improvement is needed to better characterize and quantify the chemical properties. In addition, the half-life of ^{79}Se has been reported variously ranging from 6.5×10^{4} to 1.13×10^{6} years, and the conflicting half-life data needs to be resolved.

The deep borehole GDSE model analysis has also identified the following technical issues and/or knowledge gaps to improve and enhance the confidence of future model analysis.

- Radionuclide release pathways and scenarios are important to the analysis of a generic deep borehole repository, and this may be true to any generic repository options. Additional studies are needed to update and/or improve the conceptual models for the radionuclide release pathways and scenarios that are representative of a deep borehole GDSE.
- Detailed repository thermal loading analysis is needed for the thermal-mechanical responses of deep boreholes and their effects on the hydrological and chemical processes in the deep borehole. The analysis needs to include potential interactions with the neighboring boreholes.
- Additional studies are needed to characterize and quantify the degradation process of candidate waste forms in generic deep borehole repository environments. The fractional waste form degradation rates used in the deep borehole GDSE model are based on the data for typical mined geologic repository environments. The waste form degradation process and the degradation rate in deep borehole geologic environments could be different from those for mined geologic repository environments.
- Additional studies are needed to better define and quantify the waste stream type and inventory, particularly reprocessing high-level waste. The deep borehole repository performance could be affected significantly by the waste stream type, waste inventory, and the level of waste loading in a waste form.

6. References

Åhäll, K.-I., 2006. Final Deposition of High-level Nuclear Waste in Very Deep Boreholes: An evaluation based on recent research of bedrock conditions at great depths, MKG Report 2, Swedish NGO Office of Nuclear Waste Review (MKG).

Brady, Patrick V., Arnold, Bill W., Freeze, Geoff A., Swift, Peter N., Bauer, Stephen J., Kanney, Joseph L., Rechard, Robert P., and Stein, Joshua S., 2009. *Deep Borehole Disposal of High-Level Radioactive Waste,* Sandia Report SAND2009-4401, Sandia National Laboratories, Albuquerque, NM.

Gibb, F.G.F., 1999. "High-temperature, very deep, geological disposal: a safer alternative for high-level radioactive waste?" Waste Management Vol. 19, pp. 207-211.

Gibb, F.G.F., McTaggart, N.A., Travis, K.P., Burley, D., and Hesketh, K.W., 2008. "High-density support matrices: Key to the deep borehole disposal of spent nuclear fuel," J. of Nuclear Materials, Vol. 374, pp. 370-377.

Gibb, F.G.F., Taylor, K.J., and Burakov, B.E. 2008. "The 'granite encapsulation' route to the safe disposal of Pu and other actinides," J. of Nuclear Materials, Vol. 374, pp. 364-369.

Goldsim Technology Group, 2009. "Users Guide, GoldSim Probabilistic Simulation Environment," Version 10.0.

Harrison, T. 2000. Very deep borehole: Deutag's opinion on boring, canister emplacement and retrievability, SKB Report R-0035, Swedish Nuclear Fuel and Waste Management Co.

Jiang, S.S., He, M., Diao, L.J., Guo, J.R., and Wu, S.Y., 2001. "Remeasurement of the Half-Life of 79Se with the Projectile X-Ray Detection Method," Chinese Physics Letter, Vol. 18, pp. 746-749.

Stober, I., and Bucher, K., 2005a. "Deep-Fluids: Neptune Meets Pluto," Hydrogeology Journal, Volume 13, pp. 112-115.

Stober, I., and Bucher, K., 2005b. "The upper continental crust, an aquifer and its fluid: hydaulic and chemical data from 4 km depth in fractured crystalline basement rocks at the KTB test site," Geofluids, Volume 5, pp. 8-19.

Chapter 6 Clay Generic Disposal System Environment Model: Process-Level Models

Hui-Hai Liu, Jonny Rutqvist, Liange Zheng, Eric Sonnenthal, Jim Houseworth and Jens Birkholzer

Lawrence Berkeley National Laboratory

1. Introduction

As a result of the termination of the Yucca Mountain Project, the United States Department of Energy (DOE) has started to explore various alternative avenues for the disposition of used nuclear fuel and nuclear waste. The overall scope of the investigation includes temporary storage, transportation issues, permanent disposal, various nuclear fuel types, processing alternatives, and resulting waste streams. Although geologic disposal is not the only alternative, it is still the leading candidate for permanent disposal. The realm of geologic disposal also offers a range of geologic environments that may be considered, among those clay shale formations. Figure 1-1 presents the distribution of clay/shale formations within the USA.

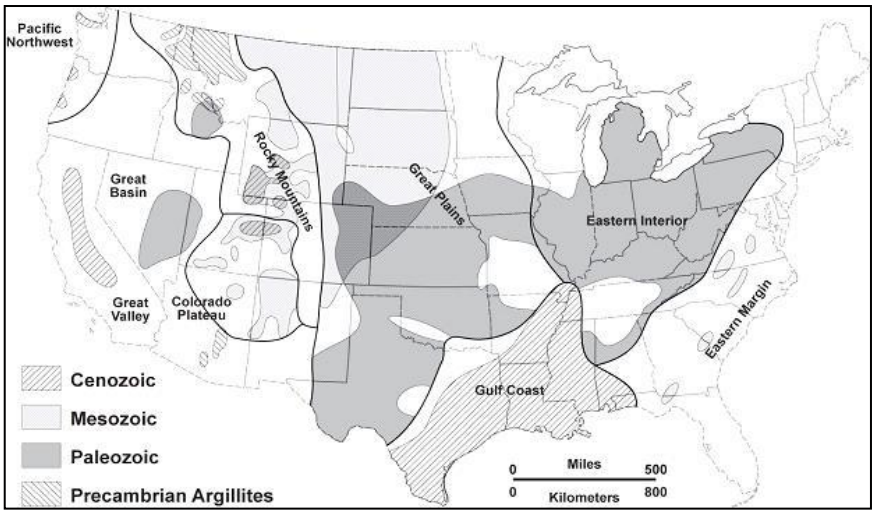

Figure 1 Clay/shale-formation distribution in the USA (Gonzales and Johnson, 1984)

Clay rock/shale has been considered as potential host rock for geological disposal of high-level nuclear waste throughout the world, because of its low permeability, low diffusion coefficient, high retention capacity for radionuclides, and capability to self-seal fractures induced by tunnel excavation. For example, Callovo-Oxfordian argillites at the Bure site, France (Fouche et al., 2004), Toarcian argillites at the Tournemire site, France (Patriarche et al., 2004), Opalinus

clay at the Mont Terri site, Switzerland (Meier et al., 2000), and Boom clay at Mol site, Belgium (Barnichon et al., 2005) have all been under intensive scientific investigations (at both field and laboratory scales) for understanding a variety of rock properties and their relations with flow and transport processes associated with geological disposal of nuclear waste.

Clay/shale formations may be generally classified as indurated and plastic clays (Tsang et al., 2005). The latter (including Boom clay) is a softer material without high cohesion; its deformation is dominantly plastic. For both clay rocks, coupled thermal, hydrological, mechanical and chemical (THMC) processes are expected to have a significant impact on the long-term safety of a clay repository. For example, the excavation-damaged zone (EDZ) near repository tunnels can modify local permeability (resulting from induced fractures), potentially leading to less confinement capability (Tsang et al., 2005). Because of clay's swelling and shrinkage behavior (depending on whether the clay is undergoing imbibition or drainage processes), fracture properties in the EDZ are quite dynamic and evolve over time as hydromechanical conditions change. Understanding and modeling of the coupled processes and their impact on repository performance is critical for the defensible performance assessment of a clay repository.

Within the Natural Barrier System (NBS) group of the Used Fuel Disposition (UFD) Campaign at DOE's Office of Nuclear Energy, LBNL's research activities have focused on understanding and modeling such coupled processes. LBNL provided a report this April on a literature survey of studies on coupled processes in clay repositories and identification of technical issues and knowledge gaps (Tsang et al., 2010). This chapter will document other LBNL research activities within the generic disposal system environment work package, including the development of constitutive relationships for elastic deformation of clay rock (Section 2), a THM modeling study (Section 3) and a THC modeling study (Section 4). The purpose of the THM and THC modeling studies is to demonstrate the current modeling capabilities in dealing with coupled processes in a potential clay repository. In Section 5, we discuss potential future R&D work based on the identified knowledge gaps. The linkage between these activities and related FEPs is presented in Section 6.

2. Constitutive Relationships for Elastic Deformation of Indurated Clay Rock

This section presents constitutive relationships for indurated clay rock and demonstrates their usefulness by comparing relevant data sets and our theoretical results. The constitutive relationships refer to relationships among hydraulic, mechanical and other properties. These relationships are the foundation for accurately modeling coupled processes. The development of constitutive relationships builds on a newly proposed stress-strain relationship for elastic deformation of fractured rock (Liu et al., 2009), as well as a concept of internal swelling stress for coal seams that can involve swelling or shrinkage during CO_2 sequestration (Liu and Rutqvist, 2010).

2.1. Stress-strain relationship

The stress-strain relationship is fundamental for modeling mechanical deformation and the associated coupled processes in porous and fractured rock. Hooke's law, an approximation

for small deformations, has been generally used to describe the stress-strain relationship for elastic mechanical processes. It states that the amount by which a material (e.g., rock) body is deformed (the strain) is linearly related to the force (stress) causing the deformation. The current application of Hooke's law to porous and fractured rock could be problematic. Strictly speaking, the proportionality in the observed stress-strain relationship should be constant if the current application of Hooke's law is to be perfectly valid. However, it is nevertheless not unusual to see studies indicating that proportionality is not always constant, but rather stress-dependent.

To more accurately model elastic deformation in rocks, Liu et al. (2009) argued that the current application of Hooke's law needs to be improved in several aspects. While the details of their methodology can be found in that paper, we give a brief introduction to their methodology here for the sake of convenience using the volumetric strain as an example (although their results can be easily extended to other types of strains). Liu et al. (2009) indicate that in Hooke's law, true strain, rather than engineering strain, should be used, except for a small degree of deformation. (The two strains will be defined later.) Assuming that a uniformly distributed force is imposed on the surface of a homogeneous and isotropic material body subject to elastic deformation, Hooke's law can be expressed as:

$$d\sigma = Kd\varepsilon_{v,t} \tag{1}$$

where σ is the hydrostatic stress (the compressive direction is positive), K is the bulk modulus, and $\varepsilon_{v,t}$ is the natural or true volumetric strain defined by:

$$d\varepsilon_{v,t} = -\frac{dV}{V} \tag{2}$$

where V is the total volume of the material body under the current state of stress. In Eqs (1) and (2), a decrease in the volume is considered to be positive. For a very small degree of deformation, the above strain can be approximated by so-called engineering strain ($\varepsilon_{v,e}$) when applying Hooke's law:

$$d\varepsilon_{v,e} = -\frac{dV}{V_0} \tag{3}$$

where V_0 is the unstressed bulk volume. When the engineering strain is employed in Hooke's law, one can obtain the following relationship by integrating Eq (3) and using the condition that $V = V_0$ for $\sigma = 0$:

$$V = V_0(1-\frac{\sigma}{K}) \tag{4}$$

Similarly, the use of natural or true strain in Hooke's law (Eq. (2)) yields:

$$V = V_0 \exp\left(-\frac{\sigma}{K}\right) \tag{5}$$

In the literature of rock mechanics, the engineering strain has been exclusively used considering that the elastic strain is generally small. Porous and fractured rock, however, differs from purely solid materials in that it is inherently heterogeneous and includes both solid phase and pores (and/or fractures) with a variety of geometric shapes. While elastic strain is indeed small in most of the rock volume for stress changes of practical interest, the strain can be considerably larger within some portions of a rock body. For example, some pores (or fractures) in a rock can be subject to significant deformation, and may even completely close under a certain range of stress changes encountered in practice. For these pores, the strain is not small (on the order of one). An accurate description of the deformation of this portion of the rock is important for coupled mechanical and hydrological processes, because fluid flow occurs in these pores and fractures. To deal with this issue, Liu et al. (2009) conceptualize the heterogeneous rock as having two parts, a so called soft part and hard part. Only in the hard part can true strain be approximated by engineering strain. This conceptualization can be represented by a hypothesized composite spring system shown in Fig 1. Following Liu et al. (2009), we use subscripts *0, e*, and *t* to denote the unstressed state, the hard part (where engineering-strain-based Hooke's law applies) and the soft part (where natural or true-strain-based Hooke's law must be used), respectively. Then we have:

$$V_0 = V_{0,e} + V_{0,t} \tag{6}$$

and

$$dV = dV_e + dV_t \tag{7}$$

Applying Eqs (4) and (5) to rock volumes V_e and V_t, respectively, in Eq (7) yields:

$$-\frac{dV}{V_0} = \gamma_e \frac{d\sigma}{K_e} + \gamma_t \exp\left(-\frac{\sigma}{K_t}\right)\frac{d\sigma}{K_t} \tag{8}$$

$$\gamma_t = \frac{V_{0,t}}{V_0} \tag{9}$$

$$\gamma_e = 1 - \gamma_t \tag{10}$$

where K_e and K_t refer to bulk moduli for the hard and soft parts, respectively. The parameters γ_e and γ_t are volumetric portions of hard and soft parts under unstressed conditions. Eqs (8)-(10) together comprise the stress-strain relationship proposed by Liu et al. (2009). From that stress-strain relationship (Eq (8)), the bulk modulus $K = -V_0 \frac{d\sigma}{dV}$ is given by

$$K = \frac{1}{\frac{\gamma_e}{K_e} + \frac{\gamma_t}{K_t}\exp\left(-\frac{\sigma}{K_t}\right)}. \qquad (11)$$

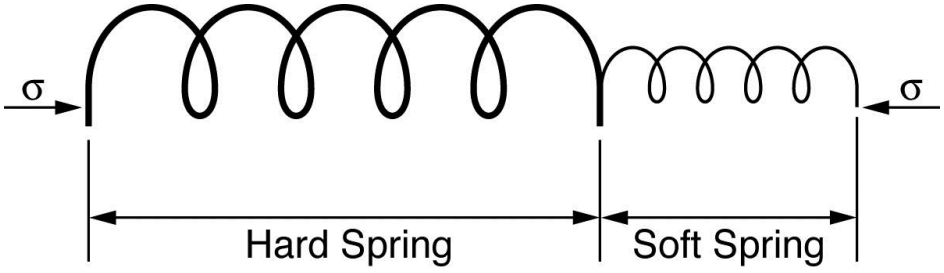

Figure 1. A composite spring system consisting of two springs. The hard and soft springs follow engineering-strain-based and true-strain-based Hooke's law, respectively (Liu et al., 2009).

The validity of the above equation was presented in Liu et al. (2009) for several sandstones. Based on laboratory measurements, Corkum and Martin (2007b) developed an empirical relation for describing the stress dependence of Young's modulus in Opalinus clay. Corkum and Martin (2007a) then performed modeling studies of a mine-by test at the Mont Terri site, Switzerland, and found that a significant portion of the short-term behavior within the damaged zone can be captured using the empirical relation for Opalinus Clay. As a matter of fact, a theoretical relation for such stress dependence is given in Eq (11). We will use the data from Corkum and Martin (2007b) to verify Eq (11).

2.2.Stress-dependent hydraulic properties

Porosity (or aperture for fractures) and permeability are the main stress-dependent hydraulic properties used as key inputs into a coupled hydro-mechanical model.

Rock Porosity: Using definition of rock porosity (ϕ) and using similar notions from Section 2.1, we have:

$$d\phi = \frac{dV^p}{V} = \frac{dV_e^{\,p} + dV_t}{V} \qquad (12)$$

where V is the bulk volume of porous rock and superscript p refers to pores. (Note that the above equation ignores the effect of V change with stress on porosity change.) For most practical applications of rock mechanics, V can be approximated by the unstressed volume V_0 for calculating rock porosity. By definition of different volumes, we also have:

$$V_0^{\,p} = V_{0,e}^{\,p} + V_{0,t} \tag{13}$$

$$V^{p} = V_e^{\,P} + V_t \tag{14}$$

Note that in the above two equations, we consider V_t to be a portion of pore volume in a rock body. Following the same procedure used to derive Eqs (3) and (4), we obtain:

$$dV_e^{\,p} = -C_e V_{0,e}^{\,p} d\sigma \tag{15}$$

where C_e is compressibility for the hard part.

$$dV_t = -\frac{V_{0,t}}{K_t}\exp\left(-\frac{\sigma}{K_t}\right)d\sigma \tag{16}$$

Combining Eqs (12), (15) and (16) yields:

$$d\phi = -\phi_e C_e d\sigma - \frac{\gamma_t}{K_t}\exp\left(-\frac{\sigma}{K_t}\right)d\sigma \tag{17}$$

where

$$\phi_e = \phi_0 - \gamma_t\,. \tag{18}$$

Integrating Eq (24) and using $\phi = \phi_0$ for $\sigma = 0$ gives (Liu et al. 2009):

$$\phi = \phi_e(1 - C_e\sigma) + \gamma_t \exp\left(\frac{\sigma}{K_t}\right)\,. \tag{19}$$

where C_e is the compressibility for the hard fraction of pore volume. This treatment is based on our argument that the entire soft part corresponds to some fraction of pore volume. Once porosity is known, permeability for a rock matrix can be estimated based on relationships between permeability and porosity. Eq (19) was validated using data from sandstones (Liu et al., 2009). At this point, measured porosity as a function of stress seems not to be available yet for clay rock considered for hosting a geological repository of nuclear waste. However, Eq (19) was derived from Eq (8), and the verification of the latter may be considered as indirect verification of the former.

Fracture aperture and permeability: In this subsection, we present a formula for the dependence of fracture aperture on normal stress based on the stress-strain relationship given in Section 2.1. Consider a fracture to be embedded into a rock sample subject to normal stress σ_n.

We again divide fracture space into "hard" and "soft" parts along the direction normal to the fracture plane. Then, the volumetrically averaged fracture aperture (b) is given by:

$$b_0 = b_{0,e} + b_{0,t} \tag{20}$$

under unstressed conditions, and

$$b = b_e + b_t \tag{21}$$

under stressed conditions. Similar to previous sections, subscripts *e* and *t* (for "engineering" and "true," respectively) refer to the "hard" and "soft" parts in a fracture. Hooke's law for the two parts can be expressed by:

$$d\sigma_n = -K_{F,e}\frac{db_e}{b_{0,e}} \tag{22}$$

$$d\sigma_n = -K_{F,t}\frac{db_t}{b_t} \tag{23}$$

where subscript F refers to the fracture. (For convenience, the volumetric strain will not be used here.) Note that the stress in the above two equations refers to far-field normal stress, rather than local stress.

Combining Eqs (22) and (23) gives:

$$db = db_e + db_t = -b_{0,e}\frac{d\sigma_n}{K_{F,e}} - b_t\frac{d\sigma_n}{K_{F,t}}. \tag{24}$$

Integrating the above equation and using Eq (20) and the following relationship obtained from Eq (2-23):

$$b_t = b_{0,t}\exp\left(-\frac{\sigma_n}{K_{F,t}}\right) \tag{25}$$

one arrives at (Liu et al. 2009):

$$b = b_{0,e}(1-\frac{\sigma_n}{K_{F,e}}) + b_{0,t}\exp\left(-\frac{\sigma_n}{K_{F,t}}\right) \tag{26}$$

Because fracture permeability is proportional to the cube of fracture aperture, the fracture permeability k is given by:

$$\left(\frac{k}{k_0}\right)^{1/3} = \frac{b_{0,e}}{b_0}\left(1-\frac{\sigma_n}{K_{F,e}}\right) + \frac{b_{0,t}}{b_0}\exp\left(-\frac{\sigma_n}{K_{F,t}}\right) \quad (27)$$

where k_0 is the permeability corresponding to b_0.

$$\left(\frac{k}{k_0}\right)^{1/3} = \exp\left(-\frac{\sigma_n}{K_{F,t}}\right) \quad (28)$$

The above equation essentially assumes that the entire fracture aperture is "soft." Given the fact that clay rock is generally viewed as soft rock, it seems logical to use Eq (28) for fractures in clay rock. This is supported by a number of laboratory measurements that show linear relationships between the log of measured fracture permeability and stress (e.g., Blumling et al., 2007; Zhang and Rothfuchs, 2008; Popp et al., 2008). However, data reported by Jobmann et al. (2010) seem to indicate that permeability relationships are better represented by a curve similar to that with $b_r > 0$. For simplicity, we focus on Eq (28), which seems to be reasonable for most clay studies reported in the literature, while Eq (27) may be employed for more general cases.

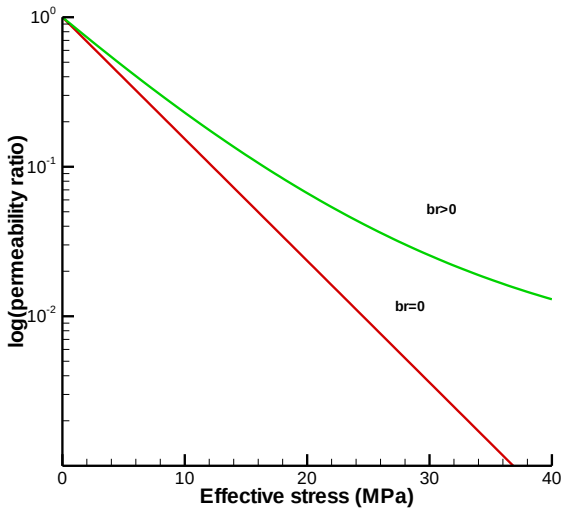

Figure 2. Log of fracture permeability as a function of stress (Eq (27)). The br denotes the first term on the right hand side of Eq (27).

2.3.Effective stress for fractures involving rock swelling

In all the above discussions, stress refers to effective stress. It is relatively straightforward to deal with the effective stress for clay rock matrix involving swelling. The treatment is

essentially the same as handling volume changes in the rock matrix owing to temperature changes (e.g., Jaeger et al., 2007). However, some special consideration needs to be given to fractures when swelling processes are involved. To do so, the same methodology developed for estimating coal permeability is adopted here (Liu et al., 2010). Coal will swell when absorbing CO_2 during the CO_2 geological sequestration.

Based on Biot's theory, the effective stress is defined as (Jaeger et al., 2007):

$$\sigma = \sigma_t - \alpha P \tag{29}$$

where σ_t is total stress, P is fluid pressure, and α is Biot's coefficient. Note that compressive stress is here considered positive. Following previous studies (e.g., Gray, 1987; Shi et al., 2004), the Biot's coefficient is considered to be one in this study, although our theoretical development allows for arbitrary coefficient values.

For clay rock containing an infinite fracture (generally assumed for modeling flow and transport in fractured rock), matrix swelling will not affect fracture permeability under the constant confining (total) stress conditions commonly used in laboratory measurements. This occurs because the effective stress defined in Eq. (29) is independent of the matrix swelling as a result of the complete separation between matrix blocks coursed by through-going fractures. In this case, for a given pressure P, the swelling will result in increasing fracture spacing rather than changes in fracture aperture.

In reality, clay matrix blocks are not completely separated from each other by fractures. Figure 3 shows a simplified horizontal cross section of a clay rock with two adjacent vertical fractures, separated by a clay-matrix "bridge" that connects matrix blocks on the different sides of fractures. During matrix swelling, fractures are compressed, because they are weak and soft structures within the rock, and therefore an additional force (corresponding to stress σ_I) will be imposed on the fractures. At the same time, the matrix bridge is subject to an additional force in the opposite direction to σ_I. If these two forces are completely balanced, fractures will be subject to this additional stress σ_I, while confining stress remains unchanged. Because this stress largely results from internal structures (or the connectivity of matrix blocks) within clay rock and can be internally balanced under constant confining stress conditions, it is called "internal swelling stress". In this case, the effective stress for fractures should be given as:

$$\sigma = \sigma_t - \alpha P + \sigma_I \tag{30}$$

Note that σ_I is positive for matrix swelling and negative for matrix shrinkage. The concept of "internal swelling stress" was first put forward by Liu and Rutqvist (2010) who derived a similar effective stress equation for coal seams associated with swelling.

The concept of internal swelling stress implies that coal-matrix strain resulting from swelling (ε_s) can be divided into two parts:

$$\varepsilon_s = \varepsilon_{sB} + \varepsilon_{sI} \tag{31}$$

where ε_{sI} is the strain corresponding to the internal swelling stress, and ε_{sB} is the strain contributing to the bulk strain in fractured clay generally measured in the laboratory. It is ε_{sI} (a portion of ε_s) that results in fracture permeability (or aperture) changes under constant confining stress conditions.

The relationship between ε_s and ε_{sI} may be a complex function of matrix block connectivity within clay rock and other relevant factors. As a first approximation, following Liu and Rutqvist (2010), we assume the ratio between the two strains to be a constant:

$$\varepsilon_{sI} \approx f\varepsilon_s \tag{32}$$

where f is a value between zero and one and determined from measurements. This treatment will be evaluated against laboratory test results below—we acknowledge that more studies may be needed to develop more rigorous relationships between f and other properties in the future. Based on Hooke's law, σ_I can be related to swelling strain by:

$$\sigma_I = f\varepsilon_s K_M \tag{33}$$

where K_M is the bulk modulus for clay matrix and can be stress dependent (Eq. 11).

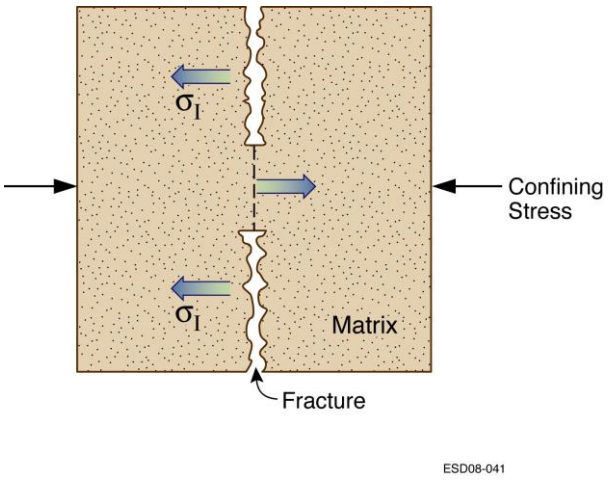

Figure 3. A schematic description of internal swelling stress (Liu et al., 2010). The arrows correspond to stresses imposed on the left part of the rock as a result of swelling.

2.4.Data Analyses

Some key constitutive relationships for elastic deformation of clay rock are presented in the above sections. The current section will demonstrate the validity of these relationships by comparing the theoretical results with selected laboratory measurements, with a focus on

examining whether the constitutive relationships can satisfactorily match the observations and explain the related processes.

Stress-Strain data of Opalinus clay: Corkum and Martin (2007) reported comprehensive laboratory measurements for the mechanical behavior of Opalinus clay (with a water content of 6.1%) at low stress. The low-stress behavior is of interest because it is closely associated with unloading around tunnels and the resultant excavation damaged zone. A number of uniaxial and triaxial compression tests were performed, indicating significant nonlinear elastic deformation in the low stress region. Cokum and Martin (2007) suggest that the nonlinear behavior can be explained from clay's micro-structure, associated with diagenetic processes over the last 180 million years.

We use uniaxial test results to verify our stress-strain relation (Eq. 11). To do so, we need to replace volumetric strain with axial strain, and bulk modulus (*K*) with the corresponding Young's modulus (*E*) in Eq (11). The test results are given as axial stress as a function of axial strain (Fig. 4). To avoid (as much as possible) the non-uniqueness of parameter values determined from curve fitting, we use a simple procedure to estimate parameter values from porosity versus confining pressure data. As shown in Figure 4, measured relations between stress and strain are very well represented by a straight line for relatively high stresses. The slope of the straight line is used to determine $\frac{E_e}{\gamma_e}$ because the second term in the denominator of Eq (11) is negligible for high stress values. The strain value at the intersection between the straight line and the strain axis in Figure 4 gives the γ_t value, considering that the straight line represents the first term in the denominator of Eq (11). The above procedure allows for direct determination of values for E_e , γ_e , and γ_t. The remaining parameter, E_t, can be estimated using a data point at relatively low pressures. As indicated in Fig 4, the data are in excellent agreement with our theoretical results for samples BRA 2-2A, BRA 1-3A and BRA 1-3B. These samples are taken from boreholes BRA-1 and BRA-2 drilled at the Mont Terri site, Switzerland. Fitted parameter values are given in Table 1.

Table 1. Fitted mechanical parameters for Opalinus clay

Rock Sample	γ_t (%)	E_e (MPa)	E_t (MPa)
BRA 2-2A	0.22	2494.5	0.22
BRA 1-3A	0.13	2596.6	0.38
BRA 1-3B	0.08	3097.6	0.65

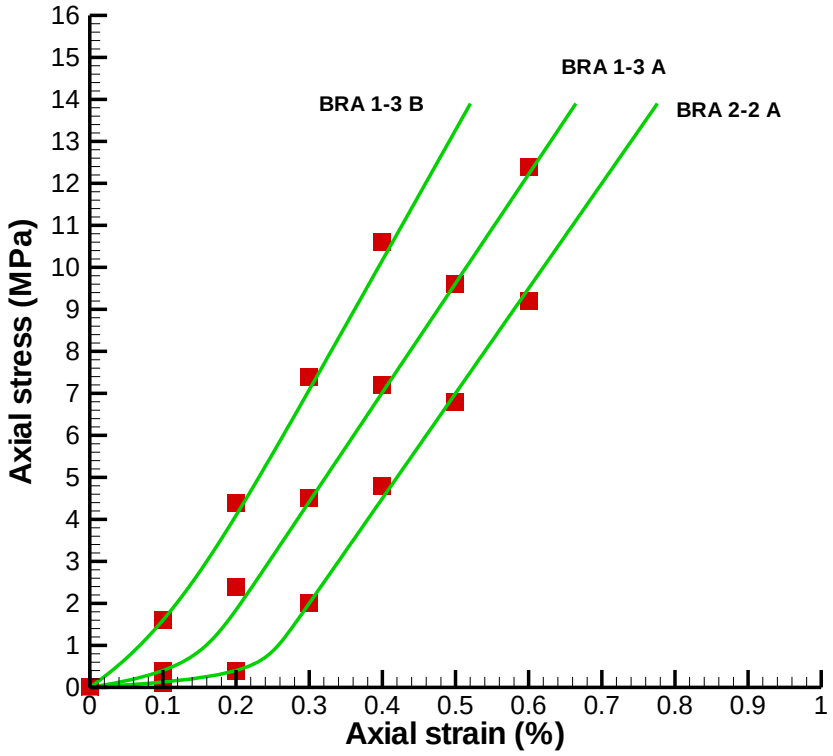

Figure 2-4. Comparison between laboratory measurements and values calculated using Eq (2-11) in which volumetric strain and a bulk modulus (K) need to be replaced with axial strain and the corresponding Young's modulus (E), respectively. The data points are measurements (Corkum and Martin, 2007) and the solid curves are theoretical results.

Water permeability measurements for a macro-cracked argillite sample: Recently, Davy et al. (2007) reported on laboratory measurements of single fractures within macro-cracked Callovo-Oxfordian argillite samples subject to both confinement and water-induced swelling. The data set provides a unique opportunity to examine our formulations for estimating fracture permeability as a function of effective stress that considers the effects of swelling.

For water permeability tests, the experimental procedure was designed so as to apply an initial, continuous fluid flow through the fracture, and then to superimpose an additional pulse flow for permeability measurements made at each confining pressure level, either right after loading or after several hours at a given confining pressure (the total stress), or right after unloading. For all of the tests, visual a posteriori inspection of water permeability samples showed very limited water penetration in the argillite sample bulk. Fig. 5 shows the test procedure in terms of changes in confining pressure and fracture closure for Sample 2 (Davy et

al., 2007). Although water permeability measurements were provided for two samples (samples 2 and 5) in Davy et al. (2007), we will analyze test results for Sample 2 only in this study, because Sample 2 is subject to a more complex test procedure (Fig 5). For a given confining pressure, the fracture closure increases from point 1 to 2, which cannot be explained based on elastic deformation and is very likely due to water-induced plastic deformation at the beginning of the test. Therefore, our analysis will focus on data points after Point 2. We also assume elastic deformation in that data range—mainly justified by the fact that our analysis based on the elastic deformation seems to be able to explain the majority of experimental observations. Also note that our Fig 5 is identical to Fig 10(b) in Davy et al. (2007), except that we renumbered the chronological order of points such that they are consistent with those in figure 12 of Davy et al. (2007), which presents fracture permeability as a function of confining pressure (Catherine A. Davy, Personal communication).

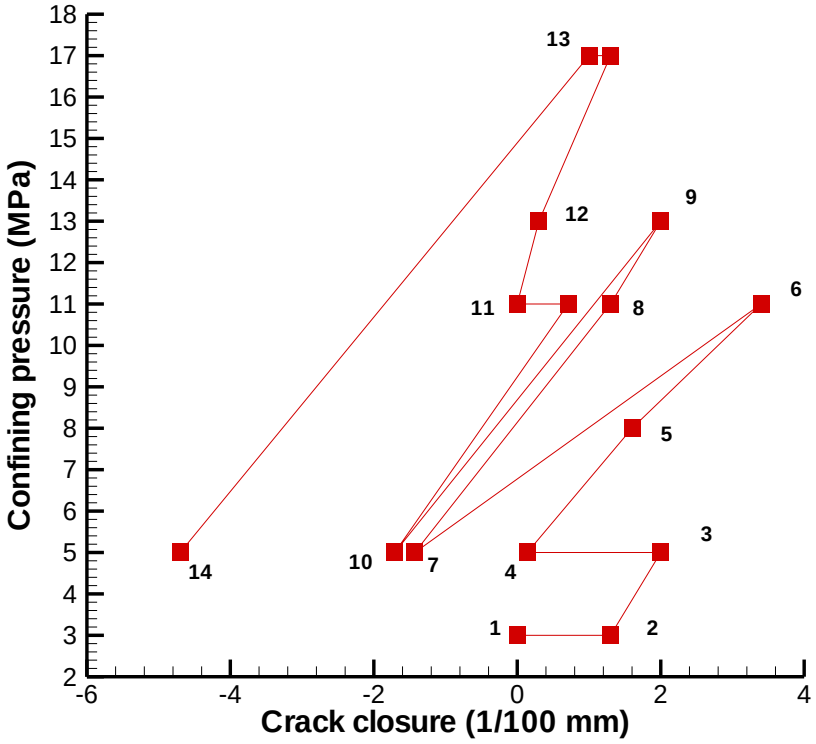

Figure 5. Test procedure of water permeability measurement (in terms of confining pressure and fracture [crack] closure) for sample 2 of Davy et al. (2007). The numbers in the figure indicate the chronological order of points (Catherine A. Davy, Personal communication).

In Fig 5, points 3, 4, 7, 10 and 14 correspond to the same confining pressure but with different amounts of swelling (measured as difference in crack closure between a given point and Point 3). We believe that it is largely due to the transient behavior of water flow from fractures into the rock matrix. A longer time corresponds to a larger water penetration depth into the rock matrix near the fracture, and therefore to a larger rock volume involving swelling. Note that during the water permeability measurement, water was injected into the fracture. For simplicity, we assume that water penetration depth as a function of time can be described by the well-known infiltration theory developed by Philip (1957). Under ponding conditions on the ground surface, Philip's theory indicates that the cumulative amount of water infiltrating into unsaturated soil

with a uniform initial water saturation is proportional to the square root of time. Consequently, if we view the fracture wall as the ground surface, then approximate the water penetration depth by the amount of accumulative infiltrating water (in depth) divided by the difference between saturated and initial water contents, and further assume that swelling within the water-penetrating zone is uniform and occurs simultaneously once water content is increased, then the total swelling, S, will be proportional to water penetration depth, or:

$$S = At^{1/2} \tag{34}$$

where A is a constant herein. The above equation (with A = 3.08E-2 mm/d$^{-1/2}$) seems to fit observed swelling for Points 3, 4, 7, 10, and 14 (corresponding to different times) satisfactorily (Fig 6), indicating that our above reasoning is justified. Note that the observed crack-closure value in Davy et al. (2007) is a combination of rock swelling and the corresponding change in fracture aperture. However, as a result of the low water permeability of fracture, the fracture aperture value (estimated from cubic law) is negligibly small, only on the order of 1E-3 mm. Therefore, in this study, the swelling is approximated by the observed crack closure.

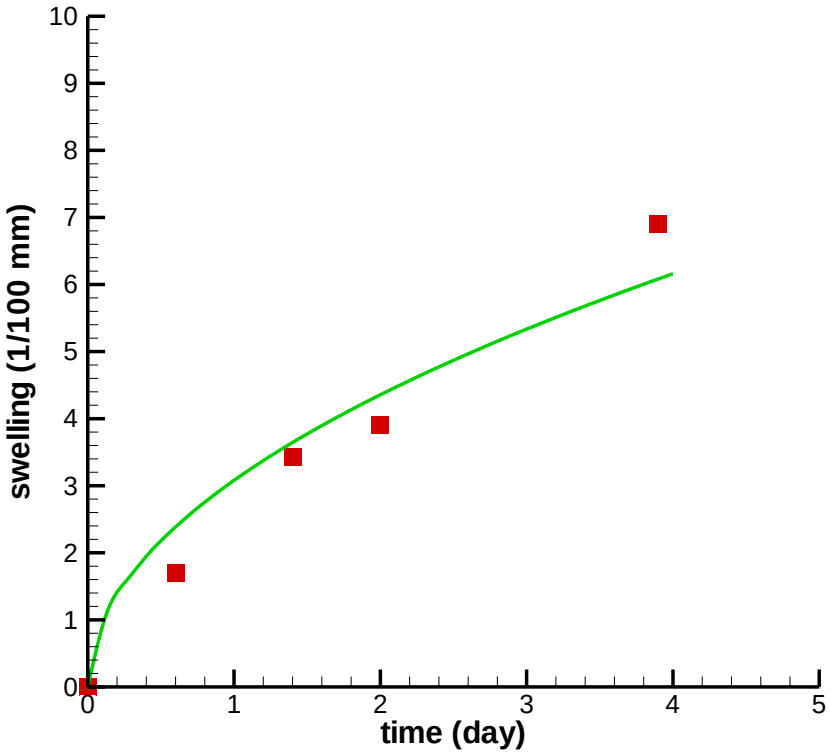

Figure 6. Comparison of observed swellings for points (3, 4, 7, 10, and 14) with those calculated from Eq (2-34) (solid curve). The fitted A value is 0.68 d-1/2.

When confining and pore pressures are constant, fracture permeability purely due to swelling may be obtained from Eqs (2-28) and (2-30) and given as:

$$\left(\frac{k}{k_3}\right)^{1/3} = \exp\left(-\frac{\Delta\sigma_I}{K_{F,t}}\right) \tag{35}$$

where k_3 is the permeability at Point 3 and $\Delta\sigma_I$ is the difference in internal swelling pressure between a given point and Point 3. Using the definition of the internal swelling stress (Eq. 32) together with Eq. (34), the difference in internal swelling pressure is given as:

$$\Delta\sigma_I = f\varepsilon_s K_M = fK_M \frac{S}{L} = \left(\frac{fK_M A}{LK_{F,t}}\right) K_{F,t} t^{1/2} = BK_{F,t} t^{1/2} \tag{36}$$

where L is fracture spacing (approximated by the rock-sample's radius in Davy et al. (2007)), and *B* is a constant. Combining Eqs. (35) and (36) yields:

$$\left(\frac{k}{k_3}\right)^{1/3} = \exp\left(-Bt^{1/2}\right) \tag{37}$$

Again, Eq. (37) fits the observations fairly well.

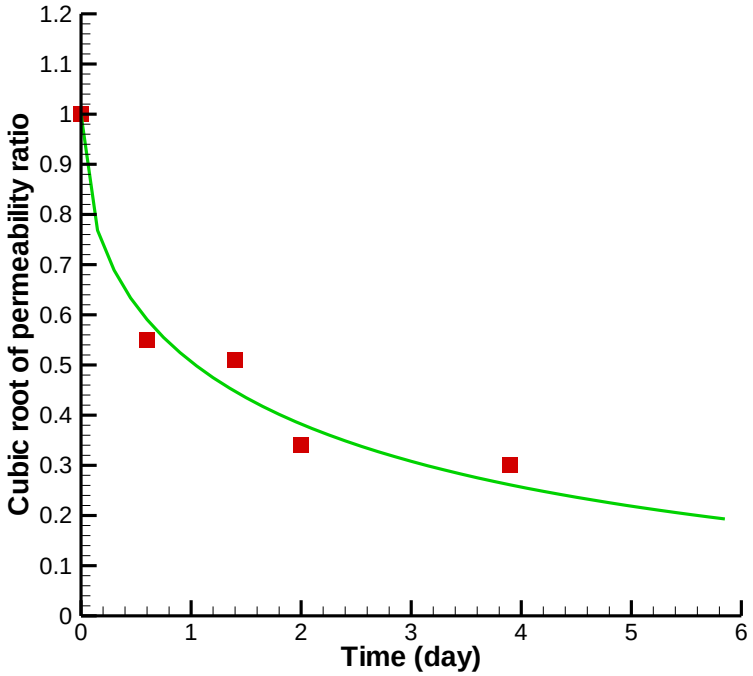

Figure 7. Match between observed values for (k/k3)1/3 for points (3, 4, 7, 10 and 14) with those calculated from Eq. (37) (solid curve).

Eq. (37) is applicable only when confining pressure (or total stress) and the pore pressure of water in the fracture is constant. In this study, we assume that pore pressure changes can be ignored compared to the much larger changes in confining pressure in the water permeability experiments of Davy et al. (2007). This can be justified by the observation that fracture permeability changes are mainly determined by confining pressure and swelling (Davy et al., 2007). In this case, a more general permeability relationship (that considers the effects of both confining pressure and swelling) can be obtained by combing Eqs (28), (30) and (37):

$$\left(\frac{k}{k_3}\right)^{1/3} = \exp\left(-\frac{\Delta\sigma_t}{K_{F,t}} - Bt^{1/2}\right) \tag{38}$$

The only unknown in the above equation is $K_{F,t}$ which can be estimated from the permeability data as a function of both confining pressure and time (Davy et al., 2007). We are especially interested in whether Eq. (38) is sufficient to represent the data. The estimated (or fitted) K_F is 16 MPa. Fig 8 shows a comparison between measured and estimated permeability values as a function of time. Note that for a given time in Fig 8, there are two data points corresponding to the observed and estimated values, respectively. Given the complexity of the experimental processes, the comparison is remarkable, supporting the validity of the relevant constitutive relationships. To further examine the usefulness of our generalized effective stress (Section 2.3), Fig 9 shows $(k/k_3)^{1/3}$ as a function of difference of effective stress (between a given point and Point #3) calculated by:

$$\Delta\sigma = \Delta\sigma_t + \Delta\sigma_I = \Delta\sigma_t + K_{F,t}Bt^{1/2} \tag{39}$$

Based on Eqs (27) and (29), the log of $(k/k_3)^{1/3}$ is a linear function of the difference in effective stress given in the above equation. Again, the data supports our theoretical results, as shown in Fig 9.

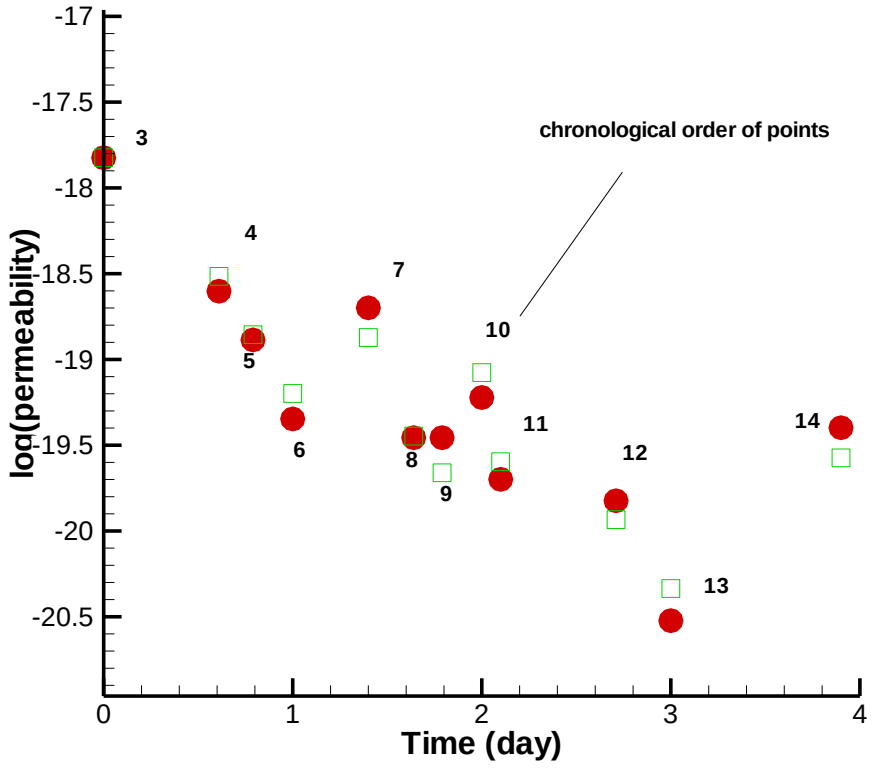

Figure 8. Comparisons between observed and simulated fracture permeability changes as a function of time. The solid circles are measurements.

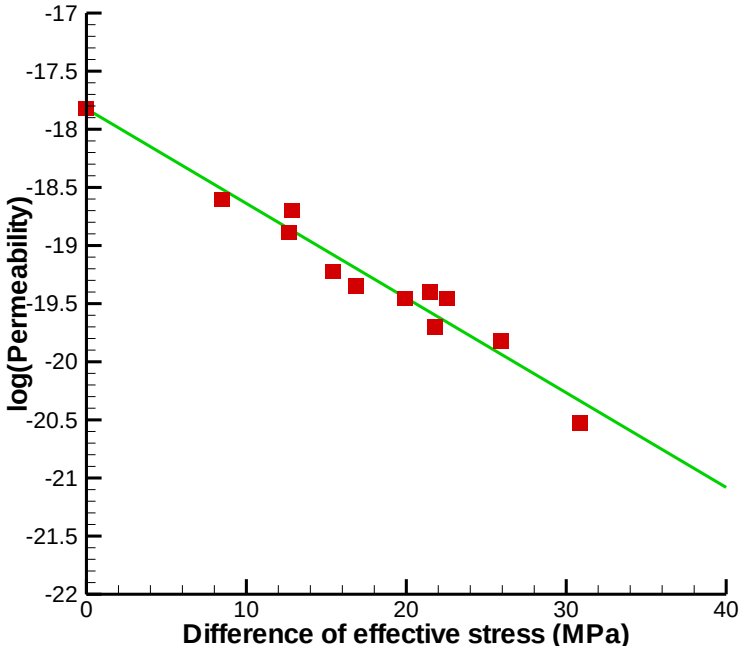

Figure 9. Comparisons between observed and simulated relationships between log of permeability and the difference in effective stress defined in Eq (39). The data points are measurements.

Finally, it is important to indicate that we ignore creeping processes in our data analysis, based on the consideration that permeability changes due to creeping are not expected to be significant in the experiments of Davy et al. (2007). For example, the laboratory experiments of Jobmann et al. (2010) showed that over about 5 days, fracture permeability was reduced by 20% only for Opalinus clay. This permeability change is much smaller than those observed in the experiments of Davy et al. (2007) (Figure 8), although Opalinus clay is softer than the Callovo-Oxfordian argillite rock studied in Davy et al. (2007) and therefore subject to a larger degree of creeping.

2.5.Summary and Directions of Future Research

In this study, we proposed several important constitutive relationships for indurated clay rock. This work is based on three recently developed concepts (or theories). First, when applying Hooke's law in clay rocks, true strain (rock volume change divided by the current rock volume), rather than engineering strain (rock volume change divided by unstressed rock volume), should be used, except when the degree of deformation is very small. In the latter case, the two strains will be practically identical. Second, because of its inherent heterogeneity, clay rock can be divided into two parts, a hard part and a soft part, with the hard part subject to a relatively small degree of deformation compared to the soft part. Third, for swelling rock like clay, the effective stress needs to be generalized to include an additional term resulting from the swelling process. To evaluate our theoretical development, we analyzed uniaxial test data for core samples of Opalinus clay and laboratory measurements of single fractures within macro-cracked Callovo-Oxfordian argillite samples subject to both confinement and water-reduced swelling. The focus of this was to test whether our constitutive relationships can adequately represent the data and explain the related observations. Given the nonlinearity and complexity shown in the data, the agreement between our theoretical results and data is remarkably reasonable, supporting the validity of our proposed constitutive relationships.

The results of this preliminary research leads to the following important outstanding questions which will need to be addressed in FY11 and beyond:

- What modifications to Hooke's law are required for anisotropic stress conditions?
- How can we include the effects of moisture-dependent mechanical properties?
- What are generalized constitutive relationships when damage and plastic deformation are important?
- How can we deal with constitutive relationships for rock mass in EDZ that includes both fractures and matrix?
- How can we incorporate effects of chemical and thermal processes on swelling?

In future studies, the development of constitutive relationships will also be integrated with numerical simulations of coupled processes.

3. THM Modeling in Clay/Shale Environments

This section provides a review of current LBNL modeling capabilities available for studying coupled THMC processes and reactive transport in clay/shale host rock materials. This

review intends to help plan UFD modeling activities with the current existing capabilities and also to help identify needs to improve these capabilities for future research activities.

3.1.Modeling Tools for Coupled THM processes

For the past decade, LBNL has been active in the development and application of coupled thermal-hydrological-mechanical (THM) modeling of bentonite-clay and rock systems associated with geological disposal of spent nuclear fuel. As part of this effort, LBNL has since 1992 been involved as a research team in the international collaborative project DECOVALEX (Development of COupled Models and their VALidation against EXperiments in nuclear waste isolation). The modeling of THM processes in expansive (swelling) clay used as a buffer in most current disposal concepts in Europe, Asia and Canada, has been conducted using LBNL's ROCMAS finite element code. More recently, through the work within the Yucca Mountain Project, LBNL has developed an alternative model called TOUGH-FLAC, which is based on linking LBNL's TOUGH family multiphase flow codes to the commercial FLAC^{3D} geomechanical code. The development of the ROCMAS and TOUGH-FLAC has always been driven by needs for solving field-scale, multiyear *in situ* experiments of EBS and rock systems, including

1) The Kamaishi Mine heater test, Japan
2) The FEBEX *in situ* experiment at the Grimsel Test Site, Switzerland
3) The Drift Scale Test at Yucca Mountain, Nevada
4) The Tunnel Sealing Experiment (TSX) at URL Canada
5) The French Tournemire site in indurate clay.

A large number of Bench Mark Tests (BMTs) have been simulated, focusing on long-term coupled THM processes, both in the near field and EBS of multiple-barrier nuclear waste repositories and in the surrounding rocks. These cases include ROCMAS and TOUGH-FLAC modeling of:

1) The Japanese H12 repository design with vertical deposition holes.
2) The proposed high-level nuclear waste repository in Sweden for the KBS-3 concept.
3) The Canadian conceptual design for a repository in granite with horizontal deposition tunnels.
4) The Spanish EBS system emplaced in granite with horizontal deposition tunnels.

Moreover, a large number of laboratory experiments have been simulated for model validation as well as for calibration of coupled THM properties.

ROCMAS Code: The ROCMAS code (ROCk Mass Analysis Scheme) is a finite-element code for analysis of coupled THM processes in saturated-unsaturated fractured porous media. It has been gradually developed and extended since the early 1980s, headed by J. Noorishad at the LBNL. A hydromechanical formulation for fractured rock, based on Biot's general effective stress theory (Biot, 1941), was first developed, and a nonisothermal version of ROCMAS was presented in Noorishad et al., (1984). While at the time numerical models existed for coupled THM processes in porous media, the ROCMAS code was probably the first for fractured rocks to

include discrete fractures with non-linear coupled hydraulic and geomechanical behavior. The formulation was further extended from fully saturated to partially saturated media by Noorishad and Tsang (1996) and thereafter in Rutqvist et al. (2001), completing the formulation regarding the heat equation and effects of grain compressibility implemented into a full three-dimensional version.

In ROCMAS, the formulation of coupled thermo-hydroelasticity in terms of Biot's theory of consolidation (Biot, 1941) is extended to partially saturated media through Philip and de Vries' (1957) theory for heat and moisture flow in soil. In this theory, three phases (solid, liquid, and gas) are present. However, it is assumed that the gas pressure P_g is constant and equal to atmospheric pressure throughout the porous medium. As a consequence, vapor transport occurs only through molecular diffusion driven by a gradient in vapor concentration (density), while advection of vapor with bulk gas flow is neglected. The vapor density in the medium is governed by Kelvin's relation, assuming thermodynamic equilibrium for pore liquid in contact with its vapor, and phase transitions occur as evaporation-condensation processes. During heat transfer, coexisting fluid and solid components are assumed to be in local thermal equilibrium (i.e., locally they are at the same temperature). The mechanical behavior of the porous media consists of the gas, liquid and solid-matter responses to local pressure and the overall material (skeleton) response to effective stresses. Fractures are treated as a "porous medium" separate from the rock matrix and would be discretely defined by special fracture elements in a finite-element mesh. Therefore, the basic balance equations are the same for rock matrix and fracture materials, while some of the constitutive relations differ. With this approach and these assumptions, three balance equations—water mass balance, energy conservation and linear momentum balance—and a number of constitutive relations are required for a full description of the THM state. The ROCMAS code includes various versions of constitutive geomechanical models for solid rocks, soils and discrete fractures including (Noorishad and Tsang, 1996):

- Linear elastic solid
- Associated and non-associated strain softening/hardening elastoplastic continuum
- Sandler/DeMaggio cap plasticity
- Oriented plasticity
- Compressible, dilating and strain softening elasto-plastic joints
- No tension continuum

The cap plasticity model may be applied to unconsolidated clay to model pore-collapse in addition to shear failure.

TOUGH-FLAC Simulator: The TOUGH-FLAC was developed as a pragmatic approach for modeling coupled multiphase flow, heat transport and geomechanics, by linking the two established codes TOUGH2 and FLAC^{3D} (Rutqvist et al., 2002). In this approach, TOUGH2 (Pruess et al., 1999) is used for solving multiphase flow and heat transport equations, whereas FLAC^{3D} (Itasca, 2009) is used for solving geomechanical stress-strain equations. The TOUGH-FLAC simulator was originally developed for analysis of coupled THM processes associated with the Yucca Mountain Project. The FLAC^{3D} code was selected for the coupling to TOUGH2, because it is a well-established commercial code that has been extensively tested and verified.

The two codes are sequentially coupled, but a TOUGH-FLAC simulation runs seamlessly. A great advantage with the adopted approach is that both codes are continuously developed and widely used in both academia and industry.

The simulator has been applied to study coupled geomechanical aspects under multiphase flow conditions for a wide range of applications, including nuclear waste disposal, CO_2 sequestration, geothermal energy extraction, naturally occurring CO_2 upwelling with surface deformations, and gas production from hydrate-bearing unconsolidated sediments. These applications have been accompanied with exploratory code developments. The most significant new development is a revised architecture compared to the earlier attempts, enabling a more rigorous and tight coupling procedure with improved computational efficiency. This development occurred when coupling the newly released TOUGH+ code to FLAC^{3D} for the analysis of the geomechanical performance of hydrate-bearing unconsolidated sediments (Rutqvist and Moridis, 2009).

For analysis of coupled THM problems, the TOUGH2 and FLAC^{3D} are executed on compatible numerical grids and linked through a coupled THM model (Figure 10) with coupling functions serving to pass relevant information between the field equations that are solved in their respective codes. Depending on the problem and specific porous media (e.g., fractured rock, unsaturated clay, or hydrate-bearing sediments), a number of coupling functions have been developed.

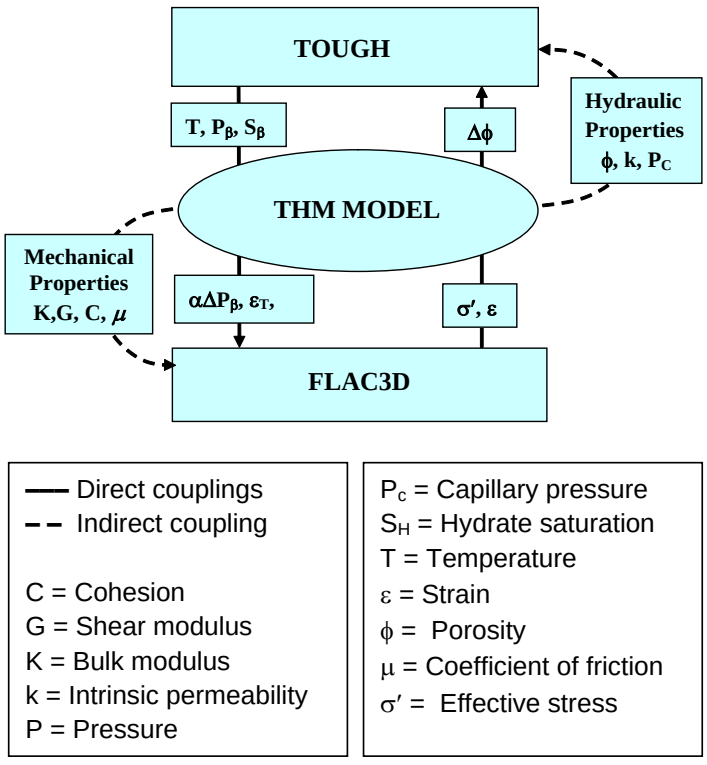

Figure 10. Schematic of linking TOUGH family code such as TOUGH+ and TOUGH2 with FLAC3D for a coupled THM simulation.

In FLAC^{3D}, the basic explicit dynamic calculation iterates between solving the equation of motion and the stress-strain constitutive equation using a sufficiently small time step to assure numerical stability. In one time step, the equation of motion is first invoked to calculate new velocities based on previous velocities and forces. The nodal velocities are then used to derive new strain rates and stress, which in turn are used to update the force vector. The final solution is reached (using a damped solution) when the body is in equilibrium or in steady-state flow (plastic flow), and the out of balance force goes to zero.

A large number of constitutive geomechanical models are readily available in FLAC^{3D}, for both solid and interface elements, including:

- Elastic, isotropic, orthotropic, and transversely anisotropic
- Strain hardening/softening Mohr-Coulomb plasticity
- Ubiquitous joint (anisotropic) strain-hardening/softening bi-linear plasticity
- Double-yield plasticity
- Modified Cam-Clay
- Various creep models

In Figure 10, the data exchanges between TOUGH and FLAC^{3D} are illustrated with arrows going through the central THM model. The arrow on the right-hand side of Figure 3-1 shows the transmission of the effective stress σ' and strain ε (that are computed in FLAC^{3D}) to TOUGH for calculation of the updated porosity ϕ and the corresponding porosity change $\Delta\phi$. This mechanically induced $\Delta\phi$ has an immediate effect on fluid flow behavior. For example, if a change in σ' and ε causes ϕ to decrease, the pore pressure is expected to rise, especially if the permeability is low.

For porous deformable media, two models for mechanically induced porosity changes are implemented in the most recent version linking FLAC^{3D} to TOUGH+

(i) A poroelastic model (based on the approach proposed by Settari and Mourits (1998) that considers macroscopic stress/strain changes and grain deformability

(ii) An empirical model (proposed by Rutqvist and Tsang, 2002) that describes a nonlinear change in porosity as a function of the effective mean stress

The $\Delta\phi$ computed from either of these models is used to estimate changes in k by means of empirical equations. The updated ϕ and k values are in turn used to estimate changes in the hydraulic and wettability properties of the porous medium (i.e., aqueous- and gas-phase relative permeabilities k_{rA} and k_{rG}, and capillary pressure P_c) by employing appropriate scaling equations. For fractured media, a similar exponential empirical model has been applied to correct permeability for changes in the stress field (e.g., Rutqvist et al., 2002).

The arrow on the left side of Figure 10 depicts the flow of data obtained from TOUGH (namely the pressure P, temperature T, and phase saturations S_β) to FLAC^{3D} for processing and estimation of their impact on the effective stress $\alpha \Delta P_\beta$ (α being Biot's effective stress parameter), as well as on thermal and swelling strains (ε_{th} and ε_{sw}, respectively).

Additionally, changes in P, T, and S_β may also result in changes in other mechanical properties listed in Figure 10. These include the bulk modulus K, the shear modulus G, the cohesion C, and the coefficient of internal friction μ. For example, in the case of hydrate-bearing sediment, geomechanical properties change as a function of solid-phase saturations, i.e., hydrate and ice saturations (S_H and S_I, respectively). In the case of unsaturated soil, the bulk modulus and friction angle is a function of suction.

3.2. Comparison of ROCMAS and TOUGH-FLAC to Other THM codes

A steadily growing interest in coupled THM phenomena in geological media has encouraged development of many computer codes at various levels of sophistication. Among those recently applied in the field of rock mechanics are THAMES (Ohnishi and Kobayashi, 1996), MOTIF (Guvanasen and Chan, 1995), FRACON (Nguyen, 1996), FEHM (Bower and Zyvoloski, 1997), GeoSys/Rockflow, (Kolditz et al. 2003), FRT-THM, (Liu et al. 2006), FRIP (Pine and Cundall, 1985), FRACture (Kohl and Hopkirk, 1995) and GEOCRACK (Swenson et al. 1997). The first four of these have been applied mostly in the field of geological disposal of nuclear waste, while the last three have been applied to the field of hot-dry-rock geothermal energy. There are also a few commercially available codes that have been applied to study these phenomena. The most frequently applied in soil and rock mechanics are ABAQUS (Börgesson, 1996), a finite-element code; FLAC (Israelsson, 1996a), a finite-difference code; and UDEC (Israelsson, 1996b), a discrete-element code.

A number of simulators have been developed focusing on oil and gas reservoir engineering, including commercial finite-element packages such as VISAGE (Koutsabeloulis, 1998), GMC-STARS, and a number of academic codes. TOUGH-FLAC is in the class of coupled simulators that is built upon coupling of a reservoir simulator to a geomechanical code. It is a delicate operation to correctly change the porosity of the reservoir simulator upon a change in stress or strain in the mechanical code. The ideas of Settari and Mourits (1998) have been implemented in TOUGH-FLAC coupling as one alternative poro-elastic model. The correct poro-elastic consideration is important when comparing simulation results to that of fully coupled poro-elastic finite element models of the Biot type. However, as described by Settari and Mourits (1998), in practice it is more important to consider the nonlinear stress-dependent effects on porosity and permeability over the range of stress expected in a problem. Such properties may be derived directly from laboratory data and fitted to theoretical or empirical functions (e.g., Liu et al., 2009) or by calibration to field experiments (e.g., Rutqvist et al., 2008a).

In summary, it can be concluded that a large number of simulators have been developed for the analysis of coupled THM processes over the past 30 years. The ROCMAS code and TOUGH-FLAC are two different types of simulators that complement each other, have been

extensively applied, and yet have the flexibilities for modifications and future improvements, such as linkage to TOUGHREACT for fully coupled THMC processes. When evaluating the capabilities of a code it is important to look at how it has been applied. The next section presents an example application of the ROCMAS and TOUGH-FLAC simulators related to nuclear waste isolation.

3.3.Simulation of a Generic Repository in Clay Host Rock

This section presents the initial results of the simulation of coupled THM processes in the EBS and host rock for high-level radioactive waste repository in clay formations. It is our intent to investigate the coupled THM behavior for a range of clay host rocks, including plastic clay and indurated, more brittle claystone. In our first base case simulation scenario we will use clay host rock properties derived from the Opalinus clay stone at Mont Terri, Switzerland (Table 2), and will use a repository design and EBS with emplacement into horizontal tunnels that are back-filled with bentonite-based swelling clays as a protective buffer. We adopt the heat load developed for the Generic Disposal System Environment (GDSE) within the UFD for Pressurized Water Reactor (PWR) used nuclear fuel. The first step in this analysis is to design the repository in terms of spacing between emplacement tunnels and individual waste packages along the tunnels, to achieve a distributed heat load that would meet criteria for desired maximum temperature.

Table 2. Some basic THM rock properties used for simulation of a repository hosted in clay stone.

Parameter	
Bulk Density, [kg/m^3]	2400
Matrix Porosity [-]	0.15
Young's Modulus, [GPa]	5
Poisson's ratio, [-]	0.3
Specific heat, [J/kg·°C]	900
Thermal conductivity, [W/m·°C]	2.2
Thermal expansion coefficient, [°C^{-1}]	1.0×10^{-5}
Permeability, [m^2]	5.0×10^{-20}
Biot's effective stress parameter	1.0
van Genuchten water retension parameter, m	0.41
van Genuchten water retnesion parameter, P_0 [MPa]	48

Repository Design and Heat Load: We chose a repository design similar to the one considered in the Swiss nuclear waste disposal program for a repository in Opalinus Clay. We assume that the drift is located at a depth of 500 m and the top boundary is located at the ground surface. The heat load for individual emplacement tunnels and their spacing are designed by a constraint of a maximum temperature of 100 ºC max in the contact between the canister and the bentonite. In repository designs with bentonite-backfilled repository tunnels, the PWR type of used fuel is typically packed into a waste package (or canister) with the dimensions of about 1 m in diameter and about 4 m long. This is dictated by the length of individual PWR fuel elements and the number of fuel elements per waste package. 4 PWR elements per waste package are commonly adopted for bentonite-backfilled repositories in various host rocks, including crystalline and clay (e.g. Swedish and Finish, Swiss, and Spanish proposed repository designs). Moreover, the emplacement tunnels may be typically up to 1 km long. The basic material properties used in this initial simulation are presented in Table 3.

Table 3. Thermal and hydraulic material parameters for the FEBEX buffer material used in the numerical modeling of swelling experiment and multiple barrier repository.

Parameter	Value/Function
Initial dry density, ρ_d [kg/m^3]	$1.6 \cdot 10^3$
Initial porosity, ϕ [-]	0.41
Saturated permeability, k [m^2]	$2.0 \cdot 10^{-21}$
Relative permeability, k_r [-]	$k_{rl} = S_l^3$
van Genuchten's (1980) parameter, P_{VG} [MPa]	30
van Genuchten's (1980) parameter, λ_{VG} [-]	0.32
Thermal expansion, β [1/°C]	$1.5 \cdot 10^{-4}$
Dry specific heat, C_s [J/kg·°C]	$c_s = 1.38T + 732.5$
Thermal conductivity, λ_m [W/m·°C]	$\lambda_m = 1.28 - \frac{0.71}{1+e^{(S_l - 0.65)/0.1}}$
Effective molecular diffusion coefficient, D_v [m^2/s]	$D_v = 2.16e-5 \times \tau \times \phi \times S_g \left(\frac{T_{abs}}{273.8}\right)^{1.8}$
Tortuosity, τ [-]	0.8

The thermal decay curves for a 10 PWR element waste package was scaled down by multiplying by 4/10 to obtain the decay curve for a 4 PWR element waste package that would match the adopted repository design. This leads to an initial thermal power of 3144 W per waste package. Assuming a waste deposition after 60 years of interim storage, the heat power has decayed to 1818 Watts per waste package. With the assumption of the 50 m tunnel spacing and

500 m emplacement depth, the average thermal power per meter drift may be scaled by adjusting the spacing between individual waste packages along the tunnel. Using model calibration and a maximum temperature kept below 100°C, we adopted an average thermal power of 200 W per meter drift. This would mean that if the individual waste packages are 4 m long, the spacing would be 4 m. Alternatively, for 3 PWR elements per waste package the spacing would be 2 m. For the adopted average thermal conductivity of the rock (2.2 W/m°C), an average thermal power of 200 W per meter drift seems to be the upper practical limit for this type of repository design. Figure 11 presents the model dimensions and the heat decay curve for these simulations.

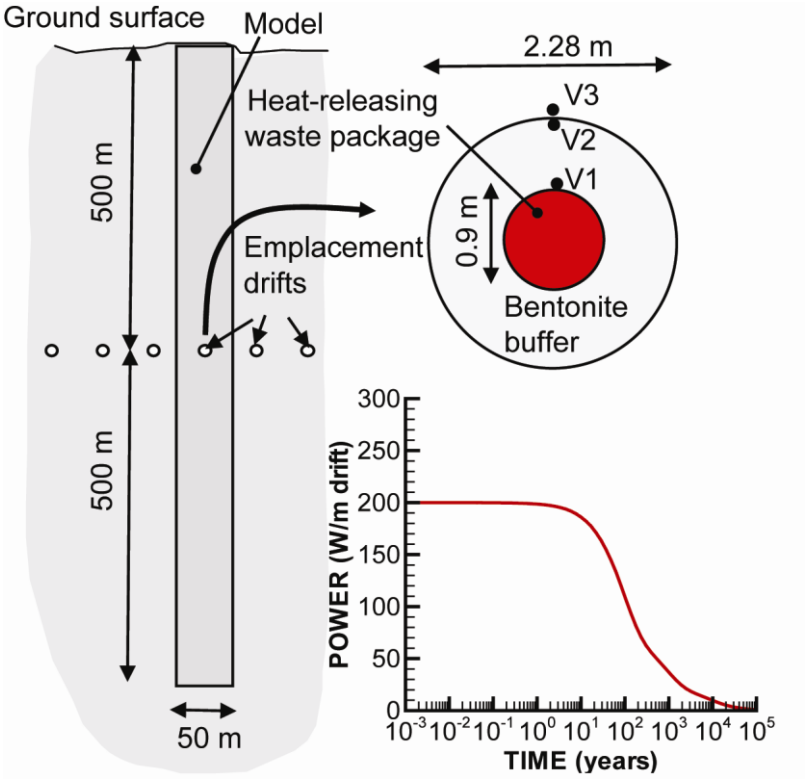

Figure 11. Model domain for a repository hosted in clay stone.

Modeling Sequence, Boundary and Initial Conditions: Figure 12 presents the detailed modeling sequence, boundary and initial conditions for the coupled THM simulation. The initial conditions for the rock mass are established at the pre-excavation stage (Figure 12(1)). The initial stress was defined as $\sigma_h = \sigma_H = \sigma_v = 2400 \cdot 9.81 \cdot D$ where D is elevation relative to ground surface (D = z – 500 and tensile stress is positive). The vertical thermal gradient is assumed to be 30°C/km with a fixed average temperature of 10°C on the ground surface and a fixed temperature of 40 °C at the bottom boundary. The groundwater table is assumed to be located at the ground surface where the pressure is fixed to 0.1 MPa (atmospheric). At the bottom of the model the fluid pressure is set to 9 MPa, which slightly less than hydrostatic. The excavation sequence can be simulated in a one-step steady state calculation with the elements in the drift

removed and constant temperature 25°C and pressure of 0.1 MPa at the drift boundary (Figure 12(2)). After the steady state excavation simulation is completed, the waste canister, bentonite buffer and back-fill are installed instantaneously and the post-closure simulation can start (Figure 12(3) and 12(4)).

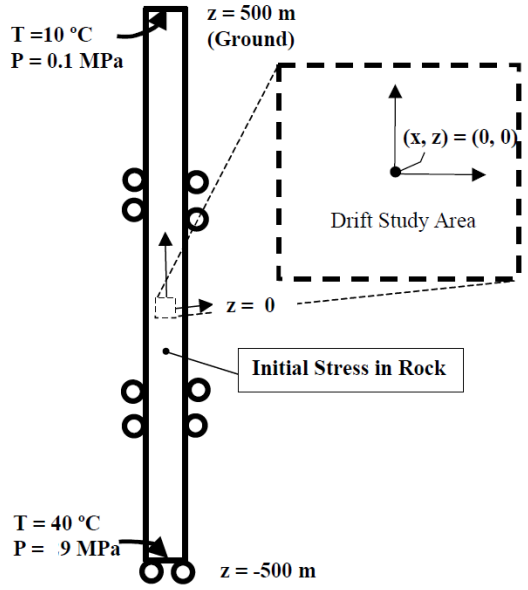

1) Pre-excavation Conditions

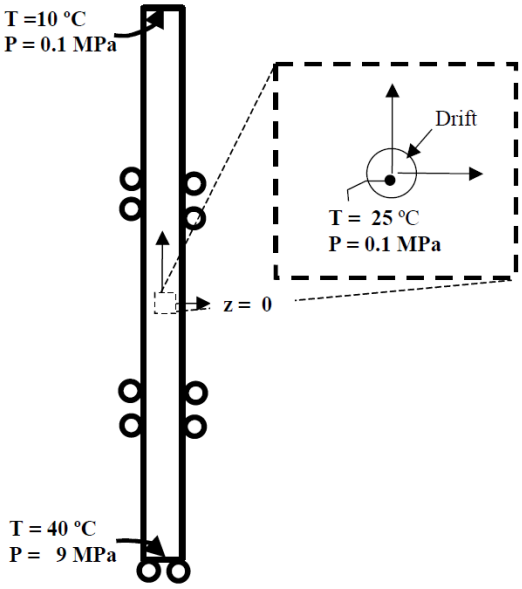

2) Steady State Simulation of Excavation

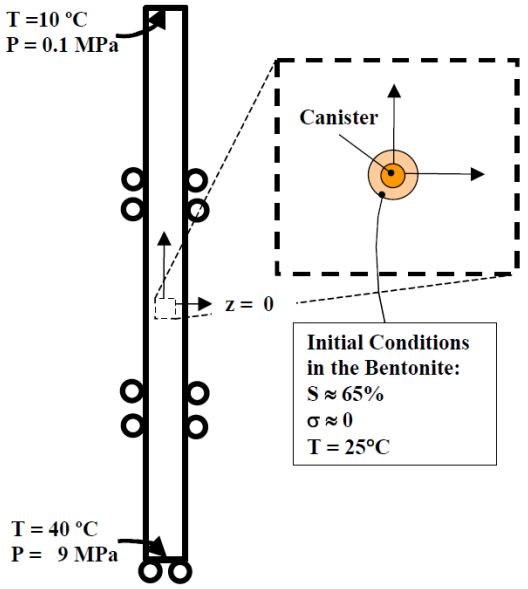

3) Installation of Bentonite Buffer

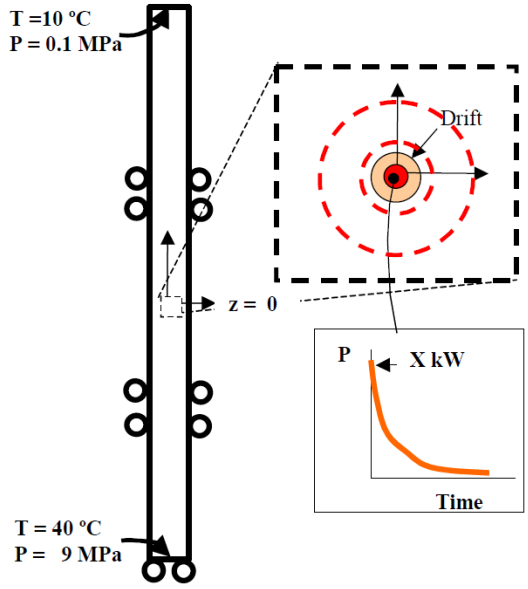

4) Transient Simulation of Post-closure THM

Figure 12. Modeling sequence, boundary and initial conditions.

Basic THM simulation results: Figure 13 presents the calculated evolution of temperature, saturation, fluid pressure, and stress within the buffer. The temperature peaks at about 95°C, which is below the 100°C maximum temperature criterion. The resaturation of the buffer is delayed as a result of the low rock permeability and a slight desaturation of the rock can be observed in Figure 13b. The fluid pressure indicates a strong coupling to the temperature field, and as a result of the low rock permeability a significant thermal pressurization occurs (Figure 13c). This increase in fluid pressure has a direct impact on the stress evolution in the buffer (Figure 13d). Thus, in this case we observe strong interaction between the host rock coupled processes and the THM evolution of the buffer. The results presented are valid for an average permeability representative of 5e-20 m^2. If the permeability is lower, a much stronger thermal pressurization can occur.

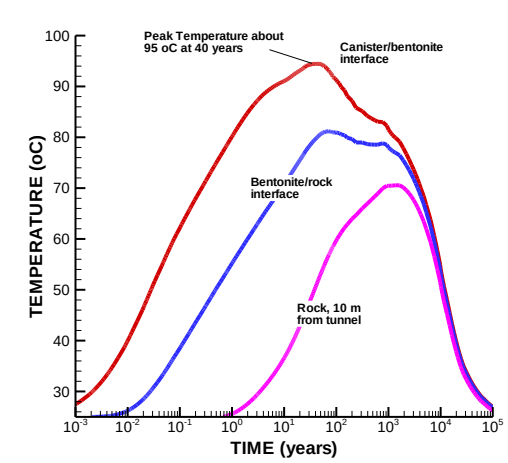

(a)

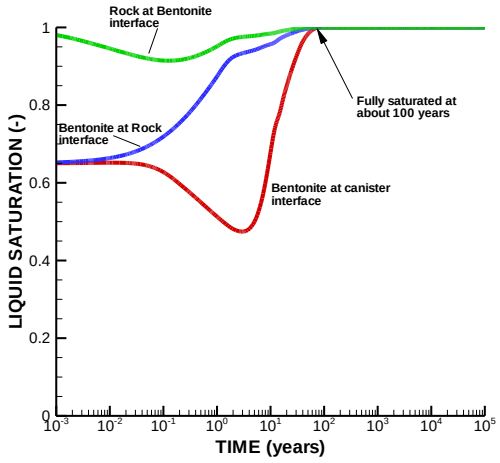

(b)

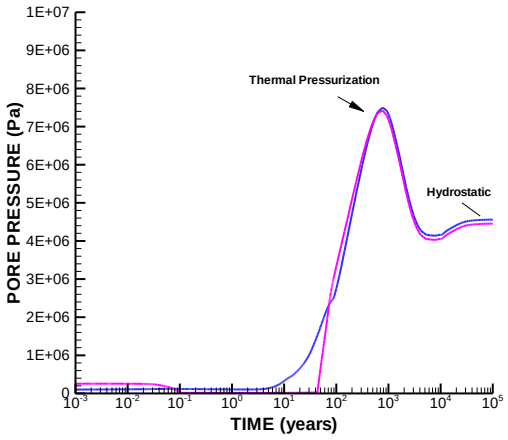

(c)

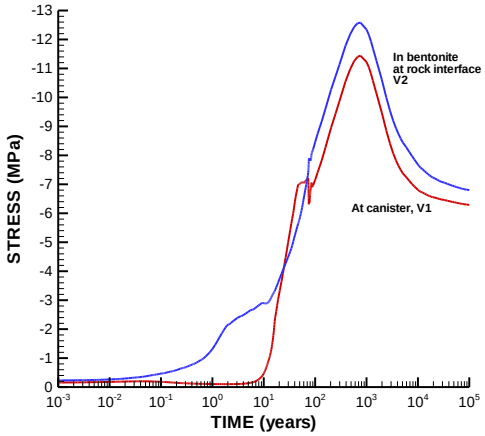

(d)

Figure 13. Simulated evolution of THM processes in the buffer: (a) temperature at V1, V3, and V6 (b) liquid saturation at V1, (c) fluid pressure at V3, and (d) total radial stress (σx) at V1 and V2. See Figure 3-2 for definitions of V1, V2, and V3.

Summary of THM Research for Clay/Shale Environments and Next Step: We have conducted initial simulation studies of coupled THM processes in the EBS and host rock for high-level radioactive waste repository in clay formations. This study highlights the important interactions between the buffer and the host rock, in particular regarding the potential for desaturation of the rock and thermal pressurization which can have a significant impact of the coupled THM evolution.

Future work is proposed to include modeling that addresses fracture growth, self-sealing and self-healing behavior. This will involve new constitutive models such as discussed in Section 2 and calibration and confirmation using experimental data.

4. THC Modeling in clay/shale Environments

In this section, a summary of the TOUGHREACT code is presented followed by modeling results for THC studies in a clay host rock.

4.1. TOUGHREACT Code

Coupled modeling of subsurface multiphase fluid and heat flow, solute transport, and chemical reactions can be applied to many geologic systems and environmental problems, including geothermal systems, diagenetic and weathering processes, nuclear waste emplacement, acid mine drainage remediation, contaminant transport, and groundwater quality. TOUGHREACT has been developed as a comprehensive non-isothermal multi-component reactive fluid flow and geochemical transport simulator to investigate these and other problems (Xu et al., 2008). A number of subsurface thermo-physical-chemical processes are considered under various thermohydrological and geochemical conditions of pressure, temperature, water saturation, and ionic strength. TOUGHREACT can be applied to one-, two- or three-dimensional porous and fractured media with physical and chemical heterogeneity. The code can accommodate any number of chemical species present in liquid, gas and solid phases. A variety of equilibrium chemical reactions are considered, such as aqueous complexation, gas dissolution/exsolution, and cation exchange. Mineral dissolution/precipitation can take place subject to either local equilibrium or kinetic controls, with coupling to changes in porosity and permeability and capillary pressure in unsaturated systems. Chemical components can also be treated by linear adsorption and radioactive decay.

The first version of the non-isothermal reactive geochemical transport code TOUGHREACT was developed (Xu and Pruess, 1998) by introducing reactive geochemistry into the framework of the existing multi-phase fluid and heat flow code TOUGH2 (Pruess, 1991). TOUGHREACT was further enhanced with the addition of (1) treatment of mineral-water-gas reactive-transport under boiling conditions, (2) an improved HKF activity model for

aqueous species, (3) gas species diffusion coefficients calculated as a function of pressure, temperature, and molecular properties, (4) mineral reactive surface area formulations for fractured and porous media, and (5) porosity, permeability, and capillary pressure changes owing to mineral precipitation/dissolution. Subsequently, TOUGH2 V2 was released with additional EOS modules and features (Pruess et al., 1999) which was incorporated into the present version of TOUGHREACT (Xu et al., 2006).

Major Processes Treated by TOUGHREACT: The major processes for fluid and heat flow are: (1) fluid flow in both liquid and gas phases occurs under pressure, viscous, and gravity forces; (2) interactions between flowing phases are represented by characteristic curves (relative permeability and capillary pressure); (3) heat flow by conduction and convection, and (4) diffusion of water vapor and air. Thermophysical and geochemical properties are calculated as a function of temperature, such as fluid (gas and liquid) density and viscosity, and thermodynamic and kinetic data for mineral-water-gas reactions. Transport of aqueous and gaseous species by advection and molecular diffusion are considered in both liquid and gas phases. Depending on the computer memory and CPU performance, any number of chemical species in the liquid, gas and solid phases can be accommodated. Aqueous complexation, acid-base, redox, gas dissolution/exsolution, and cation exchange are considered under the local equilibrium assumption. Mineral dissolution and precipitation can proceed either subject to local equilibrium or kinetic conditions. Linear adsorption and decay can be included.

Governing Equations: The primary governing equations for multiphase fluid and heat flow, and chemical transport have the same structure, derived from the principle of mass (or energy) conservation. These equations, implemented in TOUGHREACT, are presented in Xu et al. (2008). Expressions for non-isothermal multiphase flow are given in Pruess (1987) and Pruess et al. (1999). The transport equations are written in terms of total dissolved concentrations of chemical components, which are concentrations of the basis species plus their associated aqueous secondary species (Yeh and Tripathi, 1991; Steefel and Lasaga, 1994; Walter and others, 1994; Lichtner, 1996; and Xu and Pruess, 2001). If kinetically-controlled reactions occur between aqueous species, then additional ordinary differential equations need to be solved to link the total concentrations of the primary species with the evolving concentrations of the secondary species (Steefel and MacQuarrie, 1996). Kinetically-controlled reactions between aqueous species are not considered in the present version of TOUGHREACT. Slow aqueous phase reactions are common in the case of redox reactions and will be addressed in future development. Advection and diffusion processes are considered for both the aqueous and gaseous species. Aqueous species diffusion coefficients are assumed to be the same. Gaseous species, having a neutral valence, can have differing diffusion coefficients calculated as a function of T, P, molecular weight, and molecular diameter. The local chemical interactions in the transport equations are represented by reaction source/sink terms.

The primary governing equations must be complemented with constitutive local relationships that express all parameters as functions of fundamental thermophysical and chemical variables. The equations for chemical reactions are presented in Xu et al., (2008). Mass conservation in the closed chemical system is written in terms of basis (component) species. The species distribution must be governed by the total concentrations of the components. The oxygen is used for formulating redox reactions by attributing the oxidizing potential to the dissolved

oxygen (Nordstrom and Muñoz, 1986; Wolery, 1992). In contrast to the free electron in the hypothetical electron approach (Yeh and Tripathi, 1991), oxygen can be present and can be transported in natural subsurface flow systems. The formulation for cation exchange is similar to that of Appelo and Postma (1993). For kinetically-controlled mineral dissolution and precipitation, a general form of rate law (Lasaga, 1984; Steefel and Lasaga, 1994; Palandri and Kharaka, 2004) is used (Xu et al., 2008). Thermodynamic and kinetic data are functions of temperature.

Temporal changes in porosity, permeability, and unsaturated hydrologic properties owing to mineral dissolution and precipitation can modify fluid flow. This feedback between transport and chemistry can be important (e.g., Raffensperger, 1996; Dobson et al., 2003), and can be treated by TOUGHREACT. Changes in porosity during the simulation are calculated from changes in mineral volume fractions. The porosity-permeability correlation in geologic media can be complex, depending on several factors, such as pore size distribution, pore shapes, connectivity (Verma and Pruess, 1988), and crystal morphology. Several porosity-permeability and fracture aperture-permeability relationships are included in the model (Xu et al., 2008). The code can also be set to monitor changes in porosity and permeability during the simulation without considering their effects on fluid flow. In unsaturated systems, capillary pressure can be modified via permeability and porosity changes using Leverett scaling (based on Slider, 1976).

4.2.Application of TOUGHREACT to Bentonite-Filled EBS and Clay Formation

This simulation problem deals with water-rock interactions around nuclear waste packages emplaced in clay formation with bentonite backfill. The model setup is similar to the benchmark for the DECOVALEX-THMC project (Sonnenthal, 2008). The grid for the simulations is shown in Figure 14. Because the model was intended for demonstration of the code capability in simulating the THC behavior in the EBS and clay formation, it was set up in a very simplified manner (e.g., only aqueous complexation and mineral dissolution/precipitation are considered). Therefore, this problem should not be taken as an accurate representation of a nuclear waste repository. Nevertheless, this problem illustrates typical coupled thermal-hydrological-chemical processes that could occur in the EBS and clayey host rock around nuclear waste packages as influenced by the very different near-field mineralogy and water chemistry. Details of model setup and results are given in the following sections.

Model Setup: The model assumes that initially both clay formation and bentonite EBS are fully saturated. The top boundary (+500 m) has a fixed temperature of 10 ^{o}C and pressure of 0.1 MPa. The bottom boundary (-500 m) has also fixed temperature and pressure of 40 ^{o}C and 0.9 MPa respectively. The fixed pressures on the top and bottom boundary yield a downward flow around 3 mm/year. The heat input from the inner boundary is the same as that used for the THM model (see Section 3).

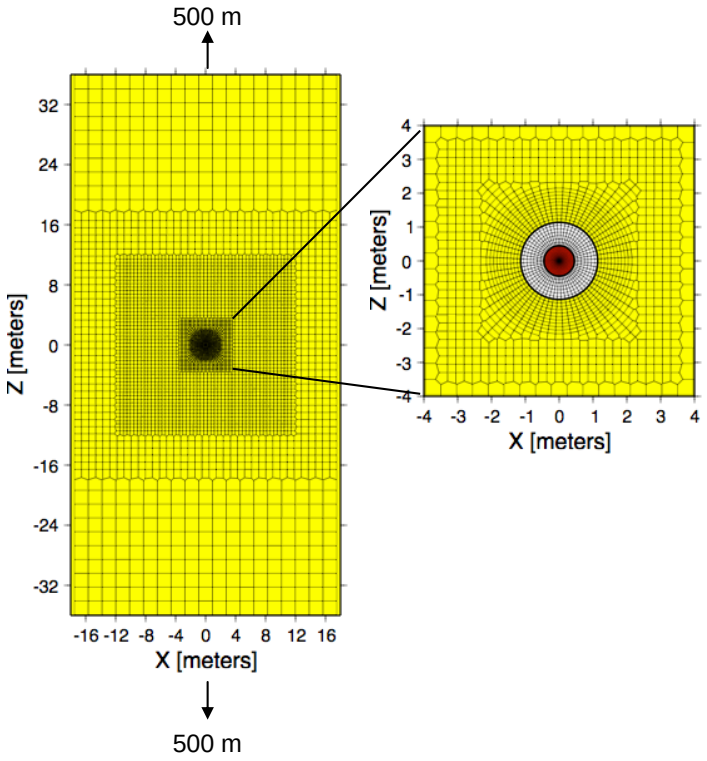

Figure 14. Two-dimensional numerical integral finite difference unstructured mesh for TOUGHREACT simulations (left) and enlargement of drift mesh (right) showing waste canister (red), bentonite buffer (white), and drift wall boundary. Mesh extends 500 m above and below the drift center, and 17.5 m to each side.

The mineralogical composition of bentonite (Table 4) is taken from the Kunigel-V1 bentonite (Ochs et al., 2004). The clay formation is assumed to be Opalinus Clay investigated in the Mont Terri underground rock laboratory in Switzerland (Thury, 2002) and the mineral composition is given in Table 5.

Table 4. Mineral composition of the bentonite used in the model (taken from the Kunigel-V1 bentonite (Ochs et al., 2004).

Mineral	Abundance (volume fraction)
Na-montmorillonite	0.475
Quartz	0.335
K-Feldspar	0.041
Calcite	0.0235
Dolomite	0.029
pyrite	0.006

Table 5. Mineral composition of the clay formation used in the model (taken from the Opalinus Clay (Thury, 2002)).

Mineral	Abundance (volume fraction)
Calcite	0.1
Illite	0.223
Kaolinite	0.174
Chlorite	0.1445
Smectite-na	0.1426
Quartz	0.1845
Siderite	0.01256
Ankerite	0.00798
Pyrite	0.01

The pore water composition of the bentonite (Ochs et al., 2004) and clay formation (Fernandez et al., 2007) are listed in Table 6. To establish a starting point for the reactive transport model, the initial pore waters are equilibrated with minerals listed in Table 4 and 5 and the equilibrated waters are listed in the last two column of Table 6.

Table 6. Initial pore water composition of bentonite and clay formation and the equilibrated water with minerals listed in Table 4 and 5 respectively (compositions in molal).

	Initial		Equilibrated	
	Bentonite (Ochs et al., 2004)	Clay formation (Fernandez et al., 2007)	Bentonite	Clay formation
pH	8.40	7.60	6.98	6.50
Eh	-0.23	-0.27	-0.18	-0.12
Cl	1.50E-05	3.32E-01	1.50E-05	3.32E-01
SO_4^{-2}	1.10E-04	1.86E-02	1.21E-04	1.86E-02
HCO_3^-	3.50E-03	5.20E-03	5.21E-03	1.26E-03
Ca^{+2}	1.10E-04	2.26E-02	2.77E-03	1.50E-01
Mg^{+2}	5.50E-05	2.09E-02	1.82E-04	5.59E-04
Na^+	3.60E-03	2.76E-01	4.80E-03	5.80E-02
K^+	6.20E-05	2.16E-03	1.05E-04	3.46E-06
Fe^{+2}	1.00E-10	2.96E-07	5.65E-06	1.44E-03
$SiO_2(aq)$	3.40E-04	1.16E-04	1.78E-04	1.80E-04
AlO_2^-	3.54E-08	3.89E-06	2.98E-08	6.55E-10

Table 7 lists the thermal and hydrodynamic parameters used in the model. Those for bentonite are taken from Sonnenthal (2008) while those for clay formation mostly are taken from Thury (2002), except thermal conductivity which is the same as used in the THM model.

Table 7. Thermal and hydrodynamic parameters

parameter	Clay formation	Bentonite
Grain density [kg/m^3]	2700	2700
Porosity	0.15	0.41
Saturated permeability [m^2]	1.0×10^{-20}	2.0×10^{-21}
Relative permeability, k_{rl}	m = 0.6, S_{rl} = 0.01	$K_{rl} = S^3$
van Genuchten α [1/Pa]	6.8×10^{-7}	3.3×10^{-8}
van Genuchten m	0.6	0.3
Compressibility, β [1/Pa]	3.2×10^{-9}	5.0×10-8
Thermal expansion coeff., [1/^{o}C]	0.0	1.0×10^{-4}
Dry specific heat, [J/kg ^{o}C]	800	8000
Thermal conductivity [W/m ^{o}C] dry/wet	2.2/2.2	0.5/1.3
Tortuosity	1.0	0.8

Mineral dissolution/precipitation are kinetically controlled, except calcite where equilibrium is assumed. TOUGHREACT (Xu et al., 2006) uses a general form of rate expression, which is based on transition state theory (TST) (Lasaga et al., 1994; Steefel and Lasaga, 1994):

$$r = kA\left[1-\left(Q/K\right)^{\theta}\right]^{\eta} \tag{40}$$

where r is the kinetic rate (positive values indicate dissolution, and negative values precipitation), k is the rate constant (moles per unit mineral surface area and unit time) which is temperature dependent, A is the specific reactive surface area per kg H_2O, K is the equilibrium constant for the mineral–water reaction written for the destruction of one mole of mineral, and Q is the reaction quotient. The parameters θ and η should be determined by experiments, but are commonly set equal to unity when experimental quantification is unavailable. The kinetic rate constants can usually be summed from three mechanisms (Lasaga et al., 1994):

$$\begin{aligned} k = {} & k_{25}^{nu}\exp\left[\frac{-E_a^{nu}}{R}\left(\frac{1}{T}-\frac{1}{198.15}\right)\right] + k_{25}^{H}\exp\left[\frac{-E_a^{H}}{R}\left(\frac{1}{T}-\frac{1}{198.15}\right)\right]\alpha_H^{n_H} \\ & + k_{25}^{OH}\exp\left[\frac{-E_a^{OH}}{R}\left(\frac{1}{T}-\frac{1}{198.15}\right)\right]\alpha_H^{n_{OH}} \end{aligned} \tag{41}$$

where superscripts *nu*, *H* and *OH* indicate neutral, acid, and base mechanisms, respectively, E is the activation energy, k_{25} is the rate constant at 25 °C, R is gas constant, T is the absolute temperature, a is the activity of the species, and n is a power term (constant).

The kinetic law for mineral dissolution/precipitation is given in Xu et al. (2006). The kinetic rate for the mineral considered in current model is given in Table 8. Note that the surface areas listed in Table 8 are calculated for tuff (Sonnenthal et al., 2005). Their applicability to the clay formation considered is questionable. Further refinement of the surface area calculation is needed in the future when the THC model is applied to a realistic scenario.

Table 8. Kinetic properties for minerals considered in the model (Xu et al., 2006)

Mineral	**A (cm^2/g)**	**Parameters for Kinetic Rate Law**							
		Neutral Mechanism		**Acid Mechanism**			**Base Mechanism**		
		k_{25} ($mol/m^2/s$)	**E_a (KJ/ mol)**	**k_{25} ($mol/m^2/s$)**	**E_a (KJ/ mol)**	**$n(H^+)$**	**k_{25} ($mol/m^2/s$)**	**E_a (KJ/ mol)**	**$n(H^+)$**
***Primary*:**									
Calcite	Assumed at equilibrium								
Quartz	9.8	1.023×10^{-14}	87.7						
K-feldspar	9.8	3.89×10^{-13}	38	8.71×10^{-11}	51.7	0.5	6.31×10^{-12}	94.1	-0.823
Kaolinite	1.95×10^{5}	6.91×10^{-14}	22.2	4.89×10^{-12}	65.9	0.777	8.91×10^{-18}	17.9	-0.472
Smectite-Ca	5.64×10^{5}	1.66×10^{-13}	35	1.05×10^{-11}	23.6	0.34	3.02×10^{-17}	58.9	-0.4
Illite	6.68×10^{5}	1.66×10^{-13}	35	1.05×10^{-11}	23.6	0.34	3.02×10^{-17}	58.9	-0.4
Chlorite	9.8	3.02×10^{-13}	88	7.76×10^{-12}	88	0.5			
Pyrite	12.9	2.52×10^{-12}	62.76	2.34×10^{-7}	43.54	1			
Dolomite	12.9	2.52×10^{-12}	62.76	2.34×10^{-7}	43.54	1			
Ankerite	9.8	1.26×10^{-9}	62.76	6.46×10^{-4}	36.1	0.5			
Smectite-Na	5.64×10^{5}	1.66×10^{-13}	35	1.05×10^{-11}	23.6	0.34	3.02×10^{-17}	58.9	-0.4
Na-montmorillonite	5.64×10^{5}	1.66×10^{-13}	35	1.05×10^{-11}	23.6	0.34	3.02×10^{-17}	58.9	-0.4

Model Results: In this problem, the heat load results in temperature at the canister-bentonite interface climbing to a maximum near 98 °C after about 70 years, then slowly dropping back to about 93 °C after 1000 years. At the bentonite-clay formation interface, temperature increases sharply at the first 100 years and then is stabilized at around 88 °C after a slow increase up to 700 years.

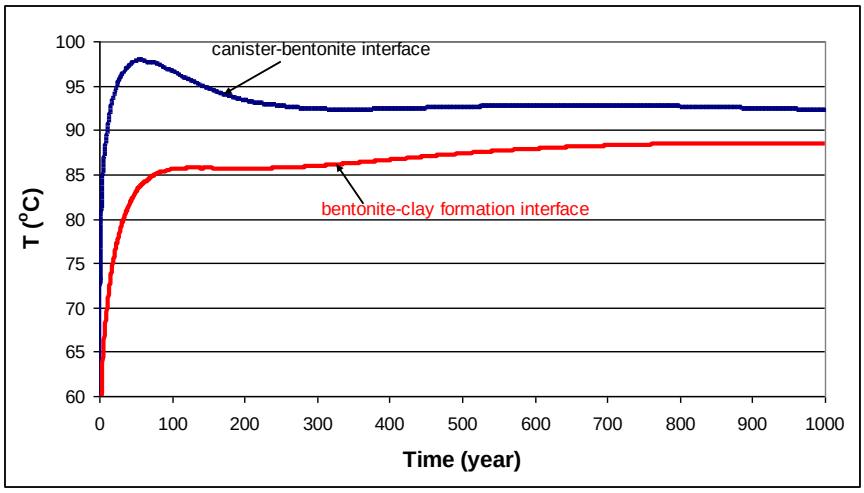

Figure 15. Time evolution of temperature at the canister-bentonite interface and bentonite-clay formation interface, respectively.

Because the simulation starts with saturated condition, some processes which would occur during the hydration of unsaturated bentonite are not considered here (e.g., see Section 2). Diffusion is the only process that controls the transport of conservative species, such as the chloride shown in Figure 16. Note that chloride is not necessarily a conservative species, but in current simulations, no chemical reactions will affect the concentration of chloride and therefore chloride is used as representative conservative species. The diffusive mass transfer between bentonite and clay formation and the change of temperature lead to mineral alteration in bentonite and clay formation, especially near the interface.

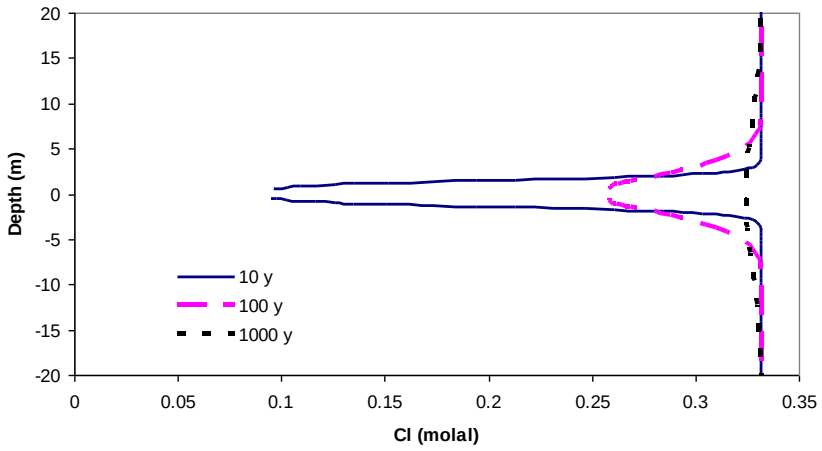

Figure 16. Profiles of chloride concentration along z direction at x =0 at different times.

Figure 17 shows the time evolution of minerals at a point inside the bentonite. Inside the bentonite, minerals alteration is characterized by the dissolution of calcite, K-feldspar and Na-montmorillonite and precipitation of quartz, illite and dolomite. Figure 18 shows the time evolution of minerals near the bentonite-clay formation interface but on the side of bentonite. Dissolution of dolomite, K-feldspar and Na-montmorillonite and precipitation of calcite, quartz, illite and chlorite are observed. Figure 19 shows the change of porosity at the two locations mentioned above. Near the canister, the porosity decreases slightly whereas near the interface, porosity increases about 2%.

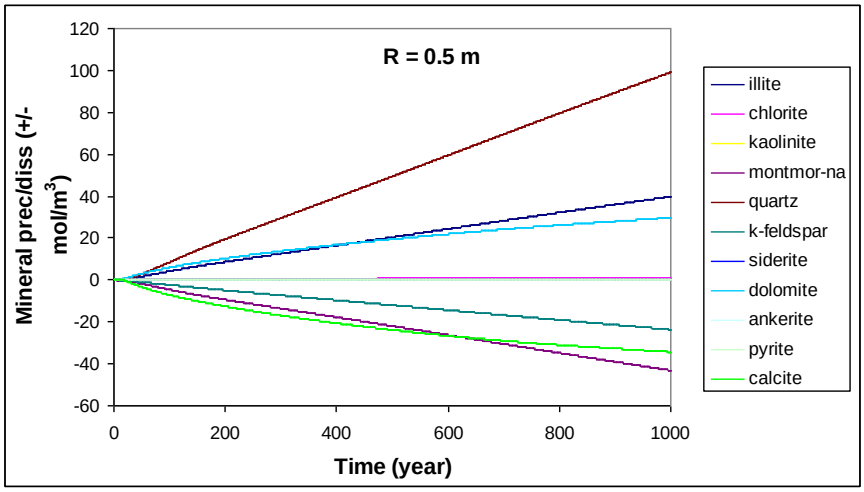

Figure 17. Time evolution of mineral dissolution/precipitation at the point inside the bentonite with a radial distance of 0.5 m.

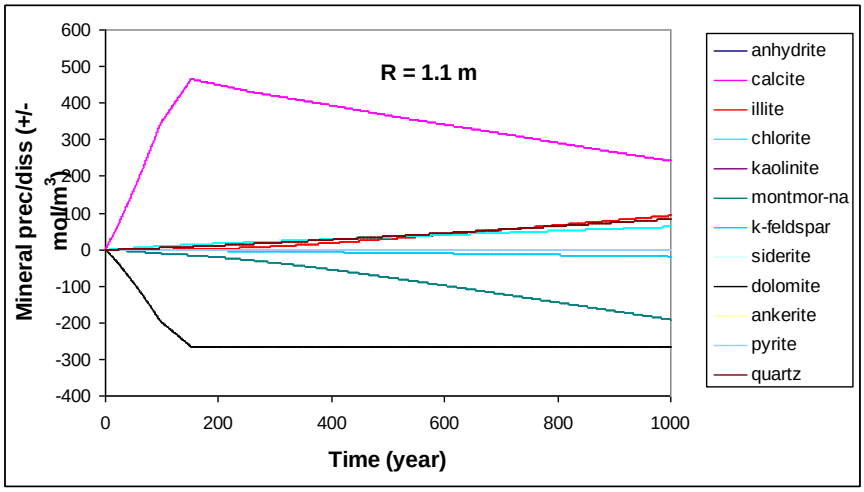

Figure 18. Time evolution of minerals dissolution/precipitation at the point inside the bentonite with a radial distance of 1.1 m (near the bentonite-clay formation interface).

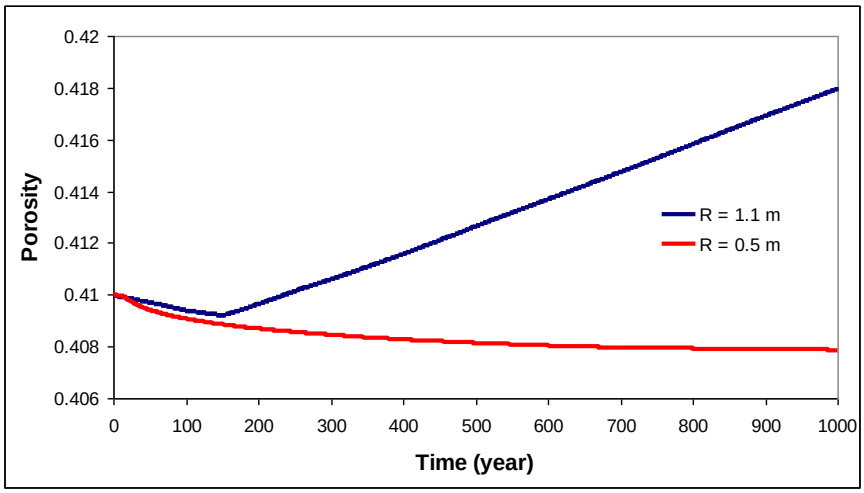

Figure 19. Time evolution of the porosity two given locations inside the bentonite.

Figure 20 shows time evolution of minerals dissolution/precipitation at the point in the clay formation with a radial distance of 1.2 m (near the bentonite-clay formation interface). Significant mineral alteration occurs due to the mass transfer between bentonite and clay formation and change of temperature. Minerals alteration at this point is characterized by the dissolution of calcite, siderite and illite and precipitation of ankerite, smectite and quartz. Note that calcite dissolves rapidly in the first 100 years and then precipitates slowly. Correspondingly, ankerite precipitates significantly in the first 100 years and dissolves slowly afterwards. Porosity change is a result of change of all minerals. As shown in Figure 22, the porosity in the clay formation near the interface increase slightly and then decrease after 800 years, although such changes are minimal. Figure 21 shows the time evolution of minerals in the clay formation far from the interface. Mineral dissolution/precipitation are insignificant and are mainly induced by the change of temperature and slight initial disequilibrium. Model results show the dissolution of ankerite, smecitite and illite and the precipitation of anhydrite, quartz and kaolinite, which results in essentially no change of porosity (see Figure 22).

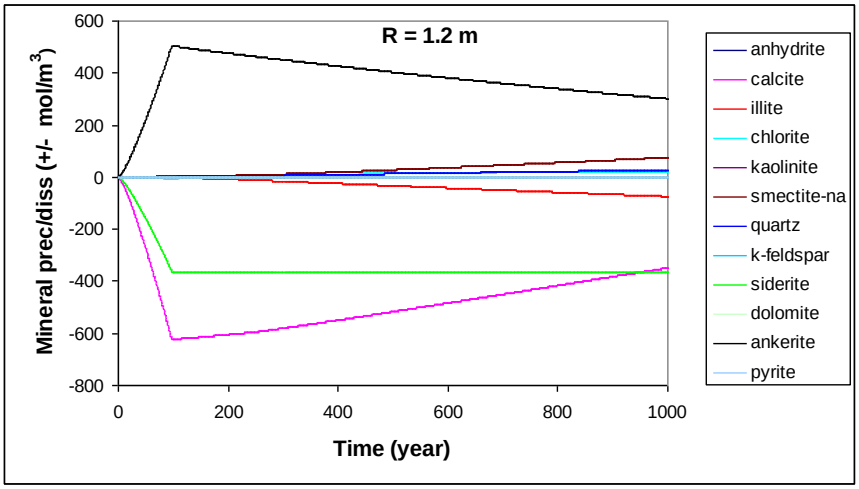

Figure 20. Time evolution of minerals dissolution/precipitation at the point in the clay formation with a radial distance of 1.2 m (near the bentonite-clay formation interface).

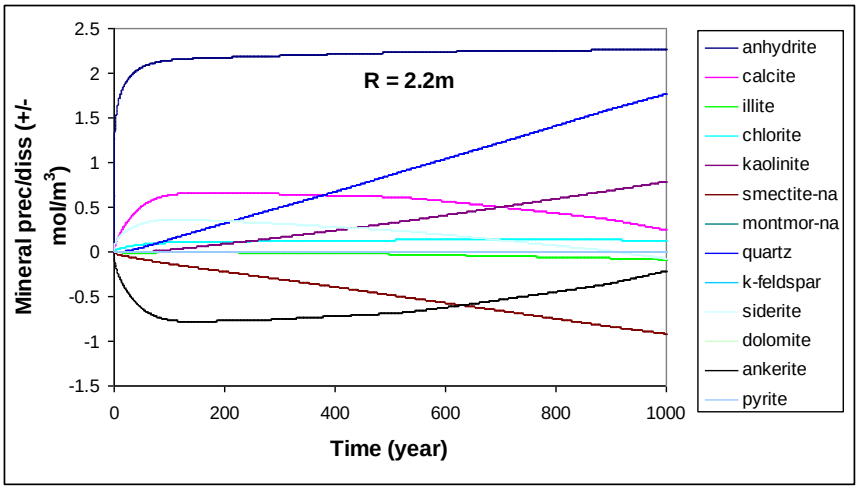

Figure 21. Time evolution of minerals dissolution/precipitation at the point in the clay formation with a radial distance of 2.2 m.

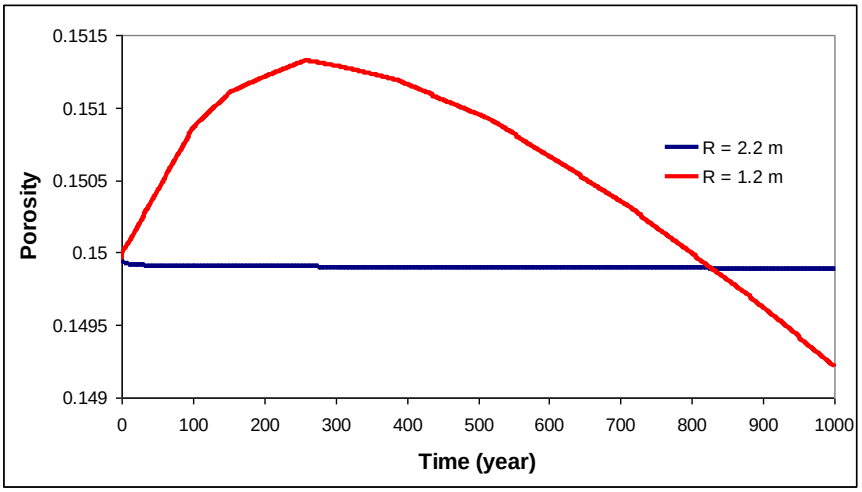

Figure 22. Time evolution of the porosity at two given locations in the clay formation.

5. Knowledge Gaps and R&D Plan

Knowledge Gaps: While much progress has been made over the last ten years or more, mostly in Europe (e.g., Tsang et al. 2010), several outstanding theoretical and practical issues remain. These issues concern (a) excavation damaged zone phenomena that result from interaction of the host rock with the excavation and engineered barrier system; (b) larger-scale disturbances to the host rock resulting from seismic, igneous and abnormal pressurization phenomena; (c) characterization of large-scale flow and transport behavior in low-permeability clay/shale formations; and (d) impacts of mineralogical and geochemical conditions on sorption. To resolve these issues, the following knowledge gaps should be investigated:

1. Constitutive relationships for plastic and indurated clays based on laboratory and analytic studies. This should address issues of elastic limits and fracturing criteria, strain softening for describing progressive change in material strength, and strain localization and shear band occurrence. The impact of hydromechanical, chemical, and thermal effects also needs to be considered (Tsang et al., 2010).
2. Long-term (slow) clay property changes, such as creep in plastic clays and subcritical crack growth in indurated clays. The effects of moisture changes and temperature gradients and chemical environments need to be studied and formulated. How to handle anisotropy and bedding planes (or in general, planes of weakness) has to be resolved (Tsang et al., 2010).
3. Thermo-hydro-mechanical processes in clays. These include damage mechanisms, phase changes, and interaction of multiple materials (such as those in the engineered barrier system). This is an area still requiring much work (Tsang et al., 2010).
4. Impact of rock-property heterogeneity as well as *in situ* stress fields. The permeability of indurated clays can vary over two orders of magnitude, while mechanical properties can vary by a factor of five or more. Spatial variability may have some characteristic length or may have a fractal character. Understanding clay variability could be key to predicting strain localization and fracturing processes. The stress field may also be spatially varying,

depending on local structures and temporal changes in clay properties (Tsang et al., 2010).

5. Changes in recharge, overburden, and regional stress. Changes in stress can lead to fault or fracture reactivation that impacts fluid flow and radionuclide transport behavior in the host rock. Faults in argillaceous rock include both tectonic and non-tectonic faults. In particular, layer-bound, non-tectonic polygonal faults are a phenomenon known to occur only in fine-grained sediments such as clay and shale (Cartwright 1997). These faults may only conduct fluid episodically upon reactivation and are difficult to identify in standard seismic surveys. Mechanisms that could lead to reactivation include sedimentation and glaciation (Mazurek et al. 2003, pp. 341; Caillet 1993), changes in tectonic stress (Darby et al. 2001), seismic or igneous activity, the accumulation of hydrocarbon or nonhydrocarbon gas (e.g, CO_2, and He, Wiprut et al. 2000), and osmosis driven by changes in recharge and natural contrasts in solute concentrations of pore waters (Neuzil 2000). Fracture and fault behavior for a clay or shale host rock is sensitive to the diagenetic history. Diagenetic history and the future path of diagenesis have important effects on mineralogical, geomechanical, and hydrological characteristics of the host rock. Some success in understanding diagenetic history has been achieved in European nuclear waste disposal research programs using basin modeling.
6. Intrusion and collapse structures. Other phenomena that can disturb the hydrologic properties of the host rock include intrusions from igneous and hydrothermal activity, clastic intrusions from sandstone or mud, and salt intrusions (Cartwright et al., 2007). Sandstone and mud intrusions occur when overpressurization conditions force sandstone or mud (e.g., mud volcanoes) up through the host rock. Magmatic activity could cause substantial changes to the host rock by the direct intrusion of magma bodies or through mechanical stress induced by the heat and associated vaporization of water. Collapse structures caused by dissolution of evaporites and collapse of source chambers for intrusion material can also lead to host-rock disturbances.
7. Characterization of host rock properties. Because of the low degree of fracturing and low bulk permeability measured from boreholes or underground excavations (such as underground research laboratories), large-scale permeability values are difficult to ascertain. Infrequent and relatively isolated (preferential) pathways may be difficult to identify based on standard measurement methods.
8. Mineralogical and geochemical conditions and their impact on sorption. There is typically significant uncertainty in the values of the sorption distribution coefficient because it depends on a variety of processes and conditions that take place on complex, heterogeneous, mineral surfaces. There are two specific processes that typically fall under the general label of sorption: ion exchange and surface complexation. Process models are needed for sorption because the number of sorption experiments that are needed to adequately cover the range of current and future geochemical conditions is impractically large. A variety of phenomena could lead to spatial and temporal variations in geochemical conditions that impact sorption including waste heat, hyperalkaline solutions from groundwater interaction with EBS cement, competition between radionuclides and other dissolved species for sorption sites, changes in natural recharge composition, and igneous and geothermal processes. Because sorption is affected by such phenomena, modeling methods to assess mineralogical and geochemical conditions are also needed.

Near-Term R&D Plans: Near-term R&D plans refer to activities that could start in the next fiscal year.

Experimental Investigation of Fracture Growth, Sealing, and Healing Associated with EDZ Evolution in Clay Formations: Long-term performance of a nuclear waste repository depends on the extent and nature of the Excavation Damaged Zone (EDZ) around underground structures and the time-dependent processes during the transient stage until an equilibrium is reached (e.g., heat production from the decay of the waste, re-saturation processes) (Blümling et al., 2007). The objective of the proposed work is to improve understanding of fundamental processes governing the long-term evolution of the EDZ in a geological repository hosted in clay formations. Specifically, the proposed work will focus on the issue of fracture growth, sealing and healing within the EDZ.

Investigations at European underground rock laboratories have shown that an EDZ occurs in both soft plastic clays as well as indurated and more brittle clays (Blümling et al., 2007). Upon excavation, the rock adjacent to a tunnel wall is subject to mechanical extension, compression, and shear, causing fracturing, shear and dilation. The resulting fracturing pattern can be complex and strongly impacted by anisotropy in the host rock, as well as by relative humidity changes during ventilation. After emplacement of waste packages and backfill, re-saturation of the rock and swelling of the clay take place as well as increases in temperature and the recovery of ground water pressure. Time-dependent deformation (convergence) of the tunnel and the swelling of clay seal (hydraulically) and heal (mechanically) fractures in the EDZ, which then diminishes in spatial extent and magnitude.

In addition to hydromechanical effects, Van Geet et al. (2008) observed that clay swelling and resultant sealing of fractures are augmented by chemical reactions affected by the chemical composition of the water. For more comprehensive understanding of fracture sealing/healing behavior, clay and clay-rich rocks with different clay content, consolidation, and clay types (e.g., smectite, kaolinite, illite) need to be examined. Also, for a fracture within relatively lithified rock with small swelling clay content, mineral precipitation and dissolution within the fractures and microcracks becomes more important, especially under elevated temperature and for long duration.

The proposed task will examine the coupled behavior of fracture healing and sealing within EDZ using millimeter-scale cores to tens-of-centimeter-long cores. Near-term tasks are to initiate hollow cylinder compression tests, shaped-core uniaxial compression tests, and true-triaxial compression tests. Fractures and microcracks will be introduced in these cores, and subsequent sealing and healing will be monitored under a range of temperature, stress, and pore and fracture fluid chemistry. Miniature-core experiments, microtomography imaging will be conducted at the x-ray synchrotron beamline 8.3.2, at LBNL Advanced Light Source, using a specifically designed micro triaxial cell. For the experiments using larger cores, a medical x-ray CT scanner will be used. The monitoring will include stress-displacement measurements, permeability measurements, acoustic (seismic) measurements, and fluid sampling (for geochemical analysis). The obtained experimental data will be used to provide quantitative information for calibrating and verifying numerical models.

Constitutive Relationships for Coupled Processes in Clay Repositories: Understanding and modeling the coupled processes and their impact on repository performance requires knowledge of constitutive relationships for the host rock, especially relationships between hydraulic and mechanical properties, because these relationships control the degree of coupling among the relevant processes. Although considerable efforts have been made in developing constitutive relationships, the following important issues (associated with clay rock) have not been fully addressed in previous studies:

Water-content dependent swelling. Multiphase flow conditions develop in the excavation damaged zone (EDZ). Clay rock swells (or shrinks) with increasing (or decreasing) water content, resulting in significant rock property changes (including self-sealing of fractures). Previous studies on constitutive relationships have been focused on single-phase flow conditions and therefore their results are not applicable to swelling conditions.

Fracture properties. Connected fractures exist within the EDZ and may serve as paths for fast flow and radionuclide transport in a clay repository. However, there are only limited studies on constitutive relationships for fractures in clay rock in the literature.

Correlation between hydraulic and mechanical properties: Assessment of the impact of rock mechanical deformation on flow and transport needs knowledge regarding how the deformation is related to hydraulic property changes. At this stage, acceptable relationships for describing such a correlation are still lacking for fractured clay rock associated with swelling and shrinkage.

Near-term tasks are:

(1) A comprehensive literature survey of laboratory testing data of clay rock deformation under different stress conditions and the associated hydraulic properties. This survey will be analyzed with a focus on improving our understanding of mechanisms of coupled hydro-mechanical processes associated with swelling. The data will also be used for developing and validating constitutive relationship models.

(2) Develop new stress-strain relationships by extending the work of Liu et al. (2009) on elastic strain-stress relations, considering the dependence of mechanical properties on water content, and incorporating the new developments in the area of damage mechanics. Relationships to be developed will be verified by laboratory test data collected under a wide range of conditions.

Improved Model for Large-Scale Radionuclide Transport in Clay Rocks: Modeling of diffusive transport in clay rocks (natural system) is complicated by the existence of heterogeneities at different scales and coupling between diffusive and electro-chemical processes (Revil and Leroy, 2004; Appelo et al., 2010; Bourg et al., 2003; Jougnot et al., 2009). At a local scale, different pore spaces co-exist within a representative elementary volume (REV), or a “point” within the context of continuum mechanics. They include pore spaces surrounded by grains other than clay, pore spaces surrounded by clay and other grains, pore spaces surrounded by clay grains only, and interlayer spaces within clay grains. Dominant transport processes of radionuclide can be quite different for different pore spaces. For example, the coupling between diffusive and electro-chemical processes, or interaction between diffusion in bulk fluid and electrical double diffusion

layer near the clay surfaces, is negligible for pores surrounded by other grain particles, but critical for small pores surrounded by clay particles and inter-layer spaces. The last two pore-spaces are especially important for compacted clay systems (such as clay buffers in EBS). At large scales, diffusive transport may be subject to a considerable degree of spatial variability as a result of variability of physical and chemical properties of pore spaces. It is also well known that large-scale diffusive processes are not isotropic in clay rocks (Motellier, 2007). The diffusion coefficient is much larger along the bedding direction than that in the direction perpendicular to the bedding.

In the literature, two kinds of modeling approaches for diffusive transport in clay materials are available (Revil and Leroy, 2004; Appelo et al., 2010; Bourg et al., 2003; Jougnot et al., 2009). One is based on the explicit consideration of coupling between diffusive and electro-chemical processes. This approach can relatively accurately capture mechanisms of diffusive transport at small scales and is specifically useful for dealing with radionuclide transport in clay buffer systems. This research topic is discussed in the proposal concerning diffusive transport in the EBS (Steefel et al. 2010). However, it is relatively computationally intensive for dealing with large-scale problems. The second kind of approaches may be referred to as a phenomenological approach. It is based on Fick's diffusion law and uses semi-empirical constants to roughly incorporate the effects of electro-chemical processes, such as using the "accessible porosity" to consider anion exclusion effects and "surface diffusion" to consider effects of charged clay surface on cation diffusion. While this type of approach cannot capture the detailed transport mechanisms, it is relatively simple, computationally efficient, and straightforward to implement. Therefore, these approaches are still widely used for modeling diffusion processes in natural clay systems. Keeping in mind that our interest here is to develop an improved model for large-scale diffusive transport in clay rocks, the focus of this proposed work will be on the phenomenological approaches.

Although different degrees of successes have been obtained by using the currently available phenomenological approaches to analyze several site-specific tests (e.g., Appelo et al., 2010; Motellier et al., 2007), some key questions regarding their usefulness are open, considering the semi-empirical feature of the approaches. For example, a systematic evaluation of their effectiveness in capturing effects of pore-scale heterogeneities (the existence of different pore spaces) is not available yet for general natural clay systems. Large-scale heterogeneity (or spatial variability) may or may not be important for diffusive transport in clay rocks. Again, this is not fully investigated. Answers to these questions are critical for developing a scientifically defensible and practically useful modeling approach.

Near-term tasks are:

(1) A comprehensive literature survey of diffusion test data in natural clay rocks and the associated analysis results will be performed. The survey results will be documented in a project report and/or journal article and employed for evaluating and developing modeling approaches for the diffusive transport processes.

(2) Data sets for typical clay formations will be analyzed with three different modeling approaches. The first one is the traditional approach that is based on Fick's law and uses

K_d-type schemes to consider sorption and the effects of electro-chemical processes. The second approach is based on generalized Fick's law that uses "accessible porosity" to consider anion exclusion effects and "surface diffusion" to consider effects of charged clay surface on cation diffusion. The third one is a new approach (proposed in this study) that borrows the dual-continuum approach (used in describing flow and transport in fractured rock) to deal with the local-scale heterogeneities or the existence of different kinds of pore spaces. This approach, in principle, is consistent with test observations that solute transport in clay rock may be subject to a fast and a slow transport path (Van Loon and Jakob, 2005).

Analytical or numerical approaches will be used for data analyses. These three approaches will be evaluated based on their accuracy in representing the data sets, their usefulness for different clay formations, consistency of parameter values for similar clay formations for a given approach, and numbers of fitting parameters for different approaches. Ultimately, this task will provide guidance on the usefulness and limitations of each approach under different conditions.

Impact of Large-Scale Natural Disturbances to Clay/Shale Host Rock: The condition of a clay/shale host rock repository can be impacted by natural geologic phenomena, both prior to or after waste emplacement. Typically, a clay or shale host rock considered for nuclear waste disposal has bulk permeability in the range of microdarcies to nanodarcies, a key performance characteristic that is significant for impeding radionuclide migration from waste emplacement locations. Therefore, it is important to understand the potential for geologic phenomena to degrade this favorable condition.

Because of their low permeability, argillaceous rocks commonly act as caprocks for trapping buoyant petroleum liquids and gasses. Extensive research into the characteristics of argillaceous rocks as caprocks for petroleum systems (and more recently as caprocks for geologic carbon sequestration) has led to significant findings about how they behave over long time periods. Furthermore, the economic incentive for petroleum exploration has enabled the investigation of argillaceous caprocks over a broader range of geologic environments than is likely to be feasible for nuclear waste disposal.

The overriding observation of significance from petroleum analogues for nuclear waste disposal is that hydrocarbon reservoirs can deplete naturally as a result of caprock failure (Nijhuis 1997). About 50% of the basins with known petroleum reserves show visible evidence of leakage (Clarke et al. 1991). In other words, although clay/shale caprocks are capable of acting as low-permeability barriers, these barriers are not absolute and their effectiveness can change over time.

There are several mechanisms leading to caprock failure (Corcoran et al. 2002), including reactivation of exiting faults through tectonic processes or hydraulic overpressure (Cartwright et al. 2007). Furthermore, numerous argillaceous formations have been found to have layer-bound, non-tectonic faults known as polygonal faults (Cartwright 1997). Other mechanisms for caprock failure include intrusions from igneous and hydrothermal activity, clastic intrusions from sandstone or mud, and salt intrusions. Magmatic activity could cause substantial changes to

caprocks by the direct intrusion of magma bodies or through mechanical stress induced by the heat and associated vaporization of water. Similarly, the temperature effects of a geothermal system on mechanical stress within the caprock could induce fracturing or fault reactivation. Collapse structures caused by dissolution of evaporites and collapse of source chambers for intrusion material (e.g., mud volcanoes) can also lead to caprock failure. Conditions that may influence such phenomena include the tectonic environment and regional stress field, surficial processes (e.g. sedimentation, erosion, glaciation), stratigraphic composition, sources and compositions of recharge, and the diagenetic history of the host rock.

The near term tasks for this effort are:

(1) The first step is to identify sites with information concerning the current material properties and mineralogy of specific petroleum reservoir caprocks, their diagenetic histories, and information concerning leakage. This task will comprise a literature survey to gather the available information.

(2) The second step is to classify the analogues in terms of leakage or no leakage. The known or suspected mechanism of leakage will be used to further classify the cases with leakage. The recent review of seal bypass systems by Cartwright et al. (2007) will serve as a guide for classification.

Longer-term R&D Plans: Longer-term R&D plans are for activities that require some prerequisite activities to complete or additional plan development.

Modeling of Fracture Growth, Sealing, and Healing Associated with EDZ Evolution in Clay Formations: Experimental work will continue longer term to complete tests discussed in Section 5.2.1.1. The laboratory test results will then be used for to check and validate modeling of sealing and healing. This includes simulation of linked reactive transport modeling and geomechanics using the reactive transport simulator TOUGHREACT linked with the geomechanical simulator FLAC^{3D}. We will also test other modeling approaches such as distinct element method (DEM) and boundary element method (BEM) for explicit modeling of fracture propagation, sealing and healing.

A second modeling effort is to investigate behavior at the tunnel scale. The modeling of fracture growth, sealing and healing explicitly will require discrete representation of each individual fracture. However, the evolution of the EDZ is driven by the time dependent processes that require a large scale model of the repository drift within a repository horizon. Therefore, the tunnel scale modeling will be divided into a near-field model domain and a large-scale model domain. The large-scale model domain will be used to derive time-dependent boundary and interior conditions to be imposed on the near-field model domain. The large-scale model simulation will include complete analyses of rock and bentonite buffer, to calculate the evolution of temperature, fluid pressure, bentonite saturation and swelling, and thermal stresses, occurring over a 100,000 year repository lifetime. The near-field model domain allows for a very fine model discretization, enabling detailed studies of fracture growth, sealing and healing in the EDZ.

A similar approach was successfully employed within the international DECOVALEX project for modeling of the EDZ associated with bentonite backfilled repository drifts in crystalline rocks (Hudson et al., 2009; Rutqvist et al., 2009).

The near-field modeling simulations will be conducting using several modeling methods:

(1) Finite element type models with fine element discretization (e.g. ROCMAS, and FLAC^{3D} coupled with TOUGHREACT).

(2) Distinct Element Method (DEM) modeling (e.g. PFC, UDEC).

(3) Boundary Element Modeling (BEM) fracture propagation modeling (FRACON).

All of these modeling methods were recently applied in the international DECOVALEX project for studying the evolution of the EDZ in crystalline rocks (Rutqvist et al., 2009).

Constitutive Relationships for Coupled Processes in Clay Repositories: The work on constitutive relationships initiated with items identified in the near-term plans will lead into the following longer-term tasks:

(1) Functional relationships will be investigated between flow properties and mechanical properties for clay rock. A methodology will be developed to estimate the relevant parameter values from common laboratory measurements. Numerical experiments will be performed for investigating multiphase flow behavior under different stress (and damage) conditions. These functional relationships will be carefully evaluated with experimental data obtained from the literature review. Hydraulic and mechanical properties are closely related to geochemical reactions. Pore-scale modeling will be performed to investigate impact of mineral dissolution and precipitation on hydraulic properties.

(2) A dual-continuum (fracture and rock matrix) approach will be developed for modeling coupled processes in the EDZ. Governing equations for multiphase flow and mechanical deformation will be investigated based on the constitutive relationships developed from Tasks 2 and 3. Simulations (using the TOUGH2-FLAC code with the dual-continuum approach to be developed) will be performed for a selected field study site where data are available to demonstrate the usefulness of the new developments from the project.

(3) In the course of these investigations, data gaps and needs will be identified. Laboratory experiments will be performed to address these gaps. They very likely deal with multiphase flow properties under different stress and geochemical conditions subject to swelling and shrinkage. Test results from Section 5.2.1.1 will also be used.

Improved Model for Large-Scale Radionuclide Transport in Clay Rocks: The work on large-scale transport modeling methods initiated with items identified in the near-term plans will lead into the following longer-term tasks:

(1) It is well known that spatial variability generally has important effects on subsurface flow and transport processes. However, it is not totally clear whether the variability is important for radionuclide (diffusive) transport in clay rock. To evaluate its relative importance, we will computationally generate spatially variable transport-parameter distributions within a two-dimensional domain, and then simulate the diffusive transport (using the numerical method discussed below) by explicitly considering the variability. The simulated breakthrough curves will be compared with those without considering spatial variability. If the difference is significant, an upscaling method will be developed to estimate large-scale transport parameters.

(2) A particle-tracking numerical modeling approach will be developed for radionuclide transport in clay rocks, because it is computationally efficient, easy to implement and has very limited numerical-dispersion for a large-scale problem. In a particle-tracking approach, a continuous concentration field is represented by a great number of solute particles whose movements are random and controlled by transport parameters. The particle-tracking approach is also developed in such a way that it can handle the anisotropy of diffusion process that, as discussed above, is common in clay formations with bedding.

(3) Using approaches developed in this investigation, conduct modeling exercises of radionuclide transport in clay formations under different conditions. The modeling results will allow for identification of key parameters, processes, and formation structures for radionuclide transport in a clay repository.

Impact of Large-Scale Natural Disturbances to Clay/Shale Host Rock: The evaluation of large-scale host rock disturbance initiated with items identified in Section 5.2.1.4 will lead into the following longer-term tasks:

(1) Select cases that are suitable for further quantitative study as analogues. This includes the development of methods to incorporate various external conditions that affect mechanical conditions in the rock. Factors such as erosion, glaciation, sedimentation, dissolution, tectonics, igneous activity, and geothermal activity need to be considered. This type of analysis is analogous to basin modeling used for petroleum exploration (e.g. Makurat et al. 1992; Kacewicz 2003), however in this case the model will be carried into the future to evaluate the repository performance period. The basin modeling approach has been used to explain burial history of the Opalinus Clay (Mazurek et al. 2003) and hydrologic phenomena in the Paris Basin (Jost et al. 2005) for nuclear waste studies.

The general basin modeling problem for a clay/shale formation includes the effects of burial and uplift, and associated thermal, mechanical, and chemical variations. The impacts of events that could occur entirely within the model domain or events driven by factors external to the model domain need to be added to the basic basin model for diagenesis. Therefore, some method to address coupled processes is required. The study by Rutqvist et al. (2008b) provides a detailed analysis of coupled hydro-geomechanical effects on caprock integrity for CO_2 sequestration. Recasting such an analysis for a

petroleum reservoir caprock analogue or nuclear waste disposal problem would need to be expanded in terms of the processes under consideration and time frame. The main focus of these exercises is to assess the potential creation or reactivation of faults or fractures and/or creation of intrusion/collapse structures during the performance period, although they may also be useful for evaluating the potential for such host-rock damage to be part of the present-day system.

(2) Use the results from above to identify hydrological, geophysical, and geochemical measurements that can help to define and constrain the effects of bypass systems on clay/shale host rock repository environments.

6. Summary and FEPs Crosswalk

Constitutive Relationships for Elastic Deformation of Indurated Clay Rock

Constitutive relationships for the hydromechanical behavior of porous and fractured clay rock are developed in this report. It was proposed that for a porous rock, the pore spaces may be subject to large relative strain as compared to the solid grains. Thus, for the pores, relative volumetric strain needs to be defined in terms of the change in rock volume upon a change in stress relative to the total volume at the new stress level. This contrasts with the conventional definition of relative volumetric strain, in which the change in rock volume is taken relative to the total volume at the original stress level. This leads to a reformulation of Hooke's law for the pore spaces within a porous rock in which the differential stress-strain ratio is not a constant but an exponential function of strain. The stress-strain relationships for the solid grains, following the traditional Hooke's law, and the new relationship for pore spaces are combined to give a bulk modulus that is not a constant, but a nonlinear function of stress. Uniaxial test data were analyzed for core samples of Opalinus clay and laboratory measurements of single fractures within macro-cracked Callovo-Oxfordian argillite samples subject to both confinement and water-reduced swelling. This data was used to test the proposed hydromechanical constitutive relationships. Given the nonlinearity and complexities shown in the data, the agreement between the theoretical results and data supports the validity of the proposed constitutive relationships.

THM Processes in Claly/Shale

There are several software codes available for analyzing THM processes in geologic media. The TOUGH-FLAC and ROCMAS codes were reviewed in detail for this report. The code TOUGH-FLAC uses a continuum method to represent fractures and couples thermal-hydrologic modeling using TOUGH with geomechanical modeling using FLAC to address THM processes. The current version of TOUGH-FLAC includes the recently developed BBM, a geomechanical constitutive relationship for thermo-elastoplastic behavior that is observed in bentonite. The code ROCMAS provides a discrete fracture representation for THM process including single-phase unsaturated flow. ROCMAS has several options for geomechanical constitutive relationships but currently does not include the BBM**.** The ROCMAS code and

TOUGH-FLAC are two different types of simulators that complement each other, have been extensively applied, and yet have the flexibilities for modifications and future improvements.

The TOUGH-FLAC software was tested on a full-scale nuclear waste repository problem involving the interaction of multiple components (buffer, canister, rock) over a 100,000 year simulation time. The simulation studies investigated coupled THM processes for a bentonite-backfilled EBS in a low-permeability clay host rock. This study highlight the important interactions between the buffer and the host rock, in particular regarding the potential for desaturation of the rock and thermal pressurization, which can have a significant impact on coupled THM evolution.

THC Modeling in Clay/Shale

The TOUGHREACT software code was evaluated as a tool reactive-diffusive transport in a clay/shale host rock. TOUGHREACT is a comprehensive non-isothermal multi-component reactive fluid flow and geochemical transport simulator. Aqueous complexation, acid-base, redox, gas dissolution/exsolution, and cation exchange are considered under the local equilibrium assumption. Mineral dissolution and precipitation can proceed either subject to local equilibrium or kinetic conditions. Linear adsorption and decay can be included. The chemical-hydrological couplings between mineral dissolution/precipitation and fluid flow are included through the treatment of temporal changes in porosity, permeability, and unsaturated hydrologic properties. Transport of aqueous and gaseous species by advection and molecular diffusion are considered in both liquid and gas phases.

An analysis of THC processes was conducted to simulate water-rock interactions around nuclear waste packages emplaced in clay formation with bentonite backfill. Although the analysis is a simplified case, the problem illustrates typical coupled thermal-hydrological-chemical processes that could occur in the EBS and clayey host rock around nuclear waste packages as influenced by the very different near-field mineralogy and water chemistry. The problem includes specific and distinct mineral and pore-water compositions of the bentonite and clay rock, and includes kinetically-controlled mineral precipitation and dissolution reactions. The model computes mineral precipitation and dissolution as well as porosity changes over the first 1000 years following waste emplacement, with a peak temperature of 98° C. The diffusive mass transfer between bentonite and clay formation and the change of temperature lead to mineral alteration in bentonite and clay formation, especially in the interface area. Minerals alteration in the clay near-field is characterized by the dissolution of calcite, siderite and illite and precipitation of ankerite, smectite and quartz, while porosity changes are minor.

The following table identifies work done in this report with the used fuel disposition (UFD) FEPs (Houseworth 2010) associated with clay/shale host rock.

Table 6-1. FEPs crosswalk

UFD FEP number	UFD FEP name	Report Sections	Information Provided
1.1.02.02	Mechanical Effects from Preclosure Operations	2, 3, and 5	Detailed treatment of THM constitutive relationships and near-field modeling; brief review of issues
1.1.02.03	Thermal-Hydrologic Effects from Preclosure Operations	3 and 5	Detailed treatment of near-field THM modeling; brief review of issues
2.1.09.01	Chemistry of Water Flowing into the Repository	4 and 5	Detailed treatment of near-field THC; brief review of issues
2.2.11.05	Effects of Influx (Seepage) on Thermal Environment	3 and 4	Very low natural influx used in analyses has negligible effect on thermal environment.
2.2.01.01	Evolution of EDZ	2, 3, and 5	Detailed treatment of THM constitutive relationships and near-field modeling; brief review of issues
2.2.08.04	Effects of Repository Excavation on Flow through the Host Rock	None	Requires additional investigation, particularly with respect to the EDZ.
2.2.08.05	Condensation Forms in Host Rock	3 and 4	Sub-boiling temperatures leads to relatively minor effects of condensation
2.2.08.06	Flow through the EDZ	2	Detailed treatment of THM constitutive relationships
2.2.09.61	Radionuclide transport through EDZ	5	Brief review of issues
2.2.05.01	Fractures	2 and 5	Detailed treatment of THM constitutive relationships and brief review of issues
2.2.05.02	Faults	5	Brief review of issues
2.2.05.03	Alteration and Evolution of NBS Flow Pathways	5	Brief review of issues
2.2.07.01	Mechanical Effects on Host Rock	2, 3, and 5	Detailed treatment of THM constitutive relationships and modeling; brief review of issues
2.2.08.01	Flow through the Host Rock	5	Brief review of issues
2.2.08.03	Effects of Recharge on NBS Flow	5	Brief review of issues
2.2.09.03	Chemical Interactions and Evolution of Groundwater in Host Rock	4 and 5	Detailed treatment of near-field THC; brief review of issues
2.2.09.51	Advection of Dissolved Radionuclides in Host Rock	5	Brief review of issues
2.2.09.53	Diffusion of Dissolved Radionuclides in Host Rock	5	Brief review of issues

7. References

Alonso E.E., Alcoverro, J., et al. (26 co-authors) The FEBEX benchmark test. Case definition and comparison of modelling approaches. International Journal of Rock Mechanics & Mining Sciences 42, 611-638, 2005.

Appelo, C.A.J., L. R. Van Loon and P. Wersin, Multicomponent diffusion of a suit of tracers in a single sample of Opalinus clay, Geomochimica Acta 74 1201-1219, 2010.

Appelo, C.A.J., and Postma, D., *Geochemistry, groundwater and pollution*, Rotterdam, The Netherlands, Balkema, 536 pp., 1993.

Barnichon J.D., Volckaert G. Observations and Predictions of Hydromechanical Coupling Effects in the Boom Clay, Mol Underground Research Laboratory, Belgium. Hydrogeology Journal 11 (1): 193-202. 2003.

Biot, M.A., General theory of three dimensional consolidation. *J. Applied Physics*, 12, 155–164., 1941.

Blumling P., Bernier F., Lebon P., Martin C.D. The Excavation Damaged Zone in Clay Formations Time-Dependent Behavior and Influence on Performance Assessment. Physics and Chemistry of the Earth 32: 588-599. 2007.

Bower, K.M. and Zyvoloski, G. A numerical model for thermo-hydro-mechanical coupling in fractured rock. *Int. J. Rock Mech. Min. Sci. & Geomech. Abstr*., 34, 1201–1211, 1997.

Börgesson, L., ABAQUS. In Stephansson, O., Jing, L., and Tsang, C.-F. editors, *Coupled Thermo-hydro-mechanical Processes of Fractured Media*. Developments in Geotechnical Engineering, Elsevier, 79, pp. 565–570, 1996.

Bourg, I.C., A. C. M. Bourg and G. Sposito, Modeling diffusion and adsorption in compacted bentonite: a critical review. Journal of Contaminant Hydrology 61, 293-302, 2003.

Caillet, G. The Caprock of the Snorre Field, Norway: A Possible Leakage by Hydraulic Fracturing, Marine and Petroleum Geology, 1993, Vol 10, February, pp. 42-50, 1993.

Cartwright, J. Polygonal Extensional Fault Systems: A New Class of Structure Formed During the Early Compaction of Shales, from Fluid Flow and Transport in Rocks: Mechanisms and Effects, Bjørn Jamtveit, B. W. D. Yardley, 1997.

Cartwright, J.; Huuse, M.; Aplin, A. Seal Bypass Systems, *AAPG Bulletin*; August 2007; v. 91; no. 8; p. 1141-1166, 2007.

Clarke, R.H., and Cleverly, R.W. Petroleum Seepage and Post-Accumulation Migration, in England, W.A., and Fleet, A.J., (eds.), Petroleum migration, London, The Geological Society: p. 265–271, 1991.

Corcoran, D.V.; Dore, A.G. Top Seal Assessment in Exhumed Basin Settings – Some Insights from Atlantic Margin and Borderland Basins, in Hydrocarbon Seal quantification: Papers Presented at the Norwegian Petroleum Society Conference. Norsk Petroleumsforening. Editors: Andreas G. Kostler and Robert Hunsdale, Elsevier 2002.

Corkum A.G., Martin C.D. The mechanical behavior of week mudstone (Opalinus Clay) at low stress. International Journal of Rock Mechanics & Mining Sciences 44: 196-209. 2007a

Corkum A.G., Martin C.D. Modeling a mine-by test at the Mont Terri rock laboratory, Switzerland. International Journal of Rock Mechanics & Mining Sciences 44: 846-859. 2007b

Darby, D.; Funnell, R.H. Overpressure Associated with a Convergent Plate Margin: East Coast Basin, New Zealand, *Petroleum Geoscience*; September 2001; v. 7; no. 3; p. 291-299. 2001.

Dobson, P.F., T.J. Kneafsey, E.L. Sonnenthal, N.F. Spycher, and J.A. Apps, Experimental and numerical simulation of dissolution and precipitation: Implications for fracture sealing at Yucca Mountain, Nevada. Journal of Contaminant Hydrology. 62-63: 459-476, 2003.

Davy C.A., Skoczylas F., Barnichon J.D., Lebon P. Permeability of Macro-Cracked Argillite under Confinement: Gas and Water Testing. Physics and Chemistry of the Earth 32: 667-680. 2007.

Fernandez A.M., M.J. Turrero, D.M. Sanchez, A. Yllera, A.M. Melon, M. Sanchez, J. Pena, A. Garralon, P. Rivas, P. Bossart P. Hernan, 2006, On site measurements of the redox and carbonate system parameters in the low- permeability Opalinus Clay formation at the Mont Terri Rock Laboratory, Physics and Chemistry of the Earth 32 (2007) 181–195

Fouche O., Wright H., Cleach J.L., Pellenard P. Fabric Control on Strain and Rupture of Heterogeneous Shale Samples by Using a Non-Conventional Mechanical Test. Applied Clay Science 26: 367-387. 2004.

Gonzales, S. and Johnson, K.S. Shale and other argillaceous strata in the United States. Oak Ridge National Laboratory. ORNL/Sub/84-64794/1. 1984.

Gray, I. Reservoir Engineering in Coal Seams: Part 1—The Physical Process of Gas Storage and Movement in Coal Seams. SPE Reserv. Eng., **2**(1), 28–34, 1987.

Guvanasen, V. and Chan, T. A new three-dimensional finite-element analysis of hysteresis thermohydromechanical deformation of fractured rock mass with dilatance in fractures. *Proceedings of the 2nd Conference on Mechanics of Jointed and Faulted Rocks*, Vienna, Austria, April 10–14, 1995, pp. 347–442.

Houseworth, J.E. The DOE Used Fuel Disposition Campaign Features, Events, and Processes (FEP) Evaluation Report for Bentonite/Clay/Shale Systems, DOE Used Fuel Disposition Campaign, Lawrence Berkeley National Laboratory. 2010.

Hudson J A, Bäckström A, Rutqvist J, Jing L, Backers T, Chijimatsu M, Christiansson R, Feng X-T, Kobayashi A, Koyama T, Lee H-S, Neretnieks I, Pan P-Z, Rinne M, Shen B-T Characterising and Modelling the Excavation Damaged Zone (EDZ) in Crystalline Rock in the Context of Radioactive Waste Disposal. Environ Geol, 57, 1275–1297, 2009.

Israelsson, J.I., Short description of FLAC version 3.2. In Stephansson, O., Jing, L., and Tsang, C.-F. editors. *Coupled Thermo-hydro-mechanical Processes of Fractured Media*. Developments in Geotechnical Engineering, Elsevier, 79, pp. 513–522, 1996a.

Israelsson, J.I., Short description of UDEC and 3DEC. In Stephansson, O., Jing, L., and Tsang, C.-F. editors. *Coupled Thermo-hydro-mechanical Processes of Fractured Media*. Developments in Geotechnical Engineering, Elsevier, 79, pp. 523–528, 1996b.

Itasca Consulting Group, FLAC3D, Fast Lagrangian Analysis of Continua in 3 Dimensions, Version 4.0, Minneapolis, Minnesota, Itasca Consulting Group, 2009.

Jaeger J.C., Cook N.G.W., Zimmerman R.W. Fundamentals of Rock Mechanics (4th Edn). Malden: Blackwell Publishing. 2007.

Jobmann M, Wilsnack Th., Voigt H.D. Investigation of Damage-Induced Permeability of Opalinus Clay. International Journal of Rock Mechanics & Mining Sciences 46: 279-285. 2010.

Jougnot, D., Revil, A., and Leroy, P. Diffusion of Ionic Tracers in the Callovo-Oxfordian Clay-Rock using the Donnan Equilibrium Model and the Formation Factor. Geochimica et Cosmochimica Acta 73, 2712-2726. 2009.

Jost, A.; Violette, S.; Goncalves, J.; Kageyama, M.; Ramstein, G.; Emmanuel, L.; de Marsily, G. Flow and Transport Modelling in the Paris Basin over Geologic Time, IAH –Spanish chapter International workshop: From data gathering and groundwater modelling to integrated management, Alicante, Spain, 4-8 October, 2005.

Kacewicz, M. 3D Basin Modeling Around the World – Example Problems and Solutions, Geological Society of America Abstracts with Programs, Vol. 35, No. 6, September, 2003, p. 338, 2003.

Kohl, T. and Hopkirk, R.J. The finite element program "FRACTure" for the simulation of Hot Dry Rock reservoir behavior. *Geothermics*, 24, 345–359, 1995.

Kolditz O., Bauer S., Beinhorn M., de Jonge J., Kalbacher T., McDermott C., Wang W., Xie M., Kaiser R., Kohlmeier M. ROCKFLOW - Theory and Users Manual, Release 3.9, Groundwater Group, Center for Applied Geosciences, University of Tübingen, and Institute of Fluid Mechanics, University of Hannover, 2003.

Koutsabeloulis, N.C. and Hope, S.A., Coupled stress/fluid/thermal multi-phase reservoir simulation studies incorporating rock mechanics. *Proceedings of SPE/ISRM EUROCK-98 symposium*, Norway, 1998, pp. 449–454.

Lasaga, A.C., J.M. Soler, J. Ganor, T.E. Burch and K.L. Nagy, 1994. Chemical weathering rate laws and global geochemical cycles. Geochimica et Cosmochimica Acta, 58, 2361-2368.

Lasaga, A. C. Chemical kinetics of water-rock interactions, *J. Geophys. Res*., v. 89, p. 4009-4025, 1984.

Lichtner, P. C. Continuum formulation of multicomponent-multiphase reactive transport, in Lichtner, P. C., Steefel, C. I., and Oelkers, E. H. (eds.), *Reactive transport in porous media*, Reviews in Mineralogy, Mineral Society of America, v. 34, p. 1-79, 1996.

Liu, H.H., J. Rutqvist, and J.C. Berryman, On the relationship between stress and elastic strain for porous and fractured rock, *Int J Rock Mech & Min Sci* 46, 289–296, 2009.

Liu H.H. and Rutqvist J. (2010) A new coal-permeability model: Internal swelling stress and fracture matrix interaction. Transport in Porous Media 82(1): 157-171.

Liu Q., Zhang C., Liu X. A practical method for coupled THM simulations of the Yucca Mountain and FEBEX case samples for task D of the DECOVALEX-THMC Project. Proc. GEOPROC2006 International symposium: 2nd International Conference on Coupled Thermo-hydro-mechanical-chemical processes in Geosystems and Engineering, HoHai University, Nanjing, China, May 22–25, 2006, 220–225, HoHai University, 2006.

Makurat, A.; Torudbakken, B.; Monse, K.; Rawlings, C. Cenezoic Uplift and Caprock Seal in the Barents Sea: Fracture Modeling and Seal Risk Evaluation, Paper Number 24740-MS, SPE Annual Technical Conference and Exhibition, October 4-7, 1992, Washington, D.C, 1992.

Mazurek, M.; Pearson, F. J.; Volckaert, G.; and Bock, H. Features, Events and Processes Evaluation Catalogue for Argillaceous Media. ISBN 92-64-02148-5. Nuclear Energy Agency. 2003.

Meier P., Trick T., Blumling P., Volckaert G. Self-Healing of Fractures within the EDZ at the Mont Terri Rock Laboratory: Results after One Year of Experimental Work. In: Proceedings of the International Workshop on Geomechanics, hydromechanical and

Thermomechanical Behavior of deep argillaceous Rocks: Theory and Experiments, Paris, October11-12, 2000.

Motellier S., I. Devol-Brown, S. Savoye, D. Thoby, and J.C. Alberto, Evaluation of Tritiated Water Diffusion through the Toarcian Clayey Formation of Tournemire Experimental Site (France). Journal of Contaminant Hydrology 94, 99-108, 2007.

Neuzil, C.E. Osmotic Generation of `Anomalous' Fluid Pressures in Geological Environments. Nature. Vol. 403 pp. 182-184 2000.

Nguyen, T.S. Description of the computer code FRACON. In Stephansson, O., Jing, L., and Tsang, C.-F. editors. *Coupled Thermo-hydro-mechanical Processes of Fractured Media*. Developments in Geotechnical Engineering, Elsevier, 79, pp. 539–544, 1996.

Nijhuis, H.J. Prediction of Volumes and Risk in Hydrocarbon Exploration: A Quantification of Geology, Geol Rundsch (1997) 86:322-331, 1997.

Noorishad, J., Tsang, C.-F. and Witherspoon, P.A. Coupled thermal-hydraulic-mechanical phenomena in saturated fractured porous rocks: numerical approach. *J. Geophys. Res.*, 89, 10365–10373, 1984.

Noorishad, J., and Tsang, C.-F. ROCMAS-simulator: A Thermohydromechanical Computer Code. In Stephansson, O., Jing, L., and Tsang, C.-F. editors. *Coupled Thermo-hydro-mechanical Processes of Fractured Media*. Developments in Geotechnical Engineering, Elsevier, 79, pp. 551–558, 1996.

Nordstrom, D. K., and Muñoz, J. L. *Geochemical Thermodynamics*, The Benjamin/Cummings Pub. Co., Menlo Park, California, 477 pp., 1986.

Ochs M., Lothenbach B., Shibata M., and Yui M., Thermodynamic modeling and sensitivity analysis of porewater chemistry in compacted bentonite, Physics and Chemistry of the Earth, Parts A/B/C, Volume 29, Issue 1, (2004), 129-136.

Ohnishi, Y. and Kobayashi, A., THAMES. In Stephansson, O., Jing, L., and Tsang, C.-F. editors. *Coupled Thermo-hydro-mechanical Processes of Fractured Media*. Developments in Geotechnical Engineering, Elsevier, 79, pp. 545–549, 1996.

Palandri, J., and Kharaka, Y. K. A compilation of rate parameters of water-mineral interaction kinetics for application to geochemical modeling, US Geol. Surv. Open File Report 2004-1068, 64 pp., 2004.

Patriarche D., Ledoux E., Simon-Coincon R., Michelot J., Cabrera J. Characterization and Modeling of Diffusive Process for Mass Transport through the Tournemire Argillites Aveyron, France. Applied Clay Science 26: 109-122, 2004.

Philip J.R. The Theory of Infiltration: 1. The Infiltration Equation and its Solution. Soil Science, 83: 345-358, 1957.

Philip, J.R. and de Vries, D.A. Moisture movement in porous material under temperature gradients. *EOS Trans*., AGU, 38, 222–232, 1957.

Pine, R.J. and Cundall, P.A. Application of the fluid rock interaction program (FRIP) to the modeling of hot dry rock geothermal energy systems. In Stephansson, O., editor. *Proceedings of the International Symposium on Fundamentals of Rock Joints*, Björkliden, Sweden, pp. 293–302, 1985.

Popp T., Salzer K., Minkley W. Influence of Bedding Planes to EDZ-Evolution and the Coupled HM Properties of Opalinus Clay. Physics and Chemistry of the Earth 33: 5374-5387. 2008.

Pruess, K., Oldenburg, C.M., and Moridis, G.M. TOUGH2 User's Guide Version 2. E. O. Lawrence Berkeley National Laboratory Report LBNL-43134, November 1999.

Pruess, K., TOUGH2: A general numerical simulator for multiphase fluid and heat flow, Lawrence Berkeley Laboratory Report LBL-29400, Berkeley, California, 1991.

Pruess, K. TOUGH user's guide, Nuclear Regulatory Commission, report NUREG/CR-4645 (also Lawrence Berkeley Laboratory Report LBL-20700, Berkeley, California), 1987.

Raffensperger, J. P. Numerical simulation of sedimentary basin-scale hydrochemical processes, In Advances in Porous Media, Corapcioglu, Y. C., (ed.), Amsterdam, The Netherlands, Elsevier Science, 440 pp., 1996.

Revil, A. and P. Leroy, Constitutive equations for ionic transport in porous shales, *J. Geophys. Res.* **109**, p. B03208, 2004.

Rutqvist J., Bäckström A., Chijimatsu M., Feng X-T, Pan P-Z., Hudson J, Jing L., Kobayashi A., Koyama T., Lee H-S, Huang X-H, Rinne M. and Shen B. Multiple-Code Simulation Study of the Long-Term EDZ Evolution of Geological Nuclear Waste Repositories. Environ Geol, 57, 1313–1324, 2009.

Rutqvist J. and Moridis G.J. Numerical Studies on the Geomechanical Stability of Hydrate-Bearing Sediments. Society of Petroleum Engineers SPE Journal 14: 267-282. SPE-126129, 2009.

Rutqvist J, Freifeld B, Min K-B, Elsworth D, Tsang Y. Analysis of thermally induced changes in fractured rock permeability during eight years of heating and cooling at the Yucca Mountain Drift Scale Test. Int J Rock Mech & Min Sci 45, 1373–1389, 2008a.

Rutqvist, J.; Birkholzer, J.T.; Tsang, C.F. Coupled Reservoir-Geomechanical Analysis of the Potential for Tensile and Shear Failure Associated with CO_2 Injection in Multilayered Reservoir-Caprock Systems, International Journal of Rock Mechanics and Mining Sciences, Vol. 45 pp. 132-143, 2008b.

Rutqvist, J. and Tsang, C.-F. A study of caprock hydromechanical changes associated with CO2-injection into a brine formation. Environmental Geology, 42: 296-305. 2002.

Rutqvist, J. and Tsang, C.-F. A fully coupled three-dimensional THM analysis of the FEBEX in situ test with the ROCMAS code: prediction of THM behavior in a bentonite barrier, In: Stephansson, O., Hudson, J.A., Jing, L., (Eds.) Coupled T-H-M-C Processes in Geo-Systems: Fundamentals, Modelling, Experiments and Applications. Elsevier Geo-Engineering Book Series, Oxford, p. 143–148, 2004.

Rutqvist J., Y.-S. Wu, C.-F. Tsang, and G. Bodvarsson A Modeling Approach for Analysis of Coupled Multiphase Fluid Flow, Heat Transfer, and Deformation in Fractured Porous Rock *Int. J. Rock Mech. & Min. Sci.* 39, 429-442, 2002.

Rutqvist J., Börgesson L., Chijimatsu M., Nguyen T. S., Jing L., Noorishad J., and Tsang C.-F. Coupled Thermo-hydro-mechanical Analysis of a Heater Test in Fractured Rock and Bentonite at Kamaishi Mine – Comparison of Field Results to Predictions of Four Finite Element Codes. *Int. J. Rock Mech. & Min. Sci.* 38, 129-142, 2001.

Settari, A., and F.M. Mourits, A Coupled reservoir and Geomechanical Simulation System, *SPE Journal*, 27(9), 219-226, SPE paper 50939, 1998.

Shi, J.Q., Durucan, S., Syahrial, E. Reservoir Depletion Induced Changes in Coalbed Permeability and Implications for Enhanced CBM Recovery Using CO_2 Injection. Geol. Belg. **7**, 123–127, 2004.

Slider, H. C., Practical petroleum reservoir engineering methods, An Energy Conservation *Science*. Tulsa, Oklahoma, Petroleum Publishing Company, 1976.

Sonnenthal, E. Chapter 5 in: Birkholzer, J. Rutqvist, E. Sonnenthal, and D. Barr, 2008, Long-Term Permeability/Porosity Changes in the EDZ and Near Field due to THM and THC Processes in Volcanic and Crystalline-Bentonite Systems, DECOVALEX-THMC Project Task D Final Report, 2008.

Sonnenthal, E., Ito, A., Spycher, N., Yui, M., Apps, J., Sugita, Y., Conrad, M., Kawakami, S., Approaches to modeling coupled thermal, hydrological, and chemical processes in the Drift Scale Heater Test at Yucca Mountain. International Journal of Rock Mechanics and Mining Sciences 42 (2005), 6987-719.

Steefel, C.; Rutqvist, J.; Tsang, C.F.; Liu, H.H.; Sonnenthal, E.; Birkholzer, J. Reactive Transport and Coupled THM Processes in Engineering Barrier Systems (EBS), DOE Used Fuel Disposition Campaign, Lawrence Berkeley National Laboratory, 2010.

Steefel, C. I., and Lasaga, A. C. A coupled model for transport of multiple chemical species and kinetic precipitation/dissolution reactions with applications to reactive flow in single phase hydrothermal system, *Am. J. Sci.*, v. 294, p. 529-592, 1994.

Steefel, C. I., and MacQuarrie, K. T. B. Approaches to modeling of reactive transport in porous media, In Lichtner, P. C., Steefel, C. I., and Oelkers, E. H. (eds.), Reactive transport in porous media, Reviews in Mineralogy, Mineral Society of America, v. 34, p. 83-129, 1996.

Swenson, D.V., DuTeau, R. and Sprecker, T. A coupled model of fluid flow in jointed rock applied to simulation of a hot dry rock reservoir. *Int. J. Rock Mech. Min. Sci. & Geomech. Abstr.*, 34, Paper 308, 1997.

Thury M. The characteristics of the Opalinus Clay investigated in the Mont Terri underground rock laboratory in Switzerland, C. R. Physique, 3(2002), 923-933.

Tsang, C.-F.; Bernier, F.; Davies, C. Geohydromechanical Processes in the Excavation Damaged Zone in Crystalline Rock, Rock Salt, and Indurated and Plastic Clays—in the Context of Radioactive Waste Disposal, *Int. J. Rock Mech.& Min. Sci.* 38, pp. 109-125, 2005.

Tsang, C.F.; Birkholzer, J.; Liu, H.H. 2010. "A Review of Key Processes and Outstanding Issues Related to Radioactive Waste Repositories in Clay Formations", DOE Used Fuel Disposition Campaign, Lawrence Berkeley National Laboratory.

Van Geet M., Bastiaens W., and Ortiz L. Self-sealing capacity of argillaceous rocks: Review of laboratory results obtained from the SELFRAC project, 2008.

Van Loon, L.R., and A. Jakob, Evidence for a Second Transport Porosity for the Diffusion of Tritiated water (HTO) in a Sedimentary Rock (Opalinus Clay-OPA): Application of Through- and Out-Diffusion Techniques. Transport in porous media 61, 193-214, 2005.

Verma, A., Pruess, K. Thermohydrologic Conditions and Silica Redistribution Near High-Level Nuclear Wastes Emplaced in Saturated Geological Formations, J. Geophysical Res., 93, B2:1159-1173. 1988.

Walter, A.L., Frind, E.O., Blowes, D.W., Ptacek, C.J., Molson, J.W. Modeling of multicomponent reactive transport in groundwater, 1, Model development and evaluation. Water Resour. Res., 30 (11), 3137-3148, 1994.

Wiprut, D.; Zoback, M.D. Fault Reactivation and Fluid Flow along a Previously Dormant Normal Fault in the Northern North Sea, Geology; July 2000; v. 28; no. 7; p. 595–598, 2000.

Wolery, T. J., EQ3/6: Software package for geochemical modeling of aqueous systems: Package overview and installation guide (version 8.0), Lawrence Livermore National Laboratory Report UCRL-MA-110662 PT I, Livermore, California, 1992.

Xu, T., and K. Pruess, Coupled modeling of nonisothermal multiphase flow, solute transport andreactive chemistry in porous and fractured media: 1. Model development and validation, Lawrence Berkeley National Laboratory Report LBNL-42050, Berkeley, California, 38 pp., 1998.

Xu, T., and Pruess, K. Modeling multiphase fluid flow and reactive geochemical transport in variably saturated fractured rocks: 1. Methodology, *Am. J. Sci.*, v. 301, p. 16-33, 2001.

Xu, T., E. Sonnenthal, N. Spycher, and K. Pruess, TOUGHREACT: A simulation program for non-isothermal multiphase reactive geochemical transport in variably saturated geologic media. LBNL-56740. *Computer & Geosciences*, *32* (2), 145–165, 2006.

Xu, T., Sonnenthal E., Spycher, N. and K. Pruess, TOUGHREACT User's guide: A simulation program for nonisothermal multiphase reactive geochemical transport in variably saturated geologic media. Lawrence Berkeley National Report LBNL-55460-2008, 2008.

Yeh, G. T., and Tripathi, V. S. A model for simulating transport of reactive multispecies components: model development and demonstration, *Water Resour. Res.*, v. 27, p. 3075-3094, 1991.

Zhang C.L. and Rothfuchs T. Damage and sealing of clay rocks detected by measurements of gas permeability. Physics and Chemistry of the Earth 33: 5363-5373. 2008.